Variability in Low Mass X-ray binaries from milliseconds to years

UNIVERSITÀ DEGLI STUDI DELL'INSUBRIA

Dottorato di Ricerca in Astronomia e Astrofisica
XXIV Ciclo

Sara Motta

Merate, Italia

Relatore:	Dr. Tomaso Belloni
Co-Relatori:	Dr. Tiziana Di Salvo Prof. Luciano Burderi
Commissione:	Dr. Alberto Franceschini Dr. Laura Maraschi Dr. Silvia Zane

Facoltà di Fisica e Matematica

The research reported in this thesis was carried out at Osservatorio Astronomico di Brera-Merate (Italia).

The fight isn't over until you won it, Fitz.
That's all you have to remember.
No matter what the other man thinks.

Burrich, in *R*oyal Assassin, ch. 1 - Robin Hobb

Ai miei genitori,
perché mi hanno sempre sostenuto

A mio fratello,
perché mi ha sempre spronata (in maniere improbabili) a farmi valere

A Luca,
perché senza di lui non ce l'avrei mai fatta

A Paco,
perché una palla di pelo nero non ha prezzo

Contents

1 Introduction

We are the sum of all we have done added to the sum of all that has been done to us.

Fitz in *F*ool's Fate, ch.1 - Robin Hobb

This thesis has the aim of discussing phenomena that occur in systems that are known as low-mass X-ray binaries (LMXRBs). These systems are the most powerful objects in our Galaxy and they emit radiation over a large range of wavelengths. Here I will focus only on the X-ray emission. In this chapter, I briefly explain what these systems are, I provide an overview on the physics of X-ray binaries (XRBs) introducing some of the main phenomena that arise in them and I discuss the methods by which these systems are studied.

1.1 X-ray binaries

Many of the stars in our universe occur in binary systems, i.e., systems of two stars in orbit around a common center of mass. If one of the members of these systems is a compact object (neutron star - NS - or black hole, BH), and the system components are sufficiently close to allow accretion causing them to become very bright in X-rays, then they are called X-ray binaries.

X-ray binaries can be divided into high-mass X-ray binaries (HMXBs) and low-mass X-ray binaries (LMXBs) depending on the mass of the companion star. The companion to the X-ray source in HMXBs is a luminous star of spectral type O or B with mass typically larger than 10 $M_\odot$, necessarily belonging to a young stellar population as these types of stars do not live longer than $\sim 10^7$ years. In LMXBs the companion is a faint star of mass lower than 1 $M_\odot$ and tends to belong to a much

older stellar population, with ages that can be thousands of millions of years.

Depending on the mass and evolution stage of the companion and on the mass ratio of the stars in the system, there are two main ways for the donor star to transfer matter to the compact object: Roche-lobe overflow and wind accretion. In this thesis, I focus on LMXBs (see Fig. 1.1), where mass transfer from the companion star to the compact object is due to Roche-lobe overflow. The material from the companion star that passes beyond the so called Roche-lobe radius flows onto the compact object attracted by its gravity. Since the Roche-lobe radius is a function only of the orbital separation and the masses of the two stars, the onset of Roche-lobe overflow requires that either the envelope of the companion star expands (due to stellar evolution), or that the binary separation shrinks (as a result of orbital angular momentum losses). In either cases, the gas cannot fall directly onto the compact object because of the conservation of angular momentum. Matter does not fall radially towards the compact object, but orbits circularly at a certain radius from the collapsed star. If the timescale of energy loss is shorter than the time needed to redistribute the angular momentum in the ring, viscous dissipation causes energy losses that force matter to distribute into a sequence of circular concentric annuli with decreasing radius. This configuration is called *accretion disc*.

The most powerful phenomena we observe from LMXBs are directly related to the accretion mechanism, as a large amount of gravitational energy is released when the matter approaches the compact object. Viscous stresses convert the kinetic energy of the infalling matter into radiative emission. At large radii, far from the compact object, the accretion disc is relatively cold and emits at optical wavelengths. In the innermost regions of the disk the accretion flow can reach temperatures higher than $\sim 10^7$ K and emits in the X-rays. The bulk of the gravitational potential is indeed released in these regions, in the vicinities of the compact object. Therefore, the analysis of the X-ray emission from these sources is a fundamental tool we have to study the properties of compact objects and accretion disks.

X-ray binaries constitute very good natural laboratories where to test theories of gravity in extreme conditions (e.g. General Relativity) and physics of ultra-dense matter. In particular the study of systems harboring a NS allow to investigate the details of the equation of state (i.e., the mathematical description of the relations between temperature, pressure and density of matter) of these collapsed stars, where densities are thought to be higher than those in atomic nuclei.

A comprehensive study of XRBs cannot focus only on the accretion process. Relativistic jets (ejections of matter at velocities approaching the speed of light), which on far larger scales in Active Galactic Nuclei (AGNs) are among the most powerful phenomena in the Universe, are now thought a near-ubiquitous phenomenon in XRBs. These jets are collimated anti-parallel outflows of matter launched at relativistic velocities from regions very close to the central compact object and seem to be strictly

related to the disk accretion mechanism onto relativistic objects.

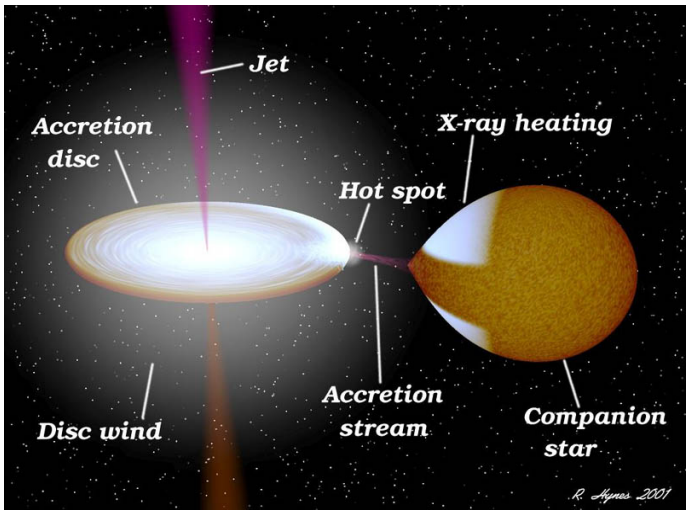

Figure 1.1: Artist's impression of an X-ray binary system, in which all its main elements are marked. Illustration from R. Hynes, 2001.

1.2 Instrumentation and techniques

In this thesis I study LMXBs by means of energy spectra and time variability analysis. The combination of these two methods has proven to be very appropriate in describing the X-ray behavior of LMXBs.

Below, I briefly describe the instruments and techniques used.

1.2.1 The Rossi X-ray Timing Explorer

The results presented in this work are based on data obtained with the *Rossi X-ray Timing Explorer* (*RXTE*, Bradt et al., 1993). It was launched on December 30^{th}, 1995 and, at the time this thesis goes to press, is still operating. Figure 1.2 shows a schematic view of the satellite.

There are three scientific instruments on board the satellite, namely the All Sky Monitor (ASM, Levine et al., 1996), the High Energy X-ray Timing Experiment (HEXTE, Gruber et al., 1996; Rothschild & Heindl, 1998) and the Proportional Counter Array (PCA; Zhang et al., 1993; Jahoda et al., 2006).

The ASM observes $\sim$80% of the sky each orbit with a spatial resolution of $3 \times 15'$, it operates in the 1.5–12 keV range and has a time resolution of 1/8 seconds. The ASM plays an important role in identifying state transitions and outbursts from tran-

sient sources, allowing us to trigger follow-up observations with other instruments within a few hours. The instrument also permits us to monitor the long-term intensity and behavior of the brightest X-ray sources.

The HEXTE has a field of view of $\sim 1^\circ$ and operates in the 15–200 keV range. It consists of two photon counter detectors, each having an area of ~ 800 cm^2, an energy resolution of 18% at 60 keV, and a time resolution of 10 μs. Due to the large field of view and the lack of spatial resolution, background estimation can be an issue. This problem is solved by making both clusters oscillate ("rock") between on and off source positions (1.5° or 3° from the source), every 16 or 32 seconds. The data from this instrument have been used in this thesis mainly to better estimate the X-ray luminosity of sources.

The PCA is the main instrument on board *RXTE*. It is a pointed instrument, co-aligned with the HEXTE and having the same collimated field of view of $\sim 1^\circ$. It consists of five Proportional Counter Units (PCUs) with a total collecting area of ~ 6250 cm^2, operates in the 2–60 keV range, has a nominal energy resolution of 18% at 6 keV and, most importantly for this thesis, a maximum time resolution of $\sim 1\mu$s. With the exception of regions near the center of the Galaxy, the source density on the sky is low enough to provide sufficient positional resolution and avoid source confusion.

1.3 X-ray observations of X-ray binaries

1.3.1 Timing analysis

The analysis of the rapid variability in the X-ray emission form XRBs constitutes one of the main instruments to probe the matter accreting onto the compact object. By means of the analysis of the rapid variability in the X-ray emission we can probe the properties of the matter orbiting in the inner accretion flow, in regions dominated by strong-gravity fields. The main analysis tool is the Fourier power spectrum of the X-ray flux time series. By applying a Fourier transform to the flux time series, it is possible to obtain an estimate of the variance, in terms of power density P_ν, as a function of the Fourier frequency ν (see van der Klis 1989 for the details). By using the Fourier analysis, we study the data in the frequency domain (i.e. power density spectrum, PDS) rather than in the time domain (i.e. the light curve). Since the Fourier power is proportional to the light curve variance, in a power spectrum we can basically see if there are preferred frequency in the signal. Therefore, we can easily spot the presence of periodicities or quasi periodicities (in case the frequency of the signal is not perfectly constant) in the light curve. Highly coherent features, such as pulsations in accreting millisecond X-ray pulsars, appear as single frequency-bin spikes. Aperiodic structures, instead, are spread over several frequency bins, sometimes cov-

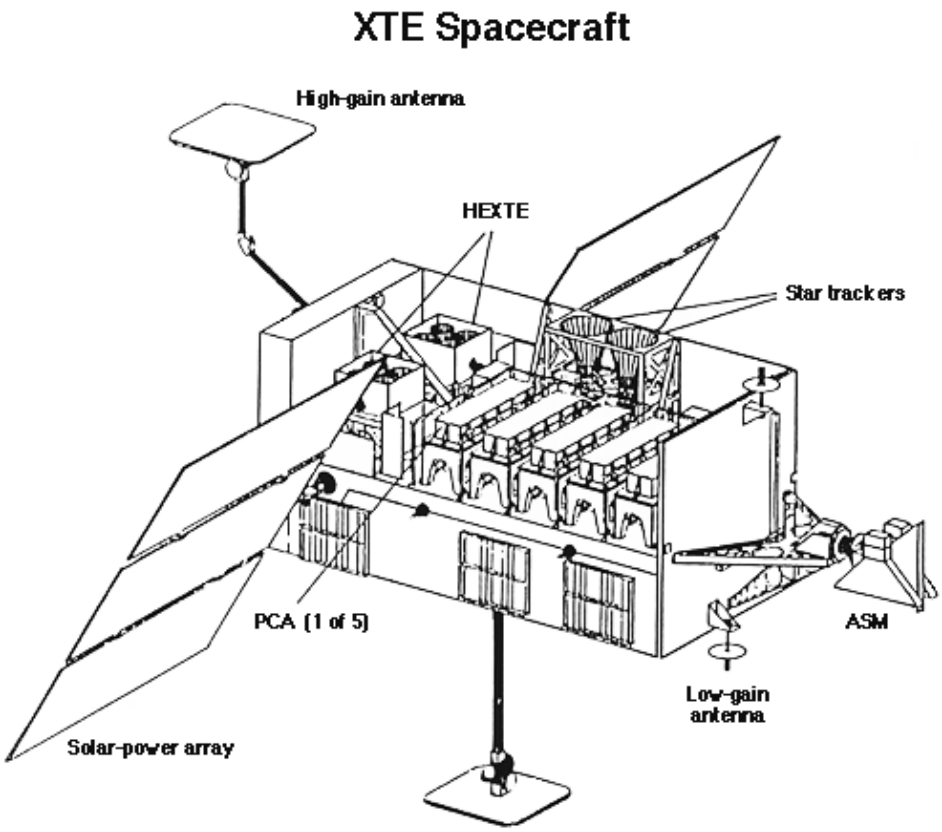

Figure 1.2: Diagram of the XTE spacecraft, with instruments labeled.

ering the entire mHz-kHz frequency range. Broad structures are usually called *noise*, while narrow-peaked features are usually referred to as quasi-periodic oscillations (QPOs). Figure 1.3 shows typical power density spectra of BHs. Although the centroid frequency of these peaks (quasi-periodic oscillations, QPOs) detected in some BHs can be as high as ∼450 Hz, in this thesis I focus on low frequency features (at frequencies lower than ∼40 Hz.). Figure 1.4 shows several power spectra typical of high-luminosity NSs, the so called Z sources (Hasinger & van der Klis 1989). As one can clearly see, a power density spectrum consists of a superposition of different components.

Despite several years of X-ray observations of XRBs at high time resolution, no exhaustive and complete physical model is available to interpret the X-ray variability features in the power spectra and robustly relate them to typical timescales of the accretion flow (see van der Klis 2006 for a review; see also Chapter 5). However, following Belloni et al. (2002), a unified phenomenological description of these timing features is possible by fitting the power density spectra with a superposition of

power spectral multi-Lorentzian components. The characteristic frequency (ν_{max}) of L_i is denoted ν_i. The *quality factor* Q is defined as $Q = \nu_0/\mathrm{FWHM}$. *FWHM* is the full width at half maximum and ν_0 the centroid frequency of the Lorentzian. Q quantifies the coherence of a certain aperiodic signal. The higher it is, the more coherent is the signal. It is particularly useful to study narrow features in the PDS. The choice of a Lorentzian is justified by the fact that it is the Fourier transform of an exponentially damped harmonic oscillator. Although the use of this function allows to fit power spectra reasonably well and to follow the evolution of the peaks in terms of frequency and strength, there is no physical reason to prefer Lorentzians to other functions, e.g. Gaussians plus power laws. The big advantage of a unified description is the possibility of comparing directly different observation and sources, in relation to other observational parameters.

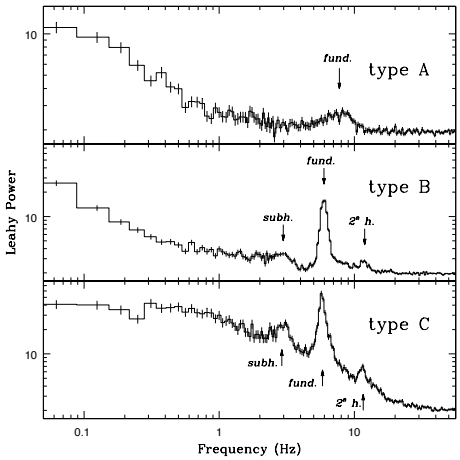

Figure 1.3: Low frequency QPOs in the BH XTE J1859+226, from Casella et al. (2004). The QPOs are named after Wijnands et al. (1999). The poissonian noise have not been subtracted from the spectra.

1.3.2 Spectral analysis

Broad-band spectral modeling and interpretation is essential to understand the physical origin of the emission coming from XRBs, i.e. thermal emission from the accretion disk, non-thermal emission from hot electron in a *corona*, synchrotron emission from the jets. Fitting energy spectra (usually by means of χ^2 test statistics) with specific theroertical models allow to extract important physical quantities (i.e. temperature of the inner disk radius, energy of the Comptonizing electrons and optical depth of the Comptonizing medium) and directly investigate the geometry of the in-

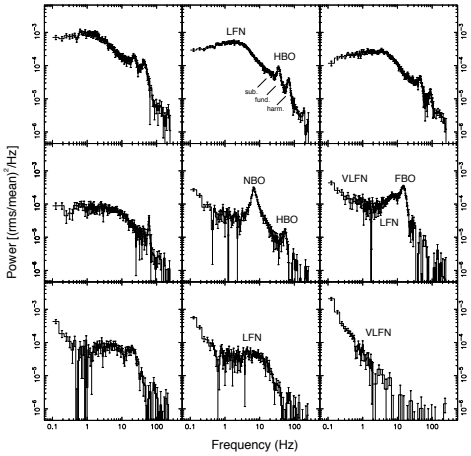

Figure 1.4: Power-density spectra from the Z source GX 17+2 form Homan et al. (2002). The QPOs are named after Hasinger & van der Klis (1989).

flow and the outflow, and their contribution to the total energy output of the system. This is fundamental also to infer how the accretion/ejection mechanism works.

Although the properties of the accretion flows of BHs are not always well determined and there is debate on many issues, their spectra are thought to be the result of the three different physical components contributions: 1) an optically thick, geometrically thick accretion disk; 2) a distribution of hot electron (what is usually called corona) able to Comptonize the emission from the accretion disk; 3) a jet (i.e. a relativistic matter outflow) produced in the very center of the system that is thought to contribute to the X-ray emission (even though its emission bulk is found in the infrared and in the radio band). In the case of NSs a fourth component is usually observed: the black-body emission from the surface is clearly visible in the spectra.

Many different refined models, built on the basis of the mentioned physical components, can be used to describe energy spectra. Fitting energy spectra with motivated models allow to follow the variations in the spectral parameters as function of the time and describe the evolution of a source in terms of changing physical quantities.

In the best case scenario the X-ray energy spectrum of a given source can be described by the combination of one or more physically motivated mathematical functions or models. However, the physical reality of these models is still uncertain and in many cases the data can be satisfactorily described by different models, making the results of such spectral analysis inconclusive. In addition, spectral fitting has the inconvenience to depend strongly on the models used. A model-independent approach that is widely adopted makes use of the X-ray colors to roughly estimate the spectral properties of XRBs. colors are defined as hardness ratios between the X-ray counts (the number of photons detected) in two different broad energy bands. Plotting two

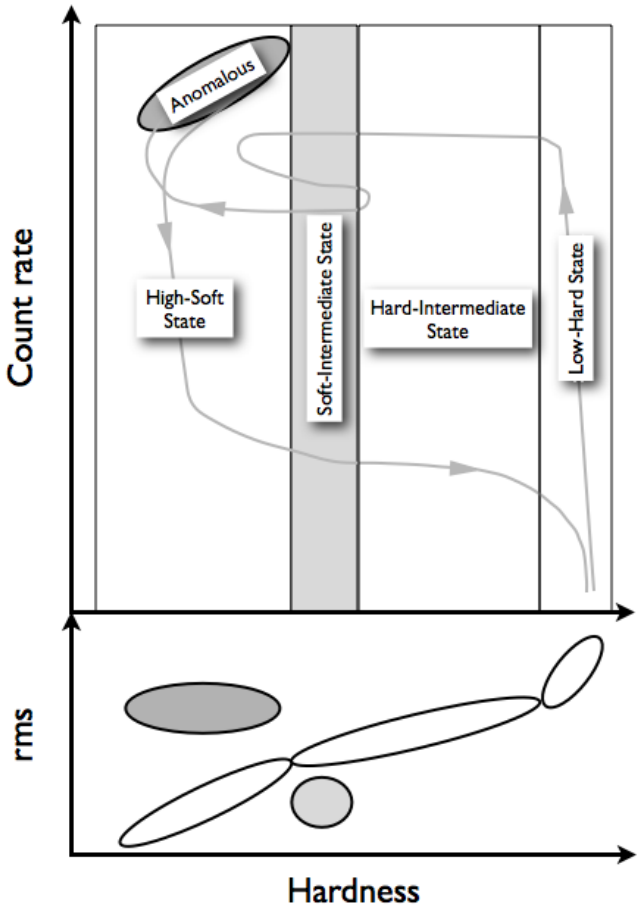

Figure 1.5: Sketch of the general behavior of a black-hole transients in the HID (top) and hardness-rms diagra (HRD, bottom).

colors against one another (color-color diagram, CCD) or a color versus the count rate (hardness-intensity diagram, HID) constitutes a powerful tool to trace recurrent characteristic patterns that occur in XRBs. The energy bands used to create the colors are about the same within the same class of XRBs (BHs or NSs). Figure 1.5 (upper panel) shows the sketch of a typical transient black-hole binary HID (from Belloni 2010). The position of a source in the X-ray HID can be used to infer its spectral status. Although the mass accretion rate is probably one of the parameters that drive the transition between the states, we still do not fully understand how and why transition happens and which other parameters interfere.

The different behaviors traced in time by XRBs is interpreted as due to different accretion regimes. Naively, softer means more relative emission coming from the accretion disk, thus an increase in mass accretion rate. Of course, when dealing with

real observations nothing is simple and straightforward.

In order to achieve a more complete picture of the phenomenology of these sources and a better understanding of the physics of XRBs, the key is the use of all the methods described combined, e.g. power spectral and energy spectral variations as a function of the position on the HID or CCD. Many properties of both power density and energy spectra are now know to be strictly correlated to the position of the source in the HID or CCD, allowing to classify sources and define *states*.

1.4 Long term X-ray variability of LMXBs

In the context of X-ray variability at time scales of hours, days and up to years, low-mass X-ray binaries can be divided into two main classes: the so called *persistent* and *transient* sources. The persistent ones are those which have been active since the beginning of X-ray astronomy. Transient sources are those which are generally very faint or not observable (quiescent state, 10^{-9}–10^{-8} L_{Edd}), but occasionally show phases during which the count rate can increase by several orders of magnitude (outbursts, X-ray luminosities of 0.1-1 L_{Edd}).

In Fig. 1.6 can be observed the long-term variability of several BH binaries, while in Fig. 1.7 one can see lightcurves for several NS binaries.

In the case of transient sources, outbursts are usually unpredictable, except in a few sources, the behavior of which can be predicted with the uncertainty of few days. Not all outbursts from the same source reach the same intensity or last for the same amount of time.

1.5 Black Hole X-ray binaries

BH XRBs shows different accretion states, defined according to the position and the path that the source follows in an X-ray HID (see chapter 2 and Belloni 2010 for a review; see also McClintock & Remillard 2006 for an alternative definition of the states). Four X-ray spectral canonical states (plus an *anomalous* state) can be identified in the HID during the outburst (indicated in Fig. 1.5).

The X-ray spectral properties of black holes can be classified into two main components: when a hard, non-thermal, power-law-like component (associated to Comptonization processes) with photon index in the range 1.5–2 dominates the energy spectrum, it is said that the source is in its *low/hard state* (LHS); when a soft, thermal, black-body like component (due to the accretion disk soft emission) with temperature $kT \lesssim 1\,\mathrm{keV}$ dominates, then the source is in its *high/soft state* (HSS).

In between the low and the high states, there is the intermediate state which links both extremes and where complex behavior, including sometimes large flares in intensity, occur. This intermediate state can be subdivided into the Soft Intermediate

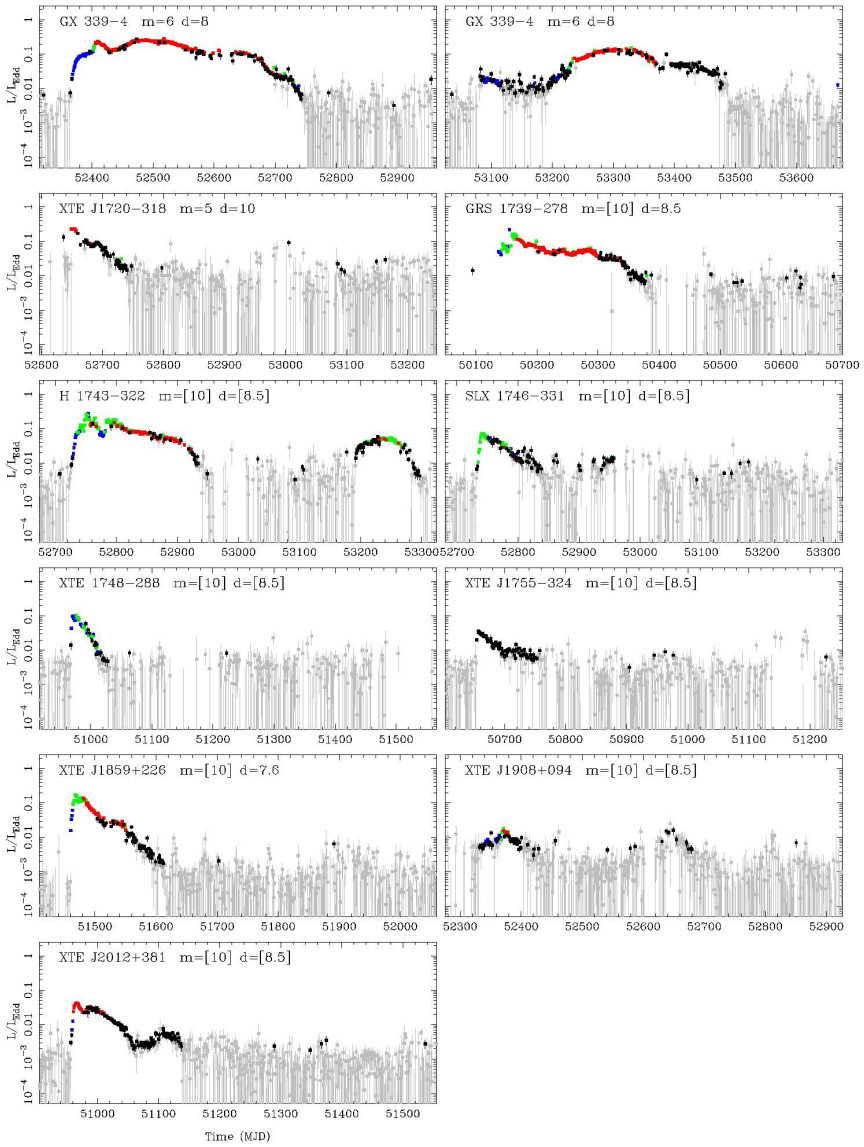

Figure 1.6: RXTE All Sky Monitor light curves of BH LMXB showing the outburst behaviour from Done et al. (2007).

State (SIMS) and the Hard Intermediate state (HIMS) based mainly on the X-ray time variability (see, e.g., a discussion in Belloni, 2005).

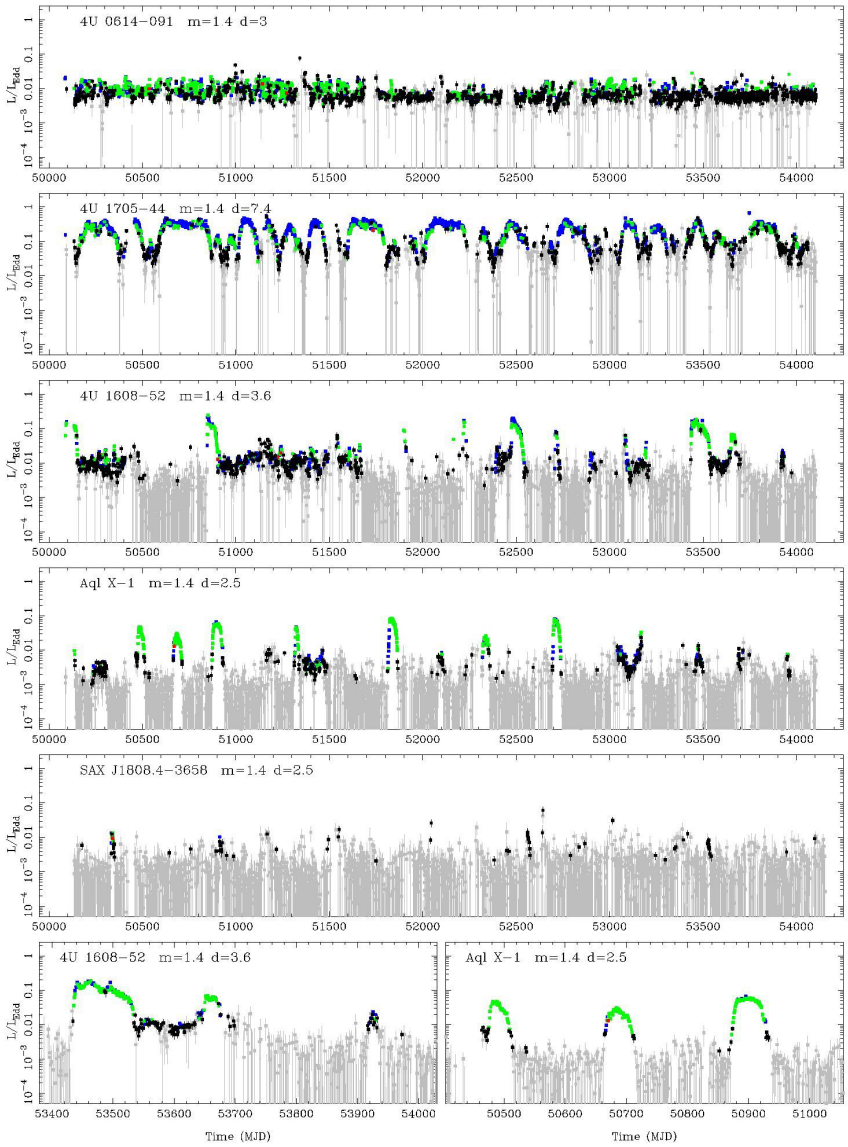

Figure 1.7: RXTE All Sky Monitor light curves of NS LMXB (Atoll sources) from Done et al. (2007). In contrast to the BH binaries, most of the known systems are persistent.

Observations suggest that during the LHS the accretion disc is cold (with temperature T $\leq$ 1 keV) and truncated at large radii (e.g. McClintock et al. 2001, Belloni

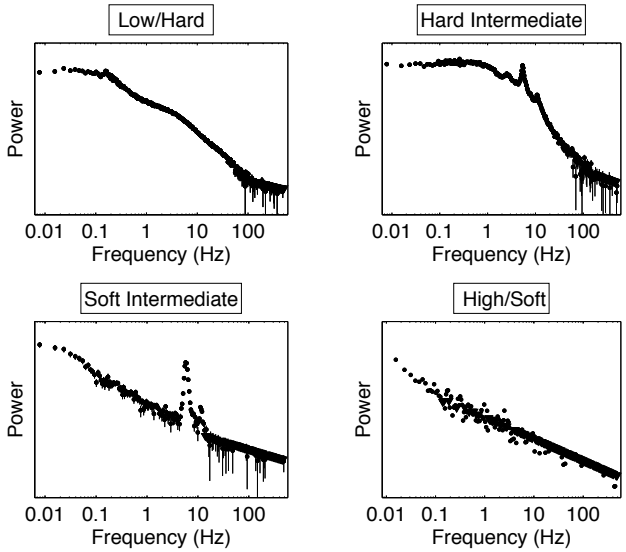

Figure 1.8: Typical power density spectra of the BH XRB GX 339-4 in outburst, from Homan et al. 2005. Each power spectrum is representative of one spectral state. See Figure 1.5 for a connection between the spectral state and the position of the BH in an X-ray HID.

2010, Belloni et al. 2011) at low luminosities (lower than 1% L_{Edd} ; Cabanac et al. 2009). During the HSS instead, it is thought that the inner accretion disk radius is close to or coincident with the innermost stable orbit and the temperature at the radius might be higher than 1 keV. During the last years it has been suggested (see e.g. Miller et al. 2006, Reis et al. 2009) that the accretion disc might extend to the vicinity black hole (close to the innermost stable orbit) even in the LHS at very low X-ray luminosities.

X-ray spectra of BH XRBs in the LHS have also been found to feature iron emission lines, produced by the reflection of the Comptonized photons off the accretion disc. It is important to ascertain whether these lines are present and to measure their broadening that, after having assumed a certain spectral model, can give information on the inner boundaries of the accretion flow.

In timing studies, the LHS and the intermediate states show strong QPOs and strong broad band noise (up to 60% fractional rms) components while the HSS and SIMS are characterized by weak/absent variability: the PDS show weak variability and a weak powerlaw noise, on top of which a QPO can be observed. Fig. 1.8 shows typical power density spectra of BHs in the four spectral states in outburst. The type-C QPO is typical of the LHS and the HIMS, while the type B has been associated with the transition between the HIMS and the SIMS. Type A is probably associated to the HSS instead. More details on this topic are given in Chapter 2 and 5

1.6 Neutron star X-ray binaries

Observationally, low-magnetic field neutron stars can be classified into two main groups, according to their X-ray spectral and timing properties. Based on the pattern that they draw in an X-ray CD, Hasinger & van der Klis (1989) named them Z sources and atoll sources (see Fig. 1.9). Atoll-type NS XRBs constitute the majority of low-magnetic field accreting neutron stars. They display a broad range of X-ray luminosities in the range ~ 0.01–0.5 L_{Edd} (where L_{Edd} is the Eddington luminosity). This class possibly includes also the accreting millisecond X–ray pulsars and several faint and very faint (with X-ray luminosities below 0.001 L_{Edd}) NS XRBs (see van der Klis 2006). Atoll sources feature three states: extreme island state (EIS), the island state (IS) and the banana branch, the latter subdivided into lower-left banana (LLB), lower banana (LB) and upper banana (UB) states (see Fig. 1.9). The hardest and lowest luminosity state is generally the EIS, which shows strong low-frequency noise. The IS is, instead, spectrally softer than the EIS. At higher luminosities the banana states are found.

Z-type NS XRBs represent a class of few persistent sources (e.g. Sco X-1, GX 17+2, GX 349+2, Cyg X-2, GX 5-1, GX 340+0) plus the transient source XTE J1701-462 (that switched to an atoll source near the end of its outburst; see Homan et al. 2007, Lin et al. 2009). Z-type NSs accrete at high rate (0.5 – 1.0 L_{Edd}) and are the brightest X- ray sources in our Galaxy. Sco X-1 is actually the first XRB ever detected (Giacconi et al. 1962). They usually draw a Z-shaped pattern in the X-ray CD (or HID; Fig. 1.9., panel c) in which the three characteristic branches are called Horizontal, Normal and Flaring branch (HB, NB and FB, respectively). Each branch defines a spectral state, with distinct timing and jet properties. Z sources are rapidly variable in the X-rays and can trace the whole Z pattern on timescales of hours to days. Interestingly, the shape of the path that they draw in the CD (and in the HID) can change with time, and the only known transient Z source (XTE J1701-462) exhibited a transition from Z-type to typical atoll-type properties. The mass accretion rate is supposed be responsible for these changes. However, it is not completely clear what drives the transition between the different spectral states (both in atoll and Z sources): both the local mass accretion rate and disc instabilities could be responsible for that (Lin et al. 2009), although other factors can not be excluded.

1.6.1 Thermonuclear burning on the neutron star surface

Unstable burning

Thermonuclear X-ray bursts constitute a very peculiar phenomenon that can only be observed in NS. They are also called Type-I X-ray bursts and manifest as a sudden, unpredictable and rapid increase in the X-ray intensity of accreting neutron stars

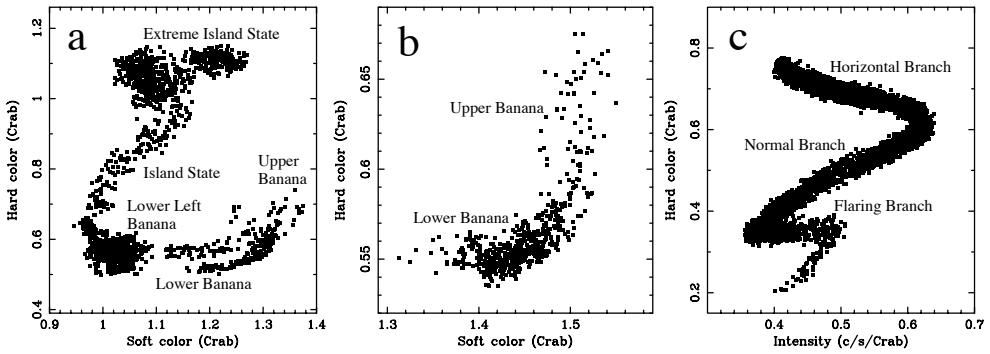

Figure 1.9: Panels a and b: CDs of two atoll sources, 4U 1608-52 and GX 9+1, respectively. Panel c: typical HID from a Z source, GX 340+0. Adapted from van der Klis (2006).

lasting between few seconds and few minutes (see Maraschi & Cavaliere 1977).

The rise is generally followed by a smooth and approximately exponential decay with variable length.

As matter accumulates on the surface of the neutron star, it is compressed and heated until the temperature and density at the base of the accreted layer become large enough for the fuel to ignite in a "burning spot". The matter burns unstably consuming the available fuel as the burning spot spreads rapidly over all the neutron star surface in matter of seconds. Time-resolved spectral analysis of this type of bursts shows that the rise and the exponential decay can be interpreted as heating resulting from the initial fuel ignition, followed by cooling of the ashes once the available fuel is exhausted.

Although X-ray bursts were known since the 1970s, it was only in the RXTE era that highly coherent (burst) oscillations associated with thermonuclear bursts were discovered (see Figure 1.10 for a typical burst with burst oscillations). These oscillations have frequencies between 45 and 620 Hz, fractional rms amplitudes between 5 and 20% and have been detected in bursts from less than 20 sources so far (Strohmayer & Bildsten 2006, Galloway & Cumming 2006). As the burst evolves, the frequency of these oscillations generally increases by a few Hz as it reaches an asymptotic value, which has been found to be stable (within $\sim$ 1 Hz) for a given source. The asymptotic frequency reached is an excellent estimate of the spin frequency (within $\sim$ 1 Hz) for a given source as has been confirmed by the detection of burst oscillations at the spin frequency in the accreting millisecond pulsars SAX J1808.4–3658 and XTE J1814–338 (Chakrabarty et al. 2003, Strohmayer et al. 2003.

Marginally stable burning?

Revnivtsev et al. (2001) discovered a new class of quasi-periodic oscillation in the

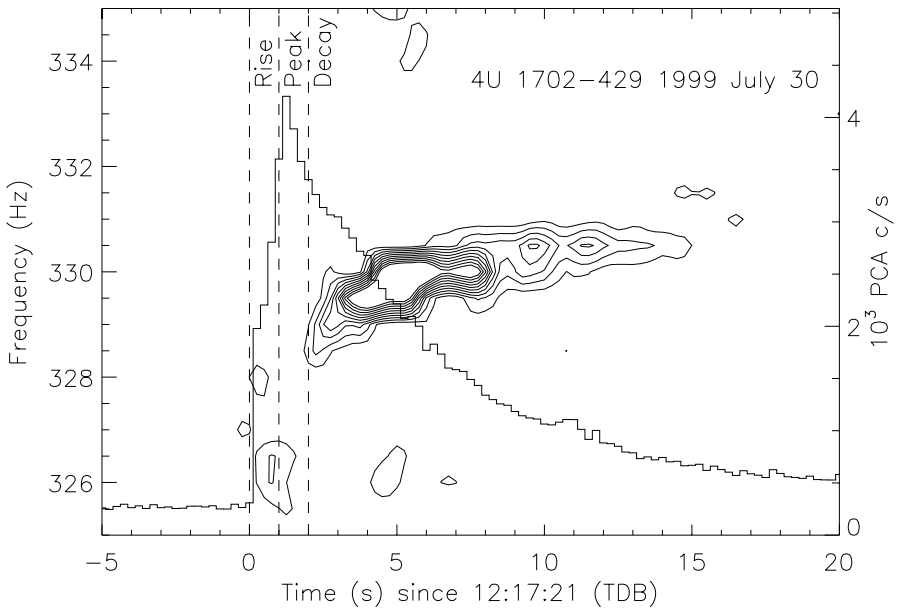

Figure 1.10: X-ray burst lightcurve (histogram) and dynamical power spectrum illustrating the typical frequency evolution of a burst oscillation (contours). The left axis marks the frequency of the oscillations and the right one the PCA count rate. Taken from Galloway & Cumming (2006).

persistent emission (i.e. not during Type-I bursts) from three neutron star X-ray binary sources. These new QPOs have frequencies in the milli-Hertz range and are usually seen before a Type-I X-ray burst, but not immediately after. It is important to notice that their properties differ from those of the other QPOs found in neutron star systems (e.g., energy dependence, see also van der Klis, 2006). Although Revnivtsev et al. (2001) could not discard an interpretation related to disk instabilities, they conclude that the mHz QPO is likely due to a special mode of nuclear burning on the neutron-star surface. Such an interpretation is strengthened by the results of Yu & van der Klis (2002), which suggest that the inner edge of the accretion disk slightly moves outward as the luminosity increases during each mHz cycle due to stresses generated by radiation coming from the neutron star surface. Based on numerical simulations, Heger et al. (2007) show that the mHz QPOs might be explained as the consequence of marginally stable nuclear burning on the neutron star surface. They find that the burning is oscillatory only close to the boundary between stable burning and unstable burning (i.e., Type-I X-ray bursts).

Figure 1.11 show a representative light curve where mHz oscillations are present

before the occurrence of an X-ray burst and not after. As it is clear from the figure, when present, these oscillations can be seen directly in the light curve.

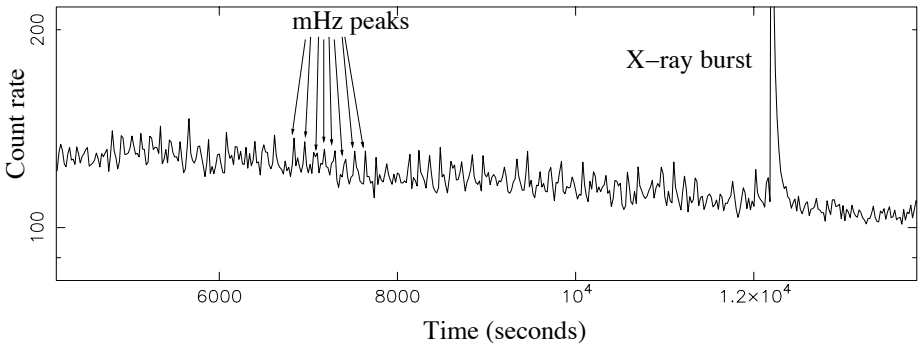

Figure 1.11: Light curve of a data segment in which the mHz QPOs are present prior to the occurrence of an X-ray burst. Before the X-ray burst occurs, the oscillations are clear from the light curve while after the burst they seem to disappear. Fourier analysis confirms this.

1.6.2 Millisecond pulsars

Radio pulsars are thought to be highly magnetized ($\gtrsim 10^8$ Gauss) rotating neutron stars which emit a collimated beam of radio waves. The youngest radio pulsars are observed to rotate rapidly, up to 100 times per second. This rapid rotation combined with the high magnetic field strength (10^{12-13} Gauss) of the neutron star produces beamed radio emission at the magnetic poles, and since the magnetic poles "are fixed" on the neutron star, the beams spin at the frequency of the neutron star (ν_s). After a radio pulsar is born, because of the energy loss due to its emission, it slows down until ν_s is so low (lower than a few tenths of Hz) that the pulsar mechanism is not able to produce detectable radio emission anymore and it is said that the pulsar has died. This process takes millions of years, depending on the initial spin frequency and magnetic field strength of the neutron star.

If it is true that new pulsars have frequencies not higher than ~ 100 Hz, and that their spin frequency decreases with time, then there is the need to identify a process able to produce radio pulsars with much higher spin frequencies than 100 Hz, the fastest now being 716 Hz (Hessels et al., 2006). In the early 1980s, Alpar et al. (1982) explained these fast pulsars as follows. If a radio pulsar is born in a binary system which does not get disrupted by the supernova explosion in which the neutron star is formed, it might be possible that the companion star or the binary orbit evolves in such a way that at a certain moment the companion star fills its Roche lobe. When this happens, matter is exchanged from the companion to the neutron star, spinning it up by the transfer of angular momentum. When accretion stops the system is left

with neutron star that rotates at several 100 Hz and appears again as a radio pulsar. The resulting neutron star has a weak magnetic field ($\sim 10^8$ Gauss, in contrast to the 10^{12-13} Gauss in the young pulsars). It is thought that the accretion is responsible for reducing the magnetic field strength, however, the process for this is as yet poorly known (Bhattacharya & van den Heuvel, 1991).

If the neutron stars in X-ray binaries are rapidly rotating as predicted by Alpar et al. (1982), it would be possible, in principle, to see pulsations in X-rays as well. The first observational indication that neutron stars in low-mass X-ray binaries rotate rapidly came in 1996 with the discovery of millisecond oscillations (with frequencies that usually show drifts) during thermonuclear X-ray bursts (see Section 1.6.1). However, it was only in 1998 that the first accreting millisecond X-ray pulsar was discovered (Wijnands & van der Klis, 1998). Since then a total of 14 (and even 15 if we consider Aql X-1 as an accreting millisecond pulsar) have been found out of a sample of more than 150 neutron star LMXBs known up to date. These systems are known as Accreting Millisecond X-ray pulsars (AMXPs, also referred to as AMPs in the literature) and are thought to be accretion-powered; gas coming from the accretion disk couples to the star's magnetic field and gets channeled, forming "hot spots" perhaps at the magnetic poles, which can be seen in X-rays. These hot spots are fixed on the neutron star surface and therefore rotate with the spin frequency of the neutron star similarly to what happens in the case of radio pulsars.

An important and not yet resolved issue is why most neutron star LMXBs do not show persistent pulsations in their X-ray emission. Several theoretical efforts have been made to explain this, the main question remaining whether the pulsation is hidden from the observer (e.g. there is a scattering medium that washes out the coherent beamed pulsations) or not produced at all (e.g., because the magnetic field is too weak to channel the accreting matter). So, given that pulsations were only seen from a few sources, in the literature (up to now) the neutron star systems were sub-classified into pulsating and non-pulsating ones. The recent discovery of HETE J1900.1–2455 showed that this classification might not cover all systems. This was the first AMXP which did not show persistent pulsations throughout the outburst, but only during the first $\sim$ 2 months. Sudden increases in the amplitude of the pulsations were apparently triggered by thermonuclear X-ray bursts; the amplitude decreased steadily on timescales of days after the bursts (Galloway et al., 2007). This source was also different from the other AMXPs, as it has been in outburst for more than 3 years, while typical AMXP outbursts last for no more than a few weeks or months. This difference suggested that the accumulation of matter on the surface was burying the magnetic field (Galloway et al., 2007) and therefore extinguishing the pulsations. If the accumulation of matter is the key process that buries the magnetic field, then this result could explain why most of neutron star LMXBs do not show pulsations.

Casella et al. (2008) and Altamirano et al. (2008a) reported the discovery of episodes

of intermittent coherent millisecond X-ray pulsations in two X-ray transients. These pulsations appear and disappear on timescales of hundreds of seconds and can be identified as occurring at the spin frequency of the respective sources. These short time scales cannot be explained by the burying scenario proposed for the intermittent AMXP HETE J1900.1–2455. Another important conclusion of these discoveries is that irrespective of the physical mechanisms behind the pulsations, it is now clear that a strict division between pulsating and non-pulsating neutron star sources cannot be made. It is possible that all sources pulsate occasionally, although the recurrence times could be very long.

1.7 Problems, objectives and techniques

In this thesis I present an extended study on variability observed in transient sources of different kind with the aim of studying the accretion process in the particular context of transient X-ray binaries, that going through large ranges of mass accretion rate during their outbursts, offer the possibility to study how their properties change within a quite large accretion rate range. I mostly worked to evidence the main relations between time and spectral variability properties in my target sources. To pursue my goals I extensively used X-ray spectral analysis applied to the data simultaneously with timing techniques mostly focused on fast aperiodic variability. I mainly dealt with low-mass X-ray binaries harboring a black hole, even though I also studied the peculiar behavior of a transient accreting millisecond X-ray pulsar featuring interesting characteristics (see Chapter 11).

For what concern the accretion process, black hole binaries can be considered rather simpler than neutron star binaries. This is mostly related to the presence of a physical surface (and therefore of a boundary layer and an atmosphere) in neutron stars that origins a number of complications when studying these objects. The typical X-ray spectrum of an accreting black hole is usually constituted by two main different components (one originated by the accretion disk and the other related to Comptonization processes) that can be relatively easily disentangled and the evolution of which can be usually followed quite well along the outburst evolution. In the case of neutron stars, instead, the energy spectrum usually shows an additional component that partly overlap with the accretion disk component and partly affects the Comptonization emission. This causes confusion between the components that results difficult to disentangle. The contribution of the surface is consistent also in the time domain: while accreting black holes show aperiodic variability mostly below few tens of Hz (only sometimes above 30 Hz and basically never above 100 Hz), neutron stars display strong variability over a much larger frequency range, sometimes up to the kHz (in the form of noise and kHz quasi periodic oscillations). Light

curves of neutron star binaries also display a number of peculiar features still related to the presence of a surface - such as bursts of various nature (i.e. type-I and -II X-ray bursts, see Chap. 11) - that makes the phenomenology of those objects rather complex. In addition, neutron stars also feature a magnetic field that can strongly affect the accretion process in the vicinity of the compact object, where most of the gravitational energy is released and consequently where the effects of accretion are more important and the emission more powerful.

Therefore black holes constitute more desirable candidates to study accretion and the related processes (such as relativistic ejections of material from the compact objects), as it is in principle possible (at order zero) to ignore whatever happens in the region enclosed in the innermost stable orbit (the same region that is dominated by the presence of a surface and a strong magnetic field in neutron stars), allowing to concentrate only on the mere effects of accretion and, by means of the accretion itself, the effect of general relativity in strong field regime. Nevertheless also among accreting black holes it is possible to find exotic objects (e.g. GRS 1915+105, Belloni et al. 1997 and its newly discovered brother IGR J17091–3624, see Altamirano et al. 2011b) whose understanding and modeling of represent a real challenge.

X-ray variability on time-scales of milliseconds to years is among the most evident properties in XRBs and also represents a key ingredient to understand physical processes acting in these systems.

Outbursts occur every several months or years depending on the source and on its properties. During outbursts X-ray energy spectra of BHBs evolve significantly on timescales often shorter than a day. Those changes generate fast transitions between different spectral states (see Chap. 2) and are thought to be the result of abrupt modifications in the geometry of the system or in its physical conditions. Even though accretion has been studied for many years and several theoretical models to explain it have been developed, we still do not have a complete understanding of the origin and evolution of the emission of XRBs, and the mechanism driving spectral transitions still remains unknown. as secular variations as well as very fast changes. Most of the power spectral components are broad (indicating the presence of aperiodic variability) and can take the form of a wide power distribution covering several decades of frequency or of a more localized peak (QPOs, see Chap. 5). Low frequency QPOs have been discovered in many black hole transients and are thought to originate in the innermost regions of the accretion flow. Therefore, they constitute an extremely valuable tool to probe accretion very close to a compact object. However, the origin of the fast time variability is still unclear and its nature remains a matter of debate.

Fast time-variability properties are clearly seen to change significantly in BHTs as a function of spectral properties and spectral and temporal domains are undeniably strictly linked to each other. Nevertheless we still lack an exhaustive model able to

fully explain simultaneously the properties of both. The results of timing analysis alone so far proved to be inconclusive for the understanding of variability, while detailed spectral studies are not enough to fully comprehend the nature of the physical processes at work when the key role of variability is ignored. However, even if we lack the capacity to fully describe the wide phenomenology of accreting binaries, spectral and timing analysis could have provided a huge amount of information that, even still needing to be placed in a coherent scheme, constitutes an essential base to the comprehension of the bigger picture.

In this thesis I present a comprehensive study extended over several sources involving simultaneous spectral and timing analysis. The results that I report here include interesting relations between spectral and timing properties that put great emphasis on the importance of the relation between these two domains. Through the systematic use of spectral and timing analysis that I successfully applied to the systems I studied, I have been able to identify source-peculiar and general relations between spectral and timing properties (e.g. specific spectral parameters - see Chap. 3 and properties of broad-band variability and/or low-frequency QPOs - see Chap. 5) that serve as constraints to study the transition mechanism by analyzing its effects on physical observables. Recent works (see Ingram et al. 2009, Ingram & Done 2010, Ingram & Done 2011) have shown that it is possible to explain broadband variability, low-frequency QPO and spectral evolution of black hole transients as the result of a combination of changes in the geometry of the accretion flow and General Relativistic effects. As the most remarkable finding of the present work, I successfully used the model presented by Ingram et al. 2009, Ingram & Done 2010, Ingram & Done 2011 to interpret the results that I obtained during my PhD strengthening the validity of a combined spectral/timing approach as a powerful tool to probe accretion. Through the results that I have obtained I significantly contributed to create a complete and coherent observational framework on which to base theoretical studies that will eventually lead to the comprehension of the accretion mechanism, that will be exploited as one of the most powerful tools to probe General Relativity.

GX 339-4 constitutes the principal subject of the research in the present work. GX 339-4 (V821 Ara) is a Low Mass X-ray Binary (LMXB) harboring a $> 6\ \mathrm{M}_{\odot}$ accreting black hole (Hynes et al. 2003; Muñoz-Darias et al. 2008). Since its discovery (Markert et al. 1973) the system has undergone several outbursts that were intensely monitored in X-rays, but also at other wavelengths (i.e. radio and optical/infrared bands). The peculiar regularity of this source, especially evident in its hardness-intensity diagrams provided to GX 339-4 the reputation of well-behaved source and for this reason it became one of the most studied X-ray transient. GX 339-4 is usually referred to as the prototypical black hole transient and it is widely used for comparison to describe the behavior of other sources of the same class.

1.8 Outline of this thesis

Here I briefly describe the content of each chapter explaining why I analyzed certain systems, the methods I applied to analyze their properties and the main results that I obtained. I had a leading role in the work reported in Chap. 3, Chap. 5, Chap. 7 and Chap. 11 and I actively participated to all the works that I report in this thesis performing a considerable part of the data analysis. I also substantially contributed to outline the ideas that guided the analysis in most of the cases as well as to the physical interpretations of the results. I include in this thesis all the works where my contribution was considerably significant. I am also co-author of other works (see *List of Publications* at the end of this thesis) that I did not report here.

- In **Chapter 2**, I review the current observational standpoint as the result of sixteen years of activity of the observations of black-hole transients with the Rossi X-ray Timing Explorer, complemented by other X-ray observatories and ground-based optical/infrared/radio telescopes. I put emphasis especially onto the spectral and timing evolution during outbursts of black hole binaries, identifying the peculiar properties of the sources during their evolution. I also describe the prospects for future missions such as ASTROSAT and LOFT.

  Based on the experience that I acquired during my PhD and mostly on the results reported in Chapter 4 and 5, I significantly contributed to draft a review containing the current state of art concerning black hole transient sources. Here I report the most important concepts and information derived from a complete observational picture that could be constructed in the recent years. The group I have been part of during my PhD and most of the researchers I had the opportunity to collaborate with had a leading role in reaching the present knowledge on compact objects in accreting sources. My major contribution to the review I present here was to improve the state classification firstly reported by Homan et al. (2001), Homan et al. (2005), Belloni (2005) adding important information related to the aperiodic variability associated to the spectral states (both in the form of broad band variability and low frequency QPOs). The rms-intensity diagram (see Chap. 4) allows to clearly separate low-hard state and hard inter mediate state, while the detailed classification of the narrow features observed in the power-density spectra allows to univocally define the soft-intermediate state and separate it from the high-soft state. According to the improved classification that I report, type-A QPOs no longer serve as landmark to identify the soft intermediate state, that is instead by definition marked by the presence of type-B QPOs and an rms level found in a well-defined range. In addition, the results I present in Chap. 3 allowed me to add to this review a precise characterization of the main spectral components in the X-ray spectrum of black hole X-ray binaries as they evolve during their outbursts.

- In **Chapter 3**, I report the results obtained from the monitoring of the black-hole candidate GX 339-4 during its 2007 outburst. Broadband (4-200 keV) spectra could be fitted with a model formed by an exponentially cutoff powerlaw plus a multicolor-disk blackbody. The high-energy cutoff could be followed in detail along the outburst thanks for the good coverage and showed a non-monotonic behavior that solve the contrasting results obtained in the past. The high-energy cutoff changes more rapidly, just like the timing properties, in comparison to several other spectral parameters. The observed behavior of the high-energy cutoff of GX 339-4 is also similar to that observed with RXTE-INTEGRAL-Swift during the 2005 outburst of GRO J1655-40.

  The unprecedented observation coverage obtained for the 2007 outburst of GX 339-4 provided an excellent dataset that I could extensively exploit to follow in detail the spectral evolution of the source along its hard-to-soft transition. In this work I focused on the spectral properties of the source. I took care of the full analysis and in particular I performed a detailed time-resolved spectral analysis along the whole transition from hard to soft state. I used the state classification - that is mainly based on the timing properties - as a framework to describe the evolution of the source emission and in particular of the hard tail of the spectrum. The result that I present is particular important as a constraint for those theoretical models attempting to explain the hard emission, the nature is still poorly understood and therefore still constitute an open problem.

- In **Chapter 4**, I present a new tool to identify and study spectral states: rms-intensity diagram for black hole transients. Using the RXTE observations of the black hole candidate GX 339-4 during outbursts 2002, 2004 and 2007 it was possible to study the relation between the root mean square (rms) amplitude of the variability and the net count-rate. The relation between rms and flux previously observed in the low hard state does not hold during all the states, but different relations can be observed and used as good tracers of different accretion regimes. Hard, soft and intermediate states can be identified in this diagram and transitions appear marked. In addition, the variability results mainly associated to the hard component of the spectrum.

  Starting from the previously used fundamental diagrams to describe black-hole transients evolution, I significantly contributed to develop the idea to define the rms-intensity diagram. Analyzing the relations between variability (in the form of total rms) and count rate already observed in persistent black hole binaries (i.e. Cyg X-1, see e.g. Uttley & McHardy 2001), we built a new tool through which is possible to clearly separate low-hard state form hard-intermediate

state in an outburst source, operation that is usually non-trivial with the sole hardness-intensity diagram. Thanks to the information that I gathered analyzing aperiodic variability - in particular low frequency QPOs - in GX 339-4 (see also Chap. 5) I was also able to define the region where type-B QPOs are found in a rms-intensity diagram. According to the analysis that I carried out this region appears always in a rms range between 5 and 10%. The rms range coincident with the soft-intermediate state is the same for different outburst of the same sources and for different sources as well. This proves that there is no or very week dependence between the rms-range where type-B QPOs are found and the characteristics of a given system. This is fundamental to put constraints in the comprehension of the transition mechanism itself.

- In **Chapter 5**, I report the result of a comprehensive study of low frequency quasi periodic oscillations in the black hole binary GX 339-4. We selected all the RXTE observations where a low frequency QPO could be observed over a time span of eight years and we performed a complete spectral and timing analysis. Most of the QPOs could be classified following the ABC classification and our results show that this classification can be extended to include spectral dependencies. Type-B QPOs show peculiar properties that differentiate them from type-A and -C QPOs. The results can be interpreted within the framework of recently proposed QPO models involving Lense-Thirring precession: type-C and -A QPOs might be connected and could be interpreted as being the result of the same phenomenon observed at different stages of the outburst evolution, while a different physical process produces type-B QPOs.

  This chapter might be considered the core of this thesis, since it proves that combined spectral and timing studies successfully leaded to new important discovery about the nature of low frequency QPOs, nature that even after 15 years of activity of RXTE satellite - specifically made for detailed timing analysis - is still unclear. I developed the idea to apply the spectral/timing approach as an attempt to fully exploit the advantages of both spectral analysis and timing and I then performed the first complete spectral *and* timing study of QPOs. I selected GX 339-4 to perform this analysis as it constitute the most desirable target source for such a study, not only thanks to its regularity, but also because it displayed a considerable number of low-frequency QPOs during its four outbursts. I took care of the whole analysis and through a deep investigation of the analysis results I discovered a previously unknown relations between certain types of QPOs and the luminosity associated to specific spectral components. This further strengthens the validity of a combined spectral/timing approach as a powerful tool to probe accretion and also provided fundamental informa-

tion to understand the transition mechanism and the physical conditions and changes under which it the transition itself takes place. I successfully interpreted my results using one of the most promising existing models to explain QPOs *and* the spectral evolution of transient sources, building the basis to develop a complete theoretical model that will be able to fully explain the evolution of transient sources under spectral and timing point of view. I am currently involved in the development of a more refined theoretical model.

- In **Chapter 6**, I present a study of the spectral properties during the soft intermediate state observed in the 2010 outburst of GX 339-4. All the RXTE observations within a certain hardness ratio range during the soft intermediate state where selected. In this sample all the observations that show a type-B QPO. The spectral analysis of all these observations show that the spectra are significantly harder during the SIMS of the soft-to-hard transition than they are during the hard-to-soft transition. In addition, type-B QPOs observed during the hard-to-soft transition are found at significantly higher frequencies than those observed during the soft-to-hard transition. This generates a strong correlation between QPO-frequency and photon index, stressing a peculiar bimodal behavior.

  Thanks to the results obtained from the spectral/timing analysis of all the QPOs of GX 339-4 (see Chap. 5) I identified a peculiar relation between specific spectral parameters and the behavior of low frequency QPOs. Thus I suggested to further investigating the relation between spectral shape and the frequency of type-B QPOs. I worked in close contact with the first author of the paper corresponding to this chapter (see Stiele et al. 2011) and solved important technical issues related to the data analysis (mainly related to background problems in RXTE data, for details, see Chap. 6, Sec. 6.4). After producing the fundamental diagrams to use as a framework where to base the subsequent analysis and the description of the source spectral evolution, I performed the timing analysis and part of the spectral analysis that allowed to evidence the relation between spectral index and type-B QPO frequency. The 2010 outburst of GX 339-4 proved to be particularly suitable to this kind of analysis because of the high number of type-B QPO detected, that is related to a very dense coverage of the soft intermediate state. The results I report constitute an interesting starting point to study in detail the relation between the appearance of type-B QPOs and the physical conditions of the system, that can be probed through the spectral analysis. In particular the fact that the hardness ratio cannot be used as a tracker of the spectral shape ad different luminosity levels - the consequence of which is the bimodal behavior - must be put in relation with the different

properties of the radio emission of the source that are equally different at different luminosity levels. This topic will be explored by myself and the group I am part of in a forthcoming work.

- In **Chapter 7**, I present the outburst evolution of the black hole candidate H 1743-322 during two different outbursts occurred in 2008 and 2009. During 2008 only the hard states were reached, while during 2009 the source displayed a complete outburst. We attempted to identify the cause of this difference performing spectral and timing analysis for all the RXTE observations obtained the two outbursts. The early evolution of the spectral parameters is consistent between the two epochs, and it does not provide clues about the subsequent behavior of the source. However, the variation of the flux associated to the two main spectral components (i.e. disk and powerlaw) allows to set a lower limit to the orbital inclination of the system of ≥ 43 degrees.

  H 1743-322 is one of the few sources that displayed a *failed* outburst and the only one that (so far) displayed both complete and failed outbursts. I assumed that the fact that this system displayed two types of outburst close in time offered a unique opportunity to investigate in detail the transition mechanism under the hypothesis that the system properties (such as black-hole mass, orbital separation of the binary, inclination with respect to the line of sight) are the same. Then I performed the whole state classification and spectral analysis of the two outburst as described in Chap.3 attempting to find differences in the spectral properties that allow to forecast the *failed* or *standard* nature of an outburst. The results the I describe confirm that the transition mechanism involves several factors that are not restricted to changes in the macroscopic properties of the system (i.e. smaller or bigger inner disk radius, higher or lower inner disk radius temperature, different Comptonization temperatures and so on). Such factors proved to be elusive also approaching the source with a combined spectral-timing analysis. This demonstrate that our comprehension of the transition mechanism - and also of the outburst mechanism itself - is far from being complete and must be revised and further developed.

- In **Chapter 8**, I present spectral and timing studies of the outburst evolution of the black-hole candidate Swift J1753.5-0127, monitored with the Rossi X-ray Timing Explorer and the Swift satellites. The outburst started in 2005 and it still on-going, since after an initial flare the X-ray luminosity decreased, but the sources never reached the quiescence state. Similarly to H 1743-322, Swift J1753.5-0127 source transited to the hard intermediate state, but it never made

it to the soft states. This behavior is observed in other sources characterized by short orbital periods (approximately $\lesssim 5$ hours). The morphology of the outburst is peculiar and reminiscent of those observed in a class of cataclysmic variables, the Z Camelopardalis. However, we show that both spectral and timing properties of Swift J1753.5-0127 are in agreement with the binary hosting a black hole.

The peculiar nature of the six-years long outburst of Swift J1753.5-0127 and the fact that, similarly to H1743-322, it is among the very few transients displaying failed outbursts, makes this source an interesting case of study to investigate the transition mechanism. I produced the first HID indicating that Swift J1753.5-0127 has left the low-hard state and then I performed the broad band spectral analysis of all the observations belonging to the *failed* outburst and part of the timing analysis that allowed to confirm that the system indeed left the hard intermediate state and reached the hard-intermediate state, without however moving to the soft states. The results of the spectral and timing analysis as well as the behavior of the source in the fundamental diagrams also provided the main clues that allowed to state that Swift J1753.5-0127 most likely host a black hole rather than a neutron star.

- In **Chapter 9**, I report the results of a two-day long RXTE observation and simultaneous Swift data of the bright X-ray transient XTE J1752-223. The spectral and timing analysis showed that the properties of the source were stable during the observation. The properties of the energy spectrum and power density spectrum, as well as the time-lags between soft and hard X-rays suggest that XTE J1752-223 is a black-hole candidate, with all timing and spectral components very similar to those of Cyg X-1 (a persistent black hole binary) during its canonical hard state.

  XTE J1752-223 completed it outbursts in 2010, showing an HID very similar to the ones displayed by GX 339-4. However, its uncommonly long and stable low-hard state allowed to study in detail a spectral phase that in many sources is sometimes so short to be missed by most of the X-ray laboratories currently working. I performed the broad band spectral analysis and I provided the fit of an extraordinarily good quality power-density spectrum. The high quality of the data also allowed to measure precisely the time-lags and to directly compare them to the case of Cyg X-1. The results of my analysis provided the most important information to state the black-hole nature of XTE J1752-223. It is remarkable that even though XTE J1752-223 proved to be a black-hole transient, its low-hard state properties could not be unambiguously distinguished from those of a persistent source such as Cyg X-1. This might provide further

clues to investigate the transition mechanism.

- In **Chapter 10**, I present a comprehensive spectral-timing study of the black hole candidate MAXI J1659-152 during its 2010 outburst. Using 65 RXTE observations taken along this period it was possible to compute the fundamental diagrams commonly used to study black hole transients. Timing and spectral analysis allowed to analyze the properties of the source along the outburst, while the study of the variability observed at different energy bands made possible to conclude that the hard emission accounts for the observed fast variability, it being strongly quenched when type-B oscillations are observed. Also the analysis of the time-lags confirm that lags are larger during the hard-to-soft transition than during the hard state.

  Even though the black hole candidate MAXI J1659-152 displayed a rather typical behavior during its evolution along its first outbursts, it showed a peculiarly high level of variability in its soft-state that made it worthy of a detailed spectral-timing analysis. I performed the spectral analysis of the full outburst as well as the timing and through the spectral deconvolution I could evidence that the main source of variability resides in the high-energy emission after the source has transited to the soft intermediate state. This results basically confirms the validity of the truncated disk model (see Done et al. 2007, predicting that the accretion disk is able to reach a steady state (i.e. no or very small variability coming from the disk) once the source gets to the high-soft state.

- In **Chapter 11**, I report a study of the morphological, spectral and temporal properties of 107 of the bursts from the 11 Hz accreting pulsar IGR J17480-2446 discovered in 2010 and located in the globular cluster Terzan 5. The source has shown several X-ray bursts with a recurrence time as short as few minutes with the shortest recurrence time ever observed from a neutron star. The analysis carried out on RXTE observations shows that the ratio between the energy generated by the accretion of mass and that liberated during bursts indicate that Helium is ignited in a Hydrogen rich layer. Therefore, despite the peculiar bursting behavior of the source, it was possible to state that bursts shown by IGR J17480-2446 are Type-I X-Ray bursts. The non-drifting pulsations observed at the spin frequency in all the brightest bursts result as phase-locked with respect to the pulsation detected in the persistent emission and they are not associated to an increase of the rms associated to the pulse frequency. This behavior would favor a scenario where the type-I burst, possibly ignited at the polar caps, immediately propagates to the entire neutron star surface.

  The behavior displayed by IGR J17480-2446 is certainly unique and makes the

source an extraordinary laboratory to investigate in details the mechanisms that origin thermonuclear X-ray bursts, especially in the limit case of extremely short recurrence time X-ray bursts. I leaded this work starting from a basic preparation on the topic acquired during my bachelor thesis (I studied thermonuclear bursts from the bursting atoll source 4U 1636-53). Making use of the litterature and learning from the experience of most of the people involved in this work (see **?**) I reached a good knowledge of the topic - and exceeding my supervisor's knowledge in this field - that allowed me to define a clear research strategy that leaded to very relevant results. I analyzed one by one all the outbursts showed by the source in the first days after the start of the outbursts, measuring the main burst properties (such as burst start time, burst peak time, decay time, fluences) that allowed to test the theoretical model on X-ray bursts. I also analyzed the persistent emission spectrum, the spectra of the bursts and I performed time-resolved spectral analysis for the first, very intense X-ray bursts observed during this outburst (the only one that was unmistakably a thermonuclear burst). The results that I report here are extremely important for two main reasons: i) despite the statement made by Galloway & in't Zand (2010) (who argued that the bursts showed by IGR J17480-2446 were type-II X-ray bursts), I could unambiguously demonstrate the thermonuclear nature of bursts that were morphologically identical to type II X-ray bursts; ii) I could demonstrate that the currently accepted theories on the production of thermonuclear bursts cannot be extended down to very short recurrence times and therefore must be reviewed to include the limit case represented by IGR J17480-2446.

2 Black-hole transients

Tomaso M. Belloni, Sara E. Motta, Teo Muñoz-Darias,

2011 September special issue of the Bulletin of the Astronomical Society of India on transients at different wavelengths, edited by D.J. Saikia and D.A. Green

Abstract

Sixteen years of observations of black-hole transients with the Rossi X-ray Timing Explorer, complemented by other X-ray observatories and ground-based optical/infrared/radio telescopes have given us a clear view onto the complex phenomenology associated to their bright outbursts. This has led to the definition of a small number of spectra/timing states which are separated by marked transition in observables. The association of these states and their transitions to changes in the radio emission from relativistic radio jets complete the picture and have led to the study of the connection between accretion and ejection. A good number of fundamental questions are still unanswered, but the existing picture provides a good framework on which to base theoretical studies. We discuss the current observational standpoint, with emphasis onto the spectral and timing evolution during outbursts, as well as the prospects for future missions such as ASTROSAT (2012) and LOFT (>2020 if selected).

2.1 Introduction

The first black hole transient (BHT), A 0620−00, was discovered more than thirty years ago (Elvis et al., 1975) and already showed that the spectral evolution of these objects was very complex. The first major step forward came with the Japanese satellite Ginga, which thanks to the presence of an all-sky monitor and a large pointed detector led to the discovery and detailed study of a few objects (Tanaka & Lewin, 1995). Complex variability patterns were discovered, including Quasi-Periodic Oscillations, which led to the extension of the hard/soft states of black hole binaries (originally developed for Cygnus X-1) to additional states (see e.g., Miyamoto et al., 1993). Because of the scarcity of sources and of coverage, Ginga data gave only a limited view of the spectral/timing evolution of BHTs. Around the same epoch, optical observations yielded the first strong dynamical evidence for a BH (i.e. compact object heavier than $\sim$3 $M_{\odot}$) in A 0620−00 (McClintock, 1986), which was fully confirmed a few years later by Casares et al. (1992) with the measurement of a mass function $>$6 $M_{\odot}$ in another BHT, the Ginga source GS 2023+338 (=V404 Cyg). The situation changed with the launch of the Rossi X-ray Timing Explorer (RXTE) at the end of 1995. Sixteen years of operations (with high level of flexibility and fast response) led to the observation of a large number of objects through extensive campaigns, often with coordinated observations at other wavelengths (see e.g., Remillard & McClintock, 2006). From this wealth of data, clear patterns emerged which are now leading to the development of theoretical models. The evolution of spectral, timing and spectral/timing parameters can now be classified into a small number of states which can be easily identified and followed throughout an outburst (see Belloni, 2010), as well as linked to observations at lower energies (see Fender et al., 2010). In this paper, we summarize the current observational status, focussing on the outburst evolution and spectral states, and briefly discuss the contributions from upcoming missions like ASTROSAT and LOFT.

2.2 The tools of the trade: fundamental diagrams

The behaviour of BHTs is known to be easily characterized in terms of spectral states and transitions between them. These states, dubbed “canonical” by Miyamoto et al. (1992), are defined on the basis of the spectral and timing properties displayed by the sources during their outburst phases (see Sec. 2.3). The canonical states become apparent in a hardness–intensity diagram (HID), where the total count rate is plotted as a function of the spectral hardness (defined as the ratio of observed counts in two energy bands). Here the spectral evolution of many BHTs can be followed along a q-shaped pattern that is traced anti-clockwise. In the HID (see Fig. 2.1, top-left panel) four different branches can be identified, corresponding to the four sides of

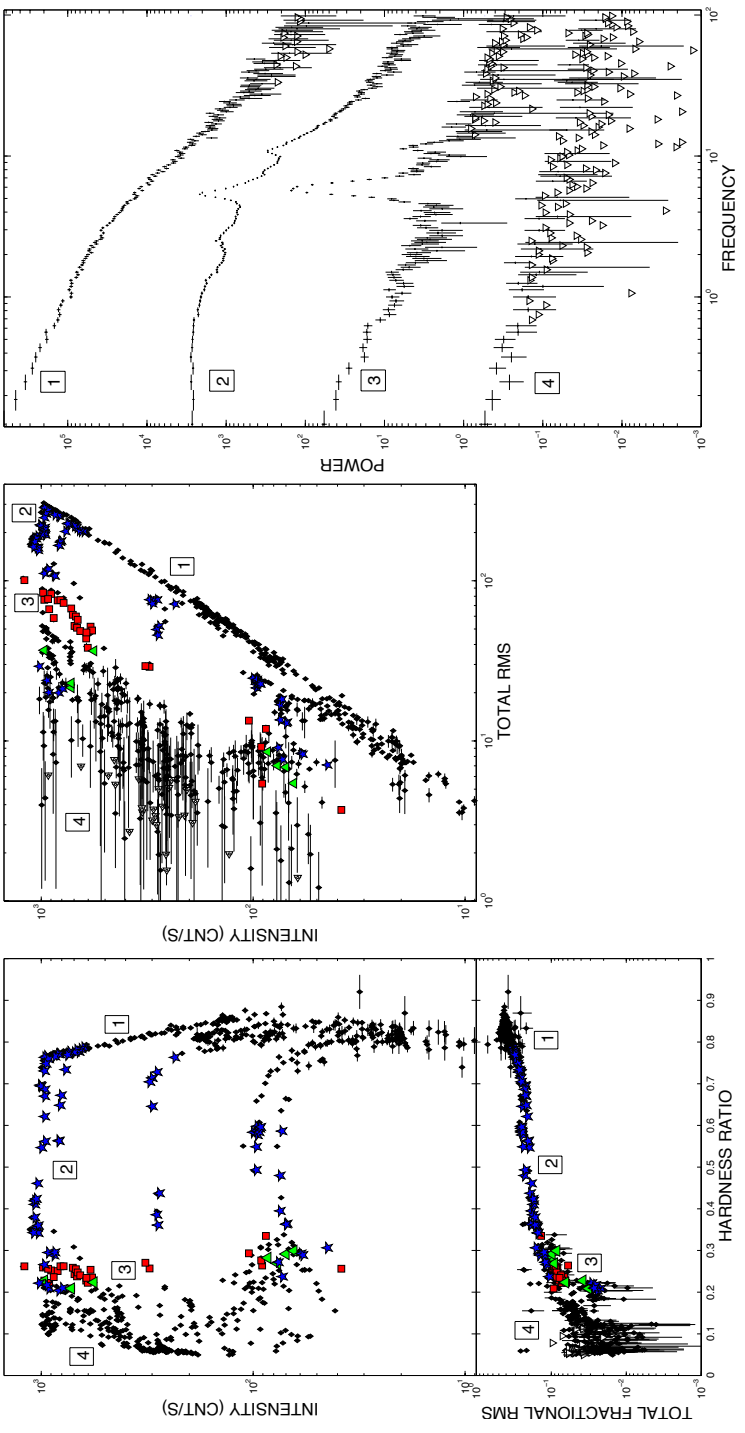

Figure 2.1: Top-left panel: HID for the 2002, 2004, 2007 and 2010 outbursts of GX 339–4, with each point representing a single RXTE observation. Bottom-left panel: the corresponding rms-hardness diagram, with empty triangles representing upper limits. The hardness ratio is defined as the ratio of net counts in the 6.1−20 keV band over those in the 3.3−6.1 keV band. Middle panel: RID for the 2002, 2004, 2007 and 2010 outbursts of GX 339–4. Symbols are as follows. Blue stars: Type-C QPOs; red squares: Type-B QPOs; green triangles: Type-A QPOs; black dots: all the other RXTE observations of GX 339–4 that do not show low-frequency QPOs. Right panel: Power density spectra for the four regions marked in the left and middle panels. The left and middle panels have been adapted from Motta et al. (2011).

the "q" (the fact that the transition from hard to soft takes place at higher flux than the reverse transition is seen in all systems, see Maccarone & Coppi, 2003). The right and left vertical branches respectively match the low hard state and the high soft state already known before the RXTE era. In between these two well-established states, the situation is rather complex and the intermediate points that fill this region roughly correspond to those previously know as very-high state and intermediate state. These two states show very similar properties in the spectral domain, making it practically impossible to distinguish between them (see Homan et al., 2001). However, when the timing properties are taken into account, the "intermediate region" of the HID can be easily divided into two well separated areas, as they show completely different features in the time-domain (see Sec. 2.3). It is important to remark that not all transients show a regular evolution like the one which will be described here. However, the basic states and their properties can be defined for all systems. For an overview of a large number of RXTE transients see Dunn et al. (2010).

The first step towards a clear distinction of the intermediate regions is made by looking at the hardness–rms diagram (HRD, see Fig. 2.1, bottom-left panel), where the fractional rms, integrated over a broad range of frequencies, is plotted versus hardness. In this diagram, unlike in the HID, most of the points follow a correlation over a single line (no hysteresis here), extended from the softest points, where the points show a low level of variability ($<5\%$), to the hardest points, where the variability is much higher (also exceeding 30%). In the region at intermediate hardness, the correlation is rather tight; however in a narrow hardness ratio band several points show a lower variability than the points on the main correlation (see Fig. 2.1). This behaviour already suggests the presence of two separate states in this region, corresponding to the points on the main correlation (spanning a very large range in hardness and rms) and to those deviating from it (found in a narrow hardness and rms range). However, it is only by examining the fast aperiodic variability that the canonical states can be distinguished clearly from one another.

Examining the Power Density Spectra (PDS) allows one to probe the fast timing properties of a source. It is worth mentioning that although important information can be extracted from higher-order timing tools (such as phase/time lags, coherence and bicoherence, see Nowak & Vaughan, 1996; Maccarone, 2005), these are not essential for the basic determination of states and state transitions. A number of different PDS shapes can be observed in BHTs, but it is now clear that we can classify them as belonging to a few basic types that are closely related to the position on the HID and HRD (in addition there are a few more complex PDS shapes, not shown here, associated to the "anomalous" state found at very high accretion rate in some sources, Belloni, 2010). The most prominent features in the PDS are narrow peaks, known as low frequency quasi periodic oscillations (QPOs). QPOs have been discovered in many systems and, even though their physical origin is still under debate (see Motta

et al., 2011, and references therein), they are thought to originate in the innermost regions of the accretion flows around stellar-mass black holes.

Low-frequency QPOs (LFQPOs) with frequencies ranging from a few mHz to ∼20 Hz were already found in several sources with Ginga and divided into different classes (see e.g., Miyamoto et al., 1993; Takizawa et al., 1997). Observations performed with the RXTE have led to an extraordinary progress in our knowledge on properties of the variability in BHBs and it was only after RXTE was launched that LFQPOs were detected in most observed BHBs (see van der Klis, 2006; Remillard & McClintock, 2006; Belloni, 2010, for recent reviews). Three main types of LFQPOs, dubbed types A, B, and C, originally identified in the PDS of XTE J1550–564 (see Wijnands et al., 1999; Homan et al., 2001; Remillard et al., 2002), have been seen and identified in several sources. All the basic types of PDS (with the exception of the additional ones related to the "anomalous" state) were observed in the outbursts of GX 339–4 between 2002 and 2011(see Fig. 2.1, right panel).

- The hard points in the HID (region [1] in Fig. 2.1, left-upper panel) show a PDS similar to [1] in Fig. 2.1 (right panel). Its shape can be fitted with a small number of very broad Lorentzian components. In some cases also a low-frequency QPO peak is observable at very low frequencies ($\nu \leq 0.01$ Hz). The characteristic frequencies (see Belloni et al., 2002) of all these components increase with source flux, while the energy spectrum (see below) softens gradually.

- PDS [2] in Fig. 2.1 can be considered a high-frequency extension of PDS [1]. It is found at intermediate hardness values (region [2] in Fig. 2.1, top-left panel). The most prominent feature is a QPO with centroid frequency varying between ∼0.01 and ∼20 Hz and a quality factor Q around 10. The characteristic frequencies of all Lorentzian components vary together, including that of the QPO. As in the previous case, they are correlated with hardness: softer spectra correspond to higher frequencies and also to lower integrated rms variability (see Fig. 2.1, middle panel). The LFQPO observed here is termed "type-C" QPO (stars in Fig. 2.1, see Casella et al., 2005; Motta et al., 2011, for a precise definition of the three QPO types) and it always appears together with moderately strong (10–30% rms) band-limited noise. It is often accompanied by two peaks harmonically related: one at half the frequency and one at twice the frequency, with the higher one having a similar Q to that of the fundamental; higher harmonics are often observed (Rao et al., 2010). The frequency of the type-C QPO is strongly correlated with the characteristic (break) frequency of the main underlying broad-band noise components (see Wijnands et al., 1999; Belloni et al., 2002), a correlation which also extends to neutron-star binaries.

- Over a narrow range of intermediate hardness, PDS similar to region [3] in Fig. 2.1 can be found (region [3] in the HID, see Fig. 2.1, top-left panel). These

PDS feature a QPO called "type-B" (squares in Fig. 2.1). This oscillation shows different properties from type-C QPOs. The fact that type-B QPOs are not simply an evolution of type-C QPOs is demonstrated by the fast transitions observed between them (see Takizawa et al., 1997; Nespoli et al., 2003; Casella et al., 2004; Belloni, 2005). Type-B QPOs are associated with a weak power-law noise that replaces the broad Lorentzian components of the previous PDS types. Type-B QPOs show a harmonic structure similar to that of type-C QPOs (harmonic peaks and a peak at 1/2 the frequency of the main peak). While type-C QPOs span large range in frequency, type-B QPOs are limited to the range 1–6 Hz, but detections during high-flux intervals are concentrated in the narrow 4–6 Hz range (see Motta et al., 2011). The centroid frequency appears positively correlated with source intensity rather than hardness.

- At hardness values systematically slightly lower than those of PDS [3], PDS showing "type-A" QPO can be observed (triangles in Fig. 2.1). Being a much weaker and broader feature, we know less details about this oscillation. Sometimes it is only detected by averaging observations. Its frequency is always in the very narrow range 6–8 Hz and it is associated to an even lower level of power-law noise than type-B.

- The three types of QPOs can be separated by plotting them against the integrated fractional rms of the PDS in which they appear (see Casella et al., 2005; Muñoz-Darias et al., 2011; Motta et al., 2011).

- The softest points in the HID (region [4] in Fig. 2.1, left panels) show PDS ([4] in Fig. 2.1, right panel) with a weak steep component, which often needs a long integration time for a detection. Weak QPOs at frequencies higher than 10 Hz are sometimes observed, as well as a steepening/break at high frequencies. The total fractional rms can be as low as 1%.

- In addition to the PDS shapes described, there are two types of PDS which are not always observed in BHTs. One PDS has a featureless curved shape, the other with additional broad and narrow features (see e.g., Belloni, 2010).

By the introduction of a third fundamental diagram, the rms-Intensity diagram (RID, see Muñoz-Darias et al., 2011), it becomes possible to clearly separate the canonical states without the intervention of any spectral information. To produce the HID and the RHD three variables are needed: spectral hardness, intensity (or count rate) and integrated fractional rms. The RID is the third possible plot between these variables: the integrated rms (not fractional) as a function of the total count rate. In the RID, the fast variability can be used as a good tracer of different accretion regimes in black hole binaries and it becomes apparent that apart from the linear

rms-flux relation (a.k.a. hard line) found during LHS (see Gleissner et al., 2004), different relations are followed during the soft and intermediate states, to the extent that it is possible to identify the states from the RID alone. State transitions produce marked changes in the rms-flux relation. It is also important to notice that, in the RID, type-B QPOs (that are the defining feature of the SIMS, see Sec. 2.3) appear in a well-defined region between 5 and 10% fractional rms. This fact virtually removes the necessity of a detailed analysis of the PDS to separate the intermediate states (see Sec. 2.3). A detailed description of the RID and its properties and peculiarities can be found in Muñoz-Darias et al. (2011).

It is important to remark that the diagrams described above are instrument dependent and source dependent, which means that a quantitative comparison between them is not always possible. However, they are also model independent and provide very precise measurements. For a discussion of similar diagrams based on spectral fits, see Dunn et al. (2010).

2.3 Timing-spectral states

The diagrams presented in the previous section lead to the definition of small number of states, whose boundaries are rather precise and defined by the data (see also Homan et al., 2005; Belloni et al., 2006; Belloni, 2010). It is important to stress that it is possible to characterize these states only by considering both spectral and timing properties, so that the concept of "spectral" states carries little meaning. While the states do not have direct physical connection, their definition is a necessary step in order not to miss major physical changes in the accretion flow.

- **The Low-Hard State (LHS)**. Only (and possibly always, but there are quite a few cases of missed starting LHS) at the beginning and at the end of an outburst. It corresponds to the right nearly-vertical branch in the HID (the spectrum softens as the flux increases). The energy spectrum is hard and usually associated to thermal Comptonization (Gilfanov, 2010). Strong ($> 30\%$ fractional rms) variability in the form of a band-limited noise is present (see PDS [1] in Fig. 2.1, right panel). As flux increases, the total fractional variability in most cases decreases. At high rates, the end of this state is marked by the leaving of the hard line (see Fig. 2.1, middle panel), while the actual shape of the power density spectrum changes more gradually across the transition.

- **The Hard-Intermediate State (HIMS)**. It corresponds to horizontal branches in the HID. It takes place after the initial LHS and before the final LHS, as well as in the central parts of the outburst, through mini state transitions. The energy spectrum is softer than in the LHS and at low hardness an accretion disc component starts contributing to the RXTE/PCA band. The variability is

dominated by a weaker band-limited noise and a type-C QPO (stars in Fig. 2.1, left and middle panels, PDS [2], right panel; for a discussion of the different types of QPO see Casella et al. 2005; Motta et al. 2011). The fractional rms decreases with hardness down to $\sim$10%; overall, the evolution of the power spectra is such that they are an extension of the LHS ones. The QPO frequency is anti-correlated with hardness and correlated with the photon index of the hard spectral component.

- **The Soft-Intermediate State (SIMS)**. When both hardness and fractional rms drop below well defined thresholds (0.71 for GX 339–4, see Fig. 2.1), the source enter the SIMS. Here the energy spectrum is similar to that of the nearby HIMS (at least below $\sim$ 10 keV, see below), but the timing properties are completely different: the band-limited noise disappears (drop in the HRD, rms below 10%) and is replaced by a power-law noise, while a marked type-B QPO is present (squares in Fig. 2.1, PDS [3]), whose frequency correlates with the hard X-ray flux (see Motta et al., 2011).

- **The High-Soft State (HSS)**. The leftmost branch in the HID. Here the spectrum is soft, dominated by a thermal disc contribution. A hard component is observed with varying intensity. Very little variability is observed (PDS [4] in Fig. 2.1, right panel), sometimes with type-A QPOs. This state spans a larger range in luminosity.

The main time evolution of a transient are: LHS – HIMS – SIMS - HSS as accretion rate increases, followed by HSS – SIMS – HIMS – LHS as accretion rate decreases (for a discussion of the reverse transition from soft to hard see Kalemci et al., 2006; Belloni et al., 2006). Intermediate minor transitions between states, usually not involving the LHS, can be observed. In some sources the initial LHS (or LHS – HIMS) is so fast that it is not observed. Some sources never leave the LHS, in very few cases reaching the HIMS without showing a transition to the SIMS (Capitanio et al., 2009; Motta & Belloni, 2010). Very few sources show a more complex time evolution, which however involves observations that can be classified in one of the four states outlined above. In addition, an "anomalous state" is present in some sources, related to very high luminosities (see Belloni, 2010; Done & Kubota, 2006). The level at which the LHS – HIMS transition takes place can vary in one source from outburst to outburst, but it is always higher than the reverse transition and their level appear to be anti-correlated: a brighter upper HIMS branch corresponds to a fainter lower HIMS branch (see Maccarone & Coppi, 2003; Dunn et al., 2010). What physical quantity determines the flux (and accretion rate) level at which the hard to soft transition takes place is currently unknown, although it has been suggested that the time from the previous outburst plays a role (Yu & Yan, 2009, and references therein).

2.4 Energy spectra

Timing properties are crucial to define the states, but although few models have been proposed to explain the origin and the nature of time-variability, still there is not a clear interpretation nor an explanation on their physical origin.

Even though we are still far from achieving a clear and complete comprehension of the full accretion mechanism acting in X-ray binaries, we have an idea of the main physical processes involved. Here we will discuss spectral variations along the HID and we will mainly focus on the changes that take places during spectral transitions. Note that the information we discuss in this section is mainly based on the 2–200 keV energy band since a good portion of it comes from RXTE data. Very detailed spectra come from instruments with higher spectral resolution.

The emission coming from X-ray binaries cover a very broad energy interval, extending from the radio to the very high energies (hard X-rays and sometimes gamma-rays). The main effects of the accretion mechanism in the region close to the compact object can be observed in the X-rays, but other fundamental processes are responsible for the emission at very different wavelengths (see also Sec. 2.7). The X-rays consist of both thermal emission coming from the very inner regions of an optically thick accretion disc as well as a harder component, extending to hundreds of keV and sometimes up to an MeV. The characteristics of this hard component are state-dependent. In the hard states (LHS and HIMS), it is usually interpreted as thermal or hybrid Compton radiation from the interaction of the soft disc photons with relativistic electrons in the inner regions of the accretion flow (see Done et al., 2007; Gilfanov, 2010, for recent reviews). It has also been suggested that non-thermal Comptonization processes (e.g., self-Compton from synchrotron emission from the jet or bulk motion Comptonization) could be responsible for this component (Laurent & Titarchuk, 2001; Markoff, 2010). For the soft states (HIMS and HSS), the hard component extends to higher energies and is possibly of non-thermal origin.

The movement of a source along the HID must be decomposed in vertical (i.e. count rate) and horizontal (i.e. spectral hardness) excursions. The vertical movement, typical of the hard state where the spectrum softens less dramatically, is thought to be driven by accretion rate, depending on the geometry of the system and of the accretion flow. The horizontal movement is caused by a combination of a steepening of the hard component and the appearance of a thermal disc component in the RXTE band. While accretion rate most likely continues increasing, the marked change in accretion properties is triggered by a hitherto unknown parameter (but see Yu & Yan, 2009).

- **LHS** ([1] in Fig. 2.1) – as already mentioned, all outbursts most likely start in this state, although at times it is not observed, probably because of its short time scale. The corresponding broad-band energy spectra are very hard and usually

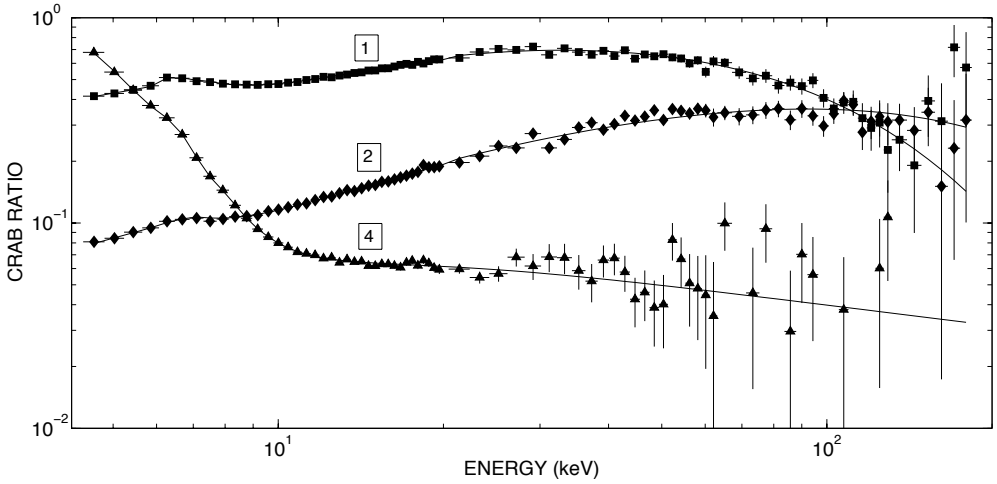

Figure 2.2: PHA ratio of GX 339–4 to Crab for three selected observations. (1) LHS spectrum, (2) HIMS spectrum, (4) HSS spectrum. Figure adapted from Motta et al. (2009).

show a high-energy cutoff around 50–100 keV (spectrum 1 in Fig. 2.2). In GX 339–4 and GRO J1655–40 this cutoff was seen to move to lower energies as flux increased (see Fig. 2.3), together with a steepening of the photon index. A faint cold disc with a large inner radius and a peak temperature of few tenths of keV is sometimes observable if the interstellar absorption is low (see e.g., Muñoz-Darias et al., 2010a). However, in few sources a hot thermal disc has been detected, suggesting that in some cases the inner disc radius could be always close to the innermost stable orbit. Sometimes an additional non-thermal component is also present in the spectrum (Markoff et al., 2002). This component has been proposed to be associated with the synchrotron jet detected at radio waves.

- **HSS** ([4] in Fig. 2.1) – the energy spectrum is dominated by the thermal emission from the disc, observed with a small inner disc radius and a temperature that reaches typical values of $\sim$1 keV. The hard component, probably the result of Comptonization of soft photons on a non-thermal distribution of relativistic electrons, is in general very faint and variable without an observed cutoff below 1 MeV (spectrum #4 in Fig. 2.2).

- **HIMS/SIMS** ([2] and [3] in Fig. 2.1) – during the HIMS and the SIMS, the transition from hard to soft state takes place. The spectrum is a combination of the soft and hard component dominating the HSS and LHS respectively (spectrum 2 in Fig. 2.2). In several sources the inner disk radius has been observed to move inward during these states. This behaviour provides a physical ex-

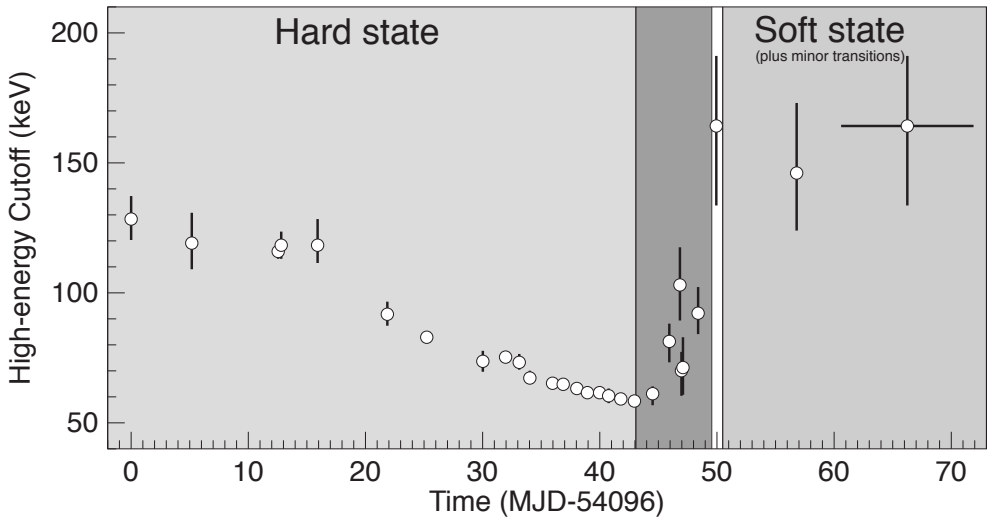

Figure 2.3: Evolution of the high-energy cutoff in the 2007 outburst of the BHT GX 339–4.

planation to the changes in the spectral shape during the transition, partially produced by the increasing soft emission coming from the disc. Whether the cutoff decreases, increases or disappears in the intermediate states has been a topic of debate for several years. This has been partially solved thanks to the good coverage achieved for some sources. In GX 339–4 (Motta et al., 2009, see Fig. 2.3) and GRO J1655–40 (Joinet et al., 2008), after the decrease during the LHS, the high-energy cutoff is observed to suddenly increase in the HIMS, to reach its maximum in the SIMS. If a high energy cutoff is present in the HSS, it is not observable below 1 MeV (Del Santo et al., 2008). The decrease seen during the LHS is thought to be produced by the cooling of the Comptonizing medium due to the higher fraction of soft photons undergoing Comptonization, while the reason for the HIMS increase is still under discussion. Spectra from the softest HIMS and from the SIMS are very similar, since their hardness is very similar and the evolution from one to the other is smooth (for a discussion, see Stiele et al., 2011).

As mentioned above, some sources (e.g., GRO 1655–40) display another state, the "anomalous" or "ultra-luminous" state. Here, the source shows very high luminosities and the energy spectrum appears dominated by a soft disc component. The disc component allows to infer a high inner-disc temperature associated to a small inner disc radius, while the hard component is steep and faint.

2.5 Rms spectra

The amount of variability as a function of energy is another observable which is seen to vary along the outburst. This is expected, since the relative contribution of each spectral component strongly depends on the accretion state. Apart from its average spectral shape, usually measured over long time scales ($\geq$ 1 ks), each component also prompts a certain level of variability in the observed light-curve. The shape of the rms spectrum (i.e., fractional rms as a function of energy) encodes information directly related to the relative contribution of each emission process and the intrinsic origin of the variability itself. Whereas the former can also be obtained from spectral studies, the latter results in unique insights into accretion physics.

As for many other cases, the RXTE/PCA has made a strong contribution, most of the results present in the literature being referred to the $\sim$ 2–20 keV energy band. In a first approximation, rms spectra with three different shapes are observed in BHT: flat, rms decreasing with energy (soft; aka., inverted) and increasing with energy (hard). The first two cases correspond to the hard states (see below), whereas a hard rms spectrum is seen as the system softens. In Fig. 2.4 we show an example of these shapes using RXTE/PCA data of GX 339-4 during its hard-to-soft transition.

- **LHS**: Flat and inverted rms spectra are observed during this state. Clear examples of the former are e.g., XTE J1550–564 (Gierliński & Zdziarski 2005), Cyg X–1 or XTE 1752–223 (Muñoz-Darias et al. 2010a). The latter behaviour is observed in XTE J1650–500 (Gierliński & Zdziarski 2005) or Swift 1753.5–0127 (Soleri et al., submitted). Flat rms spectra are easily explained by considering that variability arises from variations in the normalization of one single spectral component. This could account for what we see in the hard state, where the hard component is dominant ($\geq$ 2 keV; see Sect. 4). Variations in the spectral shape of this component (i.e., not only in normalization) need to be taken into account to explain inverted rms spectra. Gierliński & Zdziarski (2005) (see also Zdziarski et al. 2002) show that a strongly varying (disc) seed photon input can produce inverted rms spectra, since it varies the spectral shape by making the power-law to pivot around $\sim$ 50 keV. Variations in the normalization of the power-law component are also needed to reproduce the observed dependence of the rms with energy. Interestingly, in some of the cases where flat rms spectra are observed, they are still consistent with being inverted at $\sim$ 1–2% level (e.g., Fig. 2.4).

- **HIMS:** As it happens for several spectral and timing parameters, a major change in the shape of the rms spectra is observed along the HIMS. Whereas LHS-like rms spectra are observed during the early stages of the HIMS, they harden as the system approaches the soft states. This transition occurs fast; for

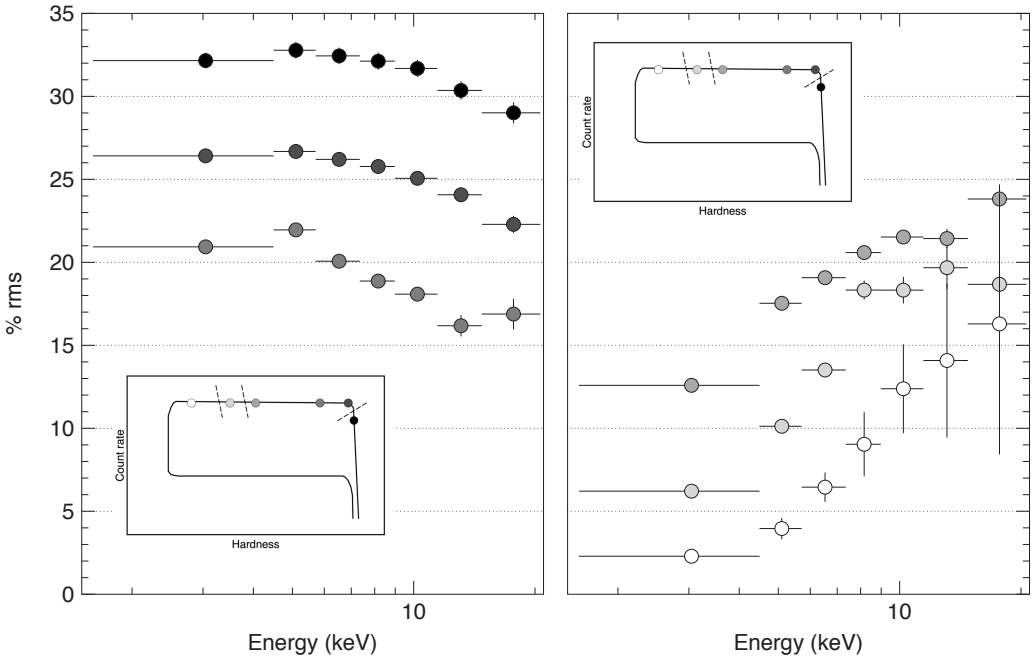

Figure 2.4: Evolution of the 0.1–32 Hz rms spectrum along the hard-to-soft transition of GX 339–4. Left panel, from top to bottom: rms spectra from a bright LHS, a hard HIMS and a softer HIMS (see inset). Right panel, from top to bottom: rms spectra from a HIMS just before the transition, a SIMS and a HSS (see inset).

instance, the two last HIMS spectra presented in Fig. 2.4 are separated by five days. Their corresponding energy spectra are different as well, since the disc component is only present in the second one. Muñoz-Darias et al. (2011) observed a flux increase at constant absolute variability in correspondence to the appearance of the disc component in the energy spectra of this system during the HIMS. The above suggests disc variability to be low at least during last (softest) stages of the HIMS.

- **SIMS and HSS:** Hard rms spectra are observed during soft states. As shown in Fig. 2.4, these are remarkably similar to those observed at the softest end of the HIMS, but with total variability decreasing as the system softens. These patterns can be explained by considering no or very little disc variability, which results in lower rms values in the soft band when disc dominates. Above 5–10 keV, where the variable power-law dominates, we recover the flat shape observed in the LHS.

2.5.1 The origin of the variability and the role of the disc component

It has been known for years that variability is mainly associated with the hard component rather than the disc. During soft states, where the disc dominates, low variability levels (≤ 5 per cent) are observed. Even there, its energy dependence also points to a hard-component origin (see e.g., Gilfanov 2010 and references therein). HIMS observations also point in the same direction (see above) and in the LHS, where only the hard component is present above ~ 2 keV, we see the highest variability levels. Paradoxically, Comptonization models aiming at explaining the inverted rms spectra require a highly variable disc during the LHS. Softer (≤ 2 keV) XMM observations have shed some light on this issue. Evidence for low frequency ($\lesssim$1 Hz) disc variability during the LHS has been reported by Wilkinson & Uttley (2009). Also at low frequencies, Uttley et al. (2011) published time-lag measurements showing disc variability leading hard-component variability. Both results represent a strong evidence for a variable disc component during the LHS at low frequencies (Gierliński & Zdziarski, 2005), whereas for time scales shorter than ~ 1 s (i.e. those typically used for variability studies) results are not conclusive.

If variability originates in the soft component, it should progressively disappear to explain the lack of variability observed as the energy spectrum softens. Hard-component variability should decrease as well, but high levels of hard-component variability are observed during soft states. Interestingly, Muñoz-Darias et al. (2011) report a dramatic fade of hard-component variability during the SIMS in MAXI J1659–152. The light curve associated to the disc component is also shown to be more stable at very low frequencies once the system reaches the HSS.

We note that the role played by the jet component, which is probably highly variable (e.g., Casella et al. 2010) and has been proposed to account in some cases for the observed X-ray emission during the LHS (e.g., Markoff et al. 2001) should be much better understood to solve this problem. The combination of multiwavelength studies and the broader spectral coverage planned for future X-ray missions, such as LOFT (Feroci & LOFT Consortium 2011) and ASTROSAT (Agrawal, 2006), should make a decisive contribution to this issue.

2.6 High-frequency oscillations

Despite the large number of available RXTE observations of black hole binaries, only a handful of detections of quasi-periodic peaks above 30 Hz is available (see Belloni et al., 2006, and references therein). Three sources show a single QPO peak, although for two of them the detection is not very significant and in the case of XTE J1650–500 the peak appears only after stacking spectra from a specific state. Four other sources

show two peaks, which when detected more than once appear at almost the same frequency: GRO J1655–40 (300 and 450 Hz), XTE J1550–564 (184 and 276 Hz), H 1743–322 (165 and 241 Hz) and GRS 1915+105 (41 and 69 Hz). In the first three cases, the frequencies are consistent with being in 3:2 ratio, for GRS 1915+105 the ratio is 5:3. Interestingly, an additional peak at 27 Hz was found in GRS 1915+105, which is in 2:3 ratio with 41 Hz (Belloni et al., 2001). These features are very important as they constitute the highest-frequency signals from accreting black holes and they are most likely related to effects of General Relativity in the strong field regime. This is not the place to discuss more details or applicability of models, but it is important to remark that all these detections correspond to sources in (or close to) the SIMS. The case of GRS 1915+105 is more complex, as the association of its features with the four states described above is not simple (see Reig et al., 2003; Soleri et al., 2008).

2.7 The multi-wavelength view

The phenomenology described above was found to have strong links with the properties of relativistic jets as observed in the infrared and radio bands. The radio emission offers the possibility to study the synchrotron emission related to the relativistic jets (see Fender et al., 2010; Gallo, 2010), while in the IR, optical and UV bands the thermal emission from the companion star and from the outer edge of the disc can be observed (see e.g., Homan et al., 2005; Russell et al., 2006; Migliari et al., 2007).

The basic properties are summarized in Fig. 2.5. In the LHS, a steady compact jet is observed, with a flat or inverted spectrum and a barely resolved spatial distribution. The radio and infrared fluxes are correlated with the X-ray flux, correlation which extends to the AGN when the proper mass scaling is considered (see Coriat et al., 2011, and references therein). The infrared flux also correlates with the X-ray one.

At the top of the LHS branch, in GX 339–4 the correlation between X-ray and infrared was observed to break down (Homan et al., 2005). As the source follows the HIMS and approaches the transition to the SIMS, the radio spectrum starts steepening (Fender et al., 2004). Around, but not exactly at the time of the transition (Fender et al. 2009), a radio flare is observed (or the ejection time of a fast relativistic resolved jet). The hardness threshold at which this happens has been dubbed “jet line”. After the source enters the HSS, no nuclear radio emission has been detected up to know, as all detections are compatible with emission from the ejecta. Recent observations of 4U 1957+11 have put the limit to more than 300 times lower than the LHS radio flux at the same X-ray flux (Russell et al., 2011).

In correspondence of additional transitions back and forth between HIMS and SIMS, there is some evidence that more radio flares are emitted in XTE J1859+226, (see Brocksopp et al., 2002), and in GRS 1915+105 where the oscillations have been

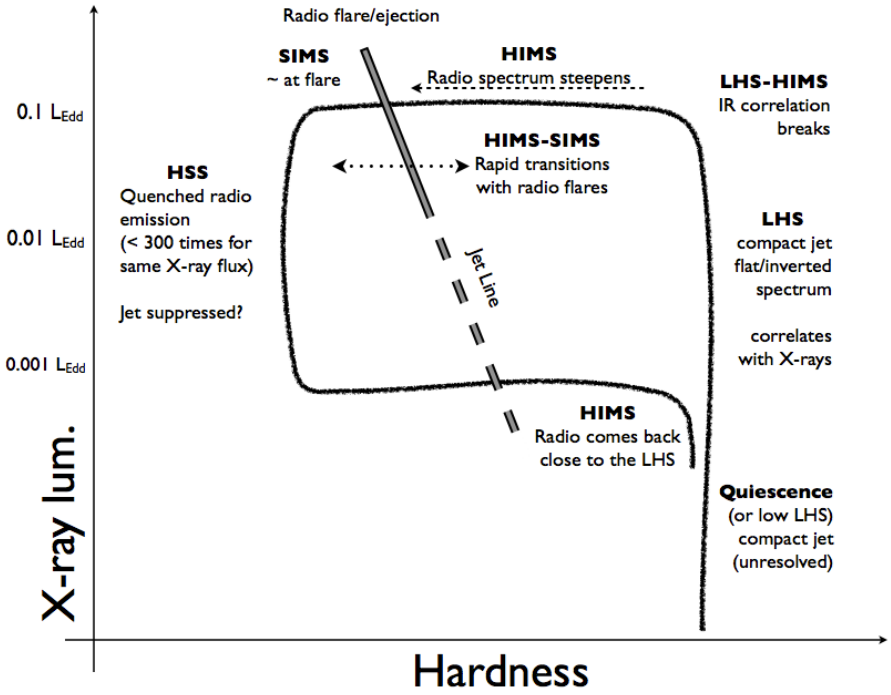

Figure 2.5: Stylized hardness-intensity diagram for a BHT with labels indicating the radio properties.

connected to such transitions (Fender et al., 2004).

On the return transition, the radio emission becomes detectable again, but at a higher hardness value than it disappeared earlier, when the source has already reached the LHS (Kalemci et al., 2006). The radio/X-ray correlation is re-established and can be followed down to very low accretion rate (Gallo et al., 2006).

2.7.1 Optical and infrared timing

The advent of new instrumentation during the last decade (e.g., ULTRACAM; Dhillon et al. 2007) has enabled us to extend some of the timing studies, classically performed at high energies, to the optical and infrared domains with unprecedented quality. In contrast to what is typically observed in neutron stars (e.g., Muñoz-Darias et al. 2007), complex cross correlation functions, with optical variability leading and anti-correlated to X-rays were found in BHT during the LHS (e.g., Kanbach et al. 2001; Durant et al. 2008). These features cannot be explained solely by reprocessing on the accretion disc (see Hynes et al. 2003) and theoretical interpretations proposed gener-

ally require of a substantial contribution to the optical emission from the synchrotron jet observed at radio waves (Malzac et al. 2004; Veledina et al. 2011). This interpretation is also supported by some spectral energy distribution studies, which point to a significant jet contribution to the OIR (optical-infrared) and maybe to higher energies during the LHS (e.g., Markoff et al. 2001; Russell et al. 2010) and by high time resolution studies performed in the near IR (Casella et al., 2010). To gauge the jet contribution to the OIR is an important open issue since it has strong implications in, e.g., understanding the amount of energy carried by the jet. New studies are being currently undertaken by several groups from both spectral and timing point of view, and much progress is expected in the forthcoming years in this relatively young field. Here, it is worthy to notice the timing capabilities of ASTROSAT in the UV, that could be exploited in the very near future.

2.8 Dynamical measurements of black hole masses

At present, more than $\sim$ 20 of X-ray binaries where the compact object is heavier than $3M_{\odot}$ have been found, with masses as high as $\sim 15M_{\odot}$ (Orosz et al. 2007). Most of these measurements come from BHT, where the companion star is usually detectable during the quiescence epoch and classical techniques based on the Kepler laws (see e.g., Casares et al. 2007 for a recent review) can be applied. However, this number is still not enough to have a good description of the mass spectrum of stellar mass BHs, and some open questions remain (e.g., is there a real gap in the distribution of masses of compact objects between NS and BHs?; see Özel et al. 2010). On the other hand, the mass is a key parameter for BH spin measurements (e.g., McClintock et al. 2011). New analysis methods (e.g., Hynes et al. 2003; Muñoz-Darias et al. 2008, Cantrell et al. 2010) and observing facilities (e.g., Corral-Santana et al. 2011) are allowing us to tackle faint systems and to infer more accurate masses. A big improvement will come with the next generation of telescopes (20–40 m), which will enable to study objects with very faint quiescence levels. Still, one of the main problems will be to discover more of those systems without the need that they go into outburst. This would increase significantly the number of dynamical mass measurements since the population of quiescence black holes is expected to be at least of the order of few thousands (see e.g., Romani 1998 and references therein).

2.9 Where do we go from here: ASTROSAT and LOFT

The natural successor of RXTE is the Indian multi-wavelength mission ASTROSAT (Agrawal, 2006), which is currently schedule for launch by the second half of 2012. While its all-sky monitor (SSM) will allow good coverage of the transient X-ray sky and its UV telescope (UVIT) will observe the very few BHTs which are not

affected by very high absorption, its X-ray pointed instruments will extend the RXTE characteristics and make it possible to continue and extend the study of bright BHT transients. The soft X-ray telescope (SXT: 0.3–8 keV) and the coded-mask imager (CZTI: 10–150 keV) will complement the large proportional counter array (LAXPC: 3–80 keV) to produce broad-band X-spectra, and the LAXPC effective area (6000 cm^2 at 10 keV) will yield the large photon counting necessary for fast-timing studies.

For the phenomenology described above, the LAXPC effective area is particularly interesting. While comparable to that of the RXTE/PCA below 10 keV, between 10 and 80 keV the LAXPC will be much more sensitive (in particular since later PCA observations are performed with 1 or 2 detector units, see Fig. 2.6). All timing signals from BHTs, with the exception of the strong noise in the LHS, are stronger at high energies. In Fig. 2.6 are shown the energy dependence of a type-C QPO and a HFQPO, superimposed on the PCA and LAXPC effective areas. It is clear that the higher sensitivity of the LAXPC above 10 keV will allow the study of weaker signals and in particular will offer the possibility to detect new HFQPOs in addition to the handful already available.

As the observational constraints of ASTROSAT will not be the same as those of RXTE, it is important to plan the best observational strategy for BHTs. An extremely dense coverage of outbursts such as that in Fig. 2.1 is most likely not going to be available, at least in the first phases of the mission. However, the detailed knowledge of the phenomenology described in the previous sections make it sure that even selected pointings, triggered by other instruments such as the SSM, MAXI, INTEGRAL/IBIS or Swift/BAT, have the potential of a late yield. In particular, a strategy of fewer longer observations in correspondence of main transition and states will generate crucial data, especially if coordinated with observations at lower wavelengths (radio, IR) from the ground.

For the most distant future, not before 2020, the LOFT mission has been proposed and is being evaluated (Feroci & LOFT Consortium, 2011). The effective area of the LAD instrument is currently being planned to be 12 m^2 at 8 keV, clearly a major step forward compared to current instrumentation. With LOFT, it will be possible to detect HFQPOs at very low fractional rms, therefore unveiling its nature by examining the distribution in detected frequencies (one of the current models predicts that the frequencies are constant), while the relative variation of the frequencies will tell us to which relativistic time scales, if any, they correspond to. Moreover, a very large collecting area will allow the detection of a sufficiently high number of photons to study low-frequency oscillations directly in the time domain, opening the possibility of understanding the nature of their quasi-periodicity and its connection to accretion and General Relativity. The good energy resolution will also make it possible to link fast variations to spectral measurements, tying two parallel aspects connected to relativistic effects, a subject that it is barely possible to touch with RXTE.

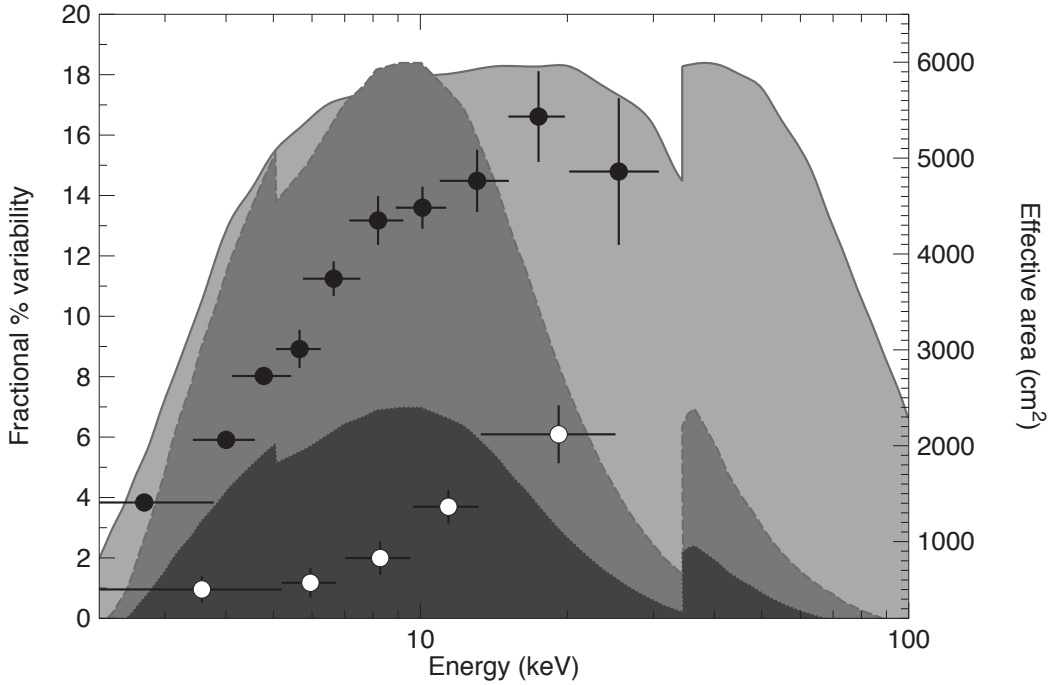

Figure 2.6: A comparison of instrument effective areas and energy-dependent variability for selected signals. Dark gray: area of RXTE/PCA (2 units); medium gray: RXTE/PCA effective area (5 units); light gray: ASTROSAT/LAXPC effective area (3 units). The black points report the energy dependent fractional rms variability of the type-C QPO in XTE J1859+226 (from Casella et al., 2004), the white points that of the HFQPO in GRS 1915+105 (from Morgan et al., 1997).

Acknowledgments

SM and TB acknowledge support from grant ASI-INAF I/009/10/. The research leading to these results has received funding from PRIN INAF 2007 and from the European Community's Seventh Framework Programme (FP7/2007-2013) under grant agreement number ITN 215212 'Black Hole Universe'. Partially funded by the Spanish MEC under the Consolider-Ingenio 2010 Program grant CSD2006-00070: 'First Science with the GTC' (http://www.iac.es/consolider-ingenio-gtc/).

3 The evolution of the high-energy cut-off in the X-ray spectrum of GX 339-4 across a hard-to-soft transition

Sara E. Motta, Tomaso M. Belloni, Jeroen Homan

Monthly Notices of the Royal Astronomical Society, 2009, 400, 160

Abstract

We report on X-ray observations of the black-hole candidate GX 339-4 during its 2006/2007 outburst. The hardness-intensity diagram of all RXTE/PCA data combined shows a q-shaped track similar to that observed in previous outbursts. The evolution through the HID suggests that in the early phase of the outburst the source underwent a sequence of state transitions, from the hard to the soft state, which is supported by our timing analysis. Broadband (4-200 keV) spectra, fitted with an exponentially cutoff powerlaw, show that the hard spectral component steepens during the transition from the hard to the soft state. The high-energy cutoff decreased monotonically from 120 to 60 keV during the brightening of the hard state, but increased again to 100 keV during the softening in the hard intermediate state. In the short-lived soft intermediate state the cutoff energy was $\sim$ 130 keV, but was no longer detected in the soft state. This is one of the first times that the high-energy cut-off has been followed in such detail across several state transitions. We find that in comparison to several other spectral parameters, the cut-off energy changes more rapidly, just like the timing properties. The observed behaviour of the high energy cutoff of GX 339-4 is also similar to that observed with RXTE-INTEGRAL-Swift during the 2005 outburst of GRO J1655-40. These results constitute a valuable reference to be considered when testing theoretical models for the production of the hard component in

these systems.

3.1 Introduction

The spectral evolution of black hole X-Ray transients (BHTs) has recently been described in terms of patterns in an X-ray hardness-intensity diagram (HID) (see Homan et al. 2005; Belloni et al. 2005; Belloni (2005), Gierliński & Newton 2006, Remillard & McClintock 2006, Belloni 2010, Fender et al. 2009). Different states are found to correspond to different branches/areas of a q-like pattern that shows up in a log-log representation. Four main states are identified within this framework: Low Hard State (LHS), Hard Intermediate State (HIMS), Soft Intermediate State (SIMS), High Soft State (HSS). Twostates correspond to the original states discovered in the 1970s: the Low/Hard State (LHS), observed usually at the beginning and at the end of an outburst, showing a spectrum dominated by an hard component with sometimes a thermal disc component (very faint) and the High/Soft State, usually observed in the central intervals of an outburst, that shows an energy spectrum dominated by a thermal disc component, with the presence of an additional weak and steep power-law component.

In between these two well-established states, the situation is rather complex and has led to a number of different classifications. Homan et al. (2005) identify two additional states, clearly defined by spectral/timing transitions. In the evolution of a transient, after the LHS comes a transition to the Hard Intermediate State: the energy spectrum softens as the combined result of a steepening of the power-law component and the appearance of a thermal disc component. At the same time, the characteristic frequencies in the power spectrum increase and the total fractional rms decreases. The transition to the Soft-Intermediate State can be very fast (sometimes over a few seconds, see Nespoli et al. 2003) and is marked by the disappearance of some particular features in the power density spectrum and by the appearance of some others.

Together with the association of the transition to the SIMS with the ejection of fast relativistic jets, this has led to the identification of a *jet line* in the HID, separating HIMS and SIMS (Fender et al. 2004). The jet line can be crossed more than once during an outburst (as in the case of XTE J1859+226: Casella et al. 2004; Brocksopp et al. 2004). Notice that recently the comparative study of different systems has shown that the jet ejection and HIMS/SIMS state transitions are not exactly simultaneous (Fender et al. 2009). For a more detailed state classification see cite-Belloni2010. McClintock et al. (2009) use another state classification based more on spectral properties than on timing properties, unlike the classification presented by Homan et al. (2005).They define three different states on the basis of precise boundaries of a number of parameters such as integrated fractional rms and the presence of QPO in the Power Density Spectrum, power law photon index and disk fraction in the energy spectra. For a comparison between the two classifications, see Belloni

(2009).

While the physical nature of the soft component in the X-Ray spectra of BHTs is commonly associated with an optically thick accretion disc, there is no consensus as to the origin of the hard spectral component. Nevertheless there are various suggestions regarding this: the hard spectral component could be due to the presence of different component, such as a hot corona, the very inner part of the accretion flow, the formation/ejection of relativistic jets. The hard component is usually interpreted as the result of thermal Comptonization or of a combination of thermal/non-thermal Comptonization involving the hot electrons of the corona and the soft photons originating in the accretion disk. When fitted with a power-law, the slope of the hard component is typically found to be $\sim$1.6 for the LHS, 1.6-2.5 in the SIMS/HIMS and 2.5-4 for the HSS (Belloni et al. 2006). It has been known for a long time (Sunyaev & Titarchuk 1980) that the LHS spectrum shows a cutoff around $\sim$ 100 keV. A comparative measurement of a number of systems with CGRO/OSSE has been presented by Grove et al. (1998). Here the energy spectra could be clearly divided into two classes: the ones with a strong soft thermal component and no evidence of a high-energy cutoff until $\sim$ 1 MeV, and those with no soft component and a $\sim$ 100 keV cutoff. Zdziarski et al. (2001) and Rodriguez et al. (2004) measured the high-energy spectrum of GRS 1915+105 and found no direct evidence of a high-energy cutoff, but spectra which appeared to contain two components. At energies of 50-150 keV, the hard spectral component often shows a cut off (Belloni et al. 2006, Joinet et al. 2008, Miyakawa et al. 2008, Del Santo et al. 2008), which can provide additional information about the properties and origin of the hard spectral component. This cut off is thought to be related to the temperature of the thermal comptonizing electrons located in an optically thin corona close to the black hole, responsible for the comptonization of the soft photons emitted by the accretion disc. More recently Miyakawa et al. (2008) performed an analysis on Rossi XTE Observation of GX 339-4 with the aim to investigate the radiation mechanism in the hard state of the source. They observed a high-energy cutoff ranging from 40 to over 200 keV. Joinet et al. (2008) presented the analysis of the high energy emission of GRO J1655-40 at the beginning of the 2005 Outburst. Their high-energy data allowed them to detect the presence of a high-energy cutoff and to study its evolution during the outburst rise. They observed a cutoff decreasing from above 200 keV down to $\sim$ 100 keV. Following that it either increases significantly or vanishes completely. Caballero-García et al. (2009) also studied GRO J1655-40 during the 2005 outburst but claimed that no cutoff was required for their INTEGRAL dataset.

The X-ray spectra of BHTs also include additional components which are important in terms of the physics of accretion onto black holes, such as emission and absorption line features (see e.g. Miller et al. 2002, Miller et al. 2004, Miller et al. 2006, Neilsen & Lee 2009) and Compton reflection humps (see e.g. George & Fabian

1991, Zdziarski et al. 2001, Frontera et al. 2001).

3.1.1 GX 339-4

GX 339–4 was one of the first two BHTs for which a complete set of transitions was observed and studied (see Miyamoto & Kitamoto 1991; Belloni et al. 1997; Mendez & van der Klis 1997), and is known to spend long periods in outbursts.

A detailed study of the evolution of the hard spectral component in GX 339-4 at energies above 3 keV was performed during its 2004 outburst which began in February of that year. To get broad-band coverage during the expected HIMS-SIMS spectral transition, simultaneous RXTE and INTEGRAL observations were made. Belloni et al. (2006) combined data from PCA, HEXTE and IBIS, and obtained good quality broad-band (3-200 keV) energy spectra before and soon-after the transition. These spectra indicated steepening of the hard, high-energy component. Also, the high-energy cut-off which was present at $\sim$70 keV before the transition was not detected later. Therefore, although spectral parameters at lower energies do not change abruptly during the transition, the energy of the cut-off increases or disappears rapidly (within 10 hours). The power spectra before and after the transition showed significant differences (see Belloni 2005): from strong band-limited noise and type-C QPO to much weaker noise and type-B QPO (for a description of the properties of different types of QPO, see Casella et al. 2005).

Del Santo et al. (2008) report on X-ray and soft γ-ray observations of the black-hole candidate during an outburst in 2006/2007, performed with the RXTE and INTEGRAL satellites. The evolution in the HID of all RXTE/PCA data suggests that a transition from hard-intermediate state to soft-intermediate state occurred, simultaneously with INTEGRAL observations performed in March. The transition was confirmed by the timing analysis which revealed that a weak type-A quasi-periodic oscillation (QPO) replaced a strong type-C QPO. At the same time, spectral analysis revealed that the flux of the high-energy component showed a significant decrease. However, Del Santo et al. (2009) observed a delay of roughly one day between variations of the spectral parameters of the high-energy component and changes in the flux and timing properties.

The aim of this work is to use RXTE data collected during the 2006/2007 outburst to study the broad-band spectral evolution of GX 339-4 during a full hard-to-soft state transitions and in particular the behaviour of the high-energy cut off. Here we study the spectral evolution of GX 339-4 over a longer period of time, covering almost the entire LHS to HSS transition (from 27 December 2006 to 18 April 2007). Thanks to the unprecedented data coverage of the main phases of the source's evolution we were able for the first time to follow in a detailed way the spectral evolution of the source and in particular of the cut-off energy component of the spectra over the LH, HIMS, SIMS and the first part of the HSS state of the sources.

3.2 Observations and data analysis

In 2006 November, X-ray activity of GX 339-4 was detected with the Rossi X-ray Timing Explorer (RXTE; Swank 2006). The source had an almost constant flux until the end of December 2006, when the hard (15-50 keV) X-ray flux increased by a large amount. It reached its brightest level since 2004 November, as detected by SWIFT/BAT (Krimm et al. 2006). In order to follow the new outburst of GX 339-4 at high energies, an RXTE ToO campaign was carried out. As expected in BHTs (Homan et al. 2005), at the beginning of the outburst GX 339-4 was in the LHS. Results of X-ray and soft $\gamma - ray$ observations of GX 339-4 during its 2006/2007 outburst, performed with RXTE and INTEGRAL satellites have already been reported in Del Santo et al. (2008). Additional results can be found in Caballero-García et al. (2009), who reported on simultaneous XMM-Newton and INTEGRAL observations.

Starting from December 27, 2006 (MJD 54096) a total of 220 RXTE pointings were performed over a period of about 10 months, covering the full outburst of the source. We report here the color analysis of all observations (MJD 54096 to 54388, see Figs. 3.1 and 3.2, top panel) and spectral analysis of 83 observations (MJD 54134 to 54208) covering the transition from the LHS to HSS.

We extracted energy spectra from the PCA and HEXTE instruments (background and deadtime corrected) for each observation using the standard RXTE software within HEASOFT V. 6.4, following the standard extraction procedures. For our spectral analysis, only Proportional Counter Unit 2 from the PCA and Cluster B from HEXTE were used. A systematic error of 0.6% was added to the PCA spectra to account for residual uncertainties in the instrument calibration. We accumulated background corrected PCU2 rates in the channel bands A = 4 - 45 (3.2 - 18.3 keV), B = 4 - 10 (3.2 - 5.4 keV) and C = 11 - 20 (5.7 - 9.0 keV). A is the total rate, while the hardness was defined as H = C/B (see Homan & Belloni 2005). PCA+HEXTE spectra were fitted with XSPEC V. 11 in the energy range 3 - 20 keV and 20-200 keV respectively. See Tab. 3.2 for the counts and hardness ratio values.

For our timing analysis, we used custom software under IDL. For each observation we produced power density spectra (PDS) from stretches 128 seconds long using two separate energy bands: PCA channel band 0-249 (corresponding to $\sim$ 2-60 keV) for the main power spectrum, and PCA channel band 18-249 ($\sim$ 7.7-60 keV) in order to look for high-frequency oscillations, which are usually more prominent in this high-energy band (see Homan et al. 2002). We averaged the power spectra and subtracted the contribution due to Poissonian noise (see Zhang et al. 1995) in order to produce two Power Density Spectra (PDS) for each observation: one for the whole energy band and one for the high one. The power spectra were normalized according to Leahy et al. (1983) and converted to squared fractional rms (Belloni & Hasinger 1990). See Tab. 3.2 for the rms values.

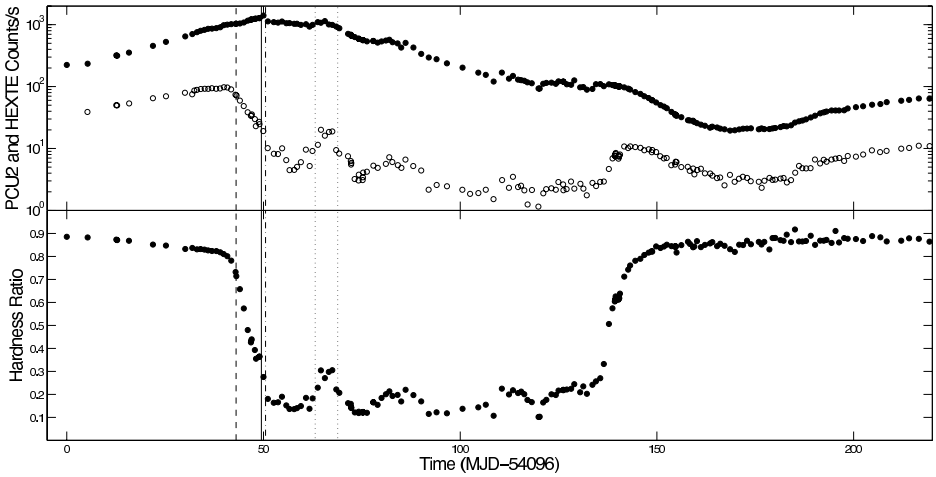

Figure 3.1: Top panel: RXTE/PCA (filled circles) and RXTE/HEXTE (empty circles) light curve of GX 339-4 during the 2006/2007 outburst. The energy range is 3.3 - 21.0 keV for PCA and 19.0 - 200.0 keV for HEXTE. The vertical lines separate the four canonical States (see Sec. 3.3.1 and 3.4). Bottom panel: Time evolution of the hardness ratio. The dashed line separates the LHS from the HIMS, the solid line marks the passage from the HIMS to the SIMS and the dot-dashed line separates the SIMS from the HSS. Notice that the source crosses the HIMS-SIMS transition line several times; we marked only the first transition from the HIMS to the SIMS and from the SIMS to the HSS. The two dotted lines indicate the time interval during which the source undergoes several transitions from and to the SIMS (See Sec. 3.4).

3.3 Results

In this section, we describe the general evolution of the outburst. In Fig. 3.1, we show the full light curve of the outburst (top panel) and the evolution of the hardness ratio (bottom panel). The Hardness Intensity diagram is shown in Fig. 3.2.

In Tab. 3.2 we list the background corrected PCU2 count rate and the hardness. As one can see from Fig. 3.1 and Fig. 3.2, the source evolution during the outburst is very similar to that of the 2002/2003 and 2004 outbursts (see also Belloni 2005): a monotonic increase in count rate at a rather high color, a horizontal branch with the source softening at a nearly constant count rate, softening with a transition to the SIMS, and further observations at very low hardness. Finally, at count rates lower than the initial LHS-HSS transition, the transition from the HSS back to the LHS takes place. A noticeable difference between this outburst and the 2004 outburst is the count rate level of the top horizontal branch, which is a factor of ~ 3.5 higher in the 2006/2007 outburst, similar to the count rate level of the 2002/2003 outburst.

In this work we concentrate on the first part of the outburst, covering the LHS and

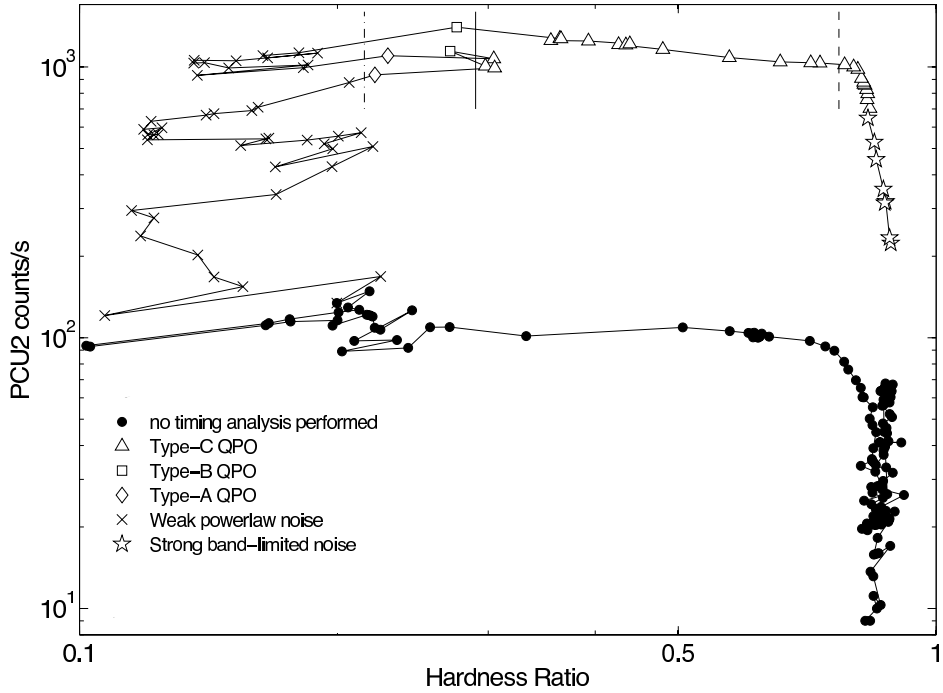

Figure 3.2: Hardness-Intensity diagram from RXTE/PCA data for the complete 2006/2007 outburst which starts from the middle right and proceeds in a counter-clockwise direction. Different symbols indicate different timing properties: type-A QPOs (diamonds), type-B QPOs (squares), type-C QPOs (triangles), strong band-limited noise components in the Power Density Spectrum (stars), weak powerlaw noise in the Power Density Spectrum (crosses). The black dots indicate observations for which we did not perform timing analysis. The vertical lines mark the transitions as in Fig. 3.1. In this plot the SIMS-HSS transition line is the same for both the main and the second SIMS-to-HSS transition (see Sec. 3.4).

the complete LHS to HSS transition, from observation #1 to observation #83. We will refer to Tab. 3.2 and Tab. 3.3 and to the observation numbers reported therein.

3.3.1 Timing Analysis

Since we usually describe the evolution of a source in terms of spectral states, defined on the basis of spectral and timing properties, first of all we have to classify all observations following stated criteria (see Homan et al. 2005; Belloni 2005, Fender et al. 2009, Belloni 2010). For this reason we need the HID and the timing informations in order to identify the branches we see in the HID in terms of canonical BHTs canonical states, which will serve as a framework for the spectral analysis (see Sec.

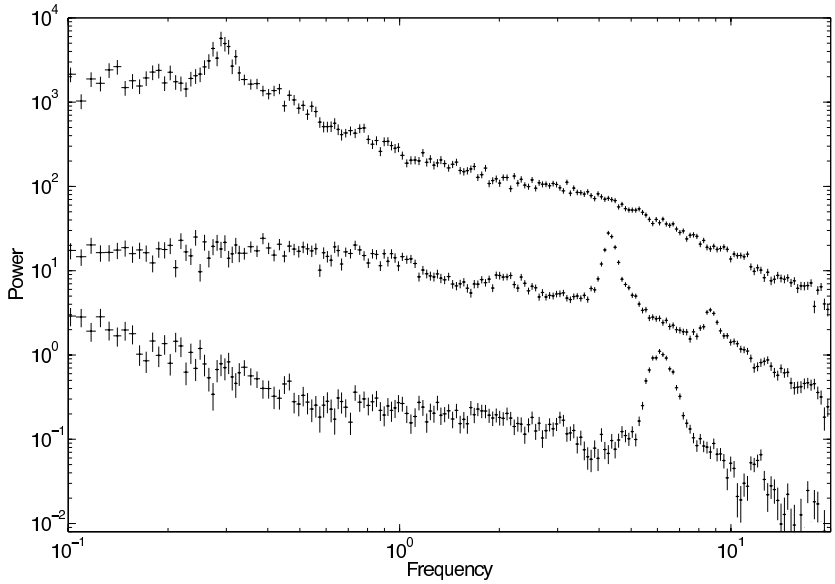

Figure 3.3: Power density spectra for PCA belonging to two different states. Top curve: Obs. $\#15$, belonging to the LHS (right vertical branch in the HID, Fig. 3.2). Middle curve: Obs. #25, belonging to the HIMS (top horizontal branch in the HID). Type-C QPOs are evident in both PDS. Bottom curve: obs. $\#47$, belonging to the SIMS, middle part of the top horizontal branch of the HID in Fig. 3.2. A strong type B QPO is evident in the PDS. We observed 2 Type B QPOs and 2 Type A QPOs during the SIMS. The top curve is multiplied by a factor of 10 and the bottom curve is scaled down by a factor of 10 for clarity.

3.3.2). Beginning form the HID and examining the power spectra, the presence of state transitions becomes more clear.

- Observations from $\#1$ to $\#19$ show a high level of aperiodic variability in the form of strong band-limited noise components (see Fig. 3.3, top curve), with total integrated fractional rms in the range $26-47\%$, positively correlated with hardness. The PDS can be decomposed in a number of Lorentzian components, one of which can take the form of a type-C QPO peak (see table 3.1). All the observations #1 to #19 correspond to the right branch in the top panel of Fig.3.2. The total fractional rms decreases as the source softens and brightens. All observations in which we found type-C QPOs are marked with triangles in Fig. 3.2, while the other observations are marked with stars.

- Observations $\#20$ to $\#31$ and observations #46, #48, #49 show fast aperiodic variability with a band-limited noise and strong type-C QPOs (see Fig. 3.3, middle curve). The PDS can be decomposed in the same Lorentzian compo-

#obs ID	Noise Type	QPO type	RMS (in %)
#1 to #8	strong band limited noise	-	26-47%
#9 to #19	strong band limited noise	C	26-47%
#20 to #31; #46,#48,#49	strong band limited noise	C	14-23%
#32,#47	weak powerlaw component	A	11%
#45,#50	weak powerlaw component	B	5-6%
#33 to #44; #51 to #83	weak powerlaw component	-	1-2%

Table 3.1: Timing properties seen in the PDS of each observation.

nents as in the preceding observations. The total fractional rms is lower than in the LHS (14-23%) and decreases as the source spectrum softens. The observations correspond to the first part of the horizontal branch in Fig. 3.2, where the largest color variations are observed. Notice that the boundary between this group and the former is somewhat arbitrary, as the evolution in parameters is rather continuous.

- Observation #32 and #47 correspond to a much weaker variability, in the form of a weak ($\sim 11\%$ fractional rms) powerlaw component. A type-B QPO is prominent in the PDS (see Fig. 3.3, bottom curve). As observed in the 2004 outburst (see Belloni 2005, Belloni et al. 2008) we see significant differences in the power spectra, with respect to the previous power spectra. Strong band limited noise and a Type-C QPO give way to a much weaker noise and Type-B QPO. Observations #45 and #50 show a Type-A QPO, weaker than the type-B QPO detected and with a total fractional rms of $\sim 5\%$ and $\sim 6\%$ respectively. These two observations were also softer than the two showing a Type-B QPO. All the observations presenting a type-A or B QPO are marked respectively with diamonds and squares in Fig. 3.2.

- Observations from #33 to #44 and #51 to #83 show weak powerlaw noise with a rms of a few %. They correspond to the softest observations in Fig. 3.2 (top panel). All these observations are marked with crosses in the HID in Fig. 3.2.

These results are summarized in Tab. 3.1.

From the PDS described above, we can identify the four groups of observations as belonging to the LHS (Observations from #1 to #19, right vertical branch of the HID in Fig. 3.2), the HIMS (Observations from #20 to #31 and observations #46, #48, #49, on the right part of the top horizontal branch of the HID in Fig. 3.2), the SIMS (observations #32, #45, #47, #50, marked with squares in the middle of the

HID in Fig. 3.2) and HSS (Observations from #33 to #44 and observations #51 to #83, left vertical branch of the HID in Fig. 3.2). Corresponding transition lines are shown in Fig. 3.2 and in Fig. 3.1. We examined all power spectra, both at low and high energies, for high-frequency features, but found no significant excesses.

In order to compare our results with the classification of McClintock et al. (2009), we follow their updated recipe. They present three states: Hard, Thermal Dominant (TD) and Steep Power Law (SPL). These three states do not fill the complete parameter space: observations which do not qualify are classified as "intermediate". For the 83 observations we analyzed in detail, we calculated the disk fraction of the total 2-20 keV unabsorbed flux, the fractional rms integrated over the range 0.1-10 Hz, the QPO amplitude if any QPO is seen and we used the values of photon index for the power-law used in the fits of our spectra (see Tab. 3.3). The criteria used for the McClintock & Remillard classification are summarized in Tab. 1 in McClintock et al. (2009). In Tab. 1, in addition to our state, we also report theirs. A comparison between the two schemes as applied to these observations can be seen in Tab. 3.5. We see that 42% of the observations fall into the intermediate state. The others show a general (expected) trend: all the LHS are Hard, most of the HSS are Thermal-Dominant and the SIMS are steep-power law. However, the association is not one to one. In conclusion we can say that for our data the classification we used and McClintock and Remillard classification are quite similar, but for the latter more than 40% of the observations remain unclassified.

3.3.2 Spectral Analysis

PCA (4-20 keV) and HEXTE (20-200 keV) spectra were combined for our broad-band spectral analysis. For fitting the spectra, we used XSPEC V.11.2.3.

Following Miyakawa et al. (2008) in Fig. 3.4 we first plot the ratio of the three representative spectra to a Crab-like spectrum. We selected Obs. #1, Obs. #19 (where we observed respectively the highest and the lowest high-energy cutoff during the LHS) and Obs. #34 (where there is not a detectable cutoff). The Crab spectrum was simulated using a simple powerlaw with photon index 2.1 and normalization 10 using `xspec`. As can be seen from the figure, there is a cutoff at high energies that changes from ~ 120 keV (Obs. #1) to ~ 60 keV (Obs. 19) with increasing flux.

In order to fit spectra we started trying a model of only one component, either cutoff power law or disk, but it could not fit all the spectra. A combination of the two was successful, with the exception of a few observations where a single component was sufficient. A simple model consisting of a multi-color disc-blackbody (`diskbb`) and a cut-off power law (`cutoffpl`) was used to fit spectra. A hydrogen column density measured with instruments having a low-energy coverage, e.g. Chandra, was taken into account by adding a `wabs` component into XSPEC, with N_H frozen to $5 \times 10^{21} \mathrm{cm}^{-2}$ (Mendez & van der Klis 1997; Kong et al. 2000). An iron emission

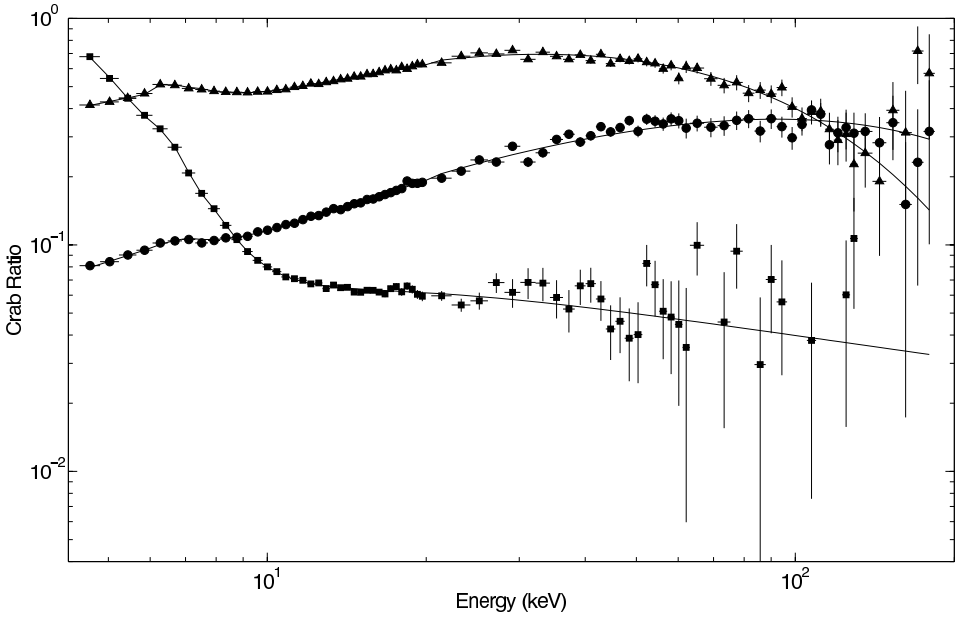

Figure 3.4: PHA ratio of GX 339-4 to Crab for three selected observations. We reported observation #1 (circles), observation #19 (triangles) and observation #34 (squares). The high energy cutoff depends on the X-Ray luminosity and decreases with increasing luminosity.

line with centroid fixed at 6.4 keV was further needed in order to obtain acceptable fits. The line never becomes wider than 0.8 keV[1]. To account for cross-calibration problems, a variable multiplicative constant for the HEXTE spectra (as compared to the PCA) was added to the fits. In order to account for a reflection component, we introduced a smeared edge with energy between 7.1 and 9.3 keV. This component is alway $\sim$ 10 keV wide and does not vary during the source evolution, so we can assert that the smeared edge component does not affect the properties of the cutoff. For the first part of the outburst (from $\#1$ to $\#23$), a disk component was not needed in order to obtain good spectral fits and was therefore removed from the fit. The average reduced χ^2 was 1.17 for 92 degrees of freedom. In Fig. 3.5 spectral fits from selected observations are shown. The upper spectrum is from observation #1 (belonging to the LHS, in the right vertical branch of the HID in Fig. 3.2). The high-energy cutoff for this spectrum is the highest seen that can be considered reliable. Several HSS

[1]Miller et al. (2004) analysed spectra of GX 339-4 obtained though simultaneous XMM-Newton/EPIC-pn and Rossi XTE observations during a brigh phase of the 2002/2003 outburst. They revealed an extremely skewed, relativistic Fe Kα emission line in the spectra with strong red wings and intrinsically broad due to the Doppler shift near the innermost stable orbit.

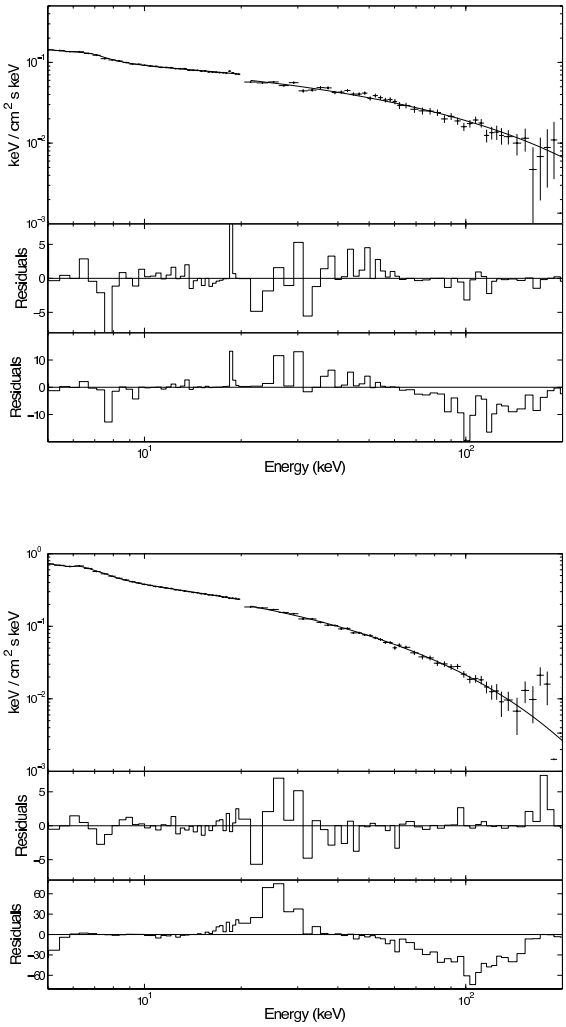

Figure 3.5: Spectral fit results of the combined PCA and HEXTE spectra of GX 339-4 for two selected observations. For both spectra we used a model consisting of an interstellar absorption component, a gaussian line, a smeared edge in order to account for the reflection component, a multicolor disk-blackbody and a cutoff powerlaw. Top panel: observation #1 (LHS, right vertical branch in the HID. 3.2). This observation shows the highest value of the cutoff we can consider reliable (small errors). The high values we found during the HSS presents too large error bands to be considered reliable. Bottom panel: observation #19 (LHS, upper part of the right vertical branch in the HID) shows one of the lowest values of the high-energy exponential cutoff we observed in our data. The top panels in both the figures show a spectrum fitted with a cut-off powerlaw model (see text), the middle panels show residuals from a fit with a simple cutoff-powerlaw model, the bottom panels show the residuals for a simple powerlaw model.

observations present very high values for the high-energy cutoff, but with very large uncertainties. The lower spectrum is from observation #19 (belonging to the LHS, in the right vertical branch very high part in the HID). This spectrum shows one of the lowest cutoff energies we observed in our data. This observation was taken just before the LHS-to-HIMS transition. For the second group of observations (from $\#24$ to #32, from #36 to #39 and from #43 to #50), a disk black body was necessary, yielding an average reduced χ^2 of 0.90 for 90 degrees of freedom. Finally, the softest observations (from $\#33$ to $\#35$, from $\#40$ to $\#42$ and from #50 to #83) did not require a high-energy cutoff. The average reduced χ^2 was 0.92 for 91 degrees of freedom.

The best fit parameters are listed in Tab. 3.3, while in Fig. 3.6 one can see the evolution of the main spectral components. The data shown in all the panels in Fig. 3.6 come from a selection of 51 observations (from #1 to #51) covering the entire hard-to-soft transition of the source. Fig. 3.7 shows the evolution of the best fit model.

In order to accumulate spectra with better statistics for soft observations where a high-energy cutoff is not measured, we summed spectra corresponding to similar hardness. The resulting fit parameters are shown in Tab. 3.4: a high-energy cutoff is detected, although with large uncertainties. In Fig. 3.6, where we also mark the transitions established through timing analysis, we can follow the evolution of spectral prameters. In the bottom panel of Fig. 3.6 we used the parameters coming from Tab. 3.4, while for the other panels of Fig. 3.6 we used parameters coming from Tab. 3.3. From Fig. 3.6 we can see that:

- The photon index undergoes a slight increase during the LHS from $\Gamma \sim 1.4$ to ~ 1.6. During the HIMS it rises from 1.6 to 2.4 in a few days. After the HIMS to SIMS transition the photon index is consistent with being constant.

- The high-energy cut off is clearly present in the LHS, during which it changes almost monotonically from $\sim$120 keV to $\sim$60 keV. After the transition to the HIMS the high-energy cut off increases considerably, from 60 keV to 100 in a few days. During the SIMS and the HSS, the high-energy cut off appears to be very high ($\sim$160 keV) and constant, while after the final transition to the HSS (taking place between observations #50 and #51) it disappears. Since in this phase of the outburst the hard tail of the spectrum is very weak and a small fluctuation in the flux can modify the spectrum, during the SIMS and the HSS the high-energy cutoff appears with large uncertainties. Therefore, we cannot assert the presence or the absence of a high-energy cutoff. The fact that this happens near the HIMS-SIMS and SIMS-HSS transitions is particularly relevant in the context of jets models, because the high-energy cutoff changes take place very close in time to the moment in which the jet emission is supposed

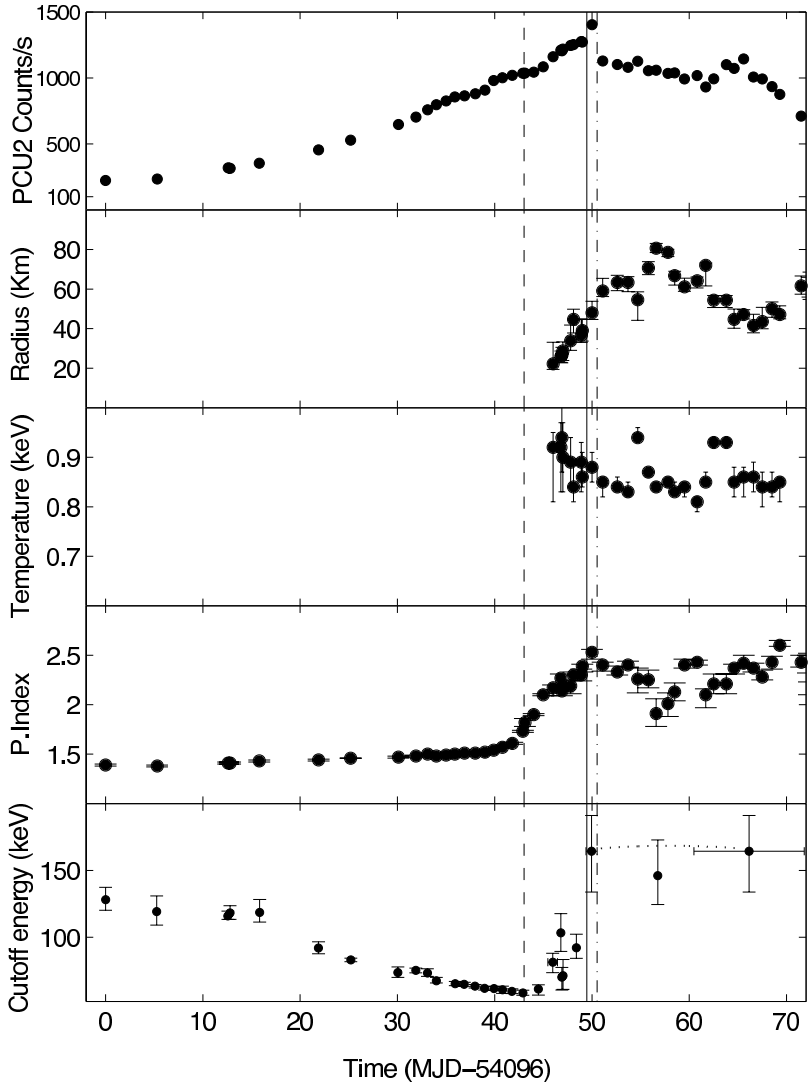

Figure 3.6: Light curve and evolution of the main spectral parameters of the source. For all the panels shown we plotted the spectral parameters for a selection of 51 observation (from #1 to #51) covering the entire hard-to-soft transition of the source, coming from Tab. 3.3. From the top to bottom: Light curve, inner radius in km (assuming a distance of 8 kpc and inclination of 60 degrees), disc temperature in keV at the inner radius, photon index, cutoff energy in keV. The vertical lines mark the transitions and follow the same convention as in Fig. 3.1. Points with horizontal error band correspond spectra obtained averaging observations with similar hardness. The error bar represents the time interval corresponding to the accumulation. In the bottom panel we used the values coming from Table 3.4.

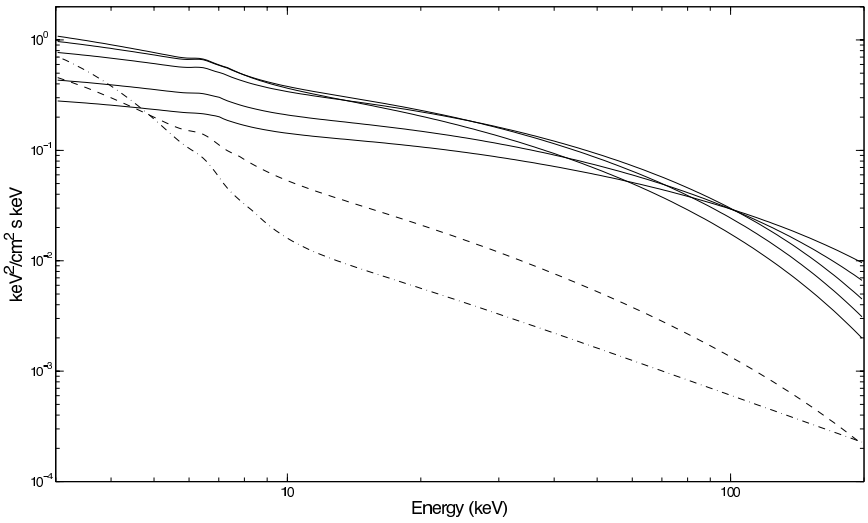

Figure 3.7: Different models fitting the Spectra in the LHS, HIMS and HSS. The solid lines correspond to LHS observations (#5, #7, #15, #19, #20), the dashed line corresponds to a HIMS observation (#25) and the dotted dashed line corresponds to an HSS observation (#33). The bottom two curves are scaled by a factor of 20 for clarity.

to happen (Fender et al. 2009).

In the first part of the outburst (corresponding roughly to the LHS), there is no measurable thermal disk component. When the disk appears, after the LHS-HIMS transition, we observe an increase in the disk radius through the HIMS-SIMS-HSS transitions, followed by a decrease. At the same time, the disk temperature decreases steadily. Given the simplified form of our model, the absolute measurements of the inner radius are not robust and therefore not reliable. While the disk component was needed it could not be constrained very well and that we cannot draw any firm conclusions about its behavior from our fits. In addition, the poow low-energy sensitivity of RXTE usually makes very difficult the measurement of the spectral parameters related to the low-energy components.

3.4 Discussion

From the results persented in the previous section, we conclude that we observed three different transitions: from LHS to HIMS, from HIMS to SIMS and from SIMS to HSS.

- The LHS-HIMS transition took place between Obs #19 and Obs. #20. It is identified through the appearance of a stronger type-C QPO in the power density spectra, by a change in the parameters of the hard spectral component, and by a large change in the hardness (see Fig. 3.2). The power-law index increases faster with time across this transition, while the high-energy cut off stops decreasing.

- The first HIMS-SIMS transition took place between Obs. #31 and Obs. #32 and, by definition, was marked by the disappearance of the type-C QPO typical of the LHS and HIMS and the onset of a type-B QPO in Obs. #32. This observation is one of the four observations in the SIMS, all of them showing a type-A or type-B QPO. At the same time the high-energy cutoff shows a large change, jumping from $\sim$150 keV to higher values.

- The first SIMS-HSS transition takes place between Obs. #32 and Obs. #33, identified through the low value of integrated fractional rms and the absence of type-A/B/C QPOs.

- Besides these three main transition we observed transitions involving the intermediates states.

  To summarize, we observed:

  - a transition from LHS to HIMS
  - a main transition and two secondary transitions from HIMS to SIMS
  - a main and a secondary transition from SIMS to HSS (this last transition is reported in Del Santo et al. 2008)

In Fig. 3.1, 3.2, 3.6, we marked the LHS-HIMS transitions and only the first transitions from HIMS to SIMS and from SIMS to HSS. We refer to these first transition as the main transitions. Due to the short time scale of the transitions to and from the SIMS, we cannot be sure that we observed all transitions underwent by the source. All we can say is that the line in the HID corresponding to the HIMS-SIMS transition was crossed at least five times in total. The location of the three main transitions in the HID (see Fig. 3.2) was consistent with those of the previous outbursts.

The observed behaviour of the photon index is also similar to that of the previous outbursts (Belloni 2005; Del Santo et al. 2008), while the high-energy cut off behavior shows different properties. In 2004, the major HIMS to SIMS transition on the primary horizontal branch was simultaneously observed with INTEGRAL and RXTE (Belloni et al. 2006): after the transition, these authors report the lack of the high energy cut-off in the SIMS (present at $\sim$70 keV in the HIMS). Del Santo et al. (2008) confirm the latter result (disappearance of the cut-off in the SIMS) for

the 2004 outburst by using simultaneous IBIS, SPI and JEM-X data collected during the same transition. However, they found a higher value of the cut-off in that same HIMS (115^{+27}_{-23} keV) because of new INTAGRAL calibrations. Del Santo et al. (2009), using RXTE/PCA, RXTE/HEXTE and INTEGRAL/IBIS/ISGRI data performed a broad band spectral analysis covering the energy range from 3 keV (PCA) to 200 keV (IBIS/ISGRI). They observed a secondary HIMS/SIMS transition in the 2006/2007 outburst of GX 339-4 and found a different behaviour in relation to what we observed: during the transition HIMS/SIMS the high-energy cut-off has moved to a lower energy, while we observed an opposite trend. Moreover, this variation is observed to take place *before* the HIMS/SIMS transition as deduced from the timing properties. Thanks to our RXTE data we clearly observed a high-energy cut off increase during the HIMS to SIMS transition.

Miyakawa et al. (2008) studied a large sample of RXTE data from GX 339-4 during the hard state through different outbursts (not including the one presented here) using the same model we adopted (powerlaw with high energy exponential cutoff, smeared edge, Fe-line component). They found that a cutoff energy is present in all their hard-state observations. They could not make a real comparisons with previous results (Zdziarski et al. 1998, because those authors used different models, but they clearly found a variable energy cut-off in GX 339-4, with values between 40 and 200 keV or more, similar to our results. The power law photon index showed an anticorrelation with the source luminosity. The cut off energy was also anticorrelated with luminosity above 10^{37} erg s^{-1}, while it was constant around $\sim$200 keV below that value. Our LHS data span luminosities from 10^{37} erg s^{-1} to 10^{38} erg s^{-1}. We observe the same anticorrelation cut off-luminosity, which continues in the HIMS up to 2.6×10^{38}erg s^{-1}.

They also calculated the absorption-corrected X-ray luminosities in the 2-200 keV range and assumed the distance of GX 339-4 to be 8 kpc (Zdziarski et al. 2004). They obtained luminosities ranging from 1.0×10^{37} erg s^{-1} to 2.1×10^{38} erg s^{-1} and they found a clear anti-correlation between luminosity and the cutoff energy for luminosities $> 7 \times 10^{37}$ erg s^{-1}. On the other hand they observed that the value of the high-energy cutoff seemed to be roughly constant at 200 keV when the luminosity was $< 7 \times 10^{37} ergs^{-1}$. We calculated the absorption-corrected luminosity of the source following the same criteria Miyakawa et al. (2008) used and we found a similar range of luminosity (from 1.01×10^{38} erg s^{-1} to 1.14×10^{37} erg s-1). We found the same anticorrelation during the LHS and during the HIMS, while the luminosity ranged from 1.01×10^{38} erg s^{-1} and 2.57×10^{38} erg s^{-1}. During the HSS the luminosity decreases from 7.25×10^{37} erg s^{-1} to 1.14×10^{37} erg s^{-1}. As we pointed out before, during the SIMS and the HSS after the final transition from SIMS to HSS, we cannot exclude the presence of a cutoff, that either remains constant in energy or disappears. This behavior is consistent with a constant cutoff around 200

keV with a luminosity $< 7 \times 10^{37}$erg s^{-1}.

The observed behaviour of the high energy cutoff of GX 339-4 is also similar to that observed with RXTE-INTEGRAL-Swift during the 2005 outburst of GRO J1655-40 (Joinet, Kalemci & Senziani 2008), in contrast to the results of Caballero-García et al. (2009) who do not find evidence of a cut off in the INTEGRAL spectra of the same source in the LHS. From their table, it is possible to reconstruct the time evolution of the high-energy cutoff, shown in Fig. 3.8. They used various models available in the standard XSPEC 11.3.1 fitting package. For all models the iron emission line, a multicolor disk blackbody and an interstellar absorption component were present. They first fitted the data with a reflection model (PEXRAV in XSPEC) consisting of a power-law with a high-energy cutoff and reflection from neutral medium. Since the hard powerlaw plus cutoff model in the LHS is usually interpreted as thermal Comptonization in a hot optically thin plasma, they also used the COMPTT model (Titarchuk 1994) in order to describe the high-energy spectrum. They observed that, with both models, the cutoff decreases through the LHS and the HIMS, starting from $\sim$ 200 keV and reaching $\sim$ 60 keV, to increase again in SIMS and HSS. The coverage of this outburst is good but unfortunately the HIMS was particularly short.

The high-energy cutoff appears to be changing much more rapidly than other spectral parameters and possibly as fast as the timing properties. From Fig. 3.2 and Fig. 3.6 (first panel from the bottom) we can see that transition from LHS to HIMS is evident both in the HID and in the cutoff evolution, while we cannot say the same thing for the HIMS-to-SIMS transition. The cutoff energy shows a big variation crossing the HIMS-to-SIMS line, jumping from $\sim$100 keV to $\sim$160 keV, and at the same time the PDSs change very quickly. It is known that the ejection of transient relativistic jets typical of most black-hole binaries (see Fender, Belloni, Gallo 2004) takes place on very short time scales. The variations of the high-energy cutoff takes place on comparable timescales. Recently a comparative study of different systems has shown (crossing of the "jet line") that the jet ejection and HIMS/SIMS state transitions are not exactly simultaneous (Fender, Homan, Belloni 2009). Our data make possible to assert that the variation of the high-energy cutoff takes place just in correspondence with the main HIMS/SIMS transition, but due to the lack of radio observations we cannot exclude that the jet line coincides to the transition. In other words, it is possible that changes in the high-energy part of the spectrum and the crossing of the jet line are always simultaneous. Clearly the idea of a "canonical" 100 keV cutoff (see Zdziarski at al. 1996) in the LHS of black-holes binaries is too simplified. Large variations are seen in at least two sources across the LHS. These are transient systems, but also for persistent sources such as Cyg X-1 this paradigm needs to be revised (see Wilms et al. 2006).

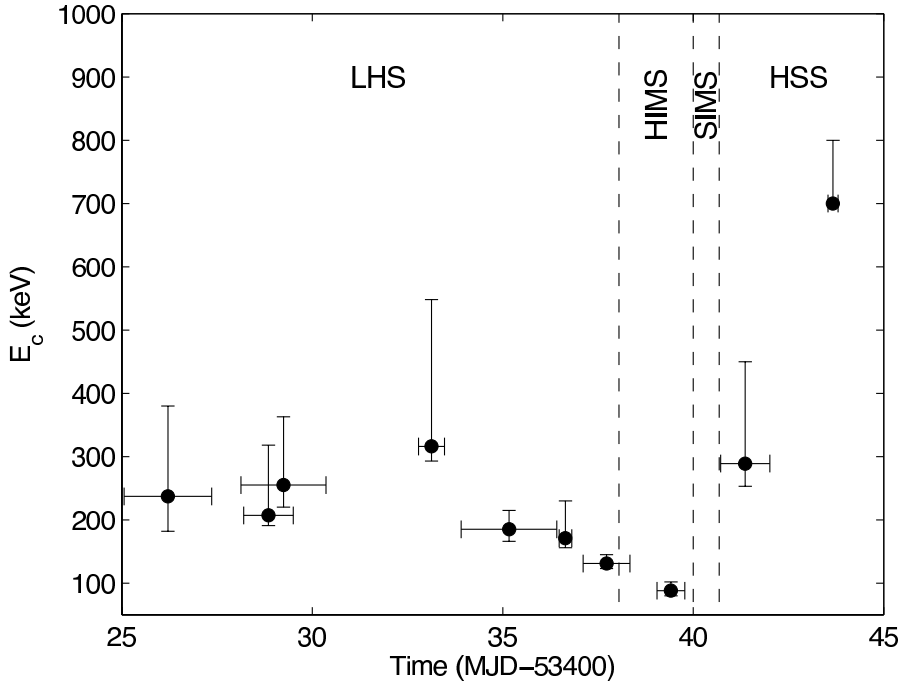

Figure 3.8: Time evolution of the high-energy cutoff for the 2005 outburst of GRO J1655-40 as measured by INTEGRAL (from the data of Joinet, Kalemci, & Senziani 2008), with RXTE-determined states.

The transition can also be seen in the photon index evolution (see Fig. 3.6, fourth panel from the top). Even though the evolution of the photon index across the transitions seem to be continuous we clearly see a change in its trend. Summarizing, in coincidence to the HIMS/SIMS transition, defined through timing properties, we see: a sudden increase n the high-energy cutoff and a reverse in the trend of the powerlaw slope. We cannot exclude that these spectral changes are directly associated to the ejection of transient relativistic jets.

Qualitatively, we can understand the reason for the softening in the LHS. Independent of whether the inner disk of the accretion disk moves inward or not, as the source becomes brighter more soft photons will be emitted by the disk. The photon input to the Comptonizing medium will therefore increase. This will steepen the power-law part of the Comptonization spectrum and will cool the population of electrons (see Sunyaev & Titarchuck, 1980). On the contrary, during the HIMS, when the softening is much more marked and the thermal disk starts to dominate, the increase in cutoff energy and hence in temperature of the Comptonizing cloud can not be explained

within this framework.

The softening can therefore be understood in terms of thermal comptonization, but not the subsequent evolution. The idea that two varying powerlaw components, one associated with a high-energy cutoff (thermal) and one without it (non-thermal), cannot explain the high-energy cutoff evolution after the LHS to HIMS transition. The behaviour seems to indicate that it is only one component that evolves. Therefore, a simple disappearing of a thermal component and its replacement with a non-thermal one is not a favored scenario. However, Del Santo et al. (2008) show that the HIMS spectra from INTEGRAL observations indicate the presence of an additional component to the thermal compton one, evidence of the presence of a non-thermal tail in the distribution of the electrons. This tail could become dominant when approaching the soft state, mimicking an increase in cutoff energy. We tried to simulate a spectrum from a model consisting of a cutoff-powerlaw (with the parameters found at the LHS/HIMS transition) plus a simple powerlaw (with the parameters corresponding to those of the SIMS and decreasing fluxes). We then fitted the simulated spectra with a cutoff powerlaw: we found that the high-energy cutoff does not vary significantly in response to the powerlaw addition. Therefore we can conclude that the non-thermal powerlaw component, if present, does not influence the high-energy cutoff evolution.

3.5 Conclusions

The results presented above constitute an important measurement of the changes of the broad-band X-ray spectrum of a BHT across the hard to soft state transition, which is necessary for the development and testing of theoretical models. We have presented RXTE observations of GX 339-4 which covered the first half of the outburst. We followed the source spectral evolution from the LHS through the HIMS and the SIMS untill the HSS. Our detailed broadband spectral analysis showed that the hard spectral component steepens during the transition from the hard to the soft state and the high-energy cutoff varies non-monotonically and rapidly though the transitions. The high-energy cutoff decreased monotonically from 120 to 60 keV during the brightening of the hard state, but increased again to 100 keV during the softening in the hard intermediate state. In the short-lived soft intermediate state the cutoff energy was $\sim$ 130 keV, but was no longer detected in the soft state. The changes in the high-energy cutoff were interpreted as a conseguence of the transitions. The high-energy cutoff behavior is similar to what observed with RXTE-INTEGRAL-Swift during the 2005 outburst of GRO J1655-40. The transitions can also be seen in the photon index evolution (see Fig. 3.6, fourth panel from the top). Even though the evolution of the photon index across the transitions seem to be continuous we clearly see a change in its trend. From our analysis it is clear that although the transition from the LHS to the HSS is a process that takes days to weeks (see e.g. Belloni 2005, a sharp transition

in the properties of fast time variability takes place on a much shorter time scales, similarly to what happens to the high-energy cutoff. From what we have shown it is clear that the transition in the properties of fast time variability corresponds also to a change in the high-energy properties.

Acknowledgments

This work has been supported by the Italian Space Agency through grants I/008/07/0 and I/088/07/0. TB acknowledges support from the International Space Science Institute

Table 3.2: The columns are: observation number in this work, RXTE observation ID, MJD, PCU2 count rate, hardness ratio, fractional rms (0.001 - 64 Hz), QPO type, and states according to Belloni (2009) and McClintock & Remillard (2006).

#	Obs. ID	MJD	PCU2 Counts/s	hardness	rms	QPO	State (B)	State (M/R)
1	92052-07-04-00	54096.00	223.50 ± 0.38	0.885 ± 0.004	47.93 ± 2.81		LHS	INT
2	92052-07-05-00	54101.26	234.30 ± 0.50	0.882 ± 0.005	45.09 ± 7.11		LHS	INT
3	92428-01-01-00	54108.57	318.70 ± 0.43	0.873 ± 0.003	45.66 ± 2.76		LHS	H
4	92428-01-01-01	54108.79	314.80 ± 0.46	0.871 ± 0.003	48.96 ± 3.76		LHS	H
5	92052-07-06-00	54111.84	354.10 ± 0.63	0.868 ± 0.004	43.68 ± 2.85		LHS	H
6	92052-07-06-01	54117.89	455.60 ± 0.75	0.851 ± 0.003	39.48 ± 3.20		LHS	H
7	92428-01-02-00	54121.21	527.70 ± 0.70	0.847 ± 0.003	38.82 ± 1.08		LHS	H
8	92428-01-03-00	54126.05	647.40 ± 1.15	0.833 ± 0.004	36.43 ± 2.69		LHS	H
9	92035-01-01-01	54127.89	703.70 ± 0.98	0.837 ± 0.003	36.65 ± 2.49	C	LHS	H
10	92035-01-01-02	54129.08	758.40 ± 1.20	0.831 ± 0.003	36.41 ± 3.51	C	LHS	H
11	92035-01-01-02	54129.08	797.40 ± 1.07	0.832 ± 0.003	35.87 ± 1.09	C	LHS	H
12	92035-01-01-04	54131.03	826.50 ± 1.12	0.830 ± 0.003	35.08 ± 1.06	C	LHS	H
13	92035-01-02-00	54131.95	856.20 ± 1.15	0.826 ± 0.003	33.33 ± 1.81	C	LHS	H
14	92035-01-02-01	54132.87	863.80 ± 1.18	0.823 ± 0.003	32.37 ± 1.94	C	LHS	H
15	92035-01-02-02	54133.98	879.50 ± 1.18	0.823 ± 0.003	32.14 ± 0.94	C	LHS	H
16	92035-01-02-03	54134.96	908.40 ± 1.22	0.818 ± 0.003	31.88 ± 0.91	C	LHS	H
17	92035-01-02-04	54135.94	981.00 ± 1.32	0.810 ± 0.003	30.93 ± 1.66	C	LHS	H
18	92035-01-02-08	54136.80	1001.00 ± 1.63	0.801 ± 0.003	28.62 ± 2.81	C	LHS	H
19	92035-01-02-07	54137.77	1020.00 ± 1.42	0.782 ± 0.003	26.20 ± 1.54	C	LHS	H
20	92035-01-02-06	54138.89	1035.00 ± 1.44	0.732 ± 0.002	22.72 ± 1.18	C	HIMS	H
21	92035-01-03-00	54139.15	1037.00 ± 1.45	0.714 ± 0.002	23.10 ± 0.46	C	HIMS	H

Continued on next page

Table 3.2 – continued from previous page

#	Obs. ID	MJD	PCU2 Counts/s	hardness	rms	QPO	State (B)	State (M/R)
22	92035-01-03-01	54140.00	1045.00 ± 1.50	0.658 ± 0.002	21.02 ± 0.60	C	HIMS	H
23	92035-01-03-02	54140.98	1084.00 ± 1.62	0.574 ± 0.002	20.21 ± 1.04	C	HIMS	H
24	92035-01-03-03	54141.96	1161.00 ± 1.84	0.480 ± 0.002	19.09 ± 0.53	C	HIMS	INT
25	92428-01-04-00	54142.80	1210.00 ± 1.99	0.426 ± 0.001	18.70 ± 0.53	C	HIMS	INT
26	92428-01-04-01	54142.90	1206.00 ± 2.06	0.434 ± 0.002	18.05 ± 1.24	C	HIMS	INT
27	92428-01-04-02	54143.03	1218.00 ± 2.12	0.439 ± 0.002	17.66 ± 1.35	C	HIMS	INT
28	92428-01-04-03	54143.82	1247.00 ± 2.22	0.393 ± 0.001	17.35 ± 0.72	C	HIMS	INT
29	92035-01-03-05	54144.06	1253.00 ± 2.18	0.355 ± 0.001	16.25 ± 0.51	C	HIMS	INT
30	92428-01-04-04	54144.91	1276.00 ± 2.30	0.364 ± 0.001	16.33 ± 0.69	C	HIMS	INT
31	92035-01-03-06	54144.97	1272.00 ± 2.19	0.365 ± 0.001	16.24 ± 0.46	C	HIMS	SPL
32	92035-01-04-00	54145.96	1404.00 ± 2.62	0.276 ± 0.001	11.22 ± 0.59	B	SIMS	SPL
33	92035-01-04-01	54147.09	1129.00 ± 2.43	0.180 ± 0.001	7.98 ± 0.69		HSS	INT
34	92035-01-04-02	54148.64	1102.00 ± 2.35	0.164 ± 0.001	6.64 ± 0.60		HSS	TD
35	92085-01-01-00	54149.69	1080.00 ± 2.29	0.166 ± 0.001	6.21 ± 0.58		HSS	INT
36	92085-01-01-04	54150.75	1126.00 ± 2.36	0.190 ± 0.001	7.36 ± 0.70		HSS	INT
37	92085-01-01-05	54151.78	1055.00 ± 2.28	0.152 ± 0.001	6.65 ± 0.59		HSS	TD
38	92085-01-01-06	54152.63	1059.00 ± 2.35	0.136 ± 0.001	4.87 ± 0.69		HSS	TD
39	92085-01-02-00	54153.81	1034.00 ± 2.29	0.136 ± 0.001	6.74 ± 0.56		HSS	TD
40	92085-01-02-01	54154.52	1038.00 ± 2.28	0.140 ± 0.001	5.75 ± 0.60		HSS	TD
41	92085-01-02-02	54155.49	991.90 ± 2.16	0.149 ± 0.001	7.17 ± 0.67		HSS	TD
42	92085-01-02-03	54156.75	1018.00 ± 2.12	0.185 ± 0.001	6.85 ± 0.55		HSS	INT
43	92085-01-02-04	54157.73	931.50 ± 2.06	0.137 ± 0.001	7.47 ± 0.66		HSS	TD
44	92085-01-02-05	54158.44	993.80 ± 2.09	0.183 ± 0.001	7.31 ± 0.62		HSS	INT

Continued on next page

Table 3.2 – continued from previous page

#	Obs. ID	MJD	PCU2 Counts/s	hardness	rms	QPO	State (B)	State (M/R)
45	92085-01-02-06	54159.84	1101.00 ± 2.20	0.229 ± 0.001	5.27 ± 0.68	A	SIMS	SPL
46	92085-01-03-00	54160.61	1072.00 ± 1.96	0.305 ± 0.001	15.10 ± 0.53	C	HIMS	SPL
47	92085-01-03-01	54161.60	1144.00 ± 2.20	0.271 ± 0.001	11.74 ± 0.84	B	SIMS	SPL
48	92085-01-03-02	54162.64	1008.00 ± 1.85	0.298 ± 0.001	14.35 ± 0.53	C	HIMS	SPL
49	92085-01-03-03	54163.49	992.60 ± 1.84	0.305 ± 0.001	14.22 ± 0.53	C	HIMS	SPL
50	92085-01-03-04	54164.47	935.20 ± 1.88	0.221 ± 0.001	6.33 ± 0.63	A	SIMS	SPL
51	92085-01-03-05	54165.26	876.40 ± 1.87	0.206 ± 0.001	6.21 ± 0.72		HSS	INT
52	92085-01-04-13	54167.48	710.60 ± 1.76	0.162 ± 0.001	7.49 ± 1.58		HSS	INT
53	92085-01-04-08	54168.20	690.70 ± 1.72	0.159 ± 0.001	6.85 ± 1.74		HSS	INT
54	92085-01-04-09	54168.26	672.60 ± 1.67	0.144 ± 0.001	6.36 ± 1.69		HSS	TD
55	92085-01-04-10	54168.33	664.00 ± 1.76	0.141 ± 0.001	7.01 ± 1.71		HSS	TD
56	92085-01-04-00	54169.17	630.20 ± 1.50	0.121 ± 0.001	5.06 ± 2.61		HSS	TD
57	92085-01-04-02	54170.16	588.50 ± 1.47	0.119 ± 0.001	5.77 ± 1.40		HSS	TD
58	92085-01-04-03	54170.22	596.80 ± 1.48	0.125 ± 0.001	5.95 ± 1.46		HSS	TD
59	92085-01-04-05	54171.21	562.20 ± 1.44	0.120 ± 0.001	6.13 ± 1.76		HSS	TD
60	92085-01-04-06	54171.27	563.50 ± 1.40	0.124 ± 0.001	7.70 ± 1.52		HSS	TD
61	92085-01-04-07	54171.34	562.10 ± 1.44	0.122 ± 0.001	6.40 ± 1.30		HSS	TD
62	92085-01-04-04	54172.28	538.00 ± 1.53	0.120 ± 0.001	7.92 ± 2.19		HSS	TD
63	92085-01-04-11	54173.93	542.70 ± 1.39	0.165 ± 0.001	13.88 ± 2.21		HSS	INT
64	92085-02-01-01	54173.95	546.40 ± 1.32	0.166 ± 0.001	10.42 ± 1.87		HSS	INT
65	92085-02-01-00	54175.02	512.60 ± 1.14	0.154 ± 0.001	6.96 ± 0.91		HSS	INT
66	92085-02-01-02	54175.97	536.90 ± 1.17	0.184 ± 0.001	7.39 ± 1.54		HSS	INT
67	92085-02-01-03	54177.12	555.50 ± 1.17	0.201 ± 0.001	5.75 ± 0.84		HSS	INT

Continued on next page

Table 3.2 – continued from previous page

#	Obs. ID	MJD	PCU2 Counts/s	hardness	rms	QPO	State (B)	State (M/R)
68	92085-02-01-04	54177.98	571.90 ± 1.20	0.213 ± 0.001	3.63 ± 1.36		HSS	INT
69	92085-02-01-05	54178.76	520.50 ± 1.16	0.193 ± 0.001	5.50 ± 1.35		HSS	INT
70	92085-02-01-06	54180.14	498.80 ± 1.12	0.198 ± 0.001	7.16 ± 1.24		HSS	INT
71	92085-02-02-03	54181.05	427.50 ± 1.00	0.169 ± 0.001	7.53 ± 1.49		HSS	INT
72	92085-02-02-00	54182.09	508.80 ± 1.06	0.220 ± 0.001	5.56 ± 1.09		HSS	INT
73	92085-02-02-02	54184.05	428.70 ± 0.93	0.197 ± 0.001	7.22 ± 1.49		HSS	INT
74	92085-02-02-01	54186.08	338.20 ± 0.77	0.170 ± 0.001	9.04 ± 1.25		HSS	INT
75	92085-02-03-00	54187.98	295.20 ± 0.73	0.115 ± 0.001	7.54 ± 1.86		HSS	TD
76	92085-02-03-01	54190.02	277.00 ± 0.70	0.122 ± 0.001	5.17 ± 2.08		HSS	TD
77	92085-02-03-02	54192.63	237.60 ± 0.62	0.118 ± 0.001	6.03 ± 2.17		HSS	TD
78	92085-02-04-00	54196.55	202.20 ± 0.51	0.137 ± 0.001	4.18 ± 2.86		HSS	INT
79	92085-02-04-02	54200.62	167.70 ± 0.44	0.144 ± 0.001	7.56 ± 2.20		HSS	INT
80	92085-02-05-00	54202.51	154.50 ± 0.41	0.155 ± 0.001	8.38 ± 2.33		HSS	INT
81	92085-02-05-01	54204.47	120.80 ± 0.35	0.107 ± 0.001	7.50 ± 2.83		HSS	INT
82	92085-02-05-02	54206.63	168.30 ± 0.41	0.225 ± 0.001	10.09 ± 2.69		HSS	INT
83	92085-02-05-03	54208.40	134.30 ± 0.35	0.200 ± 0.001	6.25 ± 4.10		HSS	INT

Table 3.3: Spectral parameters. Columns are: observation number, inner disk temperature, inner disk radius (assuming a distance of 8 kpc and an inclination of 60°, and high-energy cutoff.

#	kT (keV)	R (Km)	Γ	E_c
1	-	-	1.39 ± 0.01	128.2 ± 7.9
2	-	-	1.38 ± 0.01	119.2 ± 10.1
3	-	-	1.41 ± 0.01	116.0 ± 2.6
4	-	-	1.41 ± 0.01	118.2 ± 4.9
5	-	-	1.43 ± 0.01	118.6 ± 7.2
6	-	-	1.44 ± 0.01	91.9 ± 4.3
7	-	-	1.46 ± 0.00	83.1 ± 1.4
8	-	-	1.47 ± 0.01	73.7 ± 3.7
9	-	-	1.48 ± 0.01	75.3 ± 1.9
10	-	-	1.50 ± 0.01	73.3 ± 2.6
11	-		1.48 ± 0.01	67.4 ± 1.6
12	-	-	1.49 ± 0.01	65.8 ± 1.3
13	-	-	1.50 ± 0.01	65.2 ± 1.4
14	-	-	1.51 ± 0.01	64.9 ± 1.6
15	-	-	1.51 ± 0.01	63.5 ± 1.4
16	-	-	1.52 ± 0.01	61.8 ± 1.3
17	-	-	1.54 ± 0.01	61.6 ± 1.4
18	-	-	1.57 ± 0.01	60.6 ± 2.6
19	-	-	1.61 ± 0.01	59.5 ± 1.7
20	-	-	1.73 ± 0.01	58.4 ± 1.8
21	-	-	1.82 ± 0.04	79.6 ± 15.3

Continued on next page

Table 3.3 – continued from previous page

#	kT (keV)	R (Km)	Γ	E_c
22	-	-	1.90 ± 0.01	65.0 ± 2.8
23	-	-	2.10 ± 0.01	80.4 ± 4.9
24	$0.92^{+0.03}_{-0.11}$	$22.2^{+10.9}_{-2.8}$	$2.17^{+0.03}_{-0.08}$	83.3 ± 10.7
25	$0.92^{+0.05}_{-0.09}$	$26.0^{+2.7}_{-3.0}$	$2.27^{+0.04}_{-0.06}$	104.8 ± 22.9
26	0.94 ± 0.07	$26.7^{+3.9}_{-4.0}$	$2.14^{+0.04}_{-0.05}$	69.9 ± 9.5
27	0.90 ± 0.07	$28.7^{+4.6}_{-4.8}$	$2.18^{+0.02}_{-0.05}$	71.8 ± 11.0
28	0.89 ± 0.05	$33.9^{+7.9}_{-4.9}$	$2.19^{+0.05}_{-0.08}$	60.6 ± 8.5
29	$0.84^{+0.05}_{-0.03}$	$44.6^{+5.2}_{-6.8}$	$2.30^{+0.03}_{-0.05}$	95.3 ± 16.0
30	$0.89^{+0.04}_{-0.06}$	$36.7^{+8.2}_{-3.7}$	2.30 ± 0.06	95.5 ± 18.7
31	$0.86^{+0.05}_{-0.02}$	$39.1^{+5.6}_{-5.4}$	$2.39^{+0.02}_{-0.06}$	156.6 ± 42.0
32	0.88 ± 0.03	$48.0^{+5.8}_{-3.4}$	$2.53^{+0.03}_{-0.07}$	254.5 ± 111.9
33	$0.85^{+0.01}_{-0.03}$	$59.0^{+6.4}_{-2.8}$	$2.40^{+0.03}_{-0.06}$	–
34	$0.84^{+0.02}_{-0.01}$	$63.4^{+3.6}_{-4.2}$	$2.33^{+0.06}_{-0.03}$	–
35	$0.83^{+0.02}_{-0.01}$	$63.4^{+2.9}_{-4.7}$	$2.40^{+0.04}_{-0.02}$	–
36	$0.94^{+0.02}_{-0.01}$	$54.6^{+4.0}_{-10.4}$	$2.26^{+0.11}_{-0.14}$	118.1 ± 40.1
37	0.87 ± 0.01	$70.7^{+3.2}_{-3.4}$	$2.25^{+0.10}_{-0.08}$	163.4 ± 70.8
38	0.84 ± 0.01	$80.7^{+2.4}_{-2.2}$	$1.91^{+0.15}_{-0.13}$	50.0 ± 9.6
39	0.85 ± 0.01	$78.6^{+1.5}_{-2.2}$	$2.01^{+0.11}_{-0.13}$	88.3 ± 29.7
40	$0.83^{+0.02}_{-0.01}$	$66.8^{+2.2}_{-4.8}$	2.13 ± 0.09	–
41	$0.84^{+0.01}_{-0.02}$	$61.2^{+4.3}_{-2.3}$	$2.40^{+0.06}_{-0.03}$	–
42	$0.81^{+0.01}_{-0.02}$	$64.2^{+1.9}_{-3.6}$	$2.43^{+0.02}_{-0.03}$	–
43	$0.85^{+0.02}_{-0.01}$	$72.0^{+1.2}_{-10.4}$	$2.10^{+0.06}_{-0.13}$	117.4 ± 41.4
44	0.93 ± 0.01	$54.4^{+2.3}_{-3.7}$	2.21 ± 0.10	86.5 ± 18.3

Continued on next page

Table 3.3 – continued from previous page

#	kT (keV)	R (Km)	Γ	E_c
45	0.93 ± 0.01	$54.4^{+2.3}_{-3.7}$	2.21 ± 0.10	86.5 ± 18.3
46	0.85 ± 0.03	$44.7^{+5.2}_{-4.5}$	$2.37^{+0.04}_{-0.06}$	162.9 ± 45.2
47	$0.86^{+0.02}_{-0.04}$	$47.2^{+2.4}_{-2.3}$	$2.42^{+0.08}_{-0.05}$	135.7 ± 28.0
48	0.86 ± 0.03	$41.6^{+5.7}_{-3.7}$	$2.37^{+0.05}_{-0.04}$	200.8 ± 46.8
49	$0.84^{+0.03}_{-0.04}$	$43.5^{+7.3}_{-3.6}$	$2.28^{+0.07}_{-0.03}$	79.0 ± 9.8
50	$0.84^{+0.03}_{-0.02}$	$50.1^{+3.4}_{-4.4}$	$2.43^{+0.06}_{-0.07}$	99.1 ± 28.5
51	$0.85^{+0.01}_{-0.04}$	$47.2^{+4.3}_{-2.2}$	$2.60^{+0.05}_{-0.01}$	-
52	$0.78^{+0.01}_{-0.02}$	$61.6^{+5.0}_{-4.2}$	$2.43^{+0.07}_{-0.05}$	-
53	0.78 ± 0.02	$60.2^{+5.7}_{-4.2}$	$2.43^{+0.07}_{-0.11}$	-
54	0.80 ± 0.02	59.0 ± 4.2	$2.17^{+0.06}_{-0.07}$	-
55	0.77 ± 0.02	$63.6^{+5.0}_{-4.2}$	$2.44^{+0.08}_{-0.04}$	-
56	$0.77^{+0.02}_{-0.01}$	$65.2^{+2.5}_{-4.0}$	$2.42^{+0.07}_{-0.10}$	-
57	$0.77^{+0.01}_{-0.02}$	$64.0^{+7.3}_{-2.9}$	$2.34^{+0.10}_{-0.04}$	-
58	$0.74^{+0.02}_{-0.01}$	$70.5^{+3.9}_{-4.9}$	$2.40^{+0.06}_{-0.03}$	-
59	$0.75^{+0.00}_{-0.03}$	$66.7^{+5.9}_{-2.0}$	$2.45^{+0.10}_{-0.07}$	-
60	$0.75^{+0.01}_{-0.02}$	$65.5^{+4.1}_{-3.3}$	2.32 ± 0.06	-
61	$0.75^{+0.02}_{-0.01}$	$66.2^{+4.8}_{-4.1}$	2.28 ± 0.08	-
62	0.76 ± 0.02	$61.5^{+4.7}_{-4.5}$	2.26 ± 0.09	-
63	0.76 ± 0.02	$57.7^{+2.5}_{-4.8}$	2.36 ± 0.05	-
64	$0.75^{+0.01}_{-0.02}$	$59.5^{+5.2}_{-3.6}$	$2.41^{+0.03}_{-0.05}$	-
65	$0.73^{+0.02}_{-0.01}$	$66.8^{+3.0}_{-5.0}$	$2.39^{+0.03}_{-0.05}$	-
66	$0.80^{+0.01}_{-0.03}$	$47.2^{+2.8}_{-2.2}$	$2.42^{+0.05}_{-0.02}$	-
67	$0.80^{+0.01}_{-0.02}$	$46.0^{+1.6}_{-2.8}$	$2.47^{+0.04}_{-0.02}$	-

Continued on next page

Table 3.3 – continued from previous page

#	kT (keV)	R (Km)	Γ	E_c
68	0.81 ± 0.02	$43.5^{+4.6}_{-3.1}$	$2.45^{+0.03}_{-0.01}$	-
69	0.78 ± 0.02	$49.5^{+4.5}_{-3.5}$	$2.48^{+0.07}_{-0.04}$	-
70	$0.77^{+0.03}_{-0.01}$	$49.7^{+2.9}_{-5.0}$	2.46 ± 0.04	-
71	$0.73^{+0.02}_{-0.01}$	$58.0^{+4.0}_{-5.1}$	2.35 ± 0.04	-
72	0.79 ± 0.02	$43.5^{+3.5}_{-2.9}$	$2.41^{+0.03}_{-0.02}$	-
73	$0.77^{+0.01}_{-0.02}$	$45.1^{+3.2}_{-2.6}$	$2.40^{+0.04}_{-0.02}$	-
74	$0.73^{+0.01}_{-0.02}$	$49.7^{+4.6}_{-3.1}$	2.28 ± 0.04	-
75	$0.69^{+0.02}_{-0.01}$	$62.5^{+2.7}_{-4.7}$	2.18 ± 0.07	-
76	$0.70^{+0.02}_{-0.01}$	$57.8^{+2.8}_{-4.9}$	$2.09^{+0.05}_{-0.08}$	-
77	$0.67^{+0.01}_{-0.03}$	$61.0^{+5.4}_{-13.5}$	$2.00^{+0.08}_{-0.09}$	-
78	$0.68^{+0.02}_{-0.01}$	$52.5^{+4.1}_{-5.1}$	$2.13^{+0.21}_{-0.07}$	-
79	$0.68^{+0.02}_{-0.01}$	$45.6^{+1.8}_{-4.5}$	$2.17^{+0.06}_{-0.11}$	-
80	$0.67^{+0.02}_{-0.01}$	$45.3^{+4.2}_{-4.0}$	$2.10^{+0.05}_{-0.03}$	-
81	$0.87^{+0.06}_{-0.04}$	$20.0^{+4.0}_{-1.8}$	$2.12^{+0.09}_{-0.13}$	-
82	$0.73^{+0.03}_{-0.02}$	$32.9^{+1.7}_{-4.8}$	$2.23^{+0.06}_{-0.05}$	-
83	$0.70^{+0.03}_{-0.02}$	$34.4^{+3.5}_{-4.1}$	2.13 ± 0.05	-

#	kT (keV)	R (Km)	Γ	E_c
22-23	$0.98^{+0.07}_{-0.15}$	-	$1.90^{+0.02}_{-0.04}$	$61.3^{+5.5}_{-3.1}$
28-31	$0.87^{+0.01}_{-0.01}$	$38.6^{+6.7}_{-5.2}$	2.30 ± 0.02	$92.1^{+12.8}_{-10.1}$
32, 45, 45, 50	$0.87^{+0.01}_{-0.02}$	$49.9^{+3.5}_{-3.4}$	$2.48^{+0.02}_{-0.04}$	$164.4^{+40.6}_{-26.7}$
33-44, 46, 48, 49	$0.88^{+0.01}_{-0.01}$	$61.3^{+3.6}_{-4.4}$	$2.18^{+0.05}_{-0.03}$	$146.0^{+34.4}_{-26.8}$

Table 3.4: Spectral parameters of spectra averaged across multiple observations (see text). Columns are observation number, inner disc temperature, inner disc radius (assuming a distance of 8 kpc and an inclination of 60^o) and a high-energy cut-off.

	H	SPL	TD	INT
LHS	17	-	-	2
HIMS	4	3	-	7
SIMS	-	3	-	1
HSS	-	2	19	25

Table 3.5: Comparison between the two classificatin schemes of Belloni (2009) and McRem (see text). In the first row we report the states of the McClintock & Remillard classification: Hard (H), Steep Power Law (SPL), Thermal Dominated (TD) and Intermediate (INT); in the first column we report the states of the classification we used: Low Hard State (LHS), Hard Intermediate State (HIMS), Soft Intermediate State (SIMS), High Soft State (HSS). We see that more than 40% of the observations results unclassified, that is belong to the Intermediate state. The states coming from the two different classifications are also reported in Tab. 3.2.

4 Fast variability as a tracer of accretion regimes in black hole transients

Teo Muñoz-Darias, Sara E. Motta, Tomaso M. Belloni

Monthly Notices of the Royal Astronomical Society, 2011, 410, 679

Abstract

We present the rms-intensity diagram for black hole transients. Using observations taken with the Rossi X-ray timing explorer we study the relation between the root mean square (rms) amplitude of the variability and the net count-rate during the 2002, 2004 and 2007 outbursts of the black hole X-ray binary GX 339-4. We find that the rms-flux relation previously observed during the hard state in X-ray binaries does not hold for the other states, when different relations apply. These relations can be used as a good tracer of the different accretion regimes. We identify the hard, soft and intermediate states in the rms-intensity diagram. Transitions between the different states are seen to produce marked changes in the rms-flux relation. We find that one single component is required to explain the ~ 40 per cent variability observed at low count rates, whereas no or very low variability is associated to the accretion-disc thermal component.

4.1 Introduction

Black Hole X-ray transients (BHTs) are observed in different states during their outburst evolution. They correspond to particular spectral and timing properties seen in the observations. The physical interpretation of the states is still strongly discussed, but they are probably associated with different accretion regimes. A *hard* state [historically known as low/hard state (LHS)] is generally observed at the beginning and at the end of the outburst. It is roughly characterized by a power-law shaped energy spectrum with a photon index of ~ 1.6 (2-20 keV) and a high level of aperiodic variability [root mean square (rms) amplitude above ~ 30 per cent]. In the middle of the outburst, the energy spectrum is dominated by a soft thermal component and almost no variability is seen. During this *soft* state [historically known as high/soft state (HSS)] a hard tail up to ~ 1 MeV is also present (Grove et al. 1998). In contrast, a high-energy cut-off ($\lesssim 200$ keV) is observed in the LHS (e.g. Wilms et al. 2006; Motta et al. 2009). From a physical point of view, the thermal component present in the HSS is usually associated with emission from an optically thick accretion disc, whereas the emission in the hard state is believed to arise from a 'corona' of hot electrons, where seed photons from an optically thin accretion disc are up-Comptonized. Synchrotron emission from a jet, which is known to dominate the radio and infrared spectrum during the LHS (e.g. Fender 2006; Russell et al. 2006), could also have a significant contribution to the hard X-ray emission (Russell et al. 2010).
In between these two 'canonical' states the situation is rather more complex. Hard-to-soft and a soft-to-hard transitions are observed in relatively short time scales (hours/days) as compared to the ones seen for the canonical states (weeks/months). During these transitions, both timing and spectral properties change dramatically, leading to different states classifications (see e.g. Belloni 2010 for a review). Homan et al. (2005) and Belloni (2005) (B05) identify two additional states, the hard-intermediate state (HIMS) and the soft-intermediate state (SIMS) based on spectral and timing properties (see e.g Casella et al. 2004 for different types of QPOs). McClintock & Remillard (2006) propose a more quantitative but model dependent classification, which requires of a steep power-law state and an intermediate state in addition to the two canonical states (for a comparison see Motta et al. 2009; hereafter M09).
A fundamental tool for studying the evolution of BHT is the hardness-intensity diagram (HID), where the evolution of the spectral hardness as a function of the acretion rate can be followed (see e.g. Homan et al. 2001). The hard–soft–hard usual evolution and the main transitions become apparent in the HID. The latter are usually not associated with major changes in flux, with the final soft-to-hard transition occurring at count-rates $\sim$ one order the magnitude lower. While the HID provides a general description of the BHT evolution, it is not enough for detailed studies (e.g. it is not able to establish with accuracy when the main transitions occur). Complementary

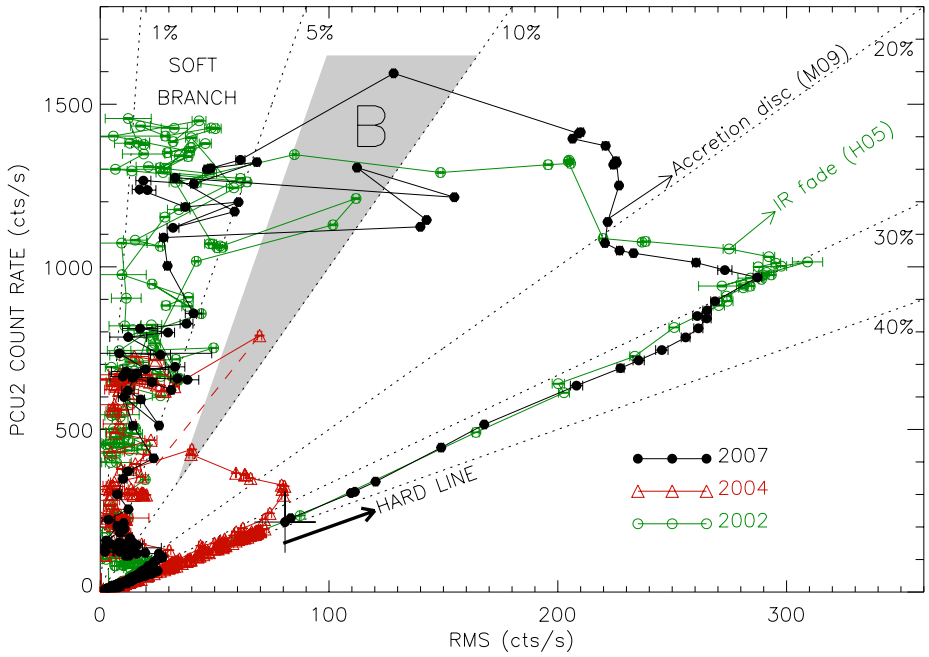

Figure 4.1: Rms-intensity diagram for the 2002, 2004 and 2007 outbursts of GX 339-4. Dotted lines represent the 1, 5, 10, 20, 30 and 40 per cent fractional rms levels. The grey area marks the part of the diagram where solely type-B QPOs (Casella et al. 2004) are seen. The dashed line joins two consecutive observations separated by 33 days due to observability constraints. The cross corresponds to the first observation of the 2007 outburst.

tools like power density spectra (PDS), the hardness-rms correlation (e.g. B05), and multiwavelength observations are used for a more complete description of the different states and transitions. In this letter we present a new tool, the rms-intensity diagram, which allows one to map BHT states by only looking at the evolution of count-rate and rms (i.e. without spectral information). As a first step we have studied the case of the BHT GX 339-4, in which detailed observing campaigns have been performed during the multiple outburst observed with the *Rossi X-ray timing explorer* (RXTE).

GX 339-4 is a low mass x-ray binary (LMXB) harbouring a > 6 $M_{\odot}$ accreting black hole (Hynes et al. 2003; Muñoz-Darias et al. 2008). Since its discovery (Markert et al. 1973) the system has undergone several outburst, becoming one of the most studied X-ray transient. The intense monitoring carried out by RXTE during the 2002, 2004 and 2007 outburst has yielded detailed studies on the evolution of black hole states along the outburst (see e.g. B05). Here, we use this rich data set to study the evolution of the flux and variability along the outburst.

4.2 Observations

We have used all the RXTE public archival observations from the 2002 (206), 2004 (295) and 2007 (239) outburst of GX 339-4. For the analysis we have considered only the data from the *Proportional Counter Array* (PCA). GOODXENON, EVENT and SINGLE-BIT data modes are used for the variability. Count-rates have been computed using PCA Standard 2 mode data corresponding to the PCU unit #2. The analysis has been performed using HEASOFT V. 6.7. and custom timing software running under IDL.

4.3 The rms-intensity diagram for the 2007 outburst

The rms-intensity diagram (RID) for the 2007 outburst of GX 339-4 is presented in Fig.4.1 as filled dots. For each observations net count rate corresponds to PCA channels 0–35 (2–15 keV). Only entire RXTE observations are initially considered, i.e. every dot corresponds to one observation. Power density spectra (PDS) for each observation have been also computed using the procedure outlined in Belloni et al. (2006). We have used stretches 16 s long and the same energy selection as for the count rate. Total power was computed within the frequency band 0.1–64 Hz and the fractional rms calculated following Belloni & Hasinger (1990). The absolute rms displayed in the diagram (Fig.4.1) is obtained by multiplying fractional rms by net count-rate (PCU #2) for each observation. The black solid line joins observations contiguous in time starting from the observation marked with a cross (i.e. observation #1). We find that the source describe a continuous hysteresis pattern in the anticlockwise direction. Four different regions can be distinguished in this diagram.

4.3.1 The hard line

Starting from the first observation (cross in Fig.4.1) and following the solid line we see rms increasing with count rate. This linear trend is seen during the first 18 observations (i.e. $\sim$ 40 days). Following the state classification reported by Motta et al. (2009), all these observations belong to the canonical LHS. In the context of this digram we will call this linear relation 'hard line' (HL). A continuous increase in hardness (M09) is observed during this HL. Weak, type-C QPOs appear in the PDS of the observations corresponding to the upper part of the HL without modifying the rms-flux relation. They become strong once the system shows fractional rms of $\sim$ 30 per cent, and it is close to abandon the HL. In Fig. 4.2 we plot the RID but using fractional instead of absolute rms. In this representation the HL we see in Fig. 4.1 corresponds to the first 18 points starting from the cross, where fractional rms drops

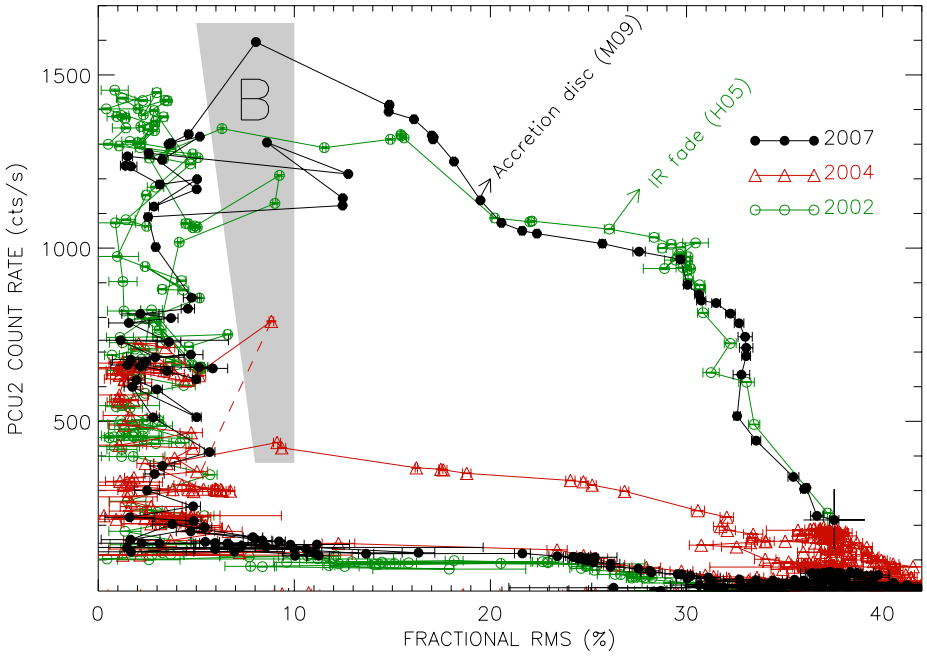

Figure 4.2: Same as Fig.4.1 but using fractional instead of absolute rms. Using this representation it is also possible to define a region where only type B QPOs are present.

from 40 to 30 percent.

4.3.2 State transitions

From observation #19 to #23 ($\sim$ 3 days), the rms starts to decrease, whereas the flux is still increasing. Therefore, the system abandons the HL and follows a different linear relation. From observation #24 to #29 ($\sim$ 3 days) rms a sudden increase in count rate is observed whereas rms is almost constant within $\sim$4 counts s^{-1}. The spectral fits performed by M09 require of a thermal black-body component from observation #25 (see Fig. 4.1). Thus, we associate this increase in flux at constant rms to the appearance (2-15 keV band) of an optically thick accretion disc with a very low variability level.

Until observation #32, type-C QPOs are observed in the corresponding PDS. From observation #32 to #33 the rms decreases dramatically, crossing the 10 per cent fractional rms line. A type-B QPO is observed in the PDS. Although the change in rms is major, the observations are only separated by $\sim$ 1 day.

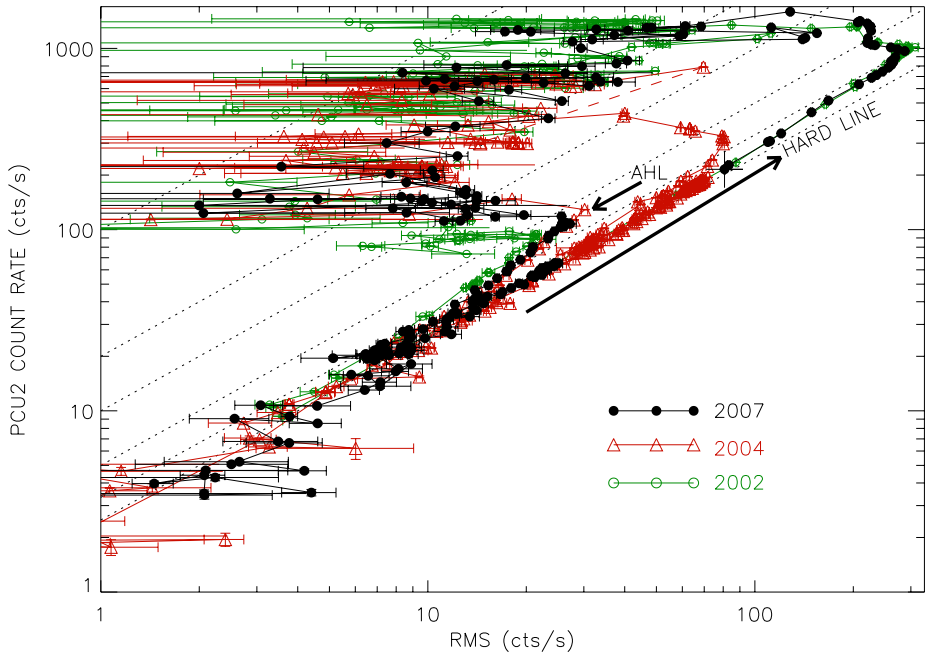

Figure 4.3: Same as Fig.4.1 but using a log-log scale. The adjacent hard line (AHL) and the hard line at lower count rate becomes evident. The presence of a flux component with no variability is ruled out (see Sec. 4.6). Dotted lines represent the same fractional rms levels as in Fig.4.1.

4.3.3 The soft branch

From observation #34, the rms is below $\sim$ 5 per cent and the count rate fades from $\sim$ 1300 to $\sim$ 100 cts s^{-1}. A linear relation can be observed, but much more scattered than during the HL (see Fig. 4.1). This new relation is followed by the system during the canonical soft state (M09).
A sudden increase in rms is also observed during four observations. Three of these cross the $\sim$ 10 per cent line and show type-C QPOs whereas a type-B is observed for the other. Observations with type-A QPOs are not well differentiated from the soft branch. However, some of them are placed close or slightly above the 5 per cent rms line, which roughly delimits the soft branch (see also Fig. 4.2).

4.3.4 Soft-to-hard transition. The adjacent hard line

Fig. 4.3 shows the RID in log-log scale, where a monotonic rms increase is observed at constant flux ($\sim$ 100 cts s^{-1}) from the bottom of the soft branch. Once the rms

cross the $\sim$ 20 per cent level a linear decrease in rms and flux towards the HL is observed. During this adjacent HL (see note in Fig. 4.3) PDS are the typical of the LHS, although the spectral color is softer (i.e. hardness is lower) than the observed during the HL.

4.4 The 2002 and 2004 outburst

In Figs. 4.1, 4.2 and 4.3 the RID corresponding to the 2002 and 2004 outburst are shown as open triangles and open dots, respectively.

- The 2002 RID is similar to the 2007 one (as in the case of the HID). The system leaves the HL roughly at the same position and an increase in flux at $\sim$ constant (absolute) rms is also seen in the region where the accretion disc is observed by M09 during 2007. Homan & Belloni (2005) performed a multiwavelength campaign during the 2002 outburst. They find that the optical and near infrared properties of GX 339-4 change on MJD 52398, which correspond to the first observation outside of the HL (see Fig. 4.1). Belloni (2005) also identify this observation as the first one belonging to the HIMS (i.e. non LHS).

- The 2004 ourburst is fainter and therefore its absolute rms is also significantly lower. In this case the variability does not decrease when the system leaves the HL, but increases with flux following a different linear relation. A clear feature related with the appearance of a thermal disc in the spectrum is not observed, suggesting a weaker disc component. Flux finally increases as rms decreases until the systems reach the soft branch. After a long permanence in this branch rms increases up to $\sim$ 20 per cent and goes back to the HL following the same adjacent HL observed in the other two outbursts.

The HL is identical for the three outbursts, independent of the maximum flux reached. We also observe this behaviour in the BHT H1743-322 (Muñoz-Darias et al. in prep). The soft branch is also very similar between the three outbursts, lying within the $\sim 1-5$ per cent fractional rms region. We notice that observations just outside this region contains fast state transitions (see Nespoli et al. 2003; Casella et al. 2004). A detailed state classification in this region of the diagram is beyond the scope of this work.

It is also possible to define a region of the diagram (count rate$\gtrsim 400$ counts s^{-1} and $\sim 7-10$ per cent fractional rms) where only observations showing type-B QPOs (grey region in Fig. 4.1 and Fig. 4.2) are seen. These observations must be classified as SIMS according to Homan et al. (2005). We also identify two observations (70110-01-47-00 and 70108-03-02-00) with fainter B QPOs at lower fractional rms than the region. A more detailed analysis of these data shows that the type-B QPO is

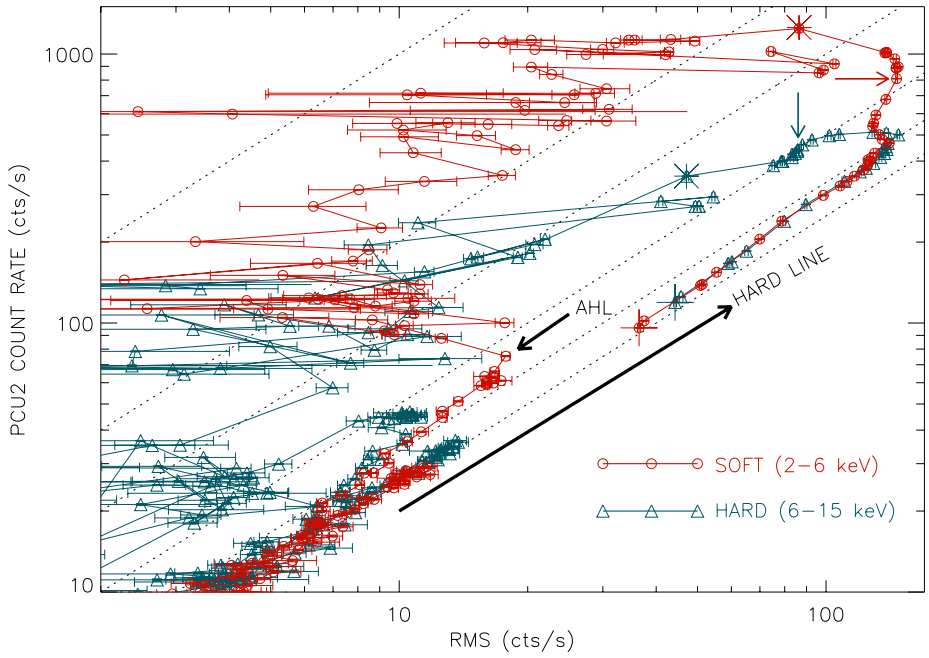

Figure 4.4: Soft (PCA 0-13; 2-6 keV) and hard (PCA 14-35; 6-15 keV) rms-intensity diagrams for the 2007 outburst of GX 339-4 plotted in log-log scale. The dotted lines represent the same fractional rms levels as in Fig.4.1. Since an accretion disc component is detected in the energy spectrum (Motta et al. 2009; see arrows in the plot), the fractional rms level becomes higher in the hard band. the first observation showing a type-B QPO is indicated with a star. Crosses indicate the first observation.

only present in part of the observation, with rms being the expected for the QPO B region.

4.5 Hard/soft rms-intensity diagrams

With the aim of tracing the evolution of soft and hard variability we have computed the RID using soft (PCA 0-13; 2-6 keV) and hard (PCA 14-35; 6-15 keV) bands for the three outburst. These energy ranges can be selected independently of the observing mode in which data were taken, and allow us to cover the whole evolution of the three outbursts. In Fig. 4.4 the soft and hard RID are plotted for the 2007 outburst as open circles and open triangles, respectively. It is clear that both RIDs show the same HL, where fractional rms drops from 40 to 30 percent rms as the system becomes brighter. This is expected since is well-known that rms is weakly

energy dependent (2-20 keV) during the LHS (see e.g. Muñoz-Darias et al. 2010a for the cases of XTE J1752-223 and Cyg X-1). Differences arise when the system leaves the HL (observation #18; 92035-01-02-04):

- During the next five observations the hard RID shows a decrease in rms at constant count-rate. Then, once the disc component appears in the spectrum (M09; see arrow in Fig. 4.4), a constant decrease in flux and rms following the 20 per cent line is seen until the type-B QPO appears (#33; star in Fig. 4.4). For the same observations an increase of flux at constant rms is observed in the soft RID.

- Since the disc component is detected by M09 (see arrows in Fig. 4.4) , more fractional rms is seen systematically at higher energies, even at the very bottom of the soft branch.

On the other hand, the same adjacent HL is observed for both RID, as expected for LHS observations with flat rms spectra.

4.5.1 The 2002 and 2004 outburst

The behavior observed during the 2002 outburst (not shown here) is similar to the one described above. During 2004, the vertical rise after leaving the HL is much less evident in the soft RID, suggesting weaker accretion disc component. The decrease in rms at constant flux is neither observed in the hard RID, although the decay following the 20 per cent rms line is seen.

4.6 Discussion

During the outburst evolution of BHT different accretions regimes are present. They yield the different states that we see when looking at the X-ray emission arising from these systems. In each one of these states, one or more physical mechanisms (e.g. thermal or non-thermal Comptonization in the corona, synchrotron emission from a jet, thermal emission from an accretion disc) play a role. The relative contribution of these mechanisms can be studied using energy spectra, but also by analysing the particular variability they prompt in the light-curves. In this work we have shown that the evolution of the fast variability (0.1-64 Hz) can be used as a good tracer of the different accretion regimes in black hole binaries. This would be impossible in case the variability associated with the different spectral components were similar. Indeed, we find evidence for the presence of highly variable and an almost non variable components in the lightcurves of GX 339-4:

- A sharp, linear relation between absolute rms and flux is observed at the beginning and at the end the three ourburst of GX 339-4 we have studied. This has been observed before by Gleissner et al. (2004) in Cyg X-1 during LHS observations. During these epochs, flux variations are probably tracing accretion rate variations and therefore rms is probably correlated with accretion rate. The rms-flux relation was firstly observed by Uttley & McHardy (2001) at much shorter time scales ($\sim$ 10 s) than the ones presented here ($\sim$ 1 ks). As a test we have studied the short term variations of the rms-flux relation by dividing the lightcurve in 32 s segments for the first and the last HL observations (2007 outburst). In both cases we also found a linear relation, with the fractional rms being consistent with the average of the entire observation. We note that a detailed study on these short-term variations is beyond the scope of this work.
  Uttley & McHardy (2001) found that the extrapolation of the rms-flux relation was consistent with no variability at lower count rates than the ones they studied. This supports the presence of two different component in the lightcurves. GX 339-4 offers the opportunity to study this linear relation over a much broader flux range. Consistently with the found by Gleissner et al. (2004) by extrapolating the relation they obtain for Cyg X-1, we do not see remaining flux when the rms is close to zero (see Fig. 4.3), thus our results are consistent with the presence of one component solely responsible for the variability at low count rates. Indeed, the system reaches its maximum variability level when this component dominates the spectrum. However, in the upper part of the HL, where Uttley & McHardy (2001) perform their study, the fractional rms decreases from 40 to 30 per cent. This could be associated with the presence of a second, less variable component.

- We find strong evidence for the presence of an extra component associated with the appearance of thermal emission in the energy spectrum of the source. This accretion disc component is not variable or varies very little. Its signature (i.e. flux increase at constant rms) is clearly seen in the 2002 and 2007 outburst once the systems leaves the HL. As expected, this becomes more evident if one only considers the 2-6 keV band (see Fig. 4.4). Indeed, The fractional variability of the system is lower at lower energies from the first observation in which the thermal component is detected until it returns to the LHS at the end of the outburst.

- The behaviour of the hard (6-14 keV) RID is complex. Once the system leaves the HL, a decrease in rms at constant flux is observed, suggesting that the properties of the physical mechanism that drives the hard emission are different. This could be explained by invoking a change in the properties of the corona

or the base of the jet. For instance, the high energy cut-off is observed to increase during the hard-to-soft transition (M09), which could be interpreted in terms of a cooling of the corona (see M09 and reference therein for details). It is remarkable that very few observations show fractional rms $\lesssim 5$ per cent in the hard band, suggesting that an underlying variable component (probably associated to power-law emission) is present even during the soft state (see Fig. 4.4).

The different rms-flux relations outlined above enable to perform a state classification of the different observations using the rms-intensity diagram. The following states can be identified using the description by Homan et al. (2005):

- Hard line observations corresponds to the LHS, with rms in the range $\sim$ 30–40 per cent. During these observations PDS are qualitatively similar between each other, and can be fitted by using several broad Lorentzians (see e.g. Fig. 3 in Belloni 2005, where the three upper PDS correspond to observations at the beginning, the middle and the end of the HL during the 2002 outburst). We associated the sharp changes we see in the rms-flux relation at the end of the HL to the transition to and from the HIMS. This is supported by spectral and timing changes (e.g. M09, B05) and particularly by the coincidence in time between the drop we see in rms and that observed in optical and infrared by Homan & Belloni (2005).

- During the HIMS, the rms is observed to drop from $\sim$ 30 to 10 per cent. The presence of the accretion disc in the spectrum is detected when the fractional rms is $\sim$ 20 per cent. We note that this point marks the transition between the hard and the steep power-law or intermediate states according to McClintock & Remillard (2006) (see M09). However, the major transition seems to occur before, when the system left the HL.

- Soft-state observations are observed to follow a different rms-flux relation, consistent with the results obtained by Gleissner et al. (2004) using relatively soft observations of Cyg X-1. The soft state in GX 339-4 is much softer than in Cyg X-1 and a soft branch very different from the HL is clearly seen in the RID. It shows a variability level lower than ~ 5 per cent and much more scatter than the HL. This suggest fast changes in (at least) one of the spectral components of the lightcurve.

- We find that between $\sim 7 - 10$ per cent fractional rms only type-B QPOs are observed (grey regions in Fig. 4.1 and 4.2). They are SIMS observations according to Homan et al. (2005) and our diagram suggest that this kind of

oscillations could follow a particular rms-flux relation. We note that transitions between soft and SIMS are very fast, which result in hybrid observations where timing properties are not constant. Thus, an accurate state classification close to the $\sim$ 5 per cent rms line is in some cases not compatible with using entire 1-3 ks observations.

- An adjacent hard line is observed at the end of the three outbursts. Observations during this adjacent HL show PDS typical of the LHS but with a slighly softer spectrum than that of the HL. Why this other linear relation, not seen when the systems leaves the HL, is present is unclear. It could suggest the presence of new components (see Russell et al. 2010) or the total absence of any of the components (e.g. accretion disc) observed during the flux rise phase at the beginning of the outburst.

4.7 Conclusions

We have proved that the evolution of the fast variability can be used as a good tracer of the different accretion regimes in black hole binaries. In particular, we find that apart from the linear rms-flux found during LHS, different relations are followed by black hole binaries during the soft and intermediate states.
In this work we have presented the rms-intensity diagram, showing that it is possible to associate the different regions of this diagram to the different states observed in black hole transients. Transitions can also be identified thanks to the marked changes they produce in the diagram. The application of this new tool to other systems and its interpretation will provide new insights in our understanding of the physical processes that take place during accretion episodes in X-ray binaries.

Acknowledgments

The research leading to these results has received funding from the European Community's Seventh Framework Programme (FP7/2007-2013) under grant agreement number ITN 215212 "Black Hole Universe". SM and TB acknowledge support from the ASI grant I/088/06/0 and PRIN-INAF 2008.

5 Low frequency oscillations in black holes: a spectral-timing approach to the case of GX 339-4

Sara E. Motta, Teo Muñoz-Darias, Piergiorgio Casella, Tomaso M. Belloni, Jeroen Homan

Accepted by Monthly Notices of the Royal Astronomical Society, 2011, ArXiv 1108.0540

Abstract

We analyzed RXTE/PCA and HEXTE data of the transient black hole binary GX 339-4, collected over a time span of eight years. We studied the properties and the behavior of low frequency quasi periodic oscillations (QPOs) as a function of the integrated broad-band variability and the spectral parameters during four outbursts (2002, 2004, 2007, 2010). Most of the QPOs could be classified following the ABC classification that has been proposed before. Our results show that the ABC classification can be extended to include spectral dependencies and that the three QPO types have indeed intrinsically different properties. In terms of the relation between QPO frequency and power-law flux, type-A and -C QPOs may follow the same relation, whereas the type-B QPOs trace out a very different relation. Type-B QPO frequencies clearly correlate with the powerlaw-flux and are connected to local increases of the count rate. The frequency of all QPOs observed in the rising phase of the 2002, 2007 and 2010 outburst correlate with the disk flux. Our results can be interpreted within the framework of recently proposed QPO models involving Lense-Thirring precession. We suggest that type-C and -A QPOs might be connected and could be interpreted as being the result of the same phenomenon observed at different stages

of the outburst evolution, while a different physical process produces type-B QPOs.

5.1 Introduction

Quasi-periodic oscillations (QPOs) have been discovered in many systems and are thought to originate in the innermost regions of the accretion flows around stellar–mass black holes. Low-frequency QPOs (LFQPOs) with frequencies ranging from a few mHz to $\sim$10 Hz are a common feature in almost all black hole X-ray binaries (BHB) and were already found in several sources with *Ginga* and divided into different classes (see e.g. Miyamoto & Kitamoto 1991 for the case of GX 339-4 and Takizawa et al. 1997 for the case of GS 1124-68). Observations performed with the Rossi X-ray Timing Explorer (RXTE) have led to an extraordinary progress in our knowledge on properties of the variability in BHBs (see van der Klis 2006, Remillard & McClintock 2006, Belloni 2010 for recent reviews) and it was only after RXTE was launched that LFQPOs were detected in most observed BHBs (see van der Klis 2004, Remillard & McClintock 2006). Three main types of LFQPOs, dubbed types A, B, and C, originally identified in the Power Density Spectra (PDS) of XTE J1550-564 (see Wijnands et al. 1999; Homan et al. 2001; Remillard et al. 2002), have been seen in several sources.

The systematic variations in the energy spectra of transient BHBs can be identified in terms of a pattern described in an X-ray hardness-intensity diagram (HID) (see Homan et al. 2001; Homan & Belloni 2005; Belloni et al. 2005, Belloni 2010). In many black hole candidates (BHC), different states are found to correspond to different branches/areas of a q-shaped HID pattern. Four main bright states (in addition to the quiescent state) have been identified in these sources, based on their spectral and timing properties (for a review Homan & Belloni 2005; McClintock & Remillard 2006; Belloni 2010). In particular, the analysis of the fast timing variations observed in the PDS plays a fundamental role in the state classification (see Homan et al. 2005, Belloni 2010).

Even though the general evolution and the main transitions become apparent in the HID, providing a general description of the BHB evolution, it is not enough for detailed studies. Many observed properties change smoothly throughout the basic diagrams (HID, see e.g. Homan et al. 2001; rms vs. hardness diagram, see e.g. Belloni 2010; rms-intensity diagram, see Muñoz-Darias et al. 2011), but some do not. It is the inspection of the fast-variability properties which indicates the presence of abrupt variations that can be taken as landmarks to separate different states. In proximity of the HIMS/SIMS transition timing properties (in particular the appearence of different types of QPOs in the PDS) constitute the sole way to distinguish between HIMS/SIMS/HSS given the absence of differences in the spectral shape.

The different types of QPOs are currently identified on the basis of their intrinsic properties (mainly centroid frequency and width, but energy dependence and phase lags as well), of the underlying broad-band noise components (noise shape and total

variability level) and of the relations among these quantities. Despite LFQPOs being known for several decades, their origin is still not understood and there is no consensus about their physical nature. However, the study of LFQPOs provides an indirect way to explore the accretion flow around black holes (and neutron stars). In particular, their association with specific spectral states and their phenomenology suggests that they could be a key ingredient in understanding the physical conditions that give origin to the different states.

Several models have been proposed to explain the origin and the evolution of LFQPO in X-ray binaries. The geometry described in Esin et al. (1997) and Done et al. (2007) allows to explain the spectral evolution seen in BHBs and forms the basis for the LFQPO model proposed by Ingram et al. (2009), Ingram & Done (2010) and Ingram & Done (2011), which invokes Lense-Thirring precession. We shall refer to this model as the *precession model*. For the case of the neutron star source 4U 1728-34, Titarchuk & Osherovich (1999) show that LFQPO frequency is associated with radial oscillations in the boundary layer and the break frequency associated to the broad band noise in the PDS is determined by the characteristic diffusion time of the inward motion of the matter in the accretion flow. Tagger & Pellat (1999) associate the existence of LFQPO in X-ray binaries to an instability occurring in the inner part of disks threaded by a moderately strong vertical poloidal magnetic field.

In this paper, we examine the QPO parameters and compare them with the results of a complete spectral analysis. Since the presence and the properties of QPOs in BHBs are related to the spectral characteristics of the source, our goal is to identify the link between the spectral and fast timing variability properties and to highlight possible physical differences between the three types. The *precession model* explains both the type-C QPO frequencies and the presence of the associated broad-band variability (see also Tagger & Pellat 1999 for an alternative in the case of BHs) and most of spectral properties. For this reason, given the success of this model to explain many of the observed properties we will interpret our results in the context of the *precession model* and we will attempt to extend its predictions to the three types of QPOs.

5.1.1 GX 339-4

GX 339-4 is a Low Mass X-Ray Binary (LMXB) harboring a $> 6M_{\odot}$ accreting black hole (Hynes et al. 2003; Muñoz-Darias et al. 2008). Since its discovery (Markert et al. 1973), the system has undergone several outbursts, becoming one of the most studied X-ray transients. The intense monitoring carried out by RXTE during the 2002, 2004, 2007 and 2010 outburst has yielded detailed studies on the evolution of black hole states throughout the outburst (see e.g. Belloni et al. 2005), making the source an ideal candidate for an extensive study on the spectral-timing properties of BHBs. Here, we use this rich data set to study the relation between the spectral and

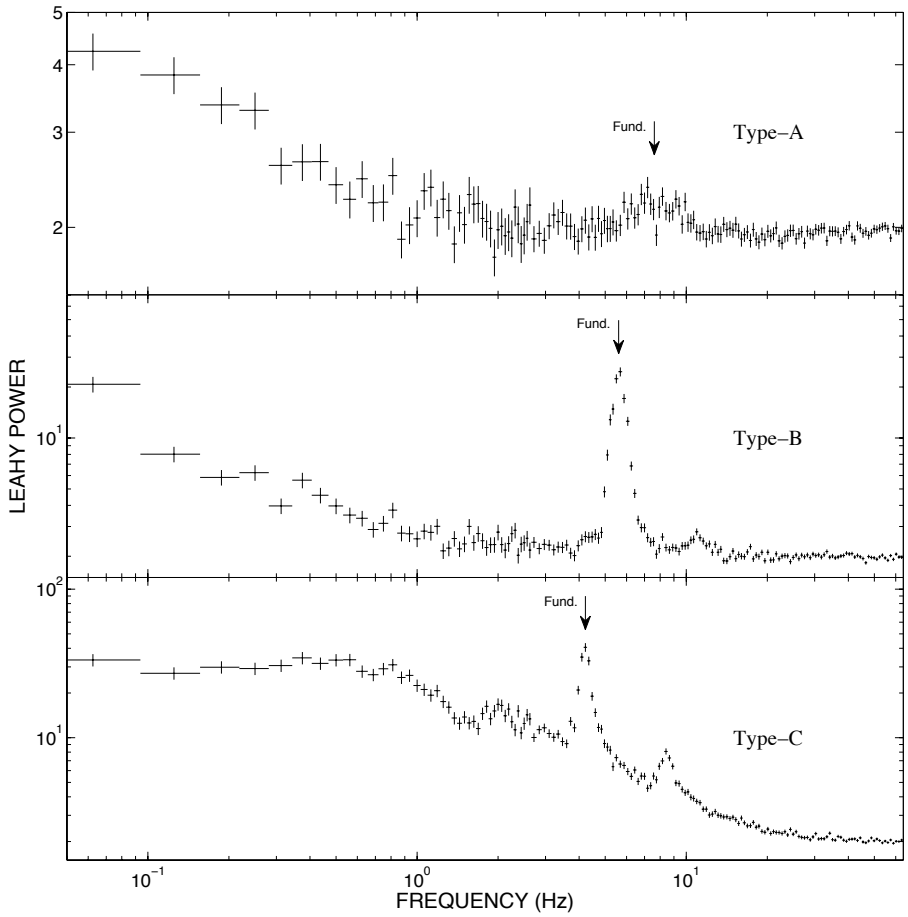

Figure 5.1: Examples of type A, B and C QPOs from our GX 339-4 observations. The centroid peak is indicated. Upper panel: Obs. 92085–01–02–06. Middle panel: Obs. 95409-01-15-06. Bottom panel: Obs. 70109-04-01-01). The Poisson noise was not subtracted.

variability properties of GX 339-4 across the different outbursts.

5.2 Observations and data analysis

We examined 1007 RXTE public archival observations of GX 339-4 from 2002, 2004, 2007 and 2010 outburst and selected for our analysis only observations where somewhat narrow (i.e. $Q \geq 2$) feature was identifiable on top of peaked or power-law shaped noise components. The selection has been done by eye, then we fitted the PDS (see below) and non-significant (below 3σ) detections were excluded from

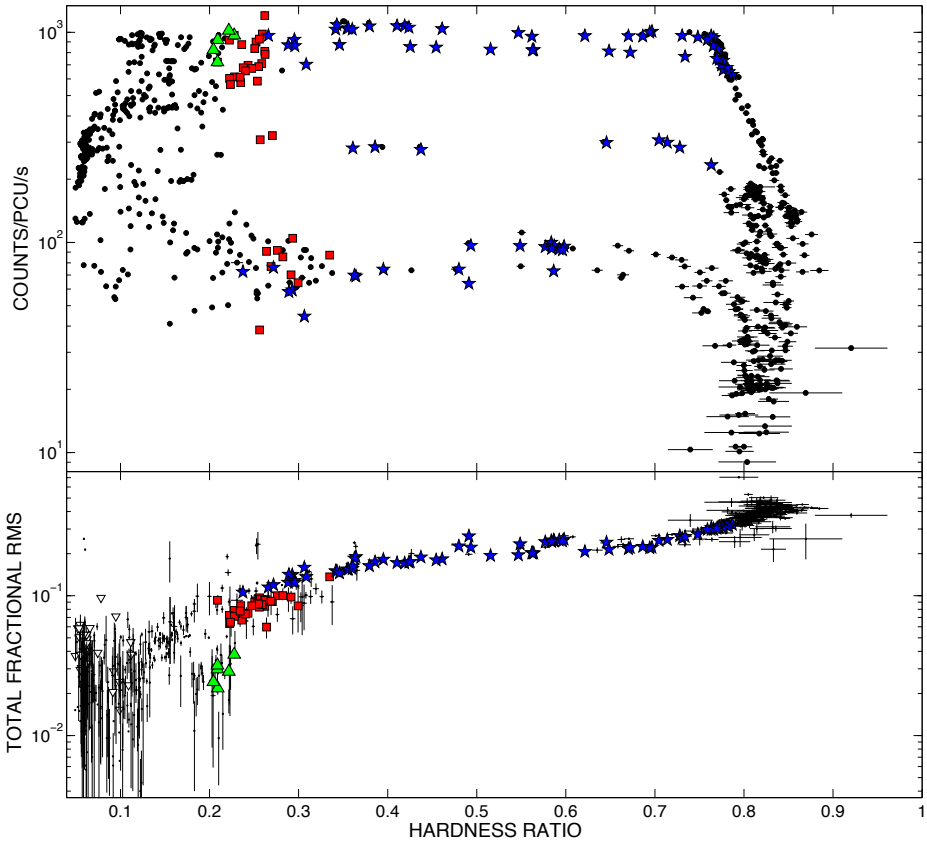

Figure 5.2: Top panel: HID for the 2002, 2004, 2007 and 2010 outburst of GX 339-4. Each point represents a single RXTE observation. Blue stars mark Type-C QPOs, red squares mark Type-B QPOs and green triangles mark Type-A QPOs. Black dots mark all the other RXTE observations of GX 339-4 that do not show low-frequency QPOs. Bottom panel: corresponding Rms-hardness diagram. Empty triangles stand for upper limits.

the subsequent analysis. A total of 115 observations and 117 oscillations have been considered.

The RXTE data were obtained in several simultaneous modes. STANDARD 2 and STANDARD modes for the PCA and HEXTE instruments respectively were used to create background and dead time corrected spectra. We extracted energy spectra from PCA and HEXTE for each observation using the standard RXTE software within HEASOFT V. 6.9. Only Proportional Counter Unit 2 from the PCA was used since only this unit was on during all the observations. A systematic error of 0.6% was

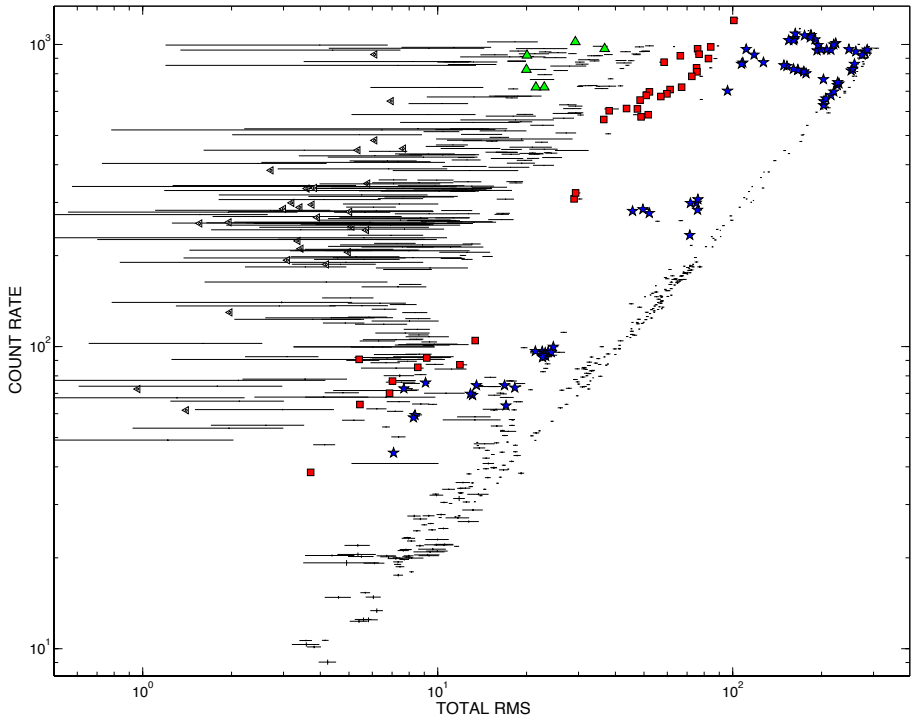

Figure 5.3: RID for the 2002, 2004, 2007 and 2010 outburst of GX 339-4. The symbols follow the same criteria as in Fig. 5.2

added to the PCA spectra to account for residual uncertainties in the instrument calibration[1]. For 2002, 2004 and 2007, we used only data coming from HEXTE/Cluster B, which was correctly working in that period. Since HEXTE/Cluster B encountered technical problems at the end of 2009 [2], we decided to use data coming from HEXTE/Cluster A to analyze observations taken subsequently. We followed the standard procedure described in the RXTE cookbook[3] to produce source and background spectra, using data coming from HEXTE/Cluster B to produce a preliminary background from which we derived a background spectrum to be used together with HEXTE/Cluster A spectrum.

We accumulated background corrected PCU2 rates in the Standard 2 channel bands A = 4 - 44 (3.3 - 20.20 keV), B = 4 - 10 (3.3 - 6.1 keV) and C = 11 - 20 (6.1 - 10.2

[1] http://www.universe.nasa.gov/xrays/programs/rxte/pca/doc/rmf/pcarmf-11.7 for a detailed discussion on the PCA calibration issues.

[2] http://heasarc.gsfc.nasa.gov/docs/xte/xhp_new.html

[3] http://heasarc.gsfc.nasa.gov/docs/xte/recipes/hexte.html

keV). A is the total count rate, while the hardness was defined as H = C/B (Homan & Belloni 2005).

PCA+HEXTE spectra were fitted with XSPEC V. 11 in the energy range 4 - 40 keV[4] and 20-200 keV respectively for data taken in 2002, 2004 and 2007 outbursts. For HEXTE spectra produced from data collected during 2010 we considered only the 20 - 150 keV spectral band. The reason for this was to exclude the harder part of the spectra that in some cases was affected by systematic problems due to an incorrect estimation of the background. For the same reason we ignored the energy range 50 - 80 keV, where line-like residuals can be found in the spectral fits[5].

We calculated unabsorbed fluxes for different spectral components from the best fit to the energy spectra (see Sec. 5.2.2). We measured the total flux between 2.0 and 20.0 keV and the disk flux between 2 and 20 keV. We also measured the power-law flux in the 6 - 20 keV energy band. Since the spectral deconvolution can be problematic, we choose this energy interval to avoid contamination due to the confusion between disk and power-law component at lower energies. All the fluxes were normalized by the Crab flux in the respective energy bands in order to correct the fluctuations due to the variations in the instrument properties. For each outburst we used a Crab spectrum coming from an observation as close as possible to the central part of the outburst. The fluxes used for the correction are summerized in Table 5.1.

For our timing analysis, we used GOODXENON, EVENT and SINGLE BIT data modes. We used custom software under IDL and for each observation we produced power density spectra (PDS) from stretches 16 seconds long in the channel band 0-35 (2-15 keV). We averaged the PDS and subtracted the contribution due to Poissonian noise (see Zhang et al. 1995). The PDS were normalized according to Leahy et al. (1983) and converted to square fractional rms (Belloni & Hasinger 1990). The integrated fractional rms was calculated over the 0.1 - 64 Hz band. PDS fitting was carried out with the standard XSPEC fitting package by using a one-to-one energy-frequency conversion and a unit response. Following Belloni et al. (2002), we fitted the noise components with three broad Lorentzian shapes, one zero-centered and other two centered at a few Hz. The QPOs were fitted with one Lorentzian each, only occasionally needing the addition of a Gaussian component to better approximate the shape of the narrow peaks and to reach values of reduced χ^2 close to 1. We examined PDS in the form of dynamical power density spectra (DPDS), computing Fast Fourier Transforms of windows of data 16s long. In some cases we used shorter time windows to better follow the evolution of a narrow feature. Where transitions between different power spectral shapes were seen, we separated different time intervals in

[4]In principle it is possible to fit RXTE/PCA spectra starting from 3 keV. However, especially with sources affected by low interstellar absorption, when fitting energy spectra residuals that cannot be explained can appear. Therefore we decided to fit spectra starting from 4 keV.

[5]See http://heasarc.gsfc.nasa.gov/docs/xte/whatsnew/ for details.

Observation ID	2 - 20 keV flux erg/s/cm^2	6 - 20 keV flux erg/s/cm^2	Outburst
70018-01-03-00	3.51E-08	1.72E-08	2002
90129-02-01-00	3.44E-08	1.69E-08	2004
92802-03-06-01	3.40E-08	1.65E-08	2007/2010

Table 5.1: Crab fluxes used for the flux correction described in Sec. 5.2. Columns are: Crab observation ID, flux measured in the 2 - 20 keV band, flux measured in the 6 - 20 keV band, outburst the correction was applied to.

order to obtain average power spectra for each shape.

5.2.1 The QPO classification

We have classified the QPOs following Casella et al. (2004). The properties that allow one to classify the QPOs are the *quality factor* ($Q = \nu_{centroid}/FWHM$) and the shape of the noise associated with the oscillation. Frequency does not allow a classification, as the characteristic frequency intervals where the three types of QPOs appear largely overlap, nor does the rms. Casella et al. (2004) and Muñoz-Darias et al. (2011) quantify the noise level associated to the QPOs in terms of the total[6] fractional rms (0.1-64). We could classify $\sim$98% of the QPOs of GX 339-4 (see 5.3.1). In Table 5.3 we summarize the QPOs classification and in Fig. 5.1 we report one example for each type of QPO.

In Figure 5.2 we show the HID of GX 339-4 (top panel) and the rms versus hardness diagram (bottom panel, see Belloni 2010) and in Fig. 10.2 we show the rms-intensity diagram, including all the RXTE observations collected during 2002, 2004, 2007 and 2010 outbursts. Type-A, -B, -C QPOs are marked with green triangles, red squares and blue circles respectively. The HID is tracked counterclockwise, starting from the bottom right corner of the track. The upper and lower horizontal branches in the HID roughly correspond to the HIMS and SIMS, while the right and left vertical branches correspond respectively to the LHS and HSS. We will refer to the first part of the loop (from the right vertical branch to the left end of the top horizontal branch) as *softening phase* of the outburst and to the last part (from the left end of the bottom horizontal branch back to the right vertical branch) as to the *hardening phase*.

In the following we summarize the results of the ABC classification applied to our sample.

Type-C QPO - In the early stages of all the four outbursts of GX339-4 (late LHS

[6]We refer to the *total fractional rms* as to the rms measured on the whole PDS.

and HIMS, see Tab. 5.3 for details), two main components can be identified in the PDS: a strong flat-top noise and one or more QPO peaks. When more than one peak is observed, the peaks are harmonically related. The strongest and narrowest peak, which is usually the central one, is taken as the fundamental. When the identification of the fundamental remained difficult because of the presence of strong harmonic peaks, we followed the evolution of the PDS shape for the selection. In Tab. 5.4 we report parameters for the strongest peak in the PDS.The QPO is usually strong and narrow ($Q \geq 6$) and the centroid frequency varies in the 0.2-9 Hz range. Only in some cases, when the oscillations are weak and appear at very low frequencies, the Q-factor is slightly lower than 10. The addition of a Gaussian component to the multi-Lorentzian model is required in a few observations in order to better approximate the peak shape. Type-C QPOs are observed also in the late stages of all the outbursts. We refer to type-C QPOs observed in the lower branch as type-C*. The PDS shows a noise component in the form of a broad Lorentzian and a QPO peak broader than at the beginning of an outburst. During the 2002 outburst, the type-C* QPOs frequencies span the 4-9 Hz range, while in the 2004 only one Type-C* QPO (at $\sim$ 3 Hz) is observed. In the 2007 outburst Type-C* QPOs are seen in a slightly lower frequency interval (2-4 Hz). A second harmonic peak is sometimes present in the PDS. Even though the Type-C* QPO centroid frequency ranges, rms properties and Q-values are different from the case of Type-C QPOs, it is possible to demonstrate that the properties of the two kinds of QPOs are continuously connected when ordered for increasing QPO frequency (see Sec. 5.3; see also Casella et al. 2005).

Type-A QPO - Type-A QPOs are observed in 2002 and 2004 during the SIMS, when the flux of the source is close to its maximum. The PDS show a broad QPO ($Q \leq 3$) with centroid frequency between 7.1 and 8.1 Hz associated to a weak power-law noise. Neither a subharmonic nor a second harmonic is observed. The PDS showing a Type-A QPOs have the lowest total fractional rms values of the sample.

Type-B QPO - They are observed in the SIMS and the oscillations that appear in the PDS ($Q \geq 6$) are observable in the frequency ranges 0.8-6.4 Hz. All the type-B QPOs seen at low frequencies (i.e. below $\sim$ 3 Hz) belongs to the lower branch in the HID, while all the QPOs at higher frequencies are observed in the upper branch in the HID. The noise seen in the PDS is weak and the QPO peak shape is often more similar to a Gaussian rather than a Lorentzian, therefore we had to combine both components (Gaussian + Lorentzian) to obtain better fits. A weak second harmonic is often present in the PDS. Sometimes the hint of a sub-harmonic appears.

5.2.2 Spectral Analysis

In order to obtain good fits and acceptable physical parameters, a model consisting of an exponentially cut off power law spectrum reflected from neutral material (Magdziarz & Zdziarski 1995) was used (`pexrav` in XSPEC). The reflection parameter was left free to vary, while the inclination angle was fixed at 30 degrees (notice that the results only weakly depend on the inclination value assumed). A multi-color disk-blackbody (`diskbb`) was added to the model and a Gaussian emission line with centroid allowed to vary between 6.4 and 6.7 keV was further needed in order to obtain acceptable fits. The line width was constrained between 0.1 and 1.0 keV to prevent artificial broadening due to the response of XTE/PCA at 6.4 keV. The hydrogen column density (`wabs`), was frozen to $0.5 \times 10^{22}\mathrm{cm}^{-2}$(Zdziarski et al. 2004). The addition of an iron edge, justified by the presence of the iron line, does not improve the fits significantly. In Table 5.4 we show the relevant spectral parameters for the best fits.

Where Type-C QPOs are detected, the photon index is seen to rise from $\sim$1.5 to $\sim$2.8 and back to $\sim$1.5 as a function of time, consistently with what previously observed (see e.g. Motta et al. 2009). Following the loop in the HID the source becomes soft while approaching the HSS and subsequently becomes hard again going back to the LHS. As a consequence the photon index increases, remains almost constant (between $\sim$2.6 and $\sim$2.8) for a while and then decreases. When Type-A and B QPOs (during the softening phase) are seen in the PDS, the photon index is at its maximum. When type-B QPOs are observed in the hardening phase, they are associated to lower values of the photon index. Indeed, the spectra from SIMS observations in the hardening phase always show systematically lower photon indices. For a detailed analysis of the transitions between soft and hard state in GX 339-4 during 2010 outburst, see Stiele et al. (2011). The photon index also correlates with the LFQPO frequency, as was already noticed by Vignarca et al. (2003) in the cases of GRS 1915+105, GRO 1655-40, XTE J1550-564, XTE J1748-288 and 4U 1630-47. The same behavior was observed in H1743-322 by McClintock et al. (2009). All type-C QPOs follow the same relation rather than several branches depending on the outburst. Type-C and type-B QPOs also overlap quite well covering the same photon index interval.

The parameters associated to the iron line and to the reflection components do not show any clear correlations with the presence of the different types of QPOs and/or particular states.

As one can see from Table 5.4, not all the components of the model are present in all the observations. In all the observations where a Type-B or Type-A QPO is detected, a disk component (`diskbb`) is visible in the spectrum. When the Type-C QPOs are detected at hardness larger than 0.6 no disk component is observed. The disk appears at hardness 0.2 - 0.6 during the softening phase. During the hardening phase a disk component was needed only in some of the spectra from 2002. All the

other spectral components (i.e. iron line, power-law and reflection components) are always necessary to obtain good fits.

Examining the parameters related to the disk-blackbody component, it is clear that our constrains on the disc parameters are usually poor. Even when a soft component is clearly present in the spectra and is required in order to obtain good fits, it is often only marginally significant. This is expected since the working range of PCA (3-40 keV) allows to see only the high energy part of the disc black body component, above the Wien peak. It is also known that, even if the *diskbb* model provides a good description of the thermal component, the derived spectral parameters should not be interpreted literally (see e.g. Merloni et al. 2000, Remillard & McClintock 2006). However, when the thermal component is dominant, the parameters can be taken as reliable.

Disentangling the different spectral components could be problematic when using spectra from RXTE. If one assumes that the hard x-ray emission comes from Comptonization of the soft disk photons on hot electrons, it is known that a simple power-law (or a power-law-like component, such as *pexrav*) is not appropriate for the description of the hard Comptonization tail of the spectrum at lower energies (i.e. where the hard component overlaps with the soft emission from the disk blackbody). A simple power-law does not have the low-energy cutoff that is typical of a proper comptonization model (i.e. *eqpair* or *compTT* in *XSPEC*) and therefore could affect the real contribution of the disk. However, when using RXTE data the adoption of a simple power-law (or power-law-like) component is justified because the energy range where PCA spectra can be analyzed (above 3 keV) does not cover this problematic overlapping zone (just below the Wien peak of the multicolor disk-blackbody). Therefore, a simple power-law or a power-law-like model such as *pexrav* is appropriated for the description of PCA spectra (see Muñoz-Darias et al. 2011 and Stiele et al. 2011). Despite the poor constraints on the disk parameters, the energy spectra are well fitted by the model used and the measures of the disk-fluxes reported in this work are to be considered reliable. This is supported by the fact that the disk flux correlates with the disk temperature.

5.3 Results

5.3.1 Rms-frequency relation

Once the QPOs of our sample were classified according to the ABC scheme, following Casella et al. (2004), we plotted the integrated fractional rms of each PDS versus the centroid frequency (see Fig. 5.4) to probe the link between the main QPO property (the frequency) and the total variability of the source. Several groups of points, associated to the Type-A, -B, -C QPOs, can be identified.

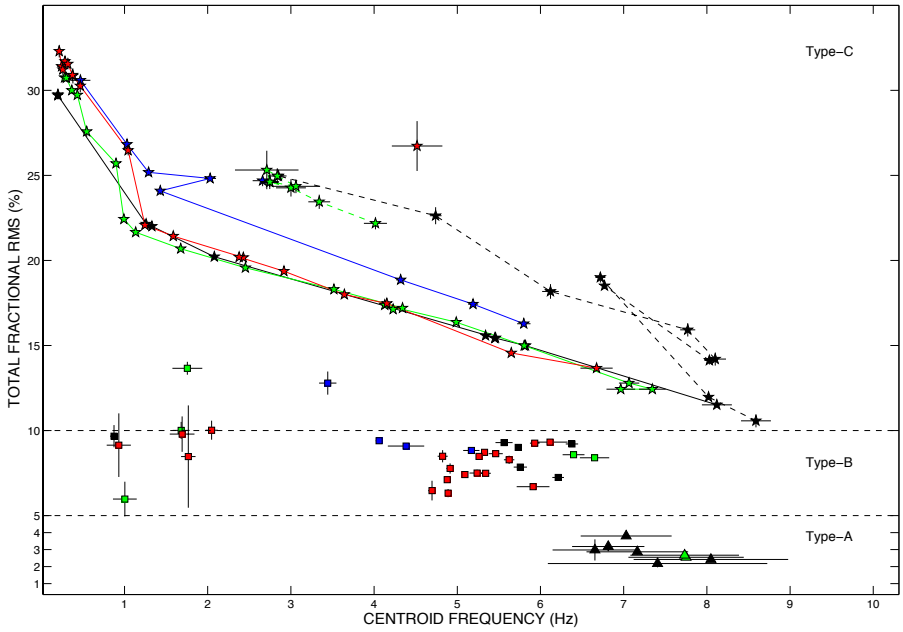

Figure 5.4: QPO centroid frequency vs. 0.1-64 Hz fractional rms. Each point corresponds to a different observation. Symbols correspond to QPO types: circles are Type-C QPOs, triangles type-A QPOs and squares type-B QPOs. The solid lines join for each outburst type-C QPOs during the outburst softening, while dashed lines join type-C QPOs during the hardening phase. Different colors mark different outburst: black 2002, blue 2004, green 2007 and red 2010.

- Type-C QPOs cover the frequency range 0.1 and 9 Hz and the rms range 10-35%. Type-C QPO frequency is clearly anti-correlated with total fractional rms.
- Type-A QPOs form a group at frequencies in the range $\sim$7 - 8 Hz and rms of $\sim$3%.
- Type-B QPOs are located at a slightly higher rms ($\sim$ 5-10%) in the 1-7 Hz range.

As one can see from Figure 5.4, the softening phase (solid lines) for each outburst shows lower rms than the hardening (dashed lines). This property has already been observed in other sources (see e.g. MAXI J1659-152, Muñoz-Darias et al. 2011) and can probably be understood in terms of a lower disk contribution to the emission. Only two outliers (i.e. the squares above and below the 5-10% of rms in Fig. 5.4)

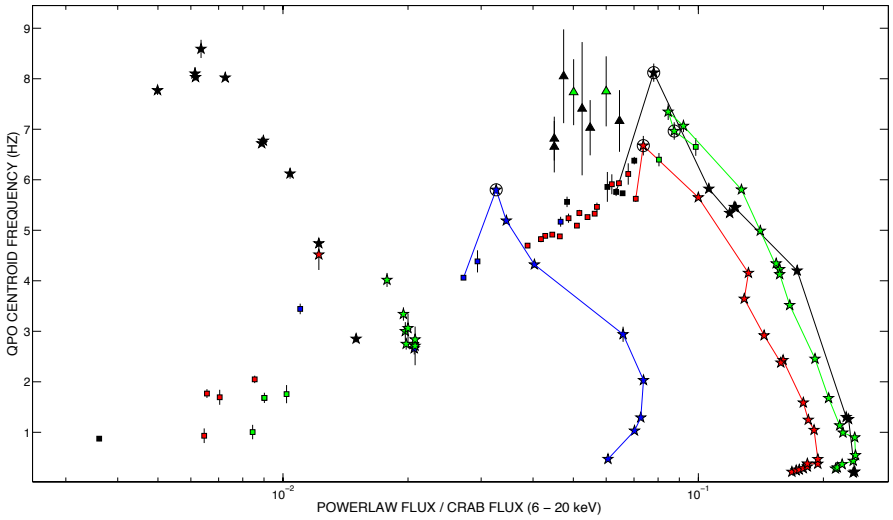

Figure 5.5: QPO centroid frequency vs. 6-20 keV powerlaw flux, normalized to the Crab flux. Colors indicate the outburst: black stands for 2002, blue for 2004, green 2007 and red 2010. Symbols correspond to QPO types: stars are Type-C QPOs, triangles type-A QPOs and squares type-B QPOs. The solid lines join for each outburst type-C QPOs and the first type-B QPO detected after the disappearing of the Type-C QPO. The empty circles mark the type-C QPOs observed immediately before the appearance of a type-B QPO. Each point in the plot represents an entire RXTE observation in which a QPO was detected, apart from the cases in which a switch between two different types of QPOs was observed (Obs. #1/#26, Obs. #4/#27-#28).

can be identified in Fig. 5.4 (Obs. #10, #15). Obs. #10 shows the typical PDS shape of a type-B QPO, even though with higher rms, while Obs. #15 shows a much more noisy PDS. Both the points lay far both from the type-C and -B region in Fig. 5.4. However, since they follow a relation similar to type-B QPOs in a flux-frequency plot (see 5.3.2), we tentatively classify those QPOs as Type-B. We notice that both the observations are taken in the decay phase of the outburst (2004 and 2007 respectively).

5.3.2 Frequency-Power-law flux relation

Since LFQPOs are known to be usually associated to the hard tail of the spectrum (see Churazov et al. 2001 and Sobolewska & Życki 2006, but also Rodriguez et al. 2004 and Rodriguez et al. 2008, who showed tha LFQPO spectra display a moving high energy cutoff), we started investigating the relations between LFQPO frequencies and the power-law fluxes. The frequency-power-law flux relation is shown in Fig. 5.5. We refer to *power-law* flux as the Crab corrected flux from the power-law component

in the 6 - 20 keV energy band (see Sec. 5.2.2)[7]. Different symbols represent the Type of QPOs and colors differentiate the four outbursts. For each outburst, a solid line connects in time all the QPOs from the first type-C to the first type-B QPO. The typical time interval between the last type-C and first type-B QPO is $\sim$1 day, even though sometimes other types of PDS are observed in between, especially if the transition period is not densely observed. When this happens, it might be possible to miss the appearance of a transient type-B QPO and see a type-A QPO after a type-C QPO. In Figure 5.5, the different QPO types follow clear and separate relations as function of the hard flux.

- **Type-C QPOs** (stars) lie on the right part of the diagram. The points trace well-defined tracks at different flux levels for each outburst (see the solid lines in the plot). The whole 0.1 - 9 Hz frequency range is spanned. Each track roughly correspond to the late LHS and HIMS observed in the softening phase of each outburst.

- **Type-C* QPOs** follow tracks on the left part of the diagram. Those QPOs were observed in all the outbursts. Differently from what happens in the right part of the diagram, points belonging to different outburst span different and smaller frequency ranges. However, the maximum frequency reached is consistent with the softening tracks. We ascribe the fact that no QPO appear at lower frequencies to the count rate being very low.

- **Type-A QPOs** (triangles) cluster on a quite narrow frequency and flux range, close in frequency to the last Type-C QPOs seen before the transition to the SIMS, but at slightly lower fluxes (see Fig. 5.4). Type-A QPOs always appear in time after the detection of a type-B QPO. No Type-A QPO is observed in the left part of the plot, i.e. during the hardening phase at the end of the outburst (see also Fig. 5.2). 5.4.

- **Type-B QPOs** (squares) are sharply correlated with the power-law flux and the relation between frequency and powerlaw-flux is well described by a power-law of the form $y = Ax^B + C$ (where A = 19.4(8) , B = 0.18(6), C= -6.1(2), see Fig. 5.6). This correlation holds for a large range of flux, showing that these oscillations frequencies depend directly on the hard X-ray flux. However, unlike type-C QPOs, the points do not follow a clear path as a function of time. No oscillations are seen in a given flux range in the middle of the plot. As happens for type-C and type-C* QPOs, this is due to the fact that also the SIMS (where type B QPOs are observed) is crossed two times, at either high or low fluxes.

[7]The result depend only very weakly on the energy band chosen. We performed the powerlaw-flux measure also in the 2–20 keV and the getting almost identical results.

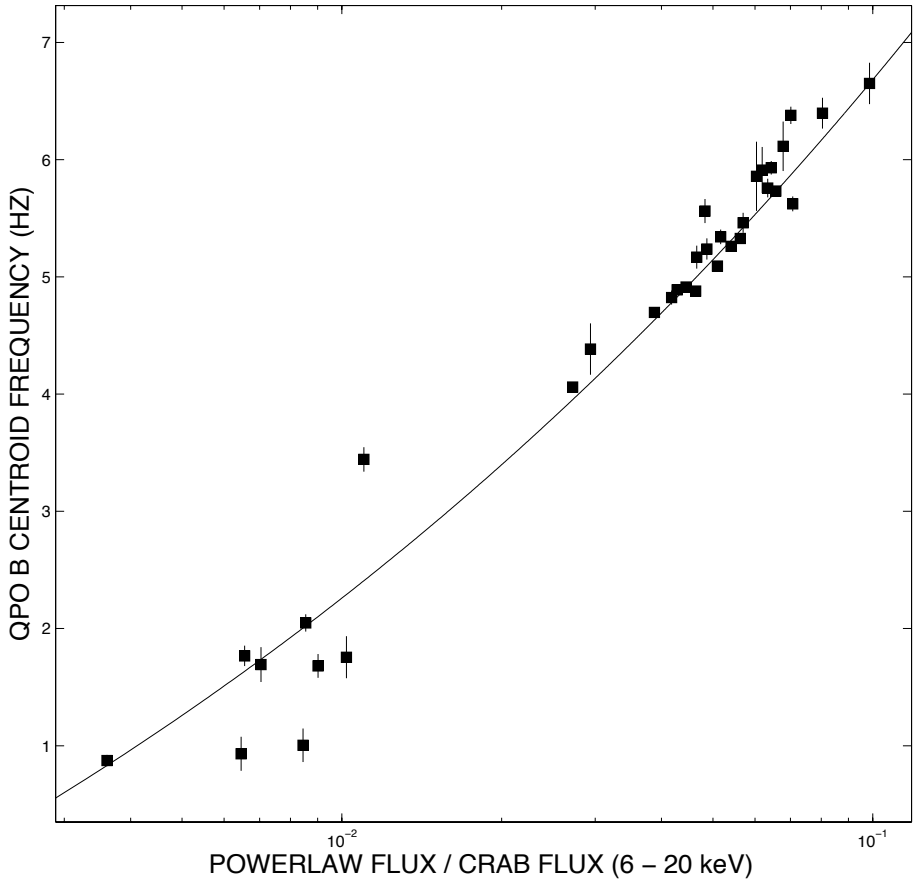

Figure 5.6: Type-B QPOs frequency as the function of the power-law flux. The correlation is well described by a power-law of the form $y = Ax^B + C$, where A = 19.4(8) , B = 0.18(6), C= -6.1(2)

Since type-B QPO are found in a small hardness range, it might be argued that they behave like type-C QPOs when observed in a small hardness range. For this reason we checked whether type-C QPOs show a behavior similar to type-B QPOs once grouped in subsamples selected as a function of the hardness. We divided type-C QPOs in six subsamples and for each group we plotted the QPO centroid frequency as a function of the power-law flux. The result is shown in Fig. 5.7.

Type-C QPOs' frequencies only show a weak anti-correlation with the power-law flux, especially at high frequencies. When type-C QPOs' range overlaps the hardness range where type-B QPOs are found (red points in Fig. 5.7 in the hardness range 0.2-

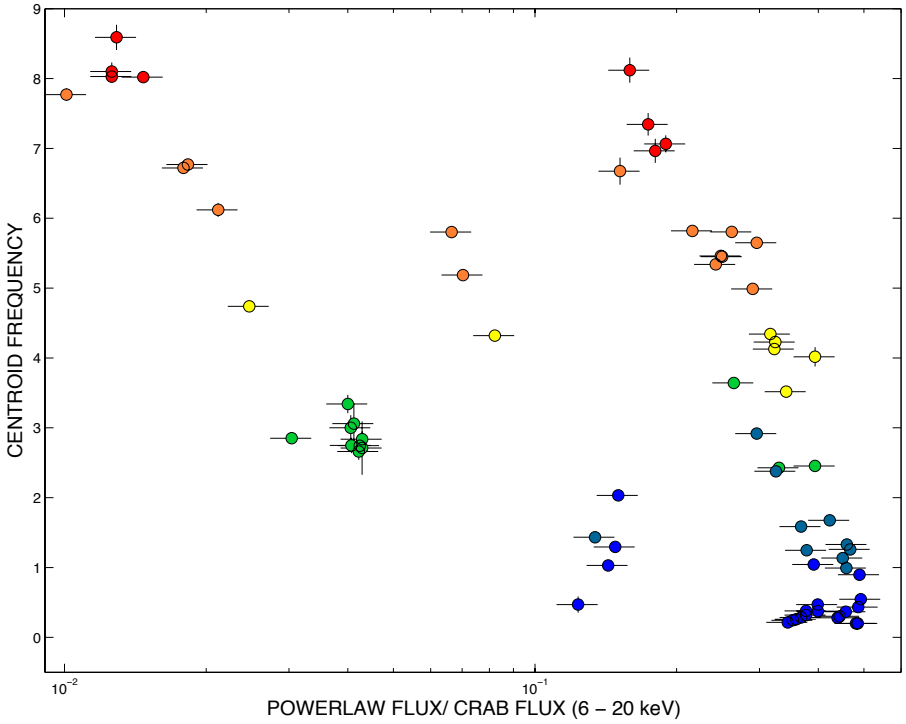

Figure 5.7: Type-C QPO centroid frequency versus power-law flux. Different colors marks the different hardness ranges in which the QPOs where divided. From the blue to the red the ranges are: 0.7-0.8, 0.6-0.7, 0.5-0.6, 0.4-0.5, 0.3-0.4, 0.2-0.3.

0.3) the (weak) correlation that they follow is exactly opposite to the one shown by type-B QPOs. This fact further strengthens the difference between type-C and B QPOs.

5.3.3 Frequency-Disk flux relation

In Fig. 5.8 we show the relations between frequency and disk flux. Symbols and colors follow the same criteria of Fig. 5.5. We refer to *disk* flux as the Crab corrected flux coming from the disk-blackbody component in the 2 - 20 keV energy range. Since we could associate a measure of the disk flux only to a subsample of type-C QPOs, not the all of them are present in this plot.

Most of the points trace out a well-defined track and the frequency clearly correlate with the disk flux. Those points correspond to all the QPOs seen during the upper branch of the four outbursts. Notice that for three of the four outburst (2002, 2007

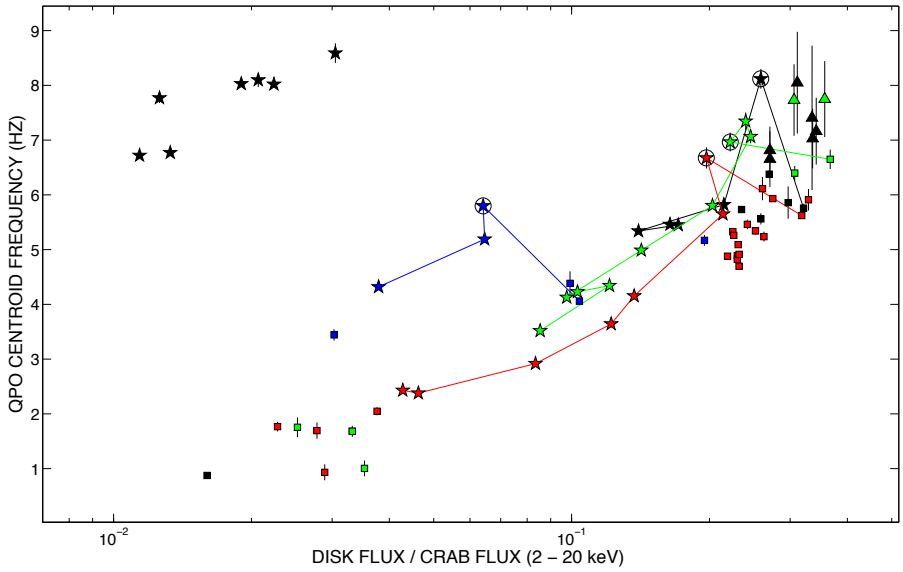

Figure 5.8: QPO centroid frequency versus soft flux. The symbols follow the same criteria as in Fig. 5.5.

and 2010 outburst) the upper branch in the HID loop is the same, while during the 2004 the upper branch is observed at a lower flux level. Note that this track includes type-C as well as type-A and B QPOs. Type-A QPOs are located in correspondence of the highest disk fluxes, while type-B QPOs cover approximately the same flux range of type-C QPOs.

We identify also a number of outliers, which correspond to two branches at different flux levels, forming other two tentative correlations. The clearest of the two is formed by all the type-C QPOs observed during the hardening phase (black points in the left upper corner of Fig. 5.8). Only during 2002 outburst it was possible to measure the disk flux during the lower branch. We ascribe this to the disk being fainter and/or colder during other outbursts than in 2002.

5.3.4 Association of Type-B QPOs with local peaks in the light curve

In Fig. 5.9 we plot sections of the light curves (PCU data, 2-20 keV) of the four outburst of GX 339-4. From this figure it is clear that most of the type-B QPOs are found at times of local peaks in the light curve. In all the cases where different types of QPOs are observed within a short time interval, they follow a precise count rate segregation: type-B QPOs at highest count rates, Type-C QPOs immediately

below and type-A QPOs are found at lower count rates. A relation QPO-type/count rate therefore seems to exist, although it is different from what Casella et al. (2005) observed in XTE J1859+226, where type-A QPOs are seen at highest count rates and type-B and -C appears below, even though they are not clearly separated in count rate. We notice that in all the outbursts, there is always a B at lower flux than some C in the same outburst, therefore the segregation in count rate in not absolutely true all along the outburst, but only for certain intervals (see Fig. 5.9). We also notice that outbursts 2002 and 2004 had a different initial evolution in comparison to 2007 and 2010, where the count-rate peak was reached after a monotonic rise.

Despite a difference segregation in count rate, also in XTE J1859+226 type-B QPOs are always found at hardness higher than that of type-A QPOs and lower than that of type-C QPOs. In the case of XTE J1859+226 a certain overlap was observed, while there is no overlapping in the case of GX 339-4 during a single outburst. A similar correlation between QPO types and hardness was found in XTE J1550–564 (Homan et al. 2001).

5.3.5 Timing and spectral evolution

In four observations of our sample the PDS show rapid transitions between different shapes. In all cases the transitions involve type-B QPOs.

In Fig. 5.10 and 5.11 we show two examples of different behaviors, for Obs. #1/#35 and #4/#36-#37 respectively. In the case of Obs. #1/#35 (Obs. ID 70109-01-07-00, Fig. 5.10), a type-A QPO ($\sim$7 Hz) is present in the first part of the observation, when the observed count rate was low. In the second part the light curve shows a net increase in count rate and simultaneously the onset of a type-B QPO ($\sim$6 Hz) is observed (see Nespoli et al. 2003 for details). At the same time, an increase of the hard flux (from $\sim$ 11% to $\sim$13% of the total flux) is observed, as the variation in hardness suggests (see Tab. 5.3).

During Obs. #4/#36-#37 (Obs. ID 70108-03-02-00, second PCA orbit, Fig. 5.11) a similar situation can be observed. In the first orbit the PDS shows a type-A QPO ($\sim$7 Hz). In the second orbit the source count rate dropped abruptly from $\sim$2200 counts/s to $\sim$2100 counts/s[8] in few seconds. A type-B QPO ($\sim$5.6 Hz), that was visible in the first part of the observation disappears leaving place to a type-A QPO ($\sim$7 Hz), observable until the end of the interval and during the complete third orbit. Analogous to the previous case, a variation in flux takes place. When the type-B QPO disappears, the power-law flux is seen to decrease abruptly (from $\sim$ 15% to $\sim$11% of the total flux in $\sim$1s). The frequency of the type-A QPO before the appearance of the type-B QPO and and after its disappearance in the light curve is the same.

[8]Note that the counts are taken from *EVENT mode data and they are not normalized per number of PCUs on*.

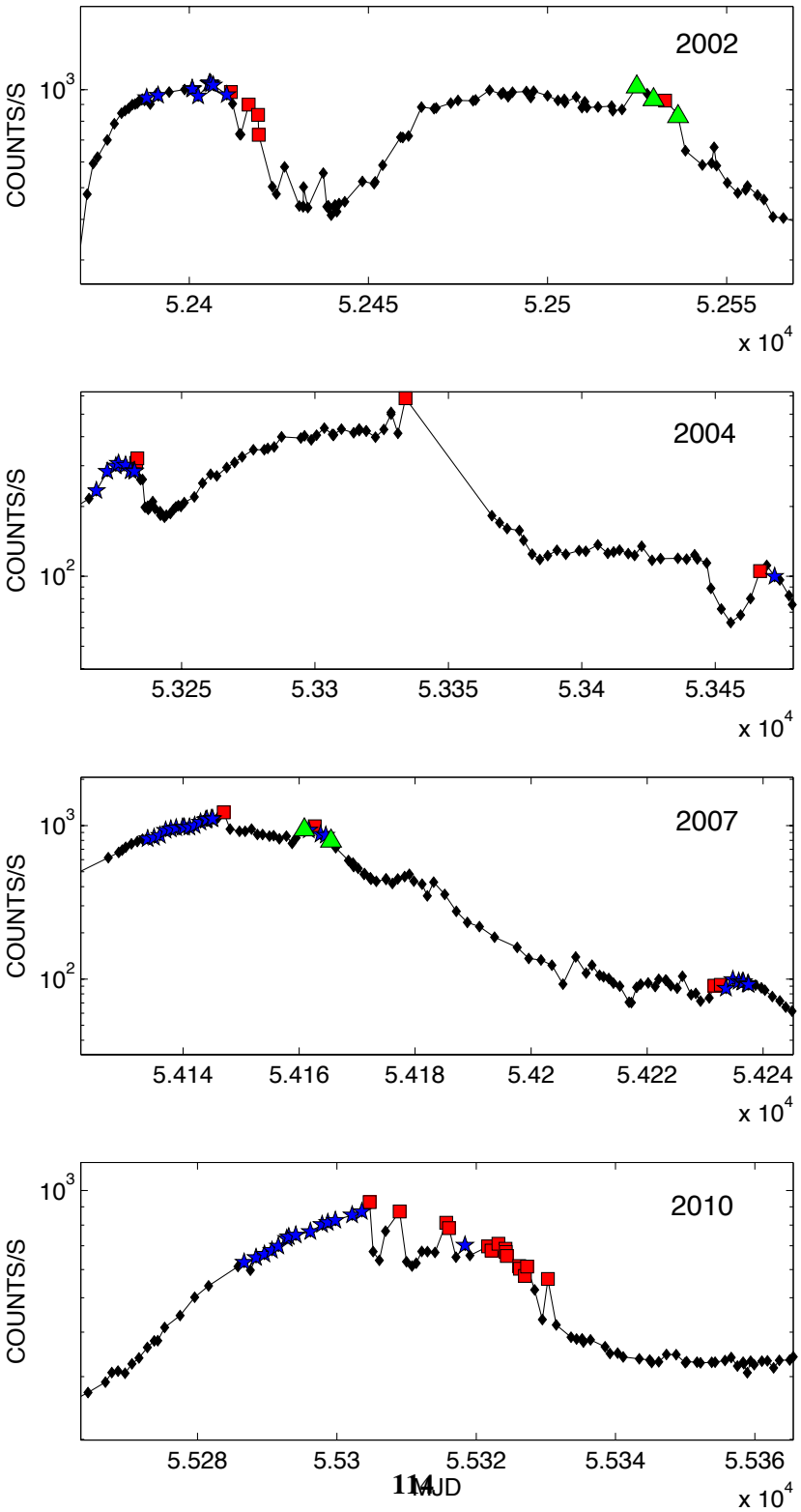
2002
COUNTS/S
10^3
5.24
5.245
5.25
5.255
x 10^4
2004
COUNTS/S
10^2
5.325
5.33
5.335
5.34
5.345
x 10^4
2007
COUNTS/S
10^3
10^2
5.414
5.416
5.418
5.42
5.422
5.424
x 10^4
2010
COUNTS/S
10^3
5.528
5.53
5.532
5.534
5.536
MJD
x 10^4

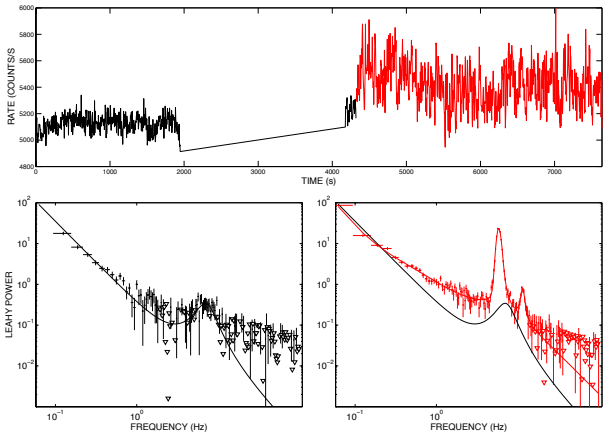

Figure 5.10: Upper panel: Light curve for Obs. #1/#35. The red line marks the light curve interval where a type-A QPO was detected. The black line marks the interval where a type-B QPO was visible. Lower panel: PDS for the two time intervals Nespoli et al. 2003.

Two other cases are found in Obs. #5 and #30 (Obs. ID 70110-01-47-00 and 95409-01-19-00), where, in correspondence of a rise in the count rate, a type-B QPO takes the place of power-law-shaped noise (i.e. no type-A or C QPO is observable before the onset of the type-B QPO). In all the mentioned cases it is clear that spectral differences can be very subtle, much more than the timing changes.

Similar fast transitions between different types of QPOs have already been observed in GX 339-4 (Miyamoto & Kitamoto 1991) and in other sources, such as XTE J1859+226 (Casella et al. 2004) and GS 1124-68 (Takizawa et al. 1997). For XTE J1859+226, the type-B QPO seems to be associated to a flaring behavior. However, also in this source the type-A QPO is always seen at slightly higher frequencies than the type-B QPOs.

As it happens for type-A/B QPOs, direct switching from/to type-C/type-B can be observed in GX339-4 as in other sources (see e.g. Miyamoto et al. 1991, Takizawa et al. 1997). However, the switch between type-B and -C QPOs is not as sharp as in the case of type-B and type-A QPOs: the transition between the two types usually comes with a complex behavior and Type-B QPOs appears in correspondence to peaks in the light curve (occurring at timescales of few seconds), consistently with what described in Sec. 5.3.4, and type-C QPOs are seen where the count rate drops. For this reason, transitions between/from type-C and type-B QPOs are not easily detectable and are worthy of a more detailed analysis that is beyond the scope of this work. For a more detailed study, see Homan et al. (in prep).

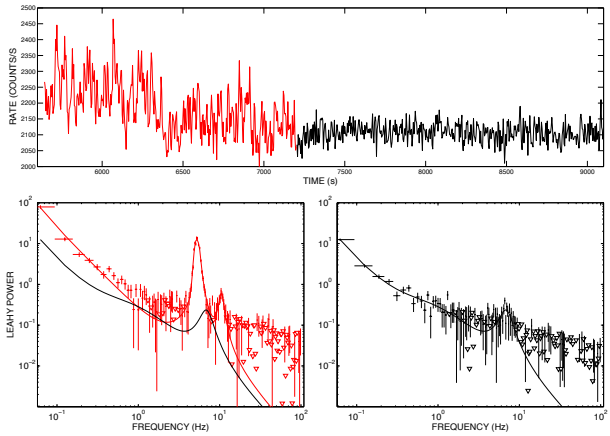

Figure 5.11: Upper panel: Light curve for Obs. #4/#36-#37 (second orbit). The red line marks the light curve interval where a type-A QPO was detected. The black line marks the interval where a type-B QPO was visible. Lower panel: PDS for the two intervals.

	A	B	C
ν	6.5-8 Hz	0.8-6.4 Hz	0.2-9 Hz
Q	1-3	$\geq 6 (\geq 2)^*$	$\geq 6 (\geq 2)^*$
rms	$\leq 5\%$	$5-10\%$	$\geq 10\%$
noise	weak red	weak red	strong flat-top

Table 5.2: Summary of type-A, -B and -C QPOs properties in GX 339-4. (*) The bracket values correspond to the hardening phases.

5.4 Discussion

We analyzed RXTE/PCA and HEXTE data collected over eight years of observations of the transient BHB GX 339-4 to study the properties and the behavior of LFQPOs. 115 out of 117 oscillations could be classified into the three main types (A, B, C). The coherent scenario we constructed can be compared to that of other systems (such as XTE 1859+226 and XTE J1550-564) for which the ABC classification has been performed. Different properties and relations emerge from the analysis, allowing a better characterization of the different types of QPOs. Our results confirm that the ABC classification can be extended to include spectral dependencies. The main parameters of the different types of LFQPOs observed in GX 339-4 are summarized in Table 5.2.

Type-C QPO: this oscillation is found in LHS and HIMS (see Belloni 2010 and Homan et al 2011 in prep.). It is observed in both the softening and hardening outburst intervals, even though during the hardening it results weaker. It appears at hardness values in the 0.2 - 0.8 range and over a large frequency range (0.2 - 9 Hz). Its centroid frequency rises as function of the time as the source undergoes the softening phase and decreases as the source hardens during the decay phase. All type-C QPOs are spread above a variability level below which only type-B and type-A QPOs are observed (see Casella et al. 2004 and Muñoz-Darias et al. 2011). The observed 0.1-64 Hz rms has values between 10 and 35%. Those are positively correlated with the hardness ratio (see e.g. Belloni 2010) and negatively correlated to the frequency (see Fig. 5.4). Type-C QPOs form a clear but complex pattern in a frequency versus power-law-flux plane. The frequency type-C QPOs correlates with the disk flux and form different branches in a frequency versus disk-flux plane, corresponding to the softening and hardening phases. Type-C QPO frequencies correlates well with the hardness, stressing a clear dependence on the spectral shape.

Type-A QPO: this QPO is usually observed in the SIMS, which is indeed defined on the basis of the appearance of type-A and -B QPOs. It is found in a narrow hardness (0.20 - 0.22), frequency (6.5 - 8.0 Hz) and rms ($\sim$ 2 - 3%) range. The frequency at which they are found is always very close to the frequency of the last type-C QPOs observed before the transition to the SIMS. We observed type-A QPO only during the softening phase (i.e. along the upper horizontal branch in HID). The lack of this type of QPO during the hardening phase can however be ascribed to the lower statistics, as the feature is weak and broad. This is the QPO type that is found to be associated to the lowest total fractional rms in our sample. In a frequency versus power-law-flux plot, type-A QPOs appear to be grouped close to the high-frequency end of the tracks defined by the type-C QPOs and are found around the same frequency of the type-C QPOs observed close to the transition to the SIMS.

Type-B QPO: its presence defines the SIMS. The frequency range where it is observed is 0.8 - 6.4 Hz. In addition, all type-B QPOs are observed at lower frequencies with respect to the type-C QPOs observed just before the transition to the SIMS. As for type-C QPOs, these oscillations are seen in both the softening and hardening outburst phase. Total fractional rms and hardness values are lower than in the case of type-C, but higher than for type-A QPOs, ranging in the intervals 5 - 10% and 0.2 - 0.3 respectively. It is noticeable that between 5 and 10% broad band total fractional rms only type-B QPOs are observed (see

Muñoz-Darias et al. 2011). This type of QPO follows a sharp frequency-flux correlation for both disk and powerlaw flux (Fig. 5.5 and 5.8).

From Fig. 5.5 one can see that type-B QPOs follow a clearly different path compared to the other classes, suggesting the presence of an intrinsic difference.

It is interesting to compare some of the properties reported here for GX 339-4 with those observed in other sources. McClintock et al. 2009 performed a detailed spectral analysis and a supporting timing analysis on the BHC H1743-322 and compared their results with the BHC XTE J1550-564, while Sobczak et al. (2000) compared the properties of XTE J1550-564 with GRO J1655-40. These three sources showed a behavior similar to GX 339-4 in the frequency-disk flux plane, spanning a larger flux range. Sobczak et al. (2000) also investigated the relations between frequency and powerlaw flux, finding opposite relations for GRO J1655-40 and XTE J1550-564. The frequency/powerlaw-flux correlation in GX 339-4 is similar to that of GRO J1655-40, but the frequency range covered by the two sources do not overlap, making impossible a direct comparison.

The relation between QPO frequency and power-law photon index is the same for GX 339-4 and H1743-322, XTE J1550-564 and GRO J1655-40 (Sobczak et al. 2000; McClintock et al. 2009), following the original correlation observed by Vignarca et al. (2003). As for the frequency-total rms plane, which was originally presented for XTE J1859+226 (Casella et al. (2005)), the same relation is present also in H1743-322 and XTE J1550-564 (McClintock et al. 2009).

5.4.1 Similarities and differences: a common origin for QPO-types?

The different types of QPOs often show similar/compatible properties (eg. centroid frequency range, QPO profile, quality factor values), some of which suggest that there could be a common origin for the different classes. However, there are systematic differences that cannot be ignored.

As is clear from Fig. 5.4, a stringent relation between the total (0.1 - 64 Hz) fractional rms values and QPO-type exists and the different types of QPOs correspond to different and well separated rms ranges (see Casella et al. 2004 and Muñoz-Darias et al. 2011). At the same frequency two or sometimes even three different types of QPOs can be seen (not simultaneously) depending on the variability level at which the system is observed.

Despite the clear separation in rms, type-C and type-A QPOs follow a similar hard-flux/frequency relation. In addition, type-A QPOs and the type-C QPOs observed just before the HIMS/SIMS transition show very similar frequencies (see 5.4

and Tab. 5.3), while type-B QPOs are systematically found at lower frequencies. Unfortunately type-A QPOs constitute only a small part of our entire sample of QPOs (8 out of 117), therefore it is not possible to completely exclude a bias in the frequency association due to the small number of detections.

It is clear that Type-A and -C QPOs are significantly different timing features, in particular for what concerns the broad band noise associated to the two types of oscillations (strong broad band noise in the case of type-C QPOs and weak power-law or weak peaked noise in the case of type-A QPOs). However, this is not enough to rule out the possibility that type-A and type-C QPOs share a common physical origin.

Here we discuss the evolution of the LFQPOs in the framework of the model proposed by Done et al. (2007), that also suggest possible explanation of the simultaneous spectral transition seen during an outburst. In the geometry that these authors assume, the outer accretion flow takes the form of a cool, geometrically thin, optically thick accretion disk truncated at some radius, which is larger than the last stable orbit (in the HIMS). The inner accretion flow, instead, forms a hot, geometrically thick, optically thin configuration. The inward movement of the truncation radius with increasing mass accretion rates within the hard states gives a physical basis for the hard-soft transition when the disk finally reaches the last stable orbit. The inner disk radius evolution gives also a possible origin for the LFQPOs and to the associated noise observed in the power density spectra. In this scenario LFQPOs (and in particular type-C QPOs) arise from the vertical Lense-Thirring precession (Stella & Vietri 1998) of the misaligned inner hot flow, while the broad band noise arises from propagation of Magneto Rotational Instability (MRI, Balbus & Hawley 1991[9]) fluctuations of the same hot flow (see Ingram et al. 2009, Ingram & Done 2010, Ingram & Done 2011 for details)[10]. The QPO frequency depends on the truncation radius and also on the optical depth of the inner hot flow that produces them, as well on the inclination of the system (see also Homan et al. 2005) and to the optical depth of the precessing inner hot flow. In this scenario, the fact that type-A QPOs and the type-C QPOs observed close to the transition are seen at the same frequency, suggest either that they are produced in a region at similar radii or in a medium at the same physical conditions (i.e. same optical depth). This second possibility is supported by the clear difference in broad-band noise level in the PDS, that is thought to be related to MRI. The type-C QPO width sets the typical timescale for the QPO signal to remain coherent. Since the QPO is not always present in the light curve, there also exists an excitation timescale responsible for the QPO appearance (Lachowicz & Done 2010).

[9]Notice that MRI is not able to produce the jets observed during the hards states, therefore a different/additional mechanism must be also at work during the hard state. This is also valid during the transition to the SIMS where relativistic ejections can be observed.

[10]For alternative models on the origin of LFQPOs see e.g. Wagoner et al. (2001), [11], Titarchuk & Osherovich (1999), Tagger & Pellat 1999.

The QPO can be broadened if the excitation timescale becomes shorter than the QPO timescale, as the excitation presumably interrupts the coherent QPO light curve by phase randomizing it. In the framework set by the global Lense-Thirring precession of the hot flow model (Fragile et al. 2007; Ingram et al. 2009; Ingram & Done 2011) the QPO could be triggered by turbulence, resulting in a vertical kick applied by the bending waves propagating in the outer accretion flow to the precessing inner hot flow at random phase. If more than one kick occur within the QPO timescale, the QPO coherent light curve is interrupted by a random phase shift. As a result, the type-C QPO would evolve in a broader and fainter feature (Chris Done, private communication). Thus, type-A and -C QPOs could be the result of the same physical process, i.e. Lense-Thirring precession. However, given the undeniable link between the type-A QPOs and very weak noise, it remains a fact that whatever the process that broadens and weakens the QPOs, should be also responsible for the collapse of the noise.

5.4.2 The peculiar case of the type-B QPO

Type-B QPOs show properties that differentiate them from the other two classes. Analyzing the frequency-hard flux relation and the frequency-rms relation, it is evident that there is a clear discontinuity within the pattern defined by type-B QPOs and other types of QPOs. While all the QPO frequencies seem to correlate with the soft flux, only type-B QPOs show a sharp correlations with the hard flux. This is remarkable because when type-B and type-A/-C QPOs are seen at similar hardness (type-C QPOs observed just before the transition and all type-A QPOs), there are no differences in the spectral shape, as one might deduce from the HID, but only in flux (see below). In addition, type-B QPOs are systematically found at lower frequencies with respect to the last type-C QPOs and type-A QPOs (see 5.4 and 5.5).

Type-B QPOs can be transient (i.e appear/disappear in few seconds and are observable only for short periods, see also Takizawa et al. 1997) and vary significantly around their centroid frequency, with a characteristic time scale of $\sim$10s (see Nespoli et al. 2003). Also type-C QPOs can appear and disappear in few seconds, but they remain observable for long periods and can be easily followed in their frequency evolution during the hard-to-soft or soft-to-hard transition. Because of its intrinsic faintness, type-A QPOs cannot be followed as can be done for type-B and -C QPOs, (see Nespoli et al. 2003).

A noticeable peculiarity of type-B QPOs is the association to flux peaks. This is particularly evident for a direct switch from or to a type-B QPO (see Sec. 5.3.5). The association of type-B QPOs with increases in the count rate can be seen both in the total light curve (i.e. peaks in the count rate observed in the total light curve of the source, see also Fender et al. 2009) and on shorter timescales (i.e. when sudden increases in count rate take place during a single RXTE pointing). Under the assump-

tion that the count rate tracks the accretion rate, type-B QPOs would be related to increases of the local accretion rate. Alternatively, the increase in the count rate associated to those QPOs could be related to the presence of a jet component that would contribute to the hard emission. A third possibility is that type-B QPOs might occur simultaneously to sudden changes in the geometry or radiative efficiency, which would possibly cause variations in the relative contribution of the emitting component to the spectrum and in the flux.

Starting from the *precession model* and following a reasoning similar to that described above, we argue that type-B QPOs are either produced in a different region located at larger radii (with respect to the region where the type-C QPOs close to the transition and type-A QPOs might originate, to match the lower frequencies observed) or coming from a modulation operated by a medium with different physical properties. In the first case, it is necessary to find a process different from the vertical Lense-Thirring precession, that would be able to produce modulations at larger radii. This hypothesis is supported by the fact that when fast switches from/to type-A/-B QPOs are observed, the type-A QPOs is consistent with being still present when the type-B QPOs appears (see also Nespoli et al. 2003). This is also valid for type-A and -B detected in separated observations. Such a property suggests that two different, eventually simultaneous mechanisms, might be responsible of the production of type-C/A QPOs and type-B QPOs. For the second case, a process able to trigger fast transitions in the physical properties of the plasma would be needed. This hypothesis is supported, as for type-A QPOs, by the fact that the transition to type-B QPOs is associated to the significant difference in the PDS broad band noise level. There is also a third possibility: type-B QPOs could be produced in the same region where type-C QPOs come from, but thanks to a different pecession mode. In the *precession model* the QPO arises from the surface density-weighed Lense-Thirring-precession over the inner hot flow. A sudden change in the surface density profile - for example due to a jet ejection from the very inner regions of the accretion flow - would result in a different weighing and also a different precession frequency.

5.5 Conclusions

The large amount of RXTE observations of GX 339-4 in the past eight years allowed us to analyze the spectral and temporal behavior of the source over four outbursts. We considered all the observations where a low frequency oscillation was observed and performed a complete spectral and timing analysis. Almost all the oscillations observed in the PDS could be classified following the ABC classification and the three types of QPOs display different dependences on the spectral and timing parameters, further strengthening their intrinsic differences.

We conclude that type-B QPOs show properties that clearly differentiate them from

other types of QPOs. Their frequencies clearly correlate with the powerlaw flux, tracing a complete different pattern with the respect to type-A and -C QPOs. Type-B QPOs follow a different behavior also in a rms vs rms plane. In addition, they show a peculiar association to increases in count rate that could reflect changes in accretion rate and/or geometry in the system.

All the types of QPOs can be explained through the *precession model* (Ingram et al. 2009, Ingram & Done 2010, Ingram & Done 2011) as the result of the vertical Lense-Thirring precession of a optical translucent inner hot flow in a truncated disk geometry. However, the characteristic properties of type-B QPOs suggest that they could be the effect of a physical phenomenon different from the Lense-Thirring precession and possibly somehow related to the transition/jet ejection mechanism.

Acknowledgments

SM acknowledges Chris Done for hospitality during her visit at University of Durham and for useful discussions that led to significant improvement of this work and the referee Jerome Rodriguez for useful comments and suggestions. SM and TB acknowledge support from grant ASI-INAF I/009/10/. TMD acknowledges Univeristy of Amsterdam and Southampton for hospitality during his visits. The research leading to these results has received funding from PRIN INAF 2007 and from the European Community's Seventh Framework Programme (FP7/2007-2013) under grant agreement number ITN 215212 "Black Hole Universe". PC acknowledges support from a EU Marie Curie Intra-European Fellowship within the 7th European Community Framework Programme, under contract no. 2009-237722. This work has been partially funded by the Spanish MEC under the Consolider-Ingenio 2010 Program grant CSD2006–00070: First Science with the GTC (http://www.iac.es/consolider-ingenio-gtc/).

Table 5.3: Power-spectral classification and variability parameters. Only observations with evidence of low frequency QPOs are listed.

#	Obs. ID	MJD	Outburst	Hardness	Tot frac. rms	QPO Frequency	QPO type	State
1	70109-01-07-00b	52411.601	2002	0.228 ± 0.001	7.9 ± 0.1	5.8 ± 0.1	B	SIMS
2	70110-01-14-00	52416.596	2002	0.252 ± 0.001	9.2 ± 0.1	6.4 ± 0.1	B	SIMS
3	70110-01-15-00	52419.238	2002	0.251 ± 0.001	9.0 ± 0.1	5.7 ± 0.03	B	SIMS
4	70108-03-02-00b	52419.432	2002	0.209 ± 0.001	9.3 ± 0.2	5.6 ± 0.1	B	SIMS
5	70110-01-47-00b	52532.749	2002	0.222 ± 0.001	7.2 ± 0.2	6.2 ± 0.1	B	SIMS
6	70110-01-89-00	52707.915	2002	0.256 ± 0.004	9.7 ± 0.7	0.9 ± 0.05	B	SIMS
7	90110-02-01-03	53232.993	2004	0.257 ± 0.001	9.4 ± 0.2	4.1 ± 0.04	B	SIMS
8	90704-01-02-00	53233.389	2004	0.271 ± 0.001	9.1 ± 0.2	4.4 ± 0.2	B	SIMS
9	60705-01-84-02	53333.899	2004	0.254 ± 0.001	8.8 ± 0.1	5.2 ± 0.1	B	SIMS
10	91105-04-10-00	53466.753	2004	0.293 ± 0.003	12.8 ± 0.7	3.4 ± 0.1	B?	SIMS
11	92035-01-04-00	54147.011	2007	0.262 ± 0.001	8.4 ± 0.1	6.7 ± 0.2	B	SIMS
12	92085-01-03-01	54162.665	2007	0.259 ± 0.001	8.6 ± 0.1	6.4 ± 0.1	B	SIMS
13	92704-03-10-00	54231.604	2007	0.264 ± 0.002	6 ± 1	1.0 ± 0.1	B	SIMS
14	92704-03-10-11	54232.658	2007	0.276 ± 0.002	10.0 ± 0.5	1.7 ± 0.1	B	SIMS
15	92704-03-10-12	54233.565	2007	0.335 ± 0.002	13.7 ± 0.4	1.8 ± 0.2	B?	SIMS
16	95409-01-15-02	55304.714	2010	0.256 ± 0.001	8.3 ± 0.2	5.6 ± 0.1	B	SIMS
17	95409-01-15-06	55308.983	2010	0.236 ± 0.001	6.7 ± 0.1	5.9 ± 0.2	B	SIMS
18	95409-01-16-05	55315.695	2010	0.262 ± 0.001	9.3 ± 0.1	6.1 ± 0.2	B	SIMS
19	95409-01-17-00	55316.114	2010	0.262 ± 0.001	9.3 ± 0.1	5.9 ± 0.1	B	SIMS
20	95409-01-17-05	55321.718	2010	0.243 ± 0.001	7.5 ± 0.1	5.3 ± 0.1	B	SIMS
21	95409-01-17-06	55322.230	2010	0.238 ± 0.001	7.5 ± 0.2	5.2 ± 0.1	B	SIMS
22	95409-01-18-00	55323.210	2010	0.259 ± 0.001	8.6 ± 0.1	5.5 ± 0.1	B	SIMS

Continued on next page

Table 5.3 – continued from previous page

#	Obs. ID	MJD	Outburst	Hardness	Tot frac. rms	QPO Frequency	QPO type	State
23	95335-01-01-07	55324.189	2010	0.255 ± 0.001	8.7 ± 0.2	5.3 ± 0.04	B	SIMS
24	95335-01-01-00	55324.254	2010	0.247 ± 0.001	8.5 ± 0.1	5.3 ± 0.03	B	SIMS
25	95335-01-01-01	55324.393	2010	0.240 ± 0.001	7.4 ± 0.1	5.1 ± 0.02	B	SIMS
26	95335-01-01-05	55326.175	2010	0.228 ± 0.001	7.1 ± 0.2	4.9 ± 0.03	B	SIMS
27	95335-01-01-06	55326.280	2010	0.223 ± 0.001	6.3 ± 0.2	4.9 ± 0.03	B	SIMS
28	95409-01-18-04	55327.041	2010	0.235 ± 0.002	8.5 ± 0.4	4.8 ± 0.1	B	SIMS
29	95409-01-18-05	55327.262	2010	0.234 ± 0.001	7.8 ± 0.3	4.9 ± 0.04	B	SIMS
30	95409-01-19-00	55330.300	2010	0.223 ± 0.001	6.5 ± 0.6	4.7 ± 0.05	B	SIMS
31	96409-01-04-04	55585.947	2010	0.282 ± 0.003	10.0 ± 0.6	2.0 ± 0.1	B	SIMS
32	96409-01-04-05	55586.896	2010	0.269 ± 0.004	9 ± 2	0.9 ± 0.1	B	SIMS
33	96409-01-05-01	55591.615	2010	0.292 ± 0.003	10 ± 1	1.7 ± 0.1	B	SIMS
34	96409-01-05-02	55593.502	2010	0.299 ± 0.003	8 ± 3	1.8 ± 0.1	B	SIMS
35	70109-01-07-00a	52411.601	2002	0.213 ± 0.001	2.6 ± 0.1	7.0 ± 0.5	A	SIMS
36	70108-03-02-00a	52419.432	2002	0.214 ± 0.001	2.8 ± 0.2	6.7 ± 0.5	A	SIMS
37	70108-03-02-00a2	52419.432	2002	0.210 ± 0.001	2.8 ± 0.2	6.8 ± 0.4	A	SIMS
38	70110-01-45-00	52524.948	2002	0.222 ± 0.001	2.2 ± 0.2	7.2 ± 0.6	A	SIMS
39	70109-01-23-00	52529.580	2002	0.209 ± 0.001	2.9 ± 0.2	7.4 ± 1.3	A	SIMS
40	70109-01-24-00	52536.358	2002	0.204 ± 0.001	2.4 ± 0.2	8.0 ± 0.9	A	SIMS
41	92085-01-02-06	54160.896	2007	0.217 ± 0.001	2.6 ± 0.2	7.8 ± 0.7	A	SIMS
42	92085-01-03-04	54165.527	2007	0.210 ± 0.001	2.7 ± 0.1	7.7 ± 0.7	A	SIMS
43	40031-03-02-05	52388.054	2002	0.766 ± 0.003	29.8 ± 0.3	0.20 ± 0.01	C	LHS
44	70109-01-05-01G	52391.318	2002	0.763 ± 0.003	29.7 ± 0.2	0.22 ± 0.02	C	HIMS
45	70109-01-06-00	52400.83	2002	0.697 ± 0.002	22.2 ± 0.1	1.26 ± 0.01	C	HIMS
46	70108-03-01-00	52400.853	2002	0.694 ± 0.002	22.0 ± 0.1	1.30 ± 0.01	C	HIMS

Continued on next page

Table 5.3 – continued from previous page

#	Obs. ID	MJD	Outburst	Hardness	Tot frac. rms	QPO Frequency	QPO type	State
47	70110-01-10-00	52402.492	2002	0.562 ± 0.002	20.1 ± 0.1	4.20 ± 0.08	C	HIMS
48	70109-04-01-00	52405.58	2002	0.354 ± 0.001	15.45 ± 0.04	5.46 ± 0.01	C	HIMS
49	70109-04-01-01	52405.713	2002	0.356 ± 0.001	15.44 ± 0.02	5.45 ± 0.01	C	HIMS
50	70109-04-01-02	52406.07	2002	0.360 ± 0.001	15.6 ± 0.1	5.34 ± 0.02	C	HIMS
51	70110-01-11-00	52406.701	2002	0.342 ± 0.001	15.0 ± 0.1	5.82 ± 0.02	C	HIMS
52	70110-01-12-00	52410.528	2002	0.266 ± 0.001	11.5 ± 0.1	8.1 ± 0.2	C	HIMS
53	70109-01-37-00	52694.922	2002	0.237 ± 0.002	10.7 ± 0.4	8.6 ± 0.2	C	HIMS
54	70128-02-02-00	52696.355	2002	0.272 ± 0.001	12.1 ± 0.1	8.02 ± 0.04	C	HIMS
55	50117-01-03-01	52706.767	2002	0.364 ± 0.003	19.2 ± 0.3	6.7 ± 0.1	C	HIMS
56	50117-01-03-00	52706.84	2002	0.363 ± 0.002	18.7 ± 0.2	6.77 ± 0.02	C	HIMS
57	70109-02-01-00	52709.859	2002	0.293 ± 0.002	14.2 ± 0.2	8.0 ± 0.1	C	HIMS
58	70109-02-01-01	52709.991	2002	0.289 ± 0.002	14.3 ± 0.4	8.1 ± 0.1	C	HIMS
59	60705-01-56-00	52710.715	2002	0.306 ± 0.003	15.1 ± 0.4	7.8 ± 0.1	C	HIMS
60	70110-01-94-00	52724.226	2002	0.395 ± 0.004	18.2 ± 0.4	6.1 ± 0.1	C	HIMS
61	70110-01-95-00	52727.252	2002	0.480 ± 0.005	22.8 ± 0.5	4.7 ± 0.1	C	HIMS
62	60705-01-59-00	52731.562	2002	0.586 ± 0.003	25.2 ± 0.2	2.9 ± 0.1	C	HIMS
63	60705-01-68-00	53218.11	2004	0.763 ± 0.005	30.8 ± 0.3	0.5 ± 0.0	C	LHS
64	60705-01-68-01	53222.24	2004	0.728 ± 0.004	26.9 ± 0.2	1.03 ± 0.04	C	HIMS
65	60705-01-69-00	53225.40	2004	0.714 ± 0.003	24.9 ± 0.2	1.3 ± 0.0	C	HIMS
66	90704-01-01-00	53226.43	2004	0.705 ± 0.003	24.9 ± 0.1	2.0 ± 0.1	C	HIMS
67	60705-01-69-01	53228.99	2004	0.646 ± 0.003	23.7 ± 0.2	2.9 ± 0.2	C	HIMS
68	60705-01-70-00	53230.96	2004	0.437 ± 0.002	18.3 ± 0.2	4.3 ± 0.1	C	HIMS
69	90110-02-01-02	53232.34	2004	0.386 ± 0.002	17.5 ± 0.1	5.2 ± 0.1	C	HIMS
70	90110-02-01-00	53232.40	2004	0.361 ± 0.001	16.35 ± 0.04	5.8 ± 0.1	C	HIMS

Continued on next page

Table 5.3 – continued from previous page

#	Obs. ID	MJD	Outburst	Hardness	Tot frac. rms	QPO Frequency	QPO type	State
71	90704-01-11-00	53472.33	2004	0.584 ± 0.004	24.9 ± 0.3	2.7 ± 0.1	C	HIMS
72	92035-01-02-01	54133.922	2007	0.771 ± 0.003	30.8 ± 0.2	0.28 ± 0.01	C	LHS
73	92035-01-02-02	54135.033	2007	0.771 ± 0.003	30.8 ± 0.2	0.30 ± 0.01	C	LHS
74	92035-01-02-03	54136.015	2007	0.766 ± 0.003	30.1 ± 0.2	0.37 ± 0.01	C	LHS
75	92035-01-02-04	54136.997	2007	0.759 ± 0.003	29.8 ± 0.2	0.43 ± 0.01	C	LHS
76	92035-01-02-08	54137.851	2007	0.748 ± 0.003	27.5 ± 0.3	0.55 ± 0.02	C	HIMS
77	92035-01-02-07	54138.83	2007	0.731 ± 0.002	25.8 ± 0.2	0.90 ± 0.01	C	HIMS
78	92035-01-02-06	54139.942	2007	0.686 ± 0.002	22.4 ± 0.1	0.99 ± 0.01	C	HIMS
79	92035-01-03-00	54140.204	2007	0.670 ± 0.002	21.7 ± 0.1	1.13 ± 0.01	C	HIMS
80	92035-01-03-01	54141.055	2007	0.621 ± 0.002	20.7 ± 0.1	1.68 ± 0.01	C	HIMS
81	92035-01-03-02	54142.036	2007	0.547 ± 0.002	19.6 ± 0.1	2.45 ± 0.01	C	HIMS
82	92035-01-03-03	54143.019	2007	0.461 ± 0.002	18.3 ± 0.1	3.52 ± 0.01	C	HIMS
83	92428-01-04-00	54143.870	2007	0.411 ± 0.001	17.1 ± 0.1	4.34 ± 0.02	C	HIMS
84	92428-01-04-01	54143.951	2007	0.419 ± 0.001	17.2 ± 0.1	4.23 ± 0.02	C	HIMS
85	92428-01-04-02	54144.086	2007	0.424 ± 0.002	17.4 ± 0.1	4.13 ± 0.03	C	HIMS
86	92428-01-04-03	54144.871	2007	0.380 ± 0.001	16.4 ± 0.1	4.99 ± 0.03	C	HIMS
87	92035-01-03-05	54145.114	2007	0.343 ± 0.001	14.9 ± 0.1	5.80 ± 0.03	C	HIMS
88	92085-01-03-00	54161.669	2007	0.295 ± 0.001	12.9 ± 0.1	7.1 ± 0.1	C	HIMS
89	92085-01-03-02	54163.698	2007	0.288 ± 0.001	12.5 ± 0.1	7.3 ± 0.2	C	HIMS
90	92085-01-03-03	54164.557	2007	0.296 ± 0.001	12.4 ± 0.1	7.0 ± 0.2	C	HIMS
91	92704-03-11-00	54234.839	2007	0.493 ± 0.004	21.3 ± 0.4	4.0 ± 0.1	C	HIMS
92	92704-03-11-01	54235.791	2007	0.549 ± 0.005	22.1 ± 0.4	3.3 ± 0.1	C	HIMS
93	92704-04-01-01	54236.446	2007	0.577 ± 0.004	22.8 ± 0.6	3.0 ± 0.2	C	HIMS
94	92704-04-01-02	54236.513	2007	0.587 ± 0.004	24.8 ± 0.4	2.7 ± 0.1	C	HIMS

Continued on next page

Table 5.3 – continued from previous page

#	Obs. ID	MJD	Outburst	Hardness	Tot frac. rms	QPO Frequency	QPO type	State
95	92704-03-12-00	54236.591	2007	0.598 ± 0.005	25.5 ± 1.1	2.7 ± 0.4	C	HIMS
96	92704-04-01-04	54237.356	2007	0.593 ± 0.004	25.2 ± 0.5	2.8 ± 0.1	C	HIMS
97	92704-04-01-05	54237.421	2007	0.584 ± 0.004	24.5 ± 0.4	3.1 ± 0.3	C	HIMS
98	92704-03-12-01	54237.488	2007	0.596 ± 0.004	24.8 ± 0.3	2.7 ± 0.1	C	HIMS
99	95409-01-12-04	55286.727	2010	0.787 ± 0.003	32.4 ± 0.4	0.22 ± 0.01	C	LHS
100	95409-01-13-03	55288.367	2010	0.783 ± 0.003	31.5 ± 0.3	0.2 ± 0.1	C	LHS
101	95409-01-13-00	55289.618	2010	0.777 ± 0.003	31.0 ± 0.3	0.26 ± 0.01	C	LHS
102	95409-01-13-04	55290.722	2010	0.781 ± 0.003	31.7 ± 0.2	0.29 ± 0.01	C	LHS
103	95409-01-13-02	55291.649	2010	0.775 ± 0.003	31.6 ± 0.3	0.32 ± 0.01	C	LHS
104	95409-01-13-05	55292.779	2010	0.777 ± 0.003	30.9 ± 0.4	0.38 ± 0.02	C	LHS
105	95409-01-13-01	55293.088	2010	0.772 ± 0.003	30.6 ± 0.4	0.38 ± 0.05	C	LHS
106	95409-01-13-06	55294.124	2010	0.770 ± 0.003	30.1 ± 0.4	0.47 ± 0.02	C	LHS
107	95409-01-14-01	55296.248	2010	0.734 ± 0.003	26.7 ± 0.3	1.04 ± 0.01	C	HIMS
108	95409-01-14-02	55297.87	2010	0.672 ± 0.002	21.9 ± 0.1	1.25 ± 0.01	C	HIMS
109	95409-01-14-03	55298.70	2010	0.648 ± 0.003	21.6 ± 0.2	1.59 ± 0.01	C	HIMS
110	95409-01-14-06	55299.766	2010	0.564 ± 0.002	20.0 ± 0.1	2.43 ± 0.01	C	HIMS
111	95409-01-14-04	55300.336	2010	0.563 ± 0.002	20.0 ± 0.2	2.38 ± 0.01	C	HIMS
112	95409-01-14-07	55300.923	2010	0.515 ± 0.002	19.4 ± 0.1	2.92 ± 0.0	C	HIMS
113	95409-01-14-05	55301.789	2010	0.454 ± 0.002	17.7 ± 0.2	3.64 ± 0.02	C	HIMS
114	95409-01-15-00	55302.196	2010	0.425 ± 0.002	17.5 ± 0.2	4.15 ± 0.03	C	HIMS
115	95409-01-15-01	55303.604	2010	0.346 ± 0.001	14.6 ± 0.1	5.65 ± 0.04	C	HIMS
116	95409-01-17-02	55318.441	2010	0.308 ± 0.001	13.7 ± 0.1	6.67 ± 0.19	C	HIMS
117	96409-01-06-01	55598.700	2010	0.491 ± 0.004	26.7 ± 1.5	4.52 ± 0.30	C	HIMS

Table 5.4: Columns are: observation number, reduced χ^2,inner disc temperature (kT), inner disc radius R (assuming a distance of 10 kpc and an inclination of 30 ^{o}), photon index Γ, fold Energy E_{fold} (corresponding to high energy cutoff), total flux, hard flux and disk flux calculated in the 2 - 20 keV band and expressed in units of Crab flux, instrument used. P = PCA and H = HEXTE. Lines marked with (*) correspond to the observations where HEXTE/Cluster A spectrum was used.

#	red. χ^2	$T_{Innradius}$	R^{Inn}_{Disk}	Γ	E_{fold}	F_{tot}/F_{Crab}	F_{hard}/F_{Crab}	F_{disk}/F_{Crab}	Inst.
1	0.92	$0.94^{+0.02}_{-0.04}$	43^{+3}_{-2}	$2.6^{+0.1}_{-0.1}$	-	0.501	0.063	0.321	P+H
2	1.01	$0.93^{+0.04}_{-0.04}$	41^{+5}_{-4}	$2.6^{+0.2}_{-0.1}$	-	0.462	0.070	0.270	P+H
3	1.11	$0.93^{+0.05}_{-0.04}$	38^{+5}_{-4}	$2.8^{+0.2}_{-0.2}$	-	0.434	0.066	0.235	P+H
4	0.81	$0.90^{+0.04}_{-0.03}$	43^{+6}_{-4}	$2.6^{+0.2}_{-0.1}$	-	0.395	0.048	0.259	P+H
5	0.96	$0.91^{+0.04}_{-0.03}$	45^{+4}_{-4}	$3.0^{+0.2}_{-0.2}$	-	0.494	0.060	0.297	P+H
6	0.81	$0.61^{+0.06}_{-0.15}$	33^{+31}_{-7}	$3.8^{+0.2}_{-0.3}$	-	0.027	0.004	0.016	P+H
7	0.85	$0.80^{+0.06}_{-0.03}$	37^{+4}_{-6}	$2.7^{+0.2}_{-0.4}$	-	0.178	0.027	0.104	P+H
8	0.84	$0.85^{+0.04}_{-0.03}$	31^{+3}_{-3}	$2.6^{+0.1}_{-0.1}$	-	0.175	0.029	0.099	P+H
9	1.07	$0.90^{+0.05}_{-0.03}$	38^{+3}_{-4}	$2.5^{+0.1}_{-0.1}$	-	0.314	0.047	0.195	P+H
10	0.93	$0.81^{+0.11}_{-0.07}$	19^{+5}_{-4}	$2.4^{+0.4}_{-0.4}$	-	0.056	0.011	0.030	P+H
11	0.92	$0.93^{+0.04}_{-0.02}$	46^{+3}_{-4}	$2.7^{+0.1}_{-0.03}$	-	0.653	0.099	0.367	P+H
12	1.08	$0.92^{+0.03}_{-0.03}$	44^{+4}_{-3}	$2.7^{+0.1}_{-0.1}$	-	0.536	0.080	0.307	P+H
13	0.89	$0.76^{+0.05}_{-0.04}$	25^{+4}_{-4}	$2.2^{+0.3}_{-0.3}$	-	0.054	0.008	0.035	P+H
14	0.99	$0.78^{+0.04}_{-0.05}$	22^{+5}_{-3}	$2.1^{+0.3}_{-0.2}$	-	0.053	0.009	0.033	P+H
15	1.04	$0.8^{+0.1}_{-0.1}$	16^{+3}_{-3}	$2.1^{+0.3}_{-0.2}$	-	0.046	0.010	0.025	P+H
16	1.26	$0.96^{+0.03}_{-0.04}$	40^{+4}_{-3}	$2.4^{+0.04}_{-0.04}$	-	0.496	0.071	0.318	P+H *
17	1.18	$0.90^{+0.02}_{-0.03}$	48^{+4}_{-3}	$2.5^{+0.1}_{-0.05}$	-	0.492	0.062	0.329	P+H *
18	1.00	$0.94^{+0.03}_{-0.04}$	38^{+4}_{-3}	$2.5^{+0.1}_{-0.1}$	-	0.438	0.068	0.261	P+H *
19	1.25	$0.91^{+0.04}_{-0.02}$	43^{+3}_{-4}	$2.3^{+0.1}_{-0.04}$	-	0.432	0.064	0.275	P+H *

Continued on next page

Table 5.4 – continued from previous page

#	red. χ^2	$T_{Innradius}$	R_{Disk}^{Inn}	Γ	E_{fold}	F_{tot}/F_{Crab}	F_{hard}/F_{Crab}	F_{disk}/F_{Crab}	Inst.
20	1.23	$0.93^{+0.04}_{-0.03}$	39^{+3}_{-4}	$2.4^{+0.1}_{-0.1}$	-	0.382	0.052	0.252	P+H *
21	1.54	$0.89^{+0.04}_{-0.04}$	44^{+4}_{-5}	$2.36^{+0.04}_{-0.04}$	-	0.383	0.049	0.263	P+H *
22	1.74	$0.93^{+0.04}_{-0.03}$	38^{+4}_{-4}	$2.38^{+0.04}_{-0.04}$	-	0.384	0.057	0.242	P+H *
23	1.07	$0.89^{+0.03}_{-0.03}$	41^{+5}_{-4}	$2.7^{+0.4}_{-0.4}$	-	0.391	0.056	0.225	P+H *
24	1.07	$0.87^{+0.04}_{-0.01}$	43^{+4}_{-4}	$2.7^{+0.2}_{-0.2}$	-	0.385	0.054	0.226	P+H *
25	1.12	$0.86^{+0.04}_{-0.03}$	45^{+3}_{-4}	$2.7^{+0.2}_{-0.2}$	-	0.380	0.051	0.231	P+H *
26	1.03	$0.84^{+0.04}_{-0.03}$	47^{+5}_{-5}	$2.9^{+0.2}_{-0.4}$	-	0.371	0.046	0.219	P+H *
27	1.28	$0.85^{+0.04}_{-0.03}$	46^{+5}_{-5}	$2.7^{+0.3}_{-0.3}$	-	0.357	0.043	0.230	P+H *
28	1.26	$0.89^{+0.05}_{-0.04}$	41^{+5}_{-5}	$2.3^{+0.1}_{-0.1}$	-	0.327	0.042	0.230	P+H *
29	1.50	$0.90^{+0.05}_{-0.05}$	40^{+7}_{-4}	$2.4^{+0.1}_{-0.03}$	-	0.342	0.045	0.232	P+H *
30	1.21	$0.86^{+0.04}_{-0.03}$	46^{+5}_{-4}	$2.4^{+0.1}_{-0.1}$	-	0.330	0.039	0.232	P+H *
31	1.27	$0.71^{+0.06}_{-0.06}$	31^{+14}_{-6}	$2.0^{+0.2}_{-0.1}$	-	0.055	0.009	0.038	P+H *
32	1.78	$0.94^{+0.14}_{-0.03}$	13^{+2}_{-3}	$1.4^{+0.1}_{-0.1}$	-	0.039	0.006	0.029	P+H *
33	0.94	$0.77^{+0.06}_{-0.07}$	22^{+4}_{-4}	$1.8^{+0.1}_{-0.1}$	-	0.042	0.007	0.028	P+H *
34	1.31	$0.85^{+0.06}_{-0.04}$	15^{+2}_{-2}	$1.8^{+0.1}_{-0.1}$	-	0.035	0.007	0.023	P+H *
35	1.09	$0.94^{+0.02}_{-0.04}$	44^{+6}_{-2}	$2.6^{+0.1}_{-0.1}$	-	0.488	0.055	0.336	P+H
36	1.31	$0.90^{+0.02}_{-0.01}$	44^{+3}_{-3}	$2.6^{+0.1}_{-0.1}$	-	0.394	0.045	0.271	P+H
37	1.31	$0.90^{+0.02}_{-0.02}$	44^{+3}_{-3}	$2.6^{+0.1}_{-0.1}$	-	0.394	0.045	0.271	P+H
38	0.97	$0.95^{+0.04}_{-0.04}$	44^{+5}_{-4}	$2.7^{+0.1}_{-0.2}$	-	0.531	0.065	0.342	P+H
39	0.85	$0.95^{+0.02}_{-0.03}$	43^{+3}_{-2}	$2.6^{+0.1}_{-0.1}$	-	0.480	0.053	0.335	P+H
40	0.89	$0.90^{+0.03}_{-0.02}$	48^{+3}_{-4}	$2.6^{+0.1}_{-0.1}$	-	0.448	0.047	0.311	P+H
41	0.86	$0.90^{+0.04}_{-0.02}$	51^{+2}_{-4}	$2.7^{+0.1}_{-0.1}$	-	0.535	0.060	0.357	P+H
42	1.08	$0.88^{+0.04}_{-0.02}$	49^{+3}_{-4}	$2.8^{+0.1}_{-0.2}$	-	0.461	0.050	0.306	P+H
43	1.19	-	-	$1.74^{+0.02}_{-0.02}$	119^{+8}_{-7}	0.401	0.236	0.000	P+H

Continued on next page

Table 5.4 – continued from previous page

#	red. χ^2	$T_{Innradius}$	R_{Disk}^{Inn}	Γ	E_{fold}	F_{tot}/F_{Crab}	F_{hard}/F_{Crab}	F_{disk}/F_{Crab}	Inst.
44	0.88	-	-	$1.78^{+0.02}_{-0.02}$	133^{+10}_{-9}	0.407	0.238	0.000	P+H
45	0.91	-	-	$1.96^{+0.02}_{-0.02}$	122^{+11}_{-10}	0.430	0.230	0.000	P+H
46	1.50	-	-	$1.98^{+0.02}_{-0.02}$	129^{+9}_{-8}	0.428	0.227	0.000	P+H
47	0.84	-	-	$2.45^{+0.03}_{-0.03}$	-	0.410	0.173	0.000	P+H
48	0.80	$1.01^{+0.05}_{-0.05}$	26^{+3}_{-2}	$2.59^{+0.07}_{-0.22}$	-	0.494	0.122	0.164	P+H
49	1.12	$0.99^{+0.04}_{-0.04}$	27^{+3}_{-2}	$2.56^{+0.06}_{-0.15}$	-	0.499	0.123	0.171	P+H
50	0.85	$1.0^{+0.1}_{-0.1}$	24^{+3}_{-4}	$2.7^{+0.1}_{-0.1}$	-	0.471	0.119	0.140	P+H
51	0.84	$1.03^{+0.06}_{-0.06}$	28^{+3}_{-3}	$2.2^{+0.4}_{-0.2}$	-	0.460	0.106	0.215	P+H
52	0.94	$0.94^{+0.04}_{-0.03}$	39^{+4}_{-3}	$2.5^{+0.1}_{-0.2}$	-	0.467	0.078	0.259	P+H
53	0.89	$0.69^{+0.05}_{-0.05}$	30^{+8}_{-5}	$2.4^{+0.6}_{-0.2}$	-	0.046	0.006	0.030	P+H
54	1.36	$0.73^{+0.03}_{-0.03}$	23^{+3}_{-3}	$2.6^{+0.1}_{-0.1}$	-	0.041	0.007	0.022	P+H
55	0.67	$0.9^{+0.1}_{-0.1}$	11^{+6}_{-2}	$2.5^{+0.2}_{-0.4}$	-	0.034	0.009	0.011	P+H
56	1.11	$0.78^{+0.07}_{-0.06}$	15^{+4}_{-3}	$2.5^{+0.2}_{-0.1}$	-	0.035	0.009	0.013	P+H
57	0.97	$0.75^{+0.04}_{-0.04}$	19^{+3}_{-2}	$2.2^{+0.2}_{-0.2}$	-	0.032	0.006	0.019	P+H
58	0.74	$0.7^{+0.1}_{-0.1}$	27^{+8}_{-5}	$2.4^{+0.3}_{-0.4}$	-	0.035	0.006	0.021	P+H
59	1.01	$0.7^{+0.1}_{-0.1}$	21^{+6}_{-6}	$2.8^{+0.4}_{-0.4}$	-	0.026	0.005	0.013	P+H
60	1.29	-	-	$3.2^{+0.1}_{-0.1}$	-	0.035	0.010	0.000	P+H
61	1.03	-	-	$2.9^{+0.1}_{-0.1}$	-	0.034	0.012	0.000	P+H
62	1.17	-	-	$2.48^{+0.03}_{-0.06}$	-	0.033	0.015	0.000	P+H
63	1.02	-	-	$1.83^{+0.03}_{-0.03}$	-	0.102	0.061	0.000	P+H
64	1.15	-	-	$1.98^{+0.03}_{-0.03}$	-	0.126	0.070	0.000	P+H
65	1.20	-	-	$1.97^{+0.03}_{-0.01}$	-	0.132	0.073	0.000	P+H
66	1.40	-	-	$2.01^{+0.03}_{-0.02}$	-	0.136	0.074	0.000	P+H
67	0.90	-	-	$2.23^{+0.03}_{-0.03}$	-	0.134	0.066	0.000	P+H

Continued on next page

Table 5.4 – continued from previous page

#	red. χ^2	$T_{Innradius}$	R_{Disk}^{Inn}	Γ	E_{fold}	F_{tot}/F_{Crab}	F_{hard}/F_{Crab}	F_{disk}/F_{Crab}	Inst.
68	0.94	$1.2^{+0.1}_{-0.1}$	8^{+6}_{-1}	$2.3^{+0.1}_{-0.1}$	-	0.124	0.040	0.038	P+H
69	1.09	$1.17^{+0.09}_{-0.09}$	11^{+2}_{-1}	$1.7^{+0.7}_{-0.1}$	64^{+13}_{-17}	0.127	0.035	0.065	P+H
70	0.88	$1.13^{+0.05}_{-0.08}$	12^{+1}_{-1}	$1.9^{+0.4}_{-0.2}$	102^{+11}_{-38}	0.127	0.033	0.064	P+H
71	1.14	-	-	$2.4^{+0.1}_{-0.1}$	-	0.046	0.021	0.000	P+H
72	1.30	-	-	$1.82^{+0.02}_{-0.02}$	163^{+15}_{-14}	0.367	0.214	0.000	P+H
73	1.19	-	-	$1.80^{+0.02}_{-0.02}$	139^{+11}_{-9}	0.371	0.216	0.000	P+H
74	1.52	-	-	$1.83^{+0.02}_{-0.02}$	146^{+13}_{-10}	0.386	0.222	0.000	P+H
75	1.25	-	-	$1.84^{+0.02}_{-0.02}$	137^{+11}_{-9}	0.413	0.236	0.000	P+H
76	1.17	-	-	$1.86^{+0.02}_{-0.02}$	131^{+16}_{-12}	0.424	0.239	0.000	P+H
77	1.13	-	-	$1.92^{+0.02}_{-0.02}$	140^{+13}_{-11}	0.433	0.238	0.000	P+H
78	1.03	-	-	$2.05^{+0.02}_{-0.02}$	142^{+14}_{-11}	0.434	0.223	0.000	P+H
79	1.05	-	-	$2.09^{+0.02}_{-0.02}$	164^{+19}_{-16}	0.436	0.219	0.000	P+H
80	0.81	-	-	$2.25^{+0.02}_{-0.02}$	-	0.443	0.206	0.000	P+H
81	0.92	-	-	$2.539^{+0.004}_{-0.004}$	-	0.475	0.191	0.000	P+H
82	1.00	$1.0^{+0.0}_{-0.1}$	19^{+6}_{-3}	$2.46^{+0.14}_{-0.22}$	-	0.501	0.166	0.085	P+H
83	1.00	$0.980^{+0.0}_{-0.004}$	$23.4^{+0.2}_{-0.2}$	$2.589^{+0.003}_{-0.003}$	-	0.533	0.154	0.121	P+H
84	0.96	$1.035^{+0.0}_{-0.005}$	$18.8^{+0.2}_{-0.2}$	$2.637^{+0.004}_{-0.004}$	-	0.529	0.157	0.103	P+H
85	0.85	$1.02^{+0.0}_{-0.01}$	$19.0^{+0.2}_{-0.2}$	$2.638^{+0.004}_{-0.004}$	-	0.522	0.157	0.098	P+H
86	0.88	$1.024^{+0.0}_{-0.004}$	$22.6^{+0.2}_{-0.2}$	$2.699^{+0.004}_{-0.004}$	-	0.538	0.141	0.142	P+H
87	1.10	$0.98^{+0.07}_{-0.02}$	30^{+3}_{-4}	$2.63^{+0.05}_{-0.05}$	-	0.554	0.127	0.203	P+H
88	1.05	$0.929^{+0.00}_{-0.002}$	$38.2^{+0.2}_{-0.2}$	$2.532^{+0.003}_{-0.003}$	-	0.488	0.092	0.246	P+H
89	1.26	$0.922^{+0.00}_{-0.002}$	$38.5^{+0.2}_{-0.2}$	$2.525^{+0.003}_{-0.003}$	-	0.462	0.085	0.240	P+H
90	0.97	$0.898^{+0.00}_{-0.002}$	$39.6^{+0.2}_{-0.2}$	$2.641^{+0.003}_{-0.003}$	-	0.465	0.088	0.222	P+H
91	0.98	-	-	$2.88^{+0.02}_{-0.01}$	-	0.048	0.018	0.000	P+H

Continued on next page

Table 5.4 – continued from previous page

#	red. χ^2	$T_{Innradius}$	R_{Disk}^{Inn}	Γ	E_{fold}	F_{tot}/F_{Crab}	F_{hard}/F_{Crab}	F_{disk}/F_{Crab}	Inst.
92	1.32	-	-	$2.53^{+0.02}_{-0.01}$	-	0.046	0.019	0.000	P+H
93	1.23	-	-	$2.46^{+0.01}_{-0.01}$	-	0.045	0.020	0.000	P+H
94	1.28	-	-	$2.45^{+0.01}_{-0.01}$	-	0.045	0.021	0.000	P+H
95	1.30	-	-	$2.38^{+0.02}_{-0.01}$	-	0.045	0.021	0.000	P+H
96	1.16	-	-	$2.45^{+0.01}_{-0.01}$	-	0.045	0.021	0.000	P+H
97	1.25	-	-	$2.52^{+0.01}_{-0.01}$	-	0.044	0.020	0.000	P+H
98	1.97	-	-	$2.45^{+0.06}_{-0.05}$	-	0.043	0.020	0.000	P+H
99	1.47	-	-	$1.81^{+0.02}_{-0.02}$	-	0.285	0.168	0.000	P+H *
100	1.77	-	-	$1.80^{+0.02}_{-0.02}$	-	0.293	0.172	0.000	P+H *
101	1.55	-	-	$1.82^{+0.02}_{-0.03}$	-	0.300	0.175	0.000	P+H *
102	1.86	-	-	$1.82^{+0.03}_{-0.03}$	-	0.307	0.179	0.000	P+H *
103	1.73	-	-	$1.85^{+0.02}_{-0.03}$	-	0.317	0.183	0.000	P+H *
104	1.68	-	-	$1.86^{+0.02}_{-0.04}$	-	0.317	0.183	0.000	P+H *
105	1.24	-	-	$1.81^{+0.03}_{-0.03}$	171.893^{+24}_{-18}	0.335	0.194	0.000	P+H *
106	1.36	-	-	$1.85^{+0.03}_{-0.02}$	-	0.340	0.194	0.000	P+H *
107	1.08	-	-	$1.92^{+0.03}_{-0.04}$	191.624^{+37}_{-31}	0.347	0.190	0.000	P+H *
108	1.25	-	-	$2.10^{+0.03}_{-0.03}$	-	0.367	0.184	0.000	P+H *
109	1.50	-	-	$2.20^{+0.00}_{-0.00}$	-	0.375	0.179	0.000	P+H *
110	1.17	$0.7^{+0.57}_{-0.3}$	39^{+330}_{-10}	$2.29^{+0.09}_{-0.16}$	-	0.405	0.160	0.043	P+H *
111	1.10	$0.8^{+0.5}_{-0.4}$	22^{+188}_{-9}	$2.2^{+0.2}_{-0.2}$	-	0.392	0.158	0.046	P+H *
112	1.55	$0.98^{+0.22}_{-0.07}$	20^{+10}_{-5}	$2.1^{+0.2}_{-0.1}$	153.15^{+150}_{-52}	0.392	0.144	0.083	P+H *
113	1.19	$1.027^{+0.004}_{-0.004}$	$20.9^{+0.2}_{-0.2}$	$2.185^{+0.004}_{-0.004}$	-	0.405	0.129	0.122	P+H *
114	1.19	$0.9^{+0.3}_{-0.1}$	30^{+15}_{-7}	$2.4^{+0.2}_{-0.4}$	-	0.429	0.132	0.137	P+H *
115	1.40	$1.002^{+0.003}_{-0.003}$	$28.9^{+0.1}_{-0.1}$	$2.274^{+0.004}_{-0.004}$	-	0.454	0.100	0.214	P+H *

Continued on next page

Table 5.4 – continued from previous page

#	red. χ^2	$T_{Innradius}$	R_{Disk}^{Inn}	Γ	E_{fold}	F_{tot}/F_{Crab}	F_{hard}/F_{Crab}	F_{disk}/F_{Crab}	Inst.
116	1.11	$0.853^{+0.002}_{-0.002}$	$42.8^{+0.2}_{-0.2}$	$2.457^{+0.004}_{-0.004}$	-	0.387	0.074	0.197	P+H *
117	1.24	-	-	$2.95316^{+0.10}_{-0.09}$	-	0.032	0.012	0.000	P+H *

6 Spectral properties of transitions between soft and hard state in GX 339-4

Holger Stiele, Sara E. Motta, Teo Muñoz-Darias, and Tomaso M. Belloni

Accepted by Monthly Notices of the Royal Astronomical Society, 2011, ArXiv 1108.2198

Abstract

We present a study of the spectral properties during state transition of GX 339-4. Data are taken from the 2010 outburst of GX 339-4, which is densely covered by Rossi X-ray Timing Explorer, providing an excellent coverage of the state transitions between the low/hard state and the high/soft state. We select all observations within a certain hardness ratio range during the soft intermediate state (SIMS). This sample was chosen in such a way to comprise all observations that show a type-B quasi-periodic oscillation (QPO). In addition, we also investigate the spectra of hard intermediate state observations. The spectra, obtained from Proportional Counter Array data in the 10 to 40 keV range, are fitted with a power law and an additional high energy cut-off if needed. We find that the spectra are significantly harder during the SIMS of the soft-to-hard transition than they are during the hard-to-soft transition. This demonstrates that during the SIMS of the soft-to-hard transition not only the luminosity and peak frequencies of type-B QPOs are lower, but that also the photon index is lower, compared to the hard-to-soft transition. Hence, type-B QPOs can be associated to a different spectral shape even though they appear at the same hardness. However, in each branch only certain combinations of centroid frequency and photon index are realised.

6.1 Introduction

GX 339-4, a black hole X-ray transient (BHT), was discovered in 1973 by the *OSO-7* satellite (Markert et al. 1973). Since then GX 339-4 showed several X-ray outburst (see e.g. Miyamoto & Kitamoto 1991; Belloni et al. 1997; Mendez & van der Klis 1997; Zdziarski et al. 2004; Belloni 2005, Belloni et al. 2006; Yu & Dolence 2007; Motta et al. 2009; Muñoz-Darias et al. 2011). The system is a low mass X-ray binary, harbouring a >6 $M_{\odot}$ black hole accreting from a subgiant star in a 1.7 d orbital period (Hynes et al. 2003 and Muñoz-Darias et al. 2008). GX 339-4 represents a prime example for the spectral and temporal evolution of a BHT during outburst. The different states through which a BHT evolves during an outburst can be identified in the hardness intensity diagram (HID, Belloni 2005); Homan et al. 2005; Gierliński & Newton 2006; McClintock & Remillard 2006; Fender et al. 2009; Belloni 2010). In a log-log representation different states are found to correspond to different branches/areas of a q-shaped pattern. Recently, Muñoz-Darias et al. (2011) showed that the rms-intensity diagram (RID) allows the identification of states based on temporal information only. It is widely agreed on that at the begin and end of an outburst a BHT is in the so-called low/hard state (LHS), and that there is in between a transition to the high/soft state (HSS). In the HSS a strong thermal component, associated with disc emission is present, while spectra taken during the LHS show characteristics of hard (comptonized) emission. However, the exact definition of the states and especially of the transition between these states are still under debate. In this work we follow the classification of Belloni (2010) (see also Belloni 2005; Homan et al. 2005), which comprises a hard as well as a soft intermediate state (HIMS/SIMS); see however McClintock & Remillard (2006) for an alternative classification and Motta et al. (2009) for a comparison.

In this paper we investigate the spectral properties of transitions between the LHS and HSS. We focus on a comparison of the spectral properties of the SIMS observed during the hard-to-soft and the soft-to-hard transition.

6.2 Observations

The 2010 outburst of GX 339-4 was densely covered by Rossi X-ray Timing Explorer (RXTE), providing the (up to now) best coverage of the state transitions between the LHS and the HSS. For each observation of the outburst we determined the hardness ratio using Proportional Counter Unit 2 (PCU2) channels 7 – 13 (2.87 – 5.71 keV) for the soft band, and channels 14 – 23 (5.71 – 9.51 keV) for the hard band. The hardness intensity diagram (HID) as well as the hardness-rms diagram (HRD) of the whole outburst is shown in Fig. 6.1. The fractional rms was computed within the 0.1 – 64 Hz frequency band following Belloni & Hasinger (1990).

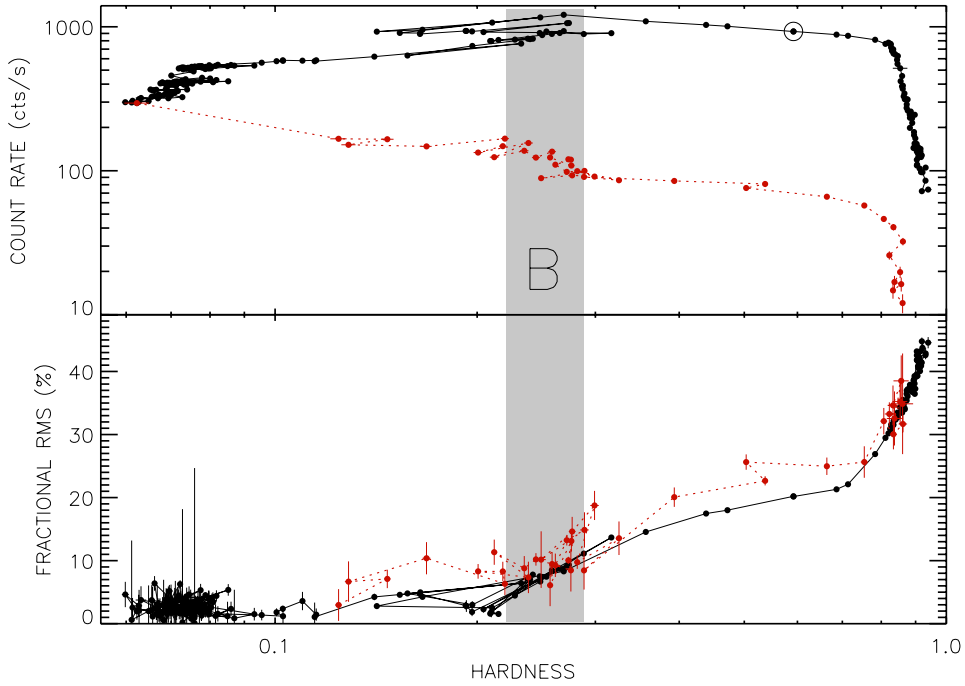

Figure 6.1: Upper panel: Hardness intensity diagram of the whole outburst, obtained using RXTE observations. Intensity corresponds to the count rate within the STD2 channels 0 – 31 (2 – 15 keV) and hardness is defined as the ratio of counts in 7 – 13 (2.87 – 5.71 keV) and 14 – 23 (5.71 – 9.51 keV) STD2 channels. Each point represents an entire observation. Consecutive observations are joined by a solid line until the softest observation is reached; after that by a (red) dashed line. The grey shaded area marks the hardness ratio range in which all observations that show type-B QPOs are located. This is also the hardness ratio range on which our study is based. Lower panel: corresponding hardness-rms diagram within the 0.1 – 64 Hz frequency band. During the soft-to-hard transition the fractional rms is higher than during the hard-to-soft transition, but in the region selected for our study (grey shaded).

GX 339-4 shows the standard q-shaped pattern in the HID of this outburst. After the passage through the LHS and HIMS, type-B QPOs (Quasi Periodic Oscillations, for a description of different types of QPOs see Motta et al. 2011) are seen in the power density spectra (see Sect. 6.3), indicating that the system is in the SIMS. Once this state is reached, several fast transitions between the SIMS and the HSS are observed with one extending to the HIMS (see Fig. 6.1). During the SIMS in the soft-to-hard transition at lower luminosities, the source also shows a few minor transitions.

In the transition from the LHS to the HSS, in the following called the upper branch, we select all observations that show a type-B QPO. These observations have a hard-

ness ratio ranging from 0.2208 to 0.2883 (grey shaded area in Fig. 6.1). Please note that this hardness ratio range also includes observations without a type-B QPO. The same hardness ratio range is used to select observations from the lower branch (the back transition from the HSS to the LHS at lower luminosities). All observations showing type-B QPOs on either branch are within the hardness ratio range used. On the upper branch the centroid frequency of the type-B QPOs is $\sim$5 Hz, while on the lower branch it reduces to $\sim$2 Hz (Motta et al. 2011). The fractional rms of observations showing type-B QPOs lies in the expected 5 – 10 % range (Muñoz-Darias et al. 2011). Furthermore, observations with a type-B QPO have a lower fractional rms during back transition than in the hard-to-soft transition. For most of the remaining parts of the outburst the fractional rms during back transition is higher than it has been in the hard-to-soft transition (observations belonging to the back transition are marked in red in Fig. 6.1).

In summary, observations were included in the sample for comparison if their hardness ratio ranged between 0.2208 and 0.2883, as this interval comprises all observations with type B-QPOs. We also analysed HIMS observations ($0.2883 < \mathrm{HR} \leq 0.8$) to cover the whole transition.

6.3 Power density spectra

We produced power density spectra (PDS) using 16 second long stretches of GOODXENON, EVENT and SINGLEBIT mode data. We limited PDS production to the Proportional Counter Array (PCA) channel band 0 – 35 (2 – 15 keV). After averaging the PDS and subtracting the contribution due to Poissonian noise (see Zhang et al. 1995), the PDS were normalised according to Leahy et al. (1983) and converted to square fractional rms (Belloni & Hasinger 1990). We fitted the PDS using the XSPEC fitting package by applying a one-to-one energy-frequency conversion and a unit response. The noise components were fitted with three broad Lorentzian shapes, one zero-centered and other two centered at a few Hz (Belloni et al. 2002). We fitted the QPOs with one Lorentzian each. Occasionally it was possible to achieve a significant improvement of the value of reduced χ^2 by adding a Gaussian component, which better approximates the shape of the narrow peaks. The QPO centroid frequency as well as the total fractional rms for each observation is listed in Tab. 6.1.

Casella et al. (2004), Casella et al. (2005) showed that QPOs could be classified by the following properties: the *quality factor* ($Q = \nu_{centroid}/FWHM$) and the shape of the noise associated with the oscillation in the PDS. It has been also proven that QPOs can be discriminated by the amount of noise present in the PDS, which is quantified by the fractional rms Muñoz-Darias et al. (2011). This leads to a more specific version of the ABC classification Motta et al. (2011), in which type-B QPOs are characterised by rms strictly within the 5 – 10% interval and are observed at

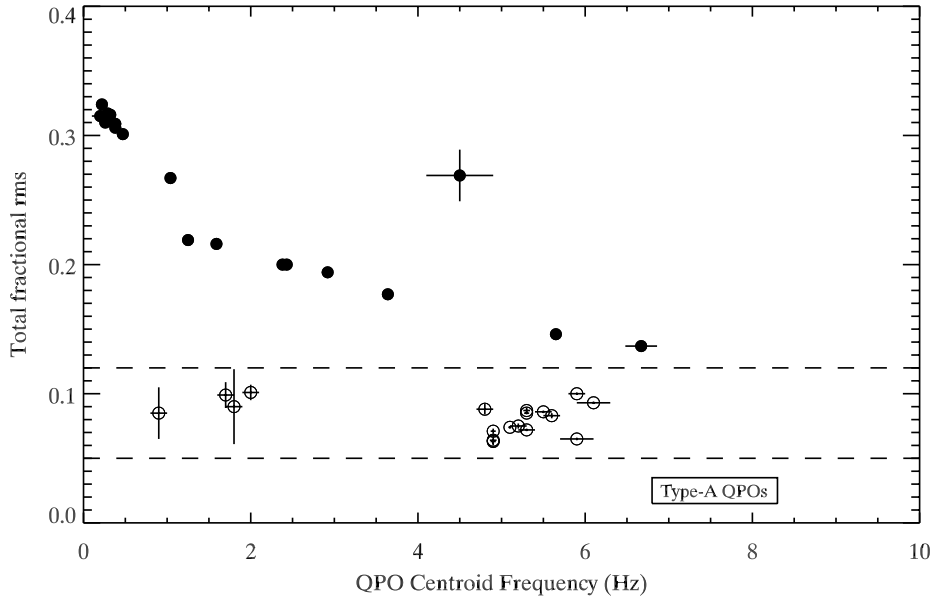

Figure 6.2: QPO centroid frequency vs. 0.1 – 64 Hz fractional rms. Each point corresponds to a different observation. Symbols correspond to QPO types: filled circles are type-C QPOs, open circles are type-B QPOs. No type-A QPOs are detected in the 2010 outburst of GX 339-4, but their location according to Motta et al. (2011) is indicated.

frequencies ranging from 1 to 7 Hz.

The relation between centroid frequency and fractional rms is shown in Fig. 6.2. This plot allows us to distinguish clearly between type-C (filled circles) and type-B QPOs (open circles). Similar plots for XTE J1859+226 and a sample of sources can be found in Casella et al. (2004) and Casella et al. (2005), respectively. The four points associated to type-B QPOs detected in the soft-to-hard transition (open circles with QPO centroid frequency between 0.9 and 2.0 Hz) are located in an area which is empty in the Casella et al. (2004) and Casella et al. (2005) plots, as these plots contain only type-B QPOs detected during the hard-to-soft transition. Furthermore, the four points associated to type-B QPOs during the soft-to-hard transition are located clearly outside the regions associated to type-C and type-A QPOs. Therefore we identify these four QPOs as type-B. A selection of PDS with type-B QPOs observed during the hard-to-soft as well as the soft-to-hard transition is shown in Fig. 6.3. For a more detailed study of different types of QPOs detected in a sample comprising data of four outbursts of GX 339-4 and a discussion of QPO properties with respect to source flux as well as spectral properties see Motta et al. (2011).

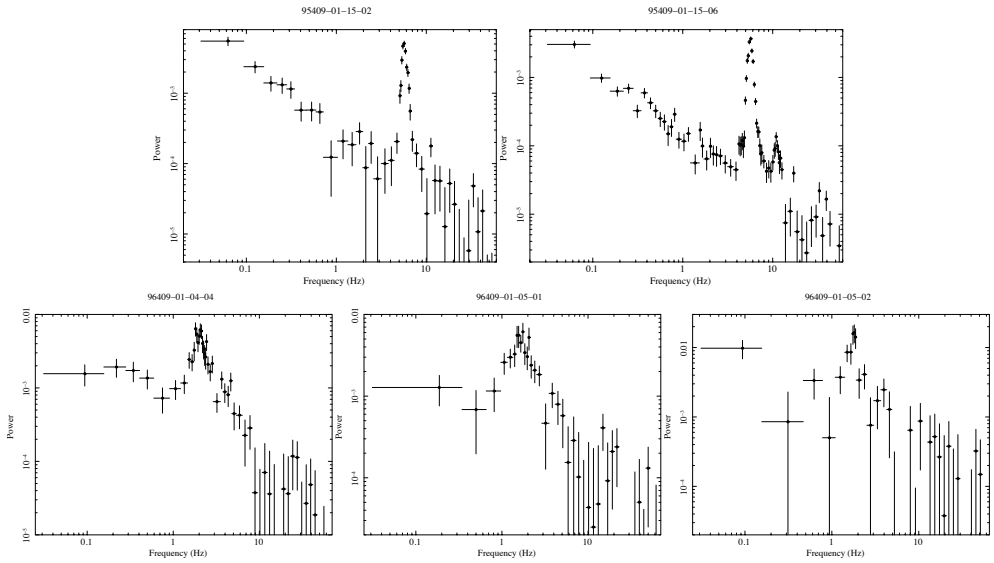

Figure 6.3: Power density spectra of some observations with type-B QPOs, detected during the hard-to-soft (upper row) and soft-to-hard transition (lower row).

6.4 Spectral analysis

Energy spectra were extracted from PCA PCU2 data using the standard RXTE software within HEASOFT V. 6.9. We had to exclude all High Energy X-ray Timing Experiment (HEXTE) data from our analysis, since most of the HEXTE spectra contain strong residuals that are related to the difficulties in determining the background contribution in the spectra since the "rocking" mechanism of HEXTE is broken. To account for residual uncertainties in the instrument calibration a systematic error of 0.6 per cent was added to the PCA spectra[1]. The spectra were fitted with ISIS V. 1.6.1 (Houck & Denicola 2000).

Since we were only interested in the behaviour of the hard spectral component we decided to neglect the contribution of the soft (disc) component and to focus our spectral analysis on the high energy range. We fitted the PCA (10 – 40 keV) data using a power law model. For the first few observations of the HIMS an additional high energy cut-off was needed to obtain good fits.

The fits resulted in formally acceptable reduced χ^2 values and the spectra were clearly free of residuals. As an iron line was present at lower energies, indicating the presence of reflection processes (Zdziarski et al. 1999), it might be possible that also a broad reflection feature showed up around 30 keV (e.g. Magdziarz & Zdziarski 1995). This feature could be due either to reflection of the comptonized emission

[1] A detailed discussion on PCA calibration issues can be found at: http://www.universe.nasa.gov/xrays/programs/rxte/pca/doc/rmf/pcarmf-11.7/

onto the accretion disk (see Gilfanov 2010 for a review) or to extended layers of material covering certain regions of the optically thick accretion disk (e.g. wind clouds surrounding the central black hole, see Shaposhnikov & Titarchuk 2006). To exclude that the value of the photon index was affected by the presence of this feature we also tried a different model, consisting of a power law multiplied by a reflection component (`reflect`). We found that the relative reflection component was only needed for the first few HIMS observations.

Taking reflection into account changes the value of the photon index in each individual observation. This has to be expected, since a "phenomenological model" such as a power law is not able to take into account the reflection features around 30 keV. However the overall behaviour of the photon index observed between upper and lower branch stays the same (Fig. 6.4). In the remaining observations the relative reflection component found was always consistent with zero within errors. In the following, we discuss only the results from the PCA 10 – 40 keV spectra.

6.5 Results and Discussion

In spite of GX 339-4 has been deeply studied by RXTE during the last years, spectral transitions are very fast, which results in a few SIMS observations per outburst. Most of these observations are usually concentrated in the upper branch. Since the SIMS was intensively covered during 2010 and many type-B QPOs could be observed, it was possible to make an unprecedented detailed direct comparison between the upper and lower branch SIMS. Hence, we investigated PCA spectra (10 – 40 keV) to search for differences in the spectral properties of both branches and how they can be addressed in the light of (non)detection of radio emission and QPO properties. Figure 6.4 shows the temporal evolution of the photon index. It increases during the HIMS and reaches a more or less constant value during the SIMS in the upper branch. In the lower branch, the SIMS spectra have a consistently lower photon index than those in the upper branch. The HIMS shows a moderate decrease in photon index. The fact that the soft-to-hard transition takes place at a much lower photon index (see also Fig. 6.5) means that the high energy part of the spectrum is harder in the lower branch than it was in the upper branch. There are numerous works on BHTs that study the evolution of the temporal and spectral properties during the whole outburst (e. g. McClintock et al. 2009; Motta & Belloni 2010; Shaposhnikov & Kazutaka 2010). Other papers are dedicated to a detailed investigation of those properties during the outburst decay (e.g. Kalemci et al. 2004, Kalemci et al. 2005, Kalemci et al. 2006). The overall evolution of the photon index throughout a BHT outburst, which – roughly speaking – consists of an increase from the LHS to the HSS followed by a decrease when the source goes back to the LHS, is already known from those studies. However none of these studies focuses on the behaviour of the photon

index during the upper and lower branch SIMS, which is most probably related to the previously sparsely sampling of (lower branch) SIMSs.

Remember that the observations were selected from the same hardness ratio range. A different contribution of the disc to the overall emission – which arises in a reduced inner disc temperature – compared to the upper branch has to be expected due to the lower luminosity in the soft-to-hard transition (Maccarone & Coppi 2003; see e. g. Shaposhnikov et al. 2010 or Stiele et al. 2011 for XTE J1752-223 or Muñoz-Darias et al. 2011 for MAXI J1659-152). This change in the disc contribution to the emission requires that also the rest of the spectrum must be modified since the hard tail depends (in a complicated way, via Comptonization processes; see e.e Sunyaev & Titarchuk 1980 and references therein for thermal Comptonization, Titarchuk et al. 1996, Titarchuk & Hua 1995 and references therein for non-thermal Comptonization, Del Santo et al. 2008 and references therein for hybrid Comptonization) from the disc itself. Thus the spectral shapes between upper and lower branch at a similar hardness ratio should differ from each other. While hardness ratio can be used as a good tracker of the spectral shape for observations obtained at more or less the same flux, our results show that one should be cautious especially when analysing spectra at very different fluxes, as it is the case for observations of the upper and lower branch. In this case it is necessary to "re-calibrate" its meaning according to the new flux level. In other words, the same hardness range tracks different photon index intervals at different fluxes.

The connection between source flux and photon index is shown in Fig. 6.6. The colour of the dots represents the temporal evolution of the parameters during the outburst. The behaviour seen is expected according to the HID.

The observations of the upper and lower branch were selected in such a way to include all observations with type-B QPOs and have a similar fractional rms. Furthermore, they are all located within a certain hardness ratio range, which is represented as a vertical strip in the HID. It is known that the jet line does not follow a vertical line in the HID, but shows a more complex behaviour (Fender et al. 2009). In the lower branch the jet does not turn on before the source is settled in the LHS (Kalemci et al. 2006, Russel & Lewis 2011). We showed that the photon index during the SIMS in the lower branch transition is smaller than in the upper branch transition. This means that lines of constant photon index run from the upper right to the lower left in the HID during state transition.

It is known that the disappearance of the steady radio jet in the upper branch and the re-appearance of the jet in the lower branch take place at different hardness ratios. Our finding of a lower photon index during the SIMS of the lower branch implies that the jet appears at a much lower photon index in the soft-to-hard transition than it disappeared at in the upper branch. This implies that there is either no relation between photon index and radio emission or that this relation has to be extremely

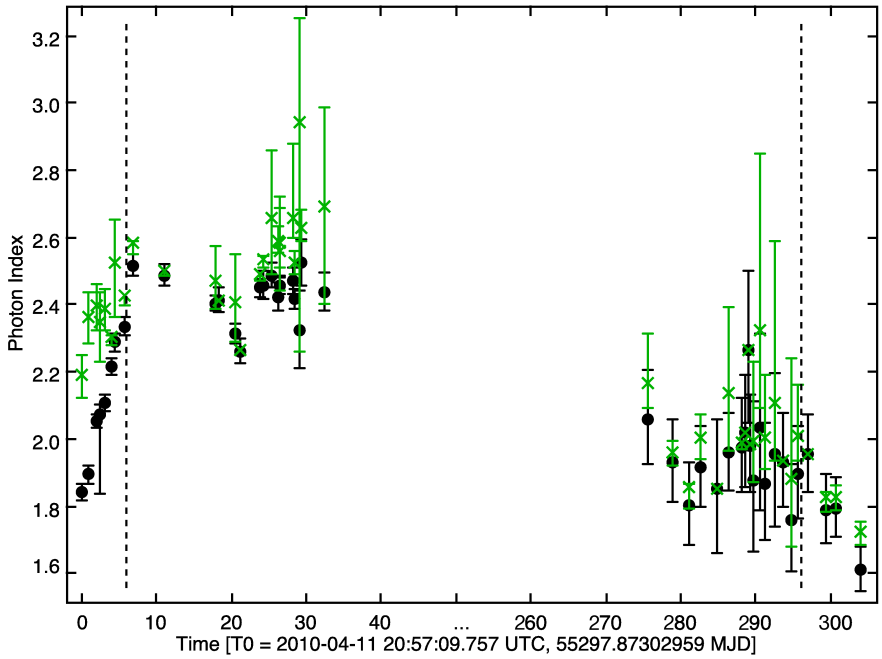

Figure 6.4: Temporal evolution of the photon index for different spectral models. The values obtained from a power law + cut-off model are given in black, the one obtained from a power law model with reflection in green. The dashed lines mark the first transition from HIMS to SIMS as well as the last transition from SIMS to HIMS. Transitions in between are not indicated (see however Tab. 6.1). The time of the first observation of the HIMS in the hard-to-soft transition was selected as T_0.

complicated.

The photon indices found in the SIMS of the lower branch correspond to values obtained at the onset of the HIMS in the upper branch (see encircled dot in Fig. 6.1). This finding is in agreement with the lagging of timing properties compared to spectral properties in the soft-to-hard transition, as reported in Kalemci et al. (2004). Furthermore Muñoz-Darias et al. (2011) showed that the onset of the upper branch HIMS and the transition form the lower branch HIMS to the LHS are situated on two different hard lines in the intensity-rms diagram of GX 339-4.

Furthermore, we found that type-B QPOs can be associated to different spectral shape. Previous studies, which did not differentiate between type-B and other types of QPOs, used a relation between photon-index and QPO centroid frequency to estimate the mass of the black hole in X-ray binaries (Shaposhnikov & Titarchuk 2007

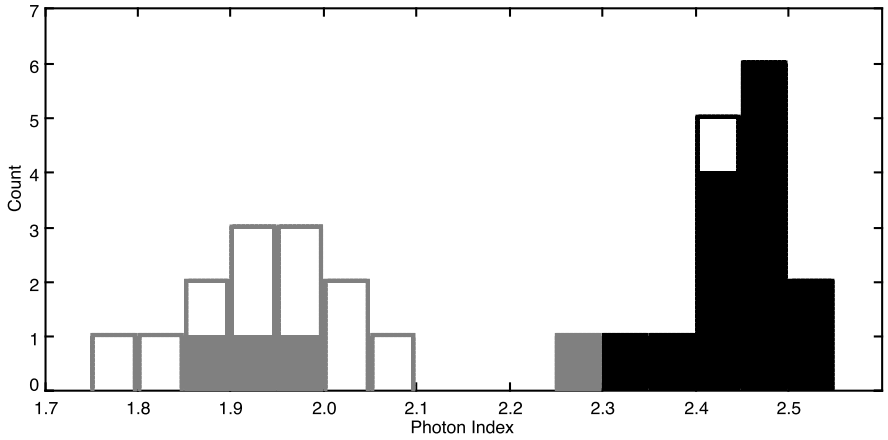

Figure 6.5: Distribution of the photon index values in the upper (black) and lower (grey) branch, with a bin size of 0.05. Only the values obtained with the power law + cut-off model are shown. In the upper branch the photon index peaks at ∼2.45, while the distribution in the lower branch is broader and peaks at ∼1.95. Photon indices obtained from observations with type-B QPOs are marked as filled bars.

and Shaposhnikov et al. 2009). In the upper branch type-B QPOs appear at a centroid frequency of ∼5 Hz (Motta et al. 2011) and in observations where the photon index is between 2.3 and 2.6. In the lower branch the centroid frequency of type-B QPOs reduces to ∼2 Hz (Motta et al. 2011) and they are mainly observed in observations which spectra have a photon index of ∼1.9 (see Fig. 6.6). However, we observe type-B QPOs neither in observations of the upper branch that have a photon index of ∼1.9 nor in observations of the lower branch which have a photon index of ∼2.4. Therefore, the physical conditions that lead to the QPO do not depend in an obvious way on the power law parameters. Figure 6.5 clearly shows that within each branch the photon index is not enough to distinguish between observations with and without type-B QPOs in the selected sample. The difference is just in the timing. In addition, Motta et al. (2011) showed that there is a correlation between centroid frequency of type-B QPOs and the count rate. We do not want to claim here a relation between centroid frequencies of type-B QPOs and photon index, but our findings underline that type-B QPOs can appear only in a very narrow range of properties of a BHT that are realised during state transitions. These properties occur in a rather narrow window in the HID and they are characterised by selected combinations of peak frequencies of type-B QPOs and photon index in the upper and lower branch, respectively.

Recent works indicate that the hard component observed in spectra of intermediate

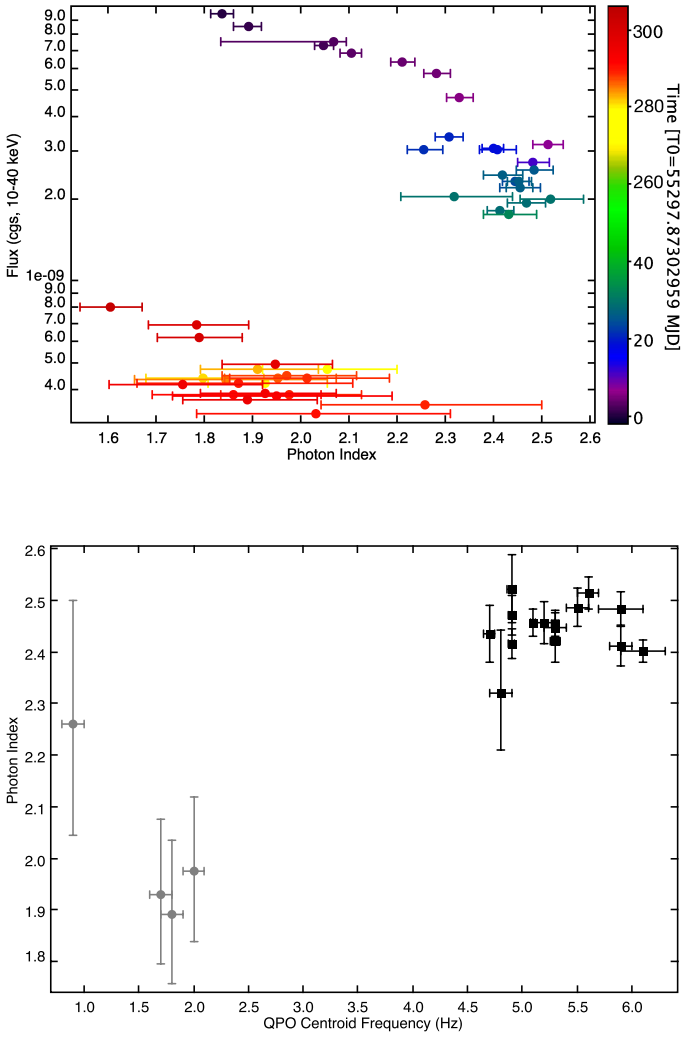

Figure 6.6: Upper pannel: Relation between source flux and photon index. The colour of the dots represents the temporal evolution of the parameters during the outburst. Lower pannel: Relation between QPO centroid frequency and photon index. Values belonging to observations of the hard-to-soft transition are marked as squares, those of the soft-to-hard transition as dots.

states arises from hybrid Comptonization (e.g. Del Santo et al. 2008 and references therein). In the intermediate states, a hard tail extended to the MeV is observable in the spectra (Done et al. 2007, like those observed in the HSS Grove et al. 1998). This intermediate state tail is softer than the tail that can be observed in the hard state and comes either in the form of a cut-off power law rolling over at energies larger than 150 keV (Motta et al. 2009) or in the form of a simple power law, with no observable cut-off up to a few MeV (Caballero-García et al. 2009). The extent of the tail shows that there must be non-thermal Compton scattering, as in the high/soft state. However, the tail is steeper, which means that the mean electron energy is lower. The observed spectral shape can only be produced by a combination of thermal/non-thermal Compton scattering. This could be produced in a single region filled with two populations of electrons (one thermal and the other non thermal). Alternatively there could be two different regions, one with thermal electrons (the same electrons that in the hard state are responsible of the thermal comptonization) and one with non-thermal, perhaps related to the jet base. Assuming that the hard component results from hybrid Comptonization, the appearance of type-B QPOs depends directly on the properties of the hybrid Comptonizing medium. In particular, the type-B QPO frequency is strictly related to the temperature distribution of the electrons, that in turn determines the inclination of the hard part of the spectrum. In this regard, it appears natural to assume that the properties (i.e. the temperature distribution) of such a medium are different in the softening and hardening phase, which are separated by the HSS, where the hard contribution to the emission is nearly negligible and therefore, our results are consistent with this scenario.

However, the presence of diverse elements acting together in spectral/temporal evolution of the system (such as different populations of electrons, accretion flow and even a magnetic field) results in several effects that are difficult to disentangle. The complexity of the situation makes it difficult to identify how the behavior of the emitting components could affect the properties of the QPOs and to determine whether the appearance of type-B QPOs is related to changes in the corona, in the disc, the accretion-ejection process, or a combination of several processes. Such issue is not trivial to the understanding of accretion and of the fundamental physics acting in presence of compact objects and strong gravitational fields and should be the topic of further investigations.

6.6 Conclusion

We investigated the spectral properties in the 10 – 40 keV band during state transitions in the 2010 outburst of GX 339-4. The sample of SIMS observations used contained all observations with type-B QPOs. Comparing the (mean) photon index found in the SIMS of the hard-to-soft transition with the one of the soft-to-hard transi-

tion a flatting of the power law is clearly evident. This means that the back transition from the soft to the hard state does not only occur at lower luminosity and with lower peak frequencies of type-B QPOs, but also at lower photon index. Hence, type-B QPOs can be associated to different spectral shape. However, in each branch only certain combinations of centroid frequency and photon index are realised.

Acknowledgments

The research leading to these results has received funding from the European Community's Seventh Framework Programme (FP7/2007-2013) under grant agreement number ITN 215212 "Black Hole Universe". SM and TB acknowledge support from grant ASI-INAF I/009/10/0.

This work makes use of EURO-VO software, tools or services. The EURO-VO has been funded by the European Commission through contracts RI031675 (DCA) and 011892 (VO-TECH) under the 6th Framework Programme and contracts 212104 (AIDA) and 261541 (VO-ICE) under the 7th Framework Programme.

Table 6.1: Photon index and flux (10 – 40 keV) derived from the best fit for each observation. A model consisting of a power-law, and – if needed – a cut-off at high energies was used. Columns are: Observation ID, MJD, spectral state, photon index, flux (in the 10 – 40 keV band in units of 10^{-9} erg s^{-1} cm^{-2}), fold energy (in keV), high-energy cutoff (keV), QPO centroid frequency, total fractional rms.

Obs. id.	MJD	state	Γ	Flux	E_{fold}	E_{cut}	ν	tot frac. rms
95409-01-14-02	55297.9	HIMS	1.84±0.02	9.43	132^{+64}_{-34}	$19.9^{+2.6}_{-2.1}$	1.25±0.01	21.9±0.1
95409-01-14-03	55298.7	HIMS	1.89±0.03	8.47	65^{+40}_{-22}	$23.1^{+3.5}_{-4.5}$	1.59±0.01	21.6±0.2
95409-01-14-06	55299.8	HIMS	2.05±0.02	7.25	61^{+68}_{-40}	$26.2^{+6.3}_{-5.5}$	2.43±0.01	20.0±0.1
95409-01-14-04	55300.3	HIMS	$2.07^{+0.03}_{-0.24}$	7.45	152^{+187}_{-142}	$20.6^{+39.7}_{-20.6}$	2.38±0.01	20.0±0.2
95409-01-14-07	55300.9	HIMS	2.10±0.02	6.78	165^{+86}_{-145}	$18.45^{+3.8}_{-2.0}$	2.92±0.01	19.4±0.1
95409-01-14-05	55301.8	HIMS	$2.21^{+0.03}_{-0.02}$	6.25	–	–	3.64±0.02	17.7±0.2
95409-01-15-00	55302.2	HIMS	2.28±0.03	5.73	–	–	–	–
95409-01-15-01	55303.6	HIMS	2.33±0.03	4.63	–	–	5.65±0.04	14.61±0.1
95409-01-15-02	55304.7	SIMS	2.51±0.03	3.14	–	–	5.6±0.1	8.3±0.2
95409-01-15-06	55309.0	SIMS	2.48±0.03	2.70	–	–	5.9±0.2	6.5±0.1
95409-01-16-05	55315.7	SIMS	2.40±0.02	3.02	–	–	6.1±0.2	9.3±0.1
95409-01-17-00	55316.1	SIMS	2.41±0.04	3.00	–	–	5.9±0.1	10.0±0.1
95409-01-17-02	55318.4	HIMS	2.31±0.03	3.34	–	–	6.67±0.19	13.69±0.13
95409-01-17-03	55319.1	HIMS	2.26±0.04	3.00	–	–	–	–
95409-01-17-05	55321.7	SIMS	2.44±0.03	2.30	–	–	5.3±0.1	7.2±0.1
95409-01-17-06	55322.2	SIMS	2.45±0.04	2.18	–	–	5.2±0.1	7.5±0.2
95409-01-18-00	55323.2	SIMS	2.48±0.04	2.53	–	–	5.5±0.1	8.6±0.1
95335-01-01-07	55324.2	SIMS	2.42±0.04	2.41	–	–	5.3±0.04	8.7±0.2
95335-01-01-00	55324.3	SIMS	2.45±0.02	2.30	–	–	5.3±0.03	8.5±0.1
95335-01-01-01	55324.4	SIMS	2.45±0.03	2.17	–	–	5.1±0.02	7.4±0.1

Continued on next page

Table 6.1 – continued from previous page

Obs. id.	MJD	state	Γ	Flux	E_{fold}	E_{cut}	ν	tot frac. rms
95335-01-01-05	55326.2	SIMS	2.47±0.04	1.91	–	–	4.9±0.03	7.1±0.2
95335-01-01-06	55326.3	SIMS	2.41±0.03	1.79	–	–	4.9±0.03	6.3±0.2
95409-01-18-04	55327.0	SIMS	$2.32^{+0.12}_{-0.11}$	2.01	–	–	4.8±0.1	8.8±0.4
95409-01-18-05	55327.3	SIMS	2.52±0.07	1.96	–	–	4.9±0.04	6.4±0.4
95409-01-19-00	55330.3	SIMS	$2.43^{+0.06}_{-0.05}$	1.73	–	–	4.7±0.05	3.3±1.1
96409-01-02-02	55573.5	SIMS	$2.05^{+0.14}_{-0.13}$	0.47	–	–	–	–
96409-01-03-00	55576.8	SIMS	$1.93^{+0.13}_{-0.12}$	0.42	–	–	–	–
96409-01-03-01	55578.9	SIMS	$1.80^{+0.13}_{-0.12}$	0.43	–	–	–	–
96409-01-03-02	55580.6	SIMS	$1.91^{+0.13}_{-0.12}$	0.47	–	–	–	–
96409-01-04-00	55582.7	SIMS	$1.85^{+0.21}_{-0.19}$	0.43	–	–	–	–
96409-01-04-01	55584.4	SIMS	$1.95^{+0.12}_{-0.11}$	0.44	–	–	–	–
96409-01-04-04	55585.9	SIMS	$1.97^{+0.15}_{-0.13}$	0.45	–	–	2.0±0.1	10.1±0.6
96409-01-04-02	55586.5	SIMS	$2.01^{+0.17}_{-0.16}$	0.43	–	–	–	–
96409-01-04-05	55586.9	SIMS	$2.26^{+0.24}_{-0.21}$	0.35	–	–	0.9±0.1	8.5±2.0
96409-01-04-03	55587.2	SIMS	$1.98^{+0.15}_{-0.14}$	0.38	–	–	–	–
96409-01-04-07	55587.5	HIMS	$1.87^{+0.24}_{-0.21}$	0.42	–	–	–	–
96409-01-04-08	55588.5	SIMS	$2.03^{+0.28}_{-0.25}$	0.32	–	–	–	–
96409-01-05-00	55589.2	SIMS	$1.86^{+0.18}_{-0.17}$	0.38	–	–	–	–
96409-01-05-04	55590.4	HIMS	$1.95^{+0.24}_{-0.21}$	0.37	–	–	–	–
96409-01-05-01	55591.6	SIMS	$1.93^{+0.15}_{-0.13}$	0.39	–	–	1.7±0.1	9.9±1.0
96409-01-05-05	55592.7	HIMS	$1.76^{+0.17}_{-0.15}$	0.41	–	–	–	–
96409-01-05-02	55593.5	SIMS	$1.89^{+0.14}_{-0.13}$	0.36	–	–	1.8±0.1	9.0±2.9
96409-01-05-03	55594.9	HIMS	$1.95^{+0.12}_{-0.11}$	0.49	–	–	–	–
96409-01-06-00	55597.3	HIMS	$1.78^{+0.11}_{-0.10}$	0.69	–	–	–	–

Continued on next page

Table 6.1 – continued from previous page

Obs. id.	MJD	state	Γ	Flux	E_{fold}	E_{cut}	ν	tot frac. rms
96409-01-06-01	55598.7	HIMS	1.79 ± 0.09	0.62	–	–	–	–
96409-01-06-02	55601.9	HIMS	$1.61^{+0.07}_{0.06}$	0.79	–	–	–	–

7 On the outburst evolution of H1743-322: a 2008/2009 comparison

Sara E. Motta, Teo Muñoz-Darias, Tomaso M. Belloni

Monthly Notices of the Royal Astronomical Society, 2010, 408, 179

Abstract

We present two observational campaigns performed with the RXTE satellite on the black hole transient H 1743-322. The source was observed in outburst on two separate occasions between October-November 2008 and May-July 2009. We have carried out timing and spectral analysis of the data set, obtaining a complete state classification of all the observations. We find that all the observations are well described by using a spectral model consisting of a disk-blackbody, a powerlaw + reflection + absorption and a gaussian emission component. During the 2009 outburst the system followed the canonical evolution through all the states seen in black hole transients. In the 2008 outburst only the hard states were reached.

The early evolution of the spectral parameters is consistent between the two epochs, and it does not provide clues about the subsequent behavior of the source. The variation of the flux associated to the two main spectral components (i.e. disk and powerlaw) allows us to set a lower limit to the orbital inclination of the system of $\geq 43^{\circ}$.

7.1 Introduction

Black holes X-ray transients (BHTs) spend most of their lives in "quiescence", displaying very low luminosities ($\sim 10^{32}$ ergs^{-1}). They also undergo occasional outbursts, when their luminosity increases by several orders of magnitude. During these events, BHTs can approach their Eddington luminosity and marked changes are observed in both time variability and energy spectrum (see e.g. Belloni 2005, Belloni 2010). We do not still have a complete understanding of all the mechanisms that lead to these changes, but, apart from the variation of the mass accretion rate, they must involve the structure of the accretion flow around the black hole as well as accretion/ejection mechanism processes.

The spectral evolution of black hole X-ray transients can be described in terms of the characteristic pattern they usually show in the in X-ray hardness-intensity diagram (HID) (see Homan et al. 2001, Homan & Belloni 2005, Belloni et al. 2006, Gierliński & Newton 2006, Belloni 2010). Different states correspond to different branches/areas of the HID, which is often travelled along a regular path during outbursts. Two of the states correspond to the original states discovered in the 1970s. The Low/Hard State (LHS) is found only at the beginning and at the end of an outburst, where the highest luminosity swings are observed. The X-ray spectrum is dominated by a component which can be approximated by a power law with a hard photon index ($\sim$ 1.5-1.8) and a variable high-energy cutoff moving between $\sim$50 keV and $\sim$300 keV (see e.g. Motta et al. 2009, Joinet et al. 2008, Miyakawa et al. 2008). In this phase, the power density spectrum (PDS) of the source is highly variable and is dominated by a strong band limited noise ($\sim 30\%$ fractional rms). The High Soft State (HSS), if reached, can be observed in the central part of an outburst, in which the spectrum is dominated by a soft thermal component, most likely associated to an optically thin accretion disk. It also shows an additional weak, steep power-law component (photon index $\sim$ 2.5 or higher). During this state, the power density spectrum shows faint components with fractional rms typically around few percent.

Between these two well-established states, the situation is more complex, leading to many different classifications. Homan & Belloni (2005) identify two additional states, defined by spectral/timing transitions. After the LHS a transition to these intermediate states occurs and the source evolves as its luminosity increases. The spectrum starts to change: the soft thermal component appears and becomes gradually important, the energy peak of the emission softens and the hard component steepens ($\Gamma \sim$ 2.0-2.5). The Hard Intermediate State (HIMS) and Soft Intermediate State (SIMS) show these spectral characteristics and can be distinguished between each other mostly by timing properties (Homan & Belloni 2005). The transition between HIMS and SIMS can be very fast (sometimes over a few seconds, see Nespoli et al. 2003) and it is marked by the disappearance/appearance of particular features

in the PDS, such as the switch between two types of QPOs and a decrease in overall fast variability. The transition to the SIMS is also associated to the ejection of fast relativistic jets. This has led to the identification of a *jet line* in the HID, separating HIMS and SIMS (Fender et al. 2004). However, recent studies of different systems have shown that the jet ejection and HIMS/SIMS state transitions are not exactly simultaneous (Fender et al. 2009). The jet line can be crossed more than once during an outburst (e.g. XTE J1859+226: Casella et al. 2004; GX339-4: Brocksopp et al. 2002, Motta et al. 2009). For a more detailed state classification see Belloni (2010).

The four states mentioned above are observed in many BHCs in a regular way, starting from the LHS, crossing the HIMS and the SIMS and reaching the HSS. After a relatively long permanence in the HSS, the flux starts to decrease, most likely following a decrease in accretion rate. At some point, a reverse transition takes place and the path is followed backwards to the LHS and then to quiescence. The luminosity of this back-transition is always lower than that of the corresponding forward-transition (see Maccarone & Coppi 2003; Dunn et al. 2010). This basic pattern can vary depending on the source. Additional transitions between SIMS and HIMS can be observed and some sources behave in a more complicated way showing additional non-canonical states (i.e. the anomalous state, see Belloni 2010). Interestingly, until now all black-hole transients have shown two types of behaviour: after the initial LHS, most sources show a transition to the HIMS at a luminosity level which is always different and might be related to the previous history of the transient (Yu & Dolence 2007). If this transition takes place, the source always reached the HSS. There is also a second group of systems (at least seven) that never left the LHS (eg. XTE1550-564, Sturner & Shrader (2005);). Until the October 2008 outburst of H1743-322 (see below) the only possible exception to this dichotomy is represented by SAX J1711.6–38 (Wijnands & Miller 2002), a faint transient X-ray binary classified as black hole candidate.

7.1.1 H1743-322

The X-ray source H1743-322 was discovered during a bright outburst in 1977 with the Ariel V satellite (Kaluzienski & Holt 1977). It is classified as a black hole candidate (McClintock & Remillard 2006), as a dynamical confirmation has not been possible due to the faintness of its optical counterpart (Steeghs et al. 2003). H1743-322 is one of the few sources where X–ray jets have been imaged (Corbel et al. 2005).

The distance to H1743-322 is not well constrained. Corbel et al. (2005) find from the proper motion of the jet an upper limit of 10.4 ± 2.9 kpc to the distance, consistent with a location in the Galactic Centre.

After displaying four outbursts (observed by different missions, such as INTEGRAL, *Swift*, RXTE), on 2008 September 23, (MJD=54732), another outburst of H1743-322 was detected by INTEGRAL during the Galactic bulge monitoring (see

Kuulkers et al. 2008) showing that the source was in a hard state with an increasing flux. *Swift*, RXTE and INTEGRAL followed the outburst evolution. This time H1743-322 did not follow the canonical pattern normally seen in the outburst phases of black-hole transients. The source only sampled the HIMS (Belloni et al. 2008). Then it decreased in luminosity and underwent a hardening of the spectrum. This behaviour was confirmed by both spectral and timing analysis (Capitanio et al. 2009, hereafter C09). Finally, a new bright outburst was detected on May 2009 by Swift/BAT (see Krimm et al. 2009). This outburst followed the standard pattern in the HID, displaying all the canonical states.

In this paper we present the results coming from the analysis of the last two outbursts (2008 and 2009). Our aim is to use RXTE data collected during the 2009 outburst to study the broadband spectral evolution of H1743-322 and compare its behavior with that of the 2008 outburst where a non-standard behavior is observed. Our purpose was to identify differences in the evolution that would have allowed to predict the presence/absence of a transition to soft states. This is important because the transition is linked to jet ejection. In 2008 the mechanism for such ejection was put in motion, but stopped early. In 2009 the transition took place.

7.2 Observations and data analysis

In May 2009, Swift/BAT detected X-ray activity from H1743-322 as part of its hard X-ray transient monitor program (Krimm et al. 2009). This flux level was comparable to the peak reached during the previous outburst of this source around 4-October-2008 (see e.g. Kuulkers et al. 2008). The brightening of H1743-322 was confirmed by the RXTE/ASM (Miller-Jones et al. 2009) during May 23-28. As a part of public target of opportunity observations H1743-322 was observed in pointing mode by RXTE. Starting from 29 May 2009, a total of 44 observations were performed during 2 months, covering a large part of the outburst of the source. We report here the results of the spectral analysis of all the 2009 observations. We also analysed the 37 RXTE outburst observations taken during 2008.

We extracted energy spectra from the PCA and HEXTE instruments (background and dead time corrected) for each observation using the standard RXTE software within HEASOFT V. 6.6.3. For our spectral analysis, only Proportional Counter Unit 2 from the PCA and Cluster B from HEXTE were used. A systematic error of 0.6% was added to the PCA spectra to account for residual uncertainties in the instrument calibration [1]. We accumulated background corrected PCU2 rates in the channel bands A = 4 - 128 (3.3 - 118 keV), B = 4 - 10 (3.3 - 6.1 keV) and C = 11

[1] See http://www.universe.nasa.gov/xrays/programs/rxte/pca/doc/rmf/pcarmf-11.7/#head-27884cefb2a102a7e53547f1631cbeab44224a04 for a detailed discussion on the PCA calibration issues.

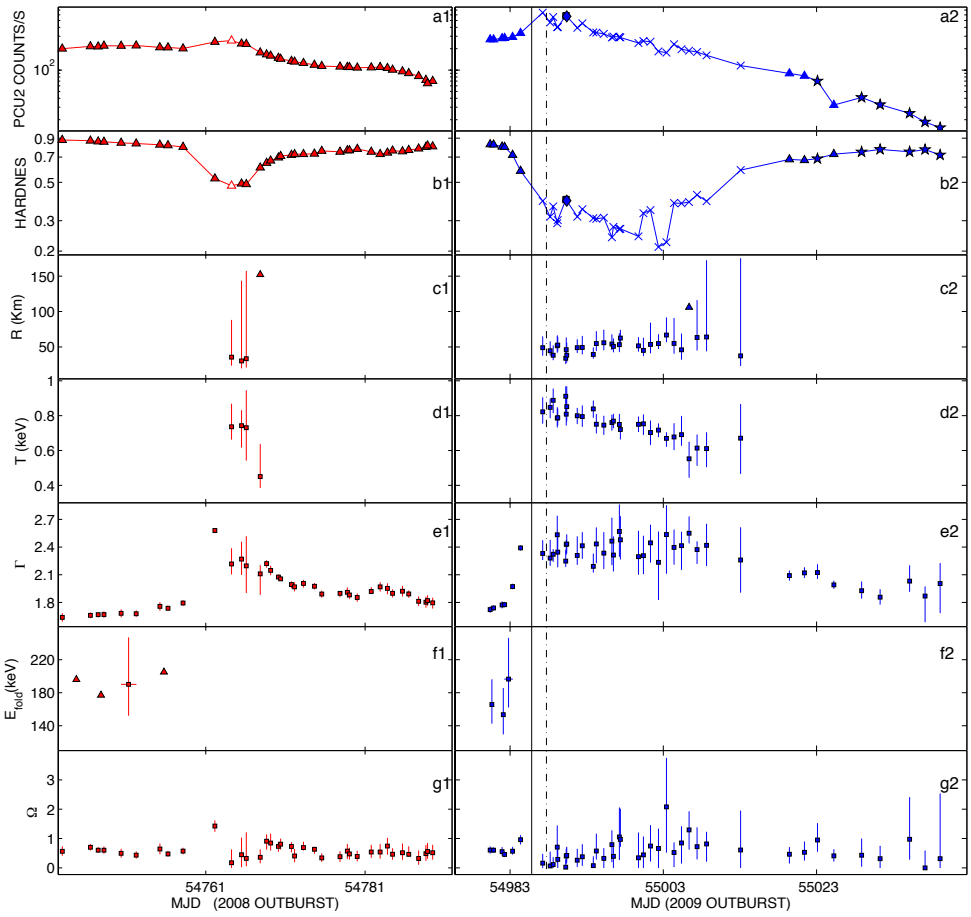

Figure 7.1: Evolution of net count rate, hardness and main spectral parameters during the 2008 (red) and 2009 (blue) outburst of H1743-322 (see Tabs. 7.3 and 7.6. From top to bottom: net PCU2 count rate, hardness ratio, inner disk radius in km (assuming a distance of 10 kpc and inclination of 65 degrees), disk temperature in keV at the inner disk radius, photon index, cutoff energy in keV, reflection factor. The solid line marks the transition from the HIMS to the SIMS and the dot-dashed line separates the SIMS from the HSS. Notice that only the primary transition from HIMS to SIMS is marked. The same transition takes place also later in the outburst (see text). No such transitions were observed in 2008. Points with horizontal error bars correspond to spectra obtained averaging observations with similar hardness: the error bars represent the time interval corresponding to the accumulation. In panel f, we used the values coming from Tab. 7.7. In panels a1, a2 and b1, b2 different symbols indicate different timing properties: type-A QPOs (diamonds), type-B QPOs (squares), type-C QPOs (filled triangles), strong band-limited noise components in the Power Density Spectrum (stars), weak band-limited noise components in the Power Density Spectrum (empty triangles), weak powerlaw noise in the Power Density Spectrum (crosses) Triangles in panels c1, c2 and f1, f2 mark upper limits.

- 20 (6.1 - 10.2 keV). A is the total count rate, while the hardness was defined as H = C/B (Homan & Belloni 2005). PCA+HEXTE spectra were fitted with XSPEC V. 11 in the energy range 3 - 22 keV and 20-200 keV respectively. To account for cross-calibration problems, a variable multiplicative constant for the HEXTE spectra (as compared to the PCA) was added to the fits.

For our timing analysis, we used custom software under IDL. For each observation we produced power density spectra (PDS) from stretches 16 seconds long in the channel band 0-35 (2-15 keV). We averaged the PDS and subtracted the contribution due to Poissonian noise (see Zhang et al. 1995) to produce a PDS for each observation. They were normalized according to Leahy et al. (1983) and converted to squared fractional rms (Belloni & Hasinger 1990). The integrated fractional rms was calculated over the 0.1 - 64 Hz band.

7.3 Results

7.3.1 The 2009 outburst of H1743-322

In this section, we describe the general evolution of the outburst. In Fig. 7.1 (panels a2 and b2) we show the count rate and hardness evolution of H1743-322 and in Fig. 7.2 we show the HID. In Tab.7.1 we list the background-corrected PCU2 count rate, the hardness ratio and the fractional rms for each observation.

As one can see from Fig. 7.2 (blue track), the source evolution during the 2009 outburst is consistent with the typical behavior observed in most other BHTs (see e.g. Gierliński & Newton 2006, Remillard & McClintock 2006, Belloni 2010, Fender et al. 2009). Unfortunately the data did not cover the whole evolution from quiescence and the right branch of the outburst (i.e. LHS) was missed. However, the source was followed during its evolution from the HIMS through all the remaining canonical states. We observed a clear horizontal branch in the HID characterized by a sligtly rising count rate and a progressive softening which drove the source from hard to soft state in few days. After a relatively long permanence in the soft state ($\sim$ 22 days), the transition from the soft back to the hard state took place at a lower count rate than the initial opposite transition, as expected.

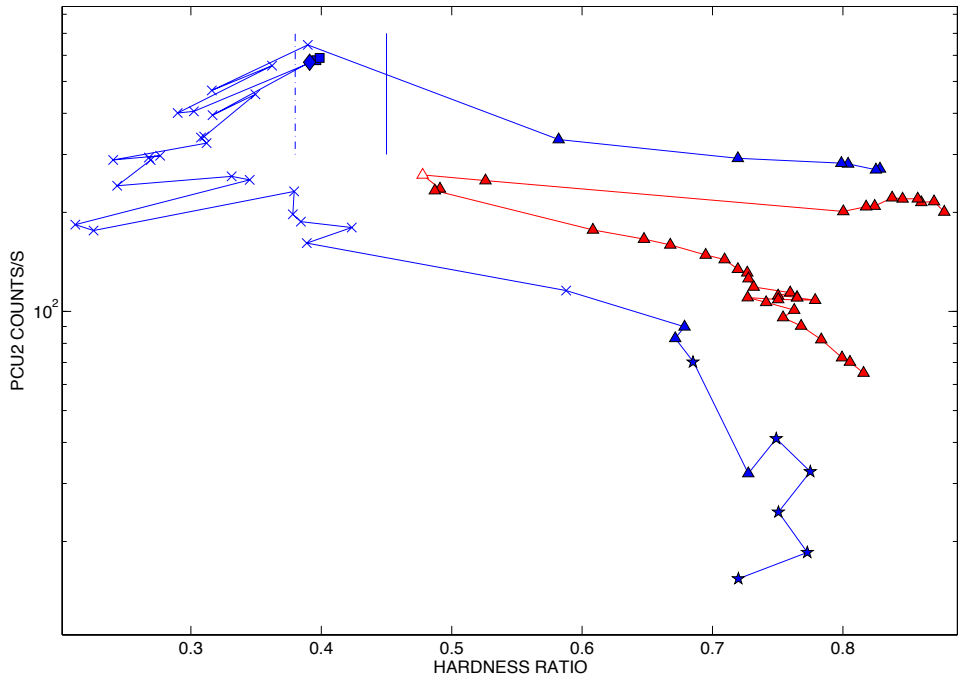

Figure 7.2: Hardness-Intensity diagram from RXTE/PCA data for the complete 2009 outburst (blue line) and 2008 outburst (red line). The two paths start from the upper right corner and proceed in a counter-clockwise direction. Different symbols indicate different timing properties: type-A QPOs (diamonds), type-B QPOs (squares), type-C QPOs (filled triangles), strong band-limited noise components in the Power Density Spectrum (stars), weak band-limited noise components in the Power Density Spectrum (empty triangles), weak powerlaw noise in the Power Density Spectrum (crosses). The solid line marks thetransition from the HIMS to the SIMS and the dot-dashed line separates the SIMS from the HSS.

Table 7.1: Outburst 2009. The columns are: observation number for the 2009 outburst, RXTE observation ID, MJD, PCU2 count rate, hardness ratio, integrated fractional rms (0.1 - 64 Hz), low-frequency QPO type, and state according to Belloni (2010).

Outburst 2009							
Obs no.	obs ID	MJD	color	PCU2 Counts s	rms	QPO	State
1	94413-01-02-00	54980.40	0.828 ± 0.004	271.2 ± 0.6	30.3 ± 0.4	C	HIMS
2	94413-01-02-02	54980.84	0.825 ± 0.003	269.5 ± 0.4	29.7 ± 0.4	C	HIMS
3	94413-01-02-01	54981.95	0.804 ± 0.004	280.9 ± 0.6	29.7 ± 0.4	C	HIMS
4	94413-01-02-05	54982.28	0.799 ± 0.004	282.2 ± 0.5	30.1 ± 0.3	C	HIMS
5	94413-01-02-04	54983.33	0.719 ± 0.003	291.9 ± 0.5	27.7 ± 0.3	C	HIMS
6	94413-01-02-03	54984.37	0.582 ± 0.002	333.1 ± 0.6	22.3 ± 0.1	C	HIMS
7	94413-01-03-00	54987.26	0.390 ± 0.002	645.3 ± 1.2	4.5 ± 0.9	-	SIMS
8	94413-01-03-01	54988.23	0.316 ± 0.001	469.6 ± 0.9	5.1 ± 0.5	-	HSS
9	94413-01-03-07	54988.63	0.362 ± 0.001	558.2 ± 1.0	3.4 ± 0.4	-	HSS
10	94413-01-03-05	54989.15	0.290 ± 0.002	400.8 ± 0.9	4.6 ± 0.7	-	HSS
11	94413-01-03-06	54989.22	0.302 ± 0.002	405.6 ± 0.9	5.7 ± 0.5	-	HSS
12	94413-01-03-02	54990.26	0.396 ± 0.002	580.1 ± 1.1	4.9 ± 0.9	B	SIMS
13	94413-01-03-03	54990.33	0.399 ± 0.002	589.3 ± 1.1	6.5 ± 0.6	B	SIMS
14	94413-01-03-04	54990.39	0.391 ± 0.002	571.6 ± 1.0	3.4 ± 0.3	A	SIMS
15	94413-01-03-08	54991.77	0.317 ± 0.001	394.7 ± 0.7	5.4 ± 0.3	-	HSS
16	94413-01-03-09	54992.43	0.349 ± 0.002	456.7 ± 0.9	3.2 ± 0.7	-	HSS
17	94413-01-03-10	54993.86	0.310 ± 0.001	340.1 ± 0.7	7.5 ± 0.4	-	HSS
18	94413-01-04-00	54994.25	0.308 ± 0.002	337.6 ± 0.8	6.0 ± 1.2	-	HSS
19	94413-01-04-01	54995.23	0.312 ± 0.002	324.7 ± 0.8	5.2 ± 0.8	-	HSS

Continued on next page

Table 7.1 – continued from previous page

Outburst 2009							
Obs no.	obs ID	MJD	color	PCU2 Counts s	rms	QPO	State
20	94413-01-04-03	54996.28	0.240 ± 0.001	288.7 ± 0.7	4.8 ± 1.7	-	HSS
21	94413-01-04-02	54996.48	0.276 ± 0.001	297.3 ± 0.6	4.7 ± 1.3	-	HSS
22	94413-01-04-08	54997.26	0.268 ± 0.002	293.5 ± 0.7	3.7 ± 1.2	-	HSS
23	94413-01-04-05	54997.39	0.269 ± 0.001	288.4 ± 0.7	4.9 ± 1.5	-	HSS
24	94413-01-04-06	54999.75	0.243 ± 0.001	241.0 ± 0.6	3.6 ± 1.3	-	HSS
25	94413-01-04-04	55000.40	0.331 ± 0.002	257.3 ± 0.6	5.2 ± 1.4	-	HSS
26	94413-01-05-00	55001.32	0.345 ± 0.002	251.1 ± 0.6	7.0 ± 0.6	-	HSS
27	94413-01-05-01	55002.36	0.211 ± 0.001	183.5 ± 0.5	2.1 ± 2.2	-	HSS
28	94413-01-05-02	55003.41	0.225 ± 0.001	176.2 ± 0.4	1.7 ± 2.6	-	HSS
29	94413-01-05-03	55004.39	0.379 ± 0.002	231.6 ± 0.5	6.4 ± 0.7	-	HSS
30	94413-01-05-04	55005.37	0.378 ± 0.002	197.3 ± 0.5	7.5 ± 0.6	-	HSS
31	94413-01-05-05	55006.35	0.384 ± 0.002	187.5 ± 0.4	6.8 ± 0.7	-	HSS
32	94413-01-05-06	55007.40	0.423 ± 0.002	179.9 ± 0.4	9.4 ± 0.4	-	HSS
33	94413-01-06-00	55008.64	0.389 ± 0.002	161.3 ± 0.4	9.2 ± 0.7	-	HSS
34	94413-01-06-01	55013.09	0.588 ± 0.005	115.7 ± 0.4	12.9 ± 1.6	-	HSS
35	94413-01-07-00	55016.32	1.266 ± 0.011	205.6 ± 0.8	16.6 ± 1.6	C	HIMS
36	94413-01-07-01	55019.45	0.679 ± 0.006	89.9 ± 0.3	19.8 ± 0.4	C	HIMS
37	94413-01-07-02	55021.42	0.671 ± 0.006	82.9 ± 0.4	18.8 ± 0.5	C	HIMS
38	94413-01-08-02	55023.11	0.685 ± 0.008	70.2 ± 0.4	18.5 ± 2.9	-	HIMS
39	94413-01-08-00	55025.25	0.727 ± 0.005	32.2 ± 0.1	18.1 ± 0.5	C	HIMS
40	94413-01-08-01	55028.88	0.749 ± 0.011	41.1 ± 0.3	16.9 ± 2.8	-	LHS
41	94413-01-09-00	55031.29	0.775 ± 0.011	32.6 ± 0.3	18.6 ± 2.3	-	LHS

Continued on next page

Table 7.1 – continued from previous page

Outburst 2009							
Obs no.	obs ID	MJD	color	PCU2 Counts s	rms	QPO	State
42	94413-01-09-01	55035.14	0.751 ± 0.013	24.6 ± 0.2	18.0 ± 3.1	-	LHS
43	94413-01-10-00	55037.16	0.773 ± 0.014	18.5 ± 0.2	15.5 ± 9.0	-	LHS
44	94413-01-10-01	55039.12	0.720 ± 0.016	15.4 ± 0.2	13.0 ± 10.0	-	LHS

Timing Analysis

Source states are defined on the basis of both spectral and timing properties (for a detailed description of state classification see Homan & Belloni 2005; Belloni 2005; Belloni 2010, Fender et al. 2009). Thus, timing information (i.e. PDS) is needed in order to identify the branches we see in the HID in terms of states. This will serve as a framework for the spectral analysis (see Sec. 7.3.1). In Tab. 7.2 we outline the main conclusions extracted from the PDS analysis.

- Observations $\#1$ to $\#6$ and observation $\#35$ to $\#39$ show a high level of aperiodic variability in the form of strong band-limited noise component (flat top noise shape), with total integrated fractional rms in the range $17 - 30\%$. The rms is positively correlated with hardness. The PDS can be decomposed in a number of Lorentzian components, one of which takes the form of a type-C QPO peak (see Casella et al. (2004) for a complete QPO classification). The observations correspond to the first part of the horizontal branch (Fig. 7.2, triangles). These observations belong to the HIMS.

- Observation #7 shows a weak variability level and a powerlaw shape noise, associated to a low fractional rms value ($\sim 5\%$). These values and the hardness are consistent with the values observed in observations $\#12$, $\#13$ and $\#14$, where the systems is in the SIMS (see below). No QPOs are observed here. However we note that Type-A QPOs are not always detected in PDS associated to the SIMS due to their faintness. We tentatively classify this observation as SIMS.

- Observations $\#8$ to $\#11$ and $\#15$ to $\#34$ show weak powerlaw noise with a rms of a few percent. They correspond to the softest observations. All these observations are marked with crosses in the HID in Fig. 7.2 and belongs to the HSS.

- Observations $\#12$ and $\#13$ correspond to a low variability ($\sim 5 - 6\%$ fractional rms). A type-B QPO is prominent in the PDS, significanly different from the ones observed in the LHS and in the HIMS (see Motta et al. 2009, Belloni 2005; Belloni et al. 2008). These observations are marked in the HID (Fig. 7.2) with diamonds and are classified as SIMS.

- Observation $\#14$ shows a Type-A QPO and has an integrated fractional rms of $\sim 3.4\%$. This observation is also softer than the two showing a Type-B QPO. This observations also belongs to the SIMS (in the middle of the HID, Fig. 7.2) and is marked in the HID with a square.

- Observation from $\#40$ to $\#44$ show a quite high level of aperiodic variability in the form of strong band-limited noise components, with fractional rms in the

2009 Outburst			
#obs ID	Noise Type	QPO type	RMS (in %)
#1 to #6, #35 to #39	strong band limited noise	C	17-30%
#7	weak powerlaw component	-	5%
#8 to #11; #15 to #34	weak powerlaw component	-	3-12%
#12,#13	weak powerlaw component	B	5-6%
#14	weak powerlaw component	A	3.4%
#40 to #44	strong band limited noise	C	13-18%

Table 7.2: Summary of the timing properties seen in the PDS of each observation from the 2009 outburst.

range $13 - 18\%$. The PDS are similar to those observed during the HIMS and can be decomposed in a number of Lorentzian components. These observations correspond to the vertical branch of the HID in Fig. 7.2 (stars), when the source undergoes the final hardening before the quiescence phase. These observations belong to the LHS.

On the basis of the state classification, we can identify three main transitions and one backward transition during the softening of the source. Here by we will call main transitions to the ones that take place in the HIMS-SIMS-HSS direction for the first time and secondary the following transitions in the same directions. Backward transitions take place in the inverse direction.

- Main transition from HIMS to SIMS, taking place between observations $\#6$ and $\#7$ at hardness ~ 0.4.
- Main transition from SIMS to HSS, taking place between observations $\#7$ and $\#8$ at hardness ~ 0.35.
- A secondary transition from SIMS to HSS, taking place between Obs. #14 and #15, at hardness ~ 0.35.
- Backward transition from HSS to SIMS, taking place between observations $\#11$ and $\#12$ at hardness ~ 0.3. As it is often observed in other sources (Motta et al. 2009, Del Santo et al. 2009) the SIMS is crossed several times during the outburst evolution, either in the HISM-SIMS-HSS direction or in the opposite one.

Lines corresponding to the main transitions are shown in Fig. 1 and Fig. 2.

Table 7.3: Spectral parameters for the 2009 outburst of H1743-322. Columns are: observation number, inner disc temperature kT, inner disc radius R (assuming a distance of 10 kpc and an inclination of 65 ^{o}), photon index Γ, fold Energy E_{fold} (corresponding to high energy cutoff), reflection factor Ω.

Outburst 2009					
obs no.	kT (keV)	R (Km)	Γ	$E_f(keV)$	Ω
1	–	–	$1.72^{+0.03}_{-0.03}$	148^{+43}_{-29}	$0.6^{+0.1}_{-0.1}$
2	–	–	$1.74^{+0.03}_{-0.03}$	170^{+42}_{-29}	$0.6^{+0.1}_{-0.1}$
3	–	–	$1.77^{+0.04}_{-0.03}$	156^{+62}_{-37}	$0.6^{+0.1}_{-0.1}$
4	–	–	$1.78^{+0.03}_{-0.03}$	164^{+55}_{-29}	$0.5^{+0.1}_{-0.1}$
5	–	–	$1.97^{+0.03}_{-0.03}$	> 200	$0.6^{+0.1}_{-0.1}$
6	–	–	$2.39^{+0.02}_{-0.03}$	> 200	$1.0^{+0.1}_{-0.2}$
7	$0.82^{+0.08}_{-0.07}$	49^{+16}_{-11}	$2.33^{+0.14}_{-0.07}$	> 200	$0.2^{+0.3}_{-0.2}$
8	$0.85^{+0.05}_{-0.06}$	45^{+13}_{-7}	$2.28^{+0.20}_{-0.08}$	> 200	$0.1^{+0.5}_{-0.1}$
9	$0.89^{+0.07}_{-0.07}$	38^{+14}_{-7}	$2.32^{+0.05}_{-0.08}$	> 200	$0.1^{+0.2}_{-0.1}$
10	$0.79^{+0.06}_{-0.05}$	52^{+14}_{-10}	$2.53^{+0.20}_{-0.22}$	> 200	$0.7^{+0.7}_{-0.5}$
11	$0.79^{+0.05}_{-0.04}$	53^{+12}_{-9}	$2.35^{+0.17}_{-0.16}$	> 200	$0.3^{+0.5}_{-0.3}$
12	$0.91^{+0.05}_{-0.11}$	34^{+14}_{-8}	$2.25^{+0.12}_{-0.06}$	> 200	$0.0^{+0.3}_{-0.0}$
13	$0.81^{+0.10}_{-0.06}$	46^{+17}_{-11}	$2.43^{+0.05}_{-0.11}$	> 200	$0.4^{+0.3}_{-0.3}$
14	$0.85^{+0.12}_{-0.08}$	38^{+18}_{-10}	$2.43^{+0.10}_{-0.10}$	> 200	$0.4^{+0.3}_{-0.2}$
15	$0.80^{+0.04}_{-0.05}$	49^{+11}_{-7}	$2.31^{+0.20}_{-0.10}$	> 200	$0.3^{+0.4}_{-0.2}$
16	$0.79^{+0.06}_{-0.06}$	49^{+16}_{-9}	$2.41^{+0.15}_{-0.14}$	> 200	$0.4^{+0.4}_{-0.3}$
17	$0.84^{+0.05}_{-0.05}$	39^{+10}_{-6}	$2.19^{+0.14}_{-0.07}$	> 200	$0.1^{+0.3}_{-0.1}$
18	$0.75^{+0.06}_{-0.05}$	55^{+17}_{-10}	$2.43^{+0.18}_{-0.21}$	> 200	$0.6^{+0.6}_{-0.3}$
19	$0.75^{+0.05}_{-0.06}$	56^{+18}_{-10}	$2.33^{+0.23}_{-0.17}$	> 200	$0.3^{+0.3}_{-0.3}$

Continued on next page

Table 7.3 – continued from previous page

Outburst 2009					
Obs no.	kT (keV)	R (Km)	Γ	$E_f(keV)$	Ω
20	$0.76^{+0.04}_{-0.05}$	54^{+13}_{-8}	$2.46^{+0.25}_{-0.26}$	> 200	$0.8^{+0.5}_{-0.6}$
21	$0.77^{+0.04}_{-0.04}$	51^{+11}_{-8}	$2.31^{+0.20}_{-0.18}$	> 200	$0.4^{+0.3}_{-0.4}$
22	$0.75^{+0.06}_{-0.03}$	53^{+16}_{-10}	$2.57^{+0.29}_{-0.27}$	> 200	$1.1^{+1.0}_{-0.8}$
23	$0.72^{+0.06}_{-0.04}$	63^{+11}_{-9}	$2.48^{+0.26}_{-0.21}$	> 200	$1.0^{+1.0}_{-0.2}$
24	$0.75^{+0.04}_{-0.04}$	52^{+12}_{-8}	$2.30^{+0.28}_{-0.20}$	> 200	$0.3^{+0.9}_{-0.3}$
25	$0.75^{+0.05}_{-0.06}$	45^{+18}_{-8}	$2.31^{+0.21}_{-0.20}$	> 200	$0.4^{+0.6}_{-0.4}$
26	$0.70^{+0.07}_{-0.07}$	54^{+31}_{-12}	$2.45^{+0.19}_{-0.21}$	> 200	$0.7^{+0.7}_{-0.5}$
27	$0.72^{+0.04}_{-0.04}$	55^{+13}_{-8}	$2.23^{+0.33}_{-0.41}$	> 200	$0.7^{+0.7}_{-0.7}$
28	$0.67^{+0.03}_{-0.05}$	67^{+25}_{-10}	$2.54^{+0.32}_{-0.42}$	> 200	$2.1^{+1.7}_{-1.6}$
29	$0.68^{+0.08}_{-0.07}$	55^{+36}_{-14}	$2.40^{+0.19}_{-0.18}$	> 200	$0.5^{+0.3}_{-0.5}$
30	$0.69^{+0.11}_{-0.06}$	46^{+23}_{-14}	$2.42^{+0.15}_{-0.26}$	> 200	$0.9^{+0.6}_{-0.7}$
31	$0.55^{+0.10}_{-0.11}$	106^{+318}_{-36}	$2.55^{+0.18}_{-0.11}$	> 200	$1.3^{+0.6}_{-0.7}$
32	$0.61^{+0.08}_{-0.10}$	63^{+52}_{-18}	$2.37^{+0.09}_{-0.15}$	> 200	$0.7^{+0.7}_{-0.4}$
33	$0.61^{+0.09}_{-0.11}$	64^{+108}_{-20}	$2.42^{+0.23}_{-0.22}$	> 200	$0.8^{+0.4}_{-0.6}$
34	$0.67^{+0.20}_{-0.20}$	37^{+138}_{-14}	$2.26^{+0.35}_{-0.35}$	> 200	$0.6^{+1.3}_{-0.6}$
35	—	—	$2.36^{+0.06}_{-0.07}$	> 200	$0.9^{+0.4}_{-0.4}$
36	—	—	$2.09^{+0.05}_{-0.05}$	> 200	$0.5^{+0.2}_{-0.3}$
37	—	—	$2.12^{+0.06}_{-0.05}$	> 200	$0.5^{+0.4}_{-0.3}$
38	—	—	$2.12^{+0.09}_{-0.07}$	> 200	$0.9^{+0.6}_{-0.4}$
39	—	—	$1.99^{+0.04}_{-0.04}$	> 200	$0.4^{+0.2}_{-0.2}$
40	—	—	$1.93^{+0.10}_{-0.08}$	> 200	$0.4^{+0.6}_{-0.4}$
41	—	—	$1.86^{+0.08}_{-0.08}$	> 200	$0.3^{+0.4}_{-0.3}$

Continued on next page

Table 7.3 – continued from previous page

Outburst 2009					
Obs no.	kT (keV)	R (Km)	Γ	$E_f(keV)$	Ω
42	–	–	$2.03^{+0.17}_{-0.11}$	> 200	$1.0^{+1.4}_{-0.7}$
43	–	–	$1.87^{+0.10}_{-0.28}$	> 200	$0.0^{+0.6}_{-0.0}$
44	–	–	$2.01^{+0.22}_{-0.32}$	> 200	$0.3^{+2.2}_{-0.3}$

Spectral Analysis

Given the multitude of spectral models available, we tested several ones in a first approach. This method has been already adopted for other sources (GX 339-4, Nowak et al. 2002; Cyg X-1, Wilms et al. 2005). We started with a model consisting of only one component, either a cutoff power law or a multicolor disk blackbody, but neither could fit the spectra. Better results were obtained with a combination of these two components. However, this model does not yield good fits for all the observations: clear residuals around 30 keV are observed for some cases. They appear at the beginning and at the end of the outburst and we interpreted them as evidence of reflection of the Comptonized emission on relatively cold matter (i.e. the accretion disk). Moreover, during the initial and final periods of the outburst, the disk component has normalization values too low to be physically acceptable[2]. This model was used by C09 to fit the spectra corresponding to the 2008 outburst. The model is not able to fit the observations that do not present a disk blackbody component. As mentioned above, an additional reflection component was required in order to get acceptable fits of the spectra without a visible disk component. Considering that, if a disk component is observable, the reflection component is expected to be proportional to the disk flux and correlated with the photon index (see Gilfanov 2010 and reference therein), we concluded that the model is not able to describe the spectrum in a physical way.

Following Wilms et al. (2006), Nowak et al. (2005) and Muñoz-Darias et al. 2010b, we tried to model the data with an absorbed broken (elbow-shaped) power law associated to an exponentially high-energy cutoff. Even though the broken power-law shape mimics the effect of reflection, which is clearly seen in this source (see below), the fits suffered the same problems than using the cutoff powerlaw+diskblackbody model. We conclude that they are due to an oversimplification of the model itself, which is not sufficient to give a valid description of the spectra possibly because of the complex reflection features observed.

In order to obtain good fits and acceptable physical parameters, a model consisting of an exponentially cut off power law spectrum reflected from neutral material (Magdziarz & Zdziarski 1995) was used (`pexrav`[3] in Xspec). An gaussian emission line with centroid fixed at 6.4 keV was further needed in order to obtain acceptable fits. The iron width was constrained between 0.2 and 1.2 keV to prevent artificial

[2]Assuming a $10M_{\odot}$ black hole, the gravitational radius should be $\sim$ 30 km. The normalizations found range between $\sim$5 and $\sim$230, leading to inner disk radii ranging between $>$3-19 km (assuming an inclination angle $< 65^{o}$). This means that the maximum inner disk radius found is 0.62 gravitational radii, too small from a physical point of view.

[3]The output spectrum consists of a power law with a high-energy cutoff combined with reflection from a neutral medium. $\Omega/2\pi$ represents the fraction of the hard X-ray radiation emitted towards the disc where it is reflected.

broadening due to the bad response of XTE/PCA at 6.4 keV. The use of `pexrav` is justified by the presence of the iron line in all the spectra. In addition, a multi-color disk-blackbody (`diskbb`) was added to the model. A hydrogen column density was used (`wabs` in XSPEC), with N_H frozen to $1.6 \times 10^{22} \mathrm{cm}^{-2}$, the value derived from *Swift*/XRT (C09).

We tried to further improve the fits by adding an iron edge component to the model. This is justified by te fact that an iron edge is expected when the iron line is visible. The iron edge component was added with energy constrained between 6 and 10 keV and free optical depth. Although the χ^2_{red} was generally slightly lower for most of the observations, the absorption edge was not well constrained. It tends to move to high energies, reaching the higher limit we imposed. In addition, the component is often not clearly significant and the optical depth obtained is usually lower than $\sim$ 0.1. We then concluded that the addition of the iron absorption edge is not justified. Even though we cannot exclude the presence of the iron edge component, we can assert that, if present, it is too faint to be clearly observed and constrained.

Not all the components of the model are present trough the outburst evolution. At the beginning and at the end of the outburst (Observations #1 to #6 and Observations #35 to #44), no significant disk emission is observed in the spectra (see Fig. 7.3, top spectrum). Here, the model used did not contain the disk component and it yielded an average χ^2_{red} of $\sim$ 1.02 for 81 degrees of freedom (d.o.f.). During the central part of the outburst (from $\#7$ to $\#34$), the disk component is present, yielding an average reduced χ^2 of 1.2 for 79 d.o.f. (see Fig. 7.3, bottom spectrum). The time evolution of the spectral parameters is shown in Fig. 7.1 (panels c2 to g2). The observations started in the HIMS. During the first days of the HIMS, the source exhibited a rapid rise in flux, which reached the maximum value of the outburst in less than 8 days.

From Fig. 7.1 we notice that, as the source is moving through the HIMS, the photon index rises from $\sim$ 1.7 to $\sim$ 2.4 in less than 4 days (from Obs. #1 to Obs. #6). This progressive softening of the source is possibly associated with the rise of a soft component related to the accretion disk emission. Despite the softening, the multicolor disk component is not directly observable in the spectrum until observation $\#7$, probably because of the low temperature of the accretion disk. From observation $\#7$ the photon index remains between $\sim$ 2.3 and $\sim$ 3.1. After Obs $\#35$, when the source is about to come back to the LHS, the photon index sensibly decreases to values lower than $\sim$ 2.1. As it is expected, the higher values of the photon index (over $\sim$ 2.1) correspond to the phases in which the multicolor disk component is visible in the spectra (from Obs. #7 to Obs. #34). The high-energy cut-off is present during the HIMS, from observation $\#1$ to $\#5$. During this period it ranges between $\sim$ 140 keV and $\sim$ 200 keV. The large error bars no not allow to check for variability in the cutoff energy. Because of the response of HEXTE at its highest energies, the cutoff values are not well constrained over $\sim$180 keV. From observation $\#5$ on the

cutoff energy, if present, is over 200 keV. In order to check for the absence/presence of an high-energy cut-off in proximity of the HIMS/SIMS transition, we averaged spectra with similar hardness and compatible spectral parameters to accumulate better statistics. The mean spectra show values of the high-energy cutoff consistent with the values from single observations, although slightly better constrained. Although the large error bars still make it difficult to pinpoint a precise evolution of the high-energy cutoff, it is possible to say that it seems to decrease and then increase as the source approaches the soft states. The results are summarized in table 7.7 and the mean values obtained for the cutoff are shown in Fig. 7.1 (panel f2).

The disk component is not present between observations #1 to #6. When it appears, in correspondence to the transition to the SIMS (Obs. #7), the inner disk radius appears to be consistent with constant [4]). The values for Obs. #28 to #33 are not well constrained because of the low photon count. During this phase, the source goes back to harder states and the disk emission is expected to drop and disappear again from the PCA band. The temperature of the disk decreases as the source softes, moving from ~ 0.9 keV to ~ 0.5 keV. The reflection scaling factor remains almost constant during the whole outburst, showing slightly higher values when the disk component is visible. This is expected if the reflected emission is due to reprocessing of the corona emission by the disc.

7.3.2 The 2008 outburst of H1743-322

We extended the analysis described for the 2009 outburst to the 2008 outburst.

As can be seen in Fig. 7.2 (red track), the source traces a different path during the 2008 outburst. Following the HID (Fig. 7.2, red track), we see that the source moves horizontally to the left, then jumps to a softer state, from which it slowly returns to the hard track along a diagonal path. As one can see, the softest points of the second outburst reach intermediate values of the hardness (~ 0.5), corresponding to the HIMS of the 2009 outburst. This is clearly seen in Fig. 7.1 (panel b1 and b2): the 2008 outburst (red track) is harder than the 2009 one.

[4]The radius varies between ~ 25 and $\sim$80 km. Assuming a distance of ~ 10 kpc and a $\sim 65^o$ disk inclination angle (McClintock et al. 2009)

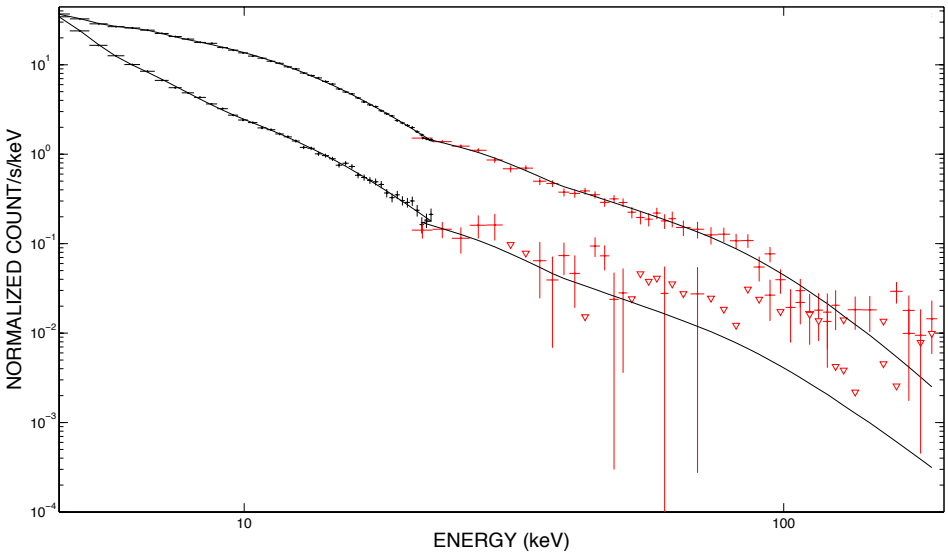

Figure 7.3: Examples of spectral fits resulted from the combined PCA and HEXTE spectra taken during the 2009 outburst of H1743-322. For both spectra we used a model consisting of interstellar absorption, a Gaussian emission line and a `pexrav` model. The top spectrum corresponds to the hardest observation of 2009 outburst (Obs. #1). The lower spectrum corresponds to the softest spectrum of 2009 outburst (Obs. #26). In this latter spectrum a disk blackbody component had to be added to the model.

Table 7.4: Outburst 2008. The columns are: observation number for 2008 outburst, RXTE observation ID, MJD, PCU2 count rate, hardness ratio, integrated fractional rms (0.001 - 64 Hz), QPO type, and state according to Belloni (2008).

Outburst 2008							
Obs no.	obs ID	MJD	color	PCU2 Counts s	rms	QPO	State
1	93427-01-09-00	54742.98	0.878 ± 0.006	200.6 ± 0.6	29.7 ± 0.8	C	HIMS
2	93427-01-09-01	54746.51	0.870 ± 0.004	215.8 ± 0.4	30.4 ± 0.3	C	HIMS
3	93427-01-09-03	54747.49	0.860 ± 0.004	214.6 ± 0.4	29.7 ± 0.3	C	HIMS
4	93427-01-09-02	54748.21	0.857 ± 0.005	220.1 ± 0.5	29.7 ± 0.5	C	HIMS
5	93427-01-10-00	54750.37	0.846 ± 0.006	219.8 ± 0.6	29.6 ± 0.5	C	HIMS
6	93427-01-10-01	54752.26	0.838 ± 0.004	221.6 ± 0.5	29.6 ± 0.4	C	HIMS
7	93427-01-10-02	54755.23	0.824 ± 0.006	209.1 ± 0.6	29.6 ± 0.5	C	HIMS
8	93427-01-11-00	54756.25	0.818 ± 0.004	208.1 ± 0.4	28.9 ± 0.2	C	HIMS
9	93427-01-11-01	54758.15	0.800 ± 0.004	201.3 ± 0.4	28.0 ± 0.2	C	HIMS
10	93427-01-11-03	54762.14	0.526 ± 0.002	249.8 ± 0.5	16.3 ± 0.4	C	HIMS
11	93427-01-12-00	54764.24	0.478 ± 0.003	260.0 ± 0.6	9.8 ± 1.0	-	HIMS
12	93427-01-12-03	54765.49	0.491 ± 0.003	235.8 ± 0.5	12.2 ± 0.4	C	HIMS
13	93427-01-12-01	54766.09	0.487 ± 0.003	233.0 ± 0.6	12.1 ± 0.5	C	HIMS
14	93427-01-12-04	54767.84	0.608 ± 0.003	176.9 ± 0.4	19.5 ± 0.3	C	HIMS
15	93427-01-12-02	54768.64	0.647 ± 0.004	165.9 ± 0.5	21.9 ± 0.8	C	HIMS
16	93427-01-12-05	54769.14	0.668 ± 0.005	159.3 ± 0.5	21.6 ± 0.5	C	HIMS
17	93427-01-13-00	54770.12	0.695 ± 0.003	148.5 ± 0.3	23.4 ± 0.3	C	HIMS
18	93427-01-13-05	54770.40	0.709 ± 0.004	143.8 ± 0.3	24.0 ± 0.3	C	HIMS
19	93427-01-13-04	54771.76	0.719 ± 0.004	134.4 ± 0.3	23.7 ± 0.3	C	HIMS

Continued on next page

Table 7.4 – continued from previous page

Outburst 2008							
Obs no.	obs ID	MJD	color	PCU2 Counts s	rms	QPO	State
20	93427-01-13-01	54772.15	0.727 ± 0.006	131.1 ± 0.5	24.3 ± 0.6	C	HIMS
21	93427-01-13-02	54773.27	0.728 ± 0.005	125.8 ± 0.4	23.8 ± 0.5	C	HIMS
22	93427-01-13-06	54774.64	0.732 ± 0.004	118.7 ± 0.3	23.9 ± 0.3	C	HIMS
23	93427-01-13-03	54775.56	0.760 ± 0.005	114.1 ± 0.3	24.4 ± 0.4	C	HIMS
24	93427-01-14-00	54777.86	0.750 ± 0.005	111.6 ± 0.3	23.7 ± 0.4	C	HIMS
25	93427-01-14-01	54778.77	0.765 ± 0.006	110.4 ± 0.4	22.5 ± 1.2	C	HIMS
26	93427-01-14-02	54779.04	0.765 ± 0.006	110.0 ± 0.4	24.6 ± 0.4	C	HIMS
27	93427-01-14-03	54780.02	0.779 ± 0.006	108.2 ± 0.4	25.1 ± 1.0	C	HIMS
28	93427-01-14-04	54781.78	0.750 ± 0.006	108.8 ± 0.4	25.6 ± 0.6	C	HIMS
29	93427-01-14-05	54782.89	0.727 ± 0.005	110.2 ± 0.4	23.7 ± 0.4	C	HIMS
30	93427-01-14-06	54783.81	0.741 ± 0.006	106.6 ± 0.4	23.0 ± 0.4	C	HIMS
31	93427-01-15-00	54784.45	0.763 ± 0.006	101.0 ± 0.3	23.9 ± 0.6	C	HIMS
32	93427-01-15-01	54785.70	0.754 ± 0.006	95.8 ± 0.4	22.8 ± 0.5	C	HIMS
33	93427-01-15-02	54786.48	0.768 ± 0.005	90.4 ± 0.3	22.6 ± 0.5	C	HIMS
34	93427-01-15-03	54787.73	0.783 ± 0.007	82.1 ± 0.3	21.4 ± 0.6	C	HIMS
35	93427-01-15-04	54788.64	0.799 ± 0.008	72.4 ± 0.3	21.3 ± 1.1	C	HIMS
36	93427-01-15-06	54789.49	0.805 ± 0.008	70.2 ± 0.3	23.2 ± 1.0	C	HIMS
37	93427-01-15-05	54788.84	0.816 ± 0.008	65.0 ± 0.3	20.6 ± 1.0	C	HIMS

2008 Outburst			
#obs ID	Noise Type	QPO type	RMS (in %)
#1 to #10, #12 to #37	strong band limited noise	C	16-30%
#11	weak band limited noise	-	10%

Table 7.5: Timing properties seen in the PDS of each observation from the 2008 outburst.

Timing analysis

The timing analysis yielded the following results:

- Observations from $\#1$ to $\#10$ and from $\#12$ to $\#37$ show a high level of aperiodic variability in the form of strong band-limited noise components (flat top noise shape). The total integrated fractional rms is in the range $16 - 30\%$. The PDS can be decomposed in a number of Lorentzian components, one of which takes the form of a type-C QPO peak. These observations correspond to the triangles in Fig. 7.2.

- Observation $\#11$ corresponds to a slightly weaker variability ($\sim 10\%$ fractional rms). The PDS is consistent with a zero-centered Laurentian, rhough noisy, with no QPOs. This observation is the only one that does not show any QPO. This observation is marked with an empty triangle in the HID of Fig. 7.2 (red track).

Results are summarized in Tab 7.5.

On the basis of the PDS properties, all that observations can be classified as HIMS. This fact is supported by the hardness ratio values observed for the corresponding spectra. Observation $\#11$ shows timing properties which are consistent with the HIMS, even though no Type-C QPO is observed. However the non-detection is compatible with neighboring observations (see C09 for details).

Table 7.6: Spectral parameters of the 2008 outburst of H1743-322. Columns are: observation number, inner disc temperature kT, inner disc radius R (assuming a distance of 10 kpc and an inclination of 65 ^{o}), photon index Γ, fold Energy E_{fold} (corresponding to high energy cutoff), reflection factor Ω. The inner disk radii are calculated from the disk-blackbody normalization, defined as $(\frac{R_{in}/km}{D/10kpc})^2 cos\Theta$, where R_{in} is the inner disc radius (km), D is the distance to the source (kpc) and Θ is the inclination angle of the disk.

Outburst 2008					
obs no.	kT (keV)	R (Km)	Γ	$E_f(keV)$	Ω
1	–	–	$1.64^{+0.04}_{-0.04}$	> 200	$0.6^{+0.2}_{-0.1}$
2	–	–	$1.66^{+0.03}_{-0.03}$	> 200	$0.7^{+0.1}_{-0.1}$
3	–	–	$1.67^{+0.03}_{-0.03}$	> 200	$0.6^{+0.1}_{-0.1}$
4	–	–	$1.67^{+0.03}_{-0.03}$	> 200	$0.6^{+0.1}_{-0.1}$
5	–	–	$1.68^{+0.04}_{-0.04}$	195^{+115}_{-56}	$0.5^{+0.2}_{-0.1}$
6	–	–	$1.68^{+0.03}_{-0.03}$	183^{+74}_{-43}	$0.4^{+0.1}_{-0.1}$
7	–	–	$1.76^{+0.04}_{-0.04}$	> 200	$0.6^{+0.2}_{-0.2}$
8	–	–	$1.74^{+0.03}_{-0.03}$	> 200	$0.5^{+0.1}_{-0.1}$
9	–	–	$1.79^{+0.03}_{-0.03}$	> 200	$0.6^{+0.1}_{-0.1}$
10	–	–	$2.58^{+0.03}_{-0.03}$	> 200	$1.4^{+0.2}_{-0.2}$
11	$0.74^{+0.13}_{-0.07}$	36^{+52}_{-12}	$2.22^{+0.17}_{-0.11}$	> 200	$0.2^{+0.4}_{-0.2}$
12	$0.74^{+0.09}_{-0.12}$	30^{+113}_{-10}	$2.27^{+0.19}_{-0.17}$	> 200	$0.4^{+0.6}_{-0.4}$
13	$0.73^{+0.21}_{-0.19}$	34^{+124}_{-12}	$2.20^{+0.32}_{-0.29}$	> 200	$0.3^{+0.9}_{-0.3}$
14	$0.45^{+0.19}_{-0.06}$	> 77	$2.11^{+0.09}_{-0.23}$	> 200	$0.4^{+0.3}_{-0.2}$
15	–	–	$2.22^{+0.04}_{-0.04}$	> 200	$0.9^{+0.2}_{-0.3}$
16	–	–	$2.15^{+0.05}_{-0.05}$	> 200	$0.8^{+0.3}_{-0.3}$
17	–	–	$2.08^{+0.03}_{-0.03}$	> 200	$0.7^{+0.1}_{-0.2}$

Continued on next page

Table 7.6 – continued from previous page

Outburst 2008					
obs no.	kT (keV)	R (Km)	Γ	$E_f(keV)$	Ω
18	–	–	$2.06^{+0.03}_{-0.02}$	> 200	$0.8^{+0.2}_{-0.2}$
19	–	–	$1.99^{+0.03}_{-0.03}$	> 200	$0.7^{+0.1}_{-0.2}$
20	–	–	$1.97^{+0.04}_{-0.05}$	> 200	$0.4^{+0.2}_{-0.2}$
21	–	–	$2.01^{+0.04}_{-0.04}$	> 200	$0.7^{+0.2}_{-0.1}$
22	–	–	$1.98^{+0.03}_{-0.03}$	> 200	$0.6^{+0.1}_{-0.2}$
23	–	–	$1.89^{+0.03}_{-0.04}$	> 200	$0.3^{+0.1}_{-0.1}$
24	–	–	$1.90^{+0.02}_{-0.04}$	> 200	$0.4^{+0.2}_{-0.2}$
25	–	–	$1.91^{+0.06}_{-0.05}$	> 200	$0.6^{+0.2}_{-0.3}$
26	–	–	$1.88^{+0.04}_{-0.04}$	> 200	$0.5^{+0.2}_{-0.2}$
27	–	–	$1.85^{+0.04}_{-0.04}$	> 200	$0.4^{+0.2}_{-0.2}$
28	–	–	$1.92^{+0.04}_{-0.02}$	> 200	$0.5^{+0.2}_{-0.2}$
29	–	–	$1.97^{+0.05}_{-0.05}$	> 200	$0.5^{+0.3}_{-0.2}$
30	–	–	$1.95^{+0.05}_{-0.06}$	> 200	$0.7^{+0.3}_{-0.3}$
31	–	–	$1.90^{+0.04}_{-0.04}$	> 200	$0.5^{+0.2}_{-0.2}$
32	–	–	$1.92^{+0.06}_{-0.06}$	> 200	$0.5^{+0.3}_{-0.2}$
33	–	–	$1.89^{+0.04}_{-0.04}$	> 200	$0.5^{+0.3}_{-0.2}$
34	–	–	$1.81^{+0.05}_{-0.05}$	> 200	$0.3^{+0.3}_{-0.2}$
35	–	–	$1.80^{+0.06}_{-0.06}$	> 200	$0.5^{+0.3}_{-0.2}$
36	–	–	$1.80^{+0.05}_{-0.06}$	> 200	$0.5^{+0.3}_{-0.2}$
37	–	–	$1.82^{+0.06}_{-0.05}$	> 200	$0.6^{+0.3}_{-0.2}$

Spectral analysis

We applied to the 2008 outburst the same approach we adopted for the 2009 outburst. A model consisting in a simple cutoff powerlaw plus disk-blackbody component as well as a broken powerlaw with high-energy cutoff plus disk-blackbody was firstly tested. As for the 2009 data, the resulting fits are good for the central part of the outburst, but they are not for the beginning and ending phases (see Sec. 7.3.1). Again, the resulting normalization of the disk-blackbody component yielded inner radius values too small to be accepted.

We therefore adopted the same model as for the 2009 outburst (pexrav+disk-blackbody) . We found that the disk black-body component is required only for the very central part of the outburst in correspondence with the softest points of the HID (Obs. #11 to #14). This is probably due to the faintness of the accretion disk, which is likely too cold to be clearly detected by PCA. The fits for those observations yield an average $\chi^2_{\rm red}$ of 1.08 for 79 d.o.f. (see Fig. 7.4, bottom spectrum). In observations #11 to #14 the disk blackbody component has to be added to the model to account of the soft excess observed. All the other observations could be fitted without a disk blackbody component, yielding an average $\chi^2_{\rm red}$ of 0.98 for 81 d.o.f. (see Fig. 7.4, top spectrum).

The spectral evolution of H1743-322 during its 2008 outburst is shown in Fig. 7.1 (red tracks) and the corresponding values are reported in Tab. 7.6. As expected during the HIMS, the photon index remains nearly constant (ranging between 1.6 and 1.7). After that, it jumps to $\sim$ 2.6 in less then two days (at Obs. $\#10$). This is due to the appearance of a soft spectral component probably associated to the accretion disk, which becomes directly observable from observation $\#11$. After observation $\#10$ the photon index moves back to slightly lower values ($\sim$ 2.2) and then moves down to $\sim$ 1.8. This is the typical behaviour observed during the HIMS, when the system is backing towards the LHS. The high-energy cutoff is not well constrained for the 2008 outburst. The fits give values which in all the cases but two (observation $\#5$ and $\#6$) are too high to be considered acceptable (see Tab. 7.6). As for the 2009 outburst, we averaged spectra corresponding to similar hardness ratio in order to acquire better statistics. The mean spectra obtained show values of the high-energy cutoff consistent with the values of the single observation spectra and still too high to be considered reliable. However the mean spectrum of observations #5 and #6 shows a clearer cutoff at $\sim$ 180 keV. The results are summarized in table 7.7 and the mean values obtained for the cutoff are shown in panel f1 in Fig. 7.1).

The reflection-scaling factor remains nearly constant along the outburst. This could be explained by a lack of disk flux. Given that the reflection component is directly tied to the disk emission (see Sec. 7.4.2), the low reflection component is consistent to the presence of a faint disk (i.e. low disk flux, see Fig. 7.5).

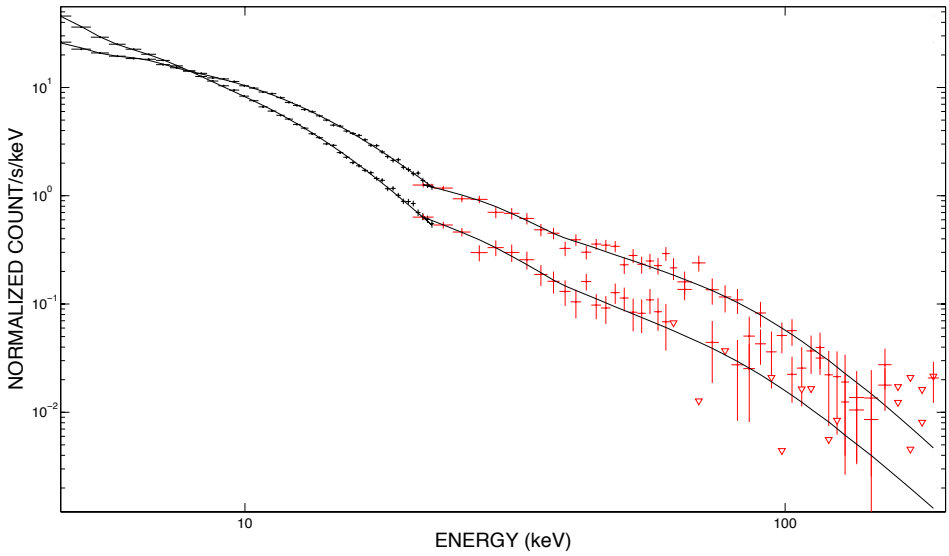

Figure 7.4: Examples of spectral fits from the combined PCA and HEXTE spectra taken during the 2008 outburst of H1743-322. For both spectra we used a model consisting of interstellar absorption, a Gaussian emission line and a `pexrav` model. The top spectrum corresponds to the hardest observation of 2008 outburst (i.e. Obs. #1). The lower spectrum corresponds to the softest spectrum of 2009 outburst (i.e. Obs. #11). In this latter spectrum a disk blackbody component had to be added to the fit.

7.4 Discussion

The different behaviour shown by H1743-322 during its outburst evolution in 2008 and 2009 allow us to study the evolution of the spectral parameters of the system at different accretion regimes.

7.4.1 The 2009 outburst

Our results show that H1743-322 underwent a typical outburst between 2009 May 29 and 2009 July 27. The source probably went through a (missed) initial LHS and then crossed the HID following the upper horizontal branch (HIMS) of the HID. After a very short SIMS and a relatively long permanence in the HSS, the source went back to the LHS passing through the lower horizontal branch (HIMS). During the softening of the source two main transitions, a secondary transition and a backward transition have been identified. All the transitions took place at hardness values consistent with what is observed in other sources. To date now, the rising phase has not been observed for this source in any of the outbursts covered by RXTE. This is probably due to the fact that the transition from quiescence to HIMS is very fast and therefore difficult to be observed.

2008 Outburst					
obs no.	kT (keV)	R (Km)	Γ	E_f	Ω
$\#1, \#2$	–	–	$1.65^{+0.03}_{-0.03}$	> 200	$0.61^{+0.09}_{-0.09}$
$\#3, \#4$	–	–	$1.67^{+0.02}_{-0.02}$	> 200	$0.60^{+0.07}_{-0.07}$
$\#5, \#6$	–	–	$1.68^{+0.03}_{-0.03}$	190^{+57}_{-38}	$0.44^{+0.09}_{-0.09}$
$\#7, \#8$	–	–	$1.75^{+0.03}_{-0.03}$	> 200	$0.6^{+0.1}_{-0.1}$
2009 Outburst					
$\#1, \#2$	–	–	$1.73^{+0.02}_{-0.02}$	166^{+30}_{-23}	$0.60^{+0.07}_{-0.07}$
$\#3, \#4$	–	–	$1.77^{+0.02}_{-0.02}$	153^{+32}_{-23}	$0.53^{+0.09}_{-0.09}$
$\#4, \#5$	–	–	$1.88^{+0.02}_{-0.02}$	196^{+50}_{-34}	$0.52^{+0.07}_{-0.07}$

Table 7.7: Spectral parameters coming from spectra averaged across multiple observations (see text). Columns are: observation number, inner disc temperature kT, inner disc radius R (assuming a distance of 10 kpc and an inclination of 65 ^{o}), photon index Γ, fold Energy E_{fold} (corresponding to high-energy cutoff), reflection factor Ω. The inner disk radii are calculated from the disk-blackbody normalization, defined as $(\frac{R_{in}/km}{D/10kpc})^2 cos\Theta$, where R_{in} is the inner disc radius (km), D is the distance to the source (kpc) and Θ is the inclination angle of the disk.

The spectral parameters evolved consistently with the ones previously observed in the source (see Prat et al. 2009) and other sources (see e.g. Motta et al. 2009, Del Santo et al. 2009, Belloni et al. 2005 for GX 339-4; see Debnath et al. 2009 for GRO J1655-40):

- the photon index showed the expected evolution in relation to the variation of the spectral components. The appearance of the soft disk-blackbody component, together with the progressive cooling of the Comptonizing medium in the spectrum, is probably the reason for the photon index rising. Independently of whether the inner radius of the accretion disk moves inward or not, more soft photons will be emitted by the disk as the source becomes brighter. The photon input to the Comptonizing medium will therefore increase. This will steepen the spectrum and will cool the population of electrons (see Sunyaev & Titarchuk 1980). As observed for GX 339-4, changes in the photon index are observed across the transition from the HIMS to the HSS. It rises during the HIMS and becomes constant when the source reaches the HSS. Then it stays constant until the source enters again the HIMS, coming back to the LHS. As the source begins the hardening, the photon index decreases again.

- The high-energy cutoff evolution could not be observed in detail, mainly be-

cause of the lack of observation in the LHS (where the high-energy cutoff is expected to be observable (e.g. Motta et al. 2009). However, the values we obtained from our fits are consistent with the presence of a high-energy cutoff before the transition towards the soft states.

- The inner disk radius is consistent with remaining constant and small (being around 50 Km), although, given the large error bars, a scenario in which the inner disk radius moves inward or outward cannot be ruled out. Observation made at lower energies and during earlier phases of the outburst evolution could provide further information to define properly the geometry of the system.

- As it is expected, the reflection scaling factor is correlated to the photon index and to the disk parameters.

  The strength of the reflected component depends on the fraction of the Comptonized radiation intercepted by the accretion disk. The latter is defined by the geometry of the accretion flow, i.e. by the solid angle Ω_{disk} subtended by the accretion disk as seen from the Comptonizing region, and by the ionization state of the disk. The bigger is the fraction of Comptonized radiation, the stronger is expected to be the reflection component. As the emission that is Comptonized is produced in the accretion disk, softer spectra (i.e. where the disk emission dominates) have a stronger reflected component, yelding a larger equivalent width of the iron fluorescent line. The large amount of reflected radiation is consistent with the relative large observed iron line width (ranging between ~ 0.4 and 1.2 keV).

7.4.2 The peculiar nature of the 2008 outburst

The two observed outburst spanned slightly different luminosity ranges. The maximum luminosity (2.73-200 keV) in the 2008 was 2.45×10^{37} erg s^{-1} cm^{-2} while in the 2009 was 2.88×10^{37} erg s^{-1} cm^{-2}. As it was observed in other sources (see e.g. Belloni 2010), the maximum luminosities are correlated with the difference in count rate between the two horizontal branches of the HID, i.e. the higher is the luminosity reached, the bigger is the difference in count rate (Maccarone & Coppi 2003).

In the 2008 case the maximum luminosity is observed at the very beginning of the outburst, where the hard emission dominates, while in the 2009 case the maximum luminosity is observed in the soft state, where the disk component starts to dominate the spectrum. As most likely, the luminosity is directly related to the accretion rate. The fact that similar luminosities are reached during the two different outbursts is relevant. This could be interpreted as the consequence of two different mechanisms that lead the source towards the maximum luminosity. The difference between the two mechanism might also explain what causes the transition occourrence.

From the analysis shown above, it is clear that the 2008 outburst of H1743-322 was peculiar. The HID shape is similar to what is usually observed in other BHTs, but after the usual path through the HIMS, it returned to harder states with no sampling of SIMS/HSS. The softest point observed in the HID roughly corresponded to the last part of the HIMS.

The timing analysis has pointed out that some changes take place when the source is approaching the softest points in the HID. The fractional rms and the PDS evolve following the behavior observed in several other sources: the rms decreases while the frequencies of the Lorentzian components in the PDS moves towards higher values. No transition to the SIMS [5] is observed before the softest point of the HID is reached (Obs. #11). The softest observation (Obs. #11) presents the typical rms and hardness values of the HIMS and the PDS display the expected shape (i.e. flat top noise), although slightly noisy. It might be possible that Obs. #11 lays close to the transition to the SIMS. As the transition to the soft state is expected to be very fast (see Nespoli et al. 2003) and given that the SIMS is crossed in less than one day during the 2009 outburst, it is possible that the source reached the SIMS and perhaps the HSS during the period where it was not observed by RXTE ($\sim$ 30 hours).

The evolution of the spectral parameter during the two different outbursts puts in evidence the lack of observed soft states.

- As it happened for the 2009 outburst, the photon index slightly increases during the HIMS and then clearly changes its trend once the source reaches the softest point. After that, it did not remain constant as for the 2009 outburst, but suddenly decreased. The track followed by the photon index during the final part of the 2008 outburst is very similar to the one of the 2009 outburst.

- As it happened for the 2009 outburst, the high-energy cutoff could not be observed in detail, mainly because of the lack of observation in the LHS (where it is usually lower). However, the values we obtained from our fits are consistent with the presence of a high-energy cutoff before the softest point is reached. The high energy cutoff seems to be slightly higher on average during the 2008 outburst. However, the values are still consistent during the 2008 and 2009 outburst. As we pointed out in Sec. 7.3.1, a trustable value of the high-energy cutoff has been obtained only for a few HIMS observations. For all the other observations it is not present or it is too high to be detected. The high-energy cutoff is thought to be related to the temperature of the thermal Comptonizing electrons located in an optically thin corona. According to this, higher cutoff values during the 2008 would suggest that the coronal temperature was higher than for the 2009. Thus, the higher temperature of the corona could have affected the subsequent evolution of the source. The inner disk radius values we

[5] The transition from HIMS to the SIMS is marked by the appearance of type-B and/or type-A QPO.

find are not consistent with the ones reported by C09. Their fits give lower normalizations associated to higher temperatures measured at the inner disk radius. The values that they obtain are not acceptable since the inner disk radii calculated from the normalization of the disk black-body component are too small to be physically acceptable. We attribute this difference to the oversimplification of the spectral model they used. C09 do not consider a reflection component, which we find necessary to obtain good fits. As we described before, we tried to use the model described by C09, but it was not enough to describe our spectra.

The spectral parameters evolutions at the beginning of the two outbursts are consistent and do not allow to predict the following evolution of the source. The 2008 outburst of H 1743-322, showing only LHS and HIMS, takes place at low luminosity and the lack of soft-state transitions is probably connected to a premature decrease of the mass accretion rate. Although the accretion rate is a likely important parameter to be considered in a transition scenario, another parameter seems to play a role. This parameter, whose nature is still not clear (Esin et al. 1997, Homan et al. 2001), could drive the source from the LHS to the HIMS and eventually to the HSS. From our study two possibilities stand: either the parameter that drives the transition is not tied to any spectral parameter or during 2008 the transition took place on a short timescale (less then one day) and therefore RXTE missed it. For the last case to work the system must have stayed in the soft state less than 30 hours. Such a short permanence in the HSS has not been observed in other sources so far and should therefore be explained. However, the peculiarity of the softest 2008 observation could be relevant. As it is observed in other sources (e.g. Belloni et al. 2005), just before the entering into the soft state, the Type-C QPOs typical of the HIMS observations shows a changing in its shape (i.e. the type-C QPO becomes blunt, see Belloni 2005) that could be seen as a loosing of coherence. This behavior is always seen before the appearance of a Type-B QPO, that marks the beginning of the SIMS. What is observed during the 2008 could indicate that the source was at least very close to the transition, even though we cannot state wether the transition took place.

Other cases previously presented in literature as failed outbursts in transient X-ray binaries, are LHS-only outbursts without any sign of state transitions at all (see e.g. Brocksopp et al. 2004 and Sturner & Shrader 2005). Conversely, the data presented here show that the full pattern (LHS, HIMS, SIMS, HSS) and LHS-only pattern are not the only two possibilities for the temporal evolution of a BHC outburst.

7.4.3 The flux evolution of the spectral components

Two clear components are present in the BHT spectra. The disk-blackbody component (soft) usually dominates in the HSS (left part of the HID), while the powerlaw

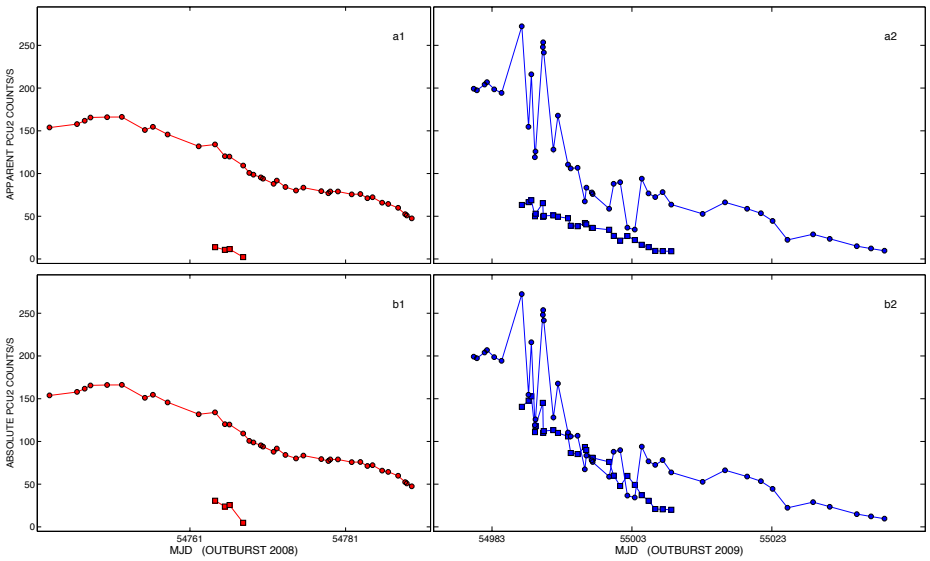

Figure 7.5: Evolution of the count rates associated to the disk blackbody and to the powerlaw components counts/s as a function of the time for the 2008 (left panels) and 2009 (right panels). The circles track the powerlaw components, the squares track the disk-blackbody component . The upper panels show the lightcurves not corrected for the inclination angle effect. The lower panels show the lightcurves corrected for the inclination angle effect. For the 2009 outburst it is clear that, correcting for the inclination angle, the disk component becomes dominant in the soft state.

component dominates in the LHS (right part of the HID). During the intermediates states (HIMS and SIMS), both components are important.

We calculated the fluxes (in the 2 - 200 keV energy band) related to the disk blackbody components and to the powerlaw components as a function of the time. For the latter we made a correction on the values by excluding the reflection contribution, which depends on the inclination angle of the source Θ. The count rates associated to both the powerlaw and the disk-blackbody component are plotted in Fig. 7.5 (upper panels). It is clear that the count rate is always powerlaw dominated. This is consistent with the fact that during the 2008 outburst the source basically never shows a strong disk component. However, during the 2009 outburst the source clearly reached the HSS and yet the disk never became dominant. We interprete the lack of soft emission in terms of the inclination of the source.

Assuming a spherical geometry for the corona, the amount of the hard photons we received can be roughly considered inclination independent. The disk emission is expected to be non-isotropic and should be corrected taking into account the inclination of the source. We calculated the minimum inclination angle to obtain a disk count rate higher than the powerlaw count rate in the soft state. We performed this oper-

ation on the softest observation (Obs. #27 of the 2009 outburst), assuming that the observed disk emission is $cos(\Theta)$ fainter than the real one. We obtained a minimum angle of $\sim 43^o$, which is consistent with the values reported by McClintock et al. (2009) ($\sim$70°).

Applying the inclination angle correction to all the 2009 observations (assuming $\Theta = 65^o$ we obtain the values shown in Fig. 7.5, panel b2. During the 2009 outburst, the disk probably becomes dominant in the central part of the outburst, in correspondence of the HSS. Given that the disk dominance in this state is usually more evident, it is possible that the inclination angle is even larger than 65°. Since the system does not show eclipses and the inclination is in the range $\sim$43° - 75°, probably the lower limit is unrealistically low because, assuming an inclination of $\sim 43^o$, only the softest observation would be dominated by the disk. No big differences are observed when correcting 2008 data from inclination effects (see Fig. 7.5). This reinforces the statement that during the 2008 outburst the disk emission never dominates the spectrum.

7.5 Conclusions

The different behavior shown by H1743 during these two events has allowed us to study the evolution of the spectral parameters at different accretion regimes. During the 2009 outburst the system followed the canonical evolution through all the states usually seen in BHTs. In the 2008 outburst only the hard states are clearly reached and we could state, from the timing analysis, that the source did not reached the soft states while observed by RXTE. We find that the energy spectrum of the 81 observations we have analyzed can be described by using a model consisting of a disk black-body, a powerlaw + reflection component, an absorption and a gaussian line component. The spectral parameters derived by using this model are acceptable from a physical point of view and consistent between each other. The evolution of the spectral parameters is consistent between the two outbursts, and it does not allow to predict the subsequent behavior of the source.

We conclude that this different behavior cannot be predicted on the basis of the initial spectral parameter evolution. The occourring of the transion is possibly driven by a parameter independent by the spectral properties of the source, even thought a scenario in which the transition took place while the source was not observed cannot be ruled out.

Acknowledgments

SM and TB acknowledge support to the ASI grant I/088/06/0. The research leading to these results has received funding from the European Community's Seventh Framework Programme (FP7/2007-2013) under grant agreement number ITN 215212 "Black Hole Universe".

8 A complex state transition from the black hole candidate Swift J1753.5-0127

Paolo Soleri, Sara Motta, Teo Muñoz-Darias, Tomaso Belloni, Piergiorgio Casella, Mariano Méndez, Diego Altamirano, Manu Linares, Rudy Wijnands, Rob Fender Michiel van der Klis

Submitted to Monthly Notices of the Royal Astronomical Society

Abstract

We present spectral and timing studies of the outburst evolution of the black-hole candidate Swift J1753.5-0127, monitored with the Rossi X-ray Timing Explorer and the Swift satellites. The source started its outburst in 2005. After an initial flare, its X-ray flux decreased but the system never reached the quiescent state, remaining at low flux for more than two years. The source transited to the hard intermediate state but it never made it to the soft states, as other sources characterized by short orbital periods (approximately $\lesssim 5$ hours) do. the morphology of the outburst is peculiar and reminiscent of those observed in a class of cataclysmic variables, the Z Camelopardalis. We show that both spectral and timing properties of Swift J1753.5-0127 are in agreement with the binary hosting a black hole, bringing further evidence in this direction, in absence of a measure of the mass of the accretor.

8.1 Introduction

Transient black hole candidates (BHCs) are low-mass X-ray binaries that usually spend most of their lives in quiescence, at very low X-ray luminosity ($10^{30} - 10^{33}$ erg/s; e.g. Hameury et al. 2003). However, they also show relatively short outbursts (typically weeks to months), in which their X-ray luminosity increases by several orders of magnitude (up to $10^{38} - 10^{39}$ erg/s; see Remillard & McClintock 2006 for a review). During these episodes, both timing and spectral properties vary, yielding to different states (see Belloni 2010 for a review). Most likely the states reflect changes in the accretion flow, as well as in the properties of the outflow (see Fender et al. 2010 and references therein). In the low/hard state (LHS), observed at the beginning and at the end of the outburst, the X-ray spectrum is dominated by a component which can be approximated by a power law with a hard photon index ($\sim 1.5 - 1.8$) with a high-energy cut-off ($\lesssim 200$ keV, e.g. Motta et al. 2009). The power density spectrum (PDS) in the LHS features a high level of aperiodic variability [root mean square (rms) amplitude usually above $\sim 30\%$] and often a quasi-periodic oscillation (QPO) that sometimes can be identified as the so-called type-C QPO (see Motta et al. 2011 and references therein for QPO type definitions). In the high/soft state (HSS) the aperiodic variability drops to values of few per cent and the energy spectrum becomes softer and dominated by a thermal disc-blackbody component. A steep and weak power-law component (with photon index ~ 2.5 or higher) is also present with no cut-off up to ~ 1 MeV (Grove et al. 1998). The HSS is usually observed in the middle of the outburst.

In between these two states the situation is more complex, with transitions hard-to-soft and soft-to-hard usually taking place on relatively short time-scales (hours to days) and associated with dramatic changes in the timing and spectral properties. Homan et al. (2005) and Belloni (2005) identified two additional states, the hard-intermediate state (HIMS) and the soft-intermediate state (SIMS), based on spectral and timing properties (see also McClintock & Remillard 2006 for an alternative state definition). The main timing feature of the HIMS is probably the type-C QPO, often together with strong broadband fractional variability (rms up to 30% but lower than in the LHS). The SIMS is characterized by a considerably weaker broadband variability than the HIMS. Two other QPOs, named type B and type A (weaker than the type B) are often observed in the SIMS (Motta et al. 2011).

To characterize the four states it is important to take into account the behaviour at longer wavelengths. In the LHS, a compact, steady jet is on and substantially contribute to the total energy output of the system (Fender 2010). Its power dominates over the accretion-powered luminosity in the LHS at $L_X \lesssim 1\% \, L_{Edd}$; L_X (L_X and L_{Edd} are the X-ray and the Eddington luminosities, respectively; e.g. Fender et al. (2003)). In the LHS, two empirical non-linear relations connect the accretion-

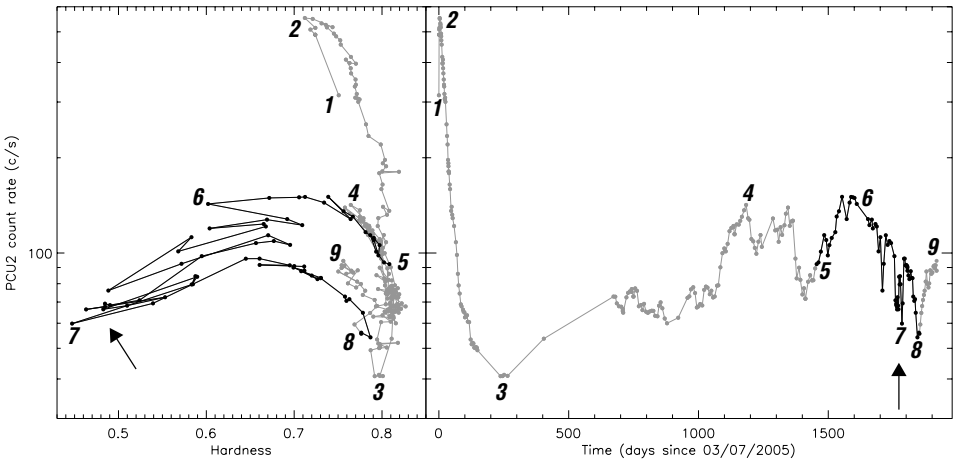

Figure 8.1: X-ray hardness-intensity diagram and light curve of Swift J1753.5-0127 (left-hand and right-hand side, respectively), from the beginning of its outburst to 2010-10-05. Every point represents one RXTE observation. Intensity and hardness are defined in §8.2. The black points mark the "failed transition" analysed in detail in §8.3.2. The numbers help the reader to follow to evolution of the outburst (#1 is its beginning). The vertical arrows mark the period in which we performed the Swift observations described in §8.2.3.

powered and the jet luminosities (probed by X-ray and radio/infrared observations, respectively; see e.g. Gallo et al. (2003) and Russell et al. (2006)), over several orders of magnitude in L_X. It is interesting to note that the clearest marker for the transition from the LHS to the HIMS seems to be a sudden change in the X-ray/infrared correlation, as observed in the BHC GX 339-4 (Homan et al. 2005). Namely, the infrared flux (H band) dropped by a factor ~ 17 in about 10 days while the X-ray flux decreased by a factor of only ~ 1.4. The transition from the HIMS to the SIMS has been tentatively associated with the emission of transient, relativistic jets (Fender et al. 2004), although clear proof is still missing (Fender et al. 2009). On the other hand, there is strong evidence that the compact, steady jet is highly quenched in the soft states of BHCs (e.g. Tananbaum et al. 1972), by factor of $\sim 300 - 800$ (in radio) compared to what expected at similar X-ray luminosities in the LHS (Russell et al. 2011).

A widely used tool to study the spectral evolution of BHCs in outburst is the X-ray hardness-intensity diagram (HID), since different spectral states correspond to different branches/areas of the HID. Namely, most BHCs draw a q-shape pattern in the HID, moving anticlockwise and featuring a transition to the intermediate states and then to the HSS (see e.g. Belloni et al. 2005 for GX 339-4). However, a number of sources stays for the whole outburst in the LHS (Brocksopp et al. 2004) or in the LHS and in the hard-intermediate state (H 1743-322 and possibly SAX J1711.6-3808; Capitanio et al. 2009 and Wijnands & Miller 2002 respectively), without tran-

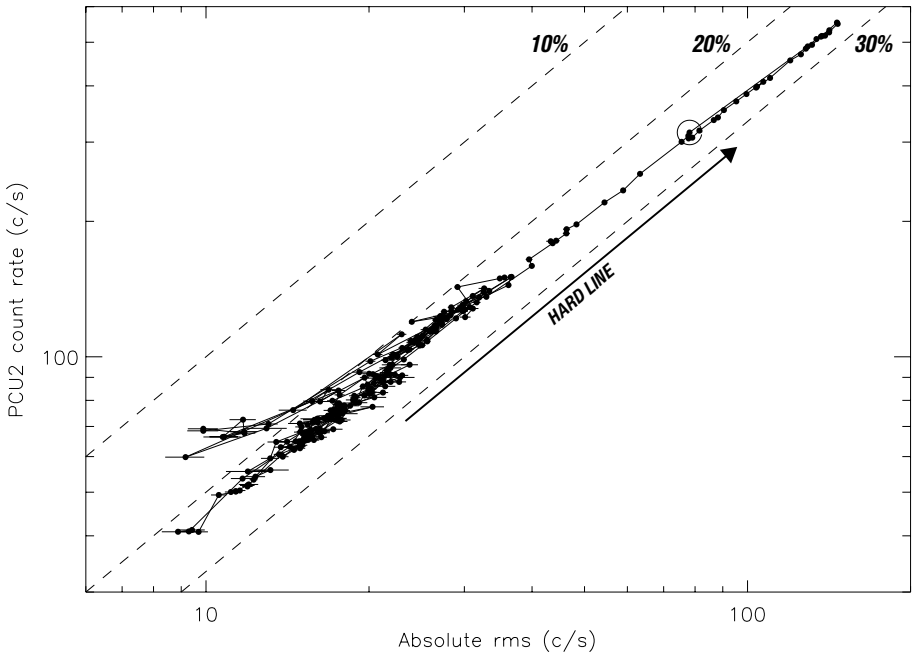

Figure 8.2: Rms-intensity diagram obtained as explained in §8.2. Each point corresponds to one RXTE observation. The first observation is marked by an open circle. Consecutive observations are connected by a solid line. The dashed lines represent 10%, 20% and 30% fractional rms levels.

siting to the soft states. Some of these systems underwent both "normal" outburst and hard outbursts (i.e. with or without a transition to the soft states, respectively; e.g. XTE J1550-564, Belloni et al. 2002). Although neutron star X-ray binaries often have outbursts characterized by different morphologies and properties than BHCs (see van der Klis 2006 for a review), they can also undergo hard outbursts, as for example Aql X-1 (Tudose et al. 2009).

To understand the mechanisms responsible for state transitions and the different type of outbursts of BHCs, it is important to be able to determine precisely when the transitions occur. This can not be achieved by means of the HID alone, so other tools (such as X-ray timing and spectral analysis, as well as multiwavelength observations) are usually needed. Recently, Muñoz-Darias et al. (2011) developed a new tool to map the states of a BHC in outburst by following the evolution of the count rate and the rms amplitude of the variability: the rms-intensity diagram (RID). They applied this tool to study three outbursts of GX 339-4, showing that it is possible to associate different regions of the RID to different states, as well as to mark the moment of the state transition from the LHS to the HIMS.

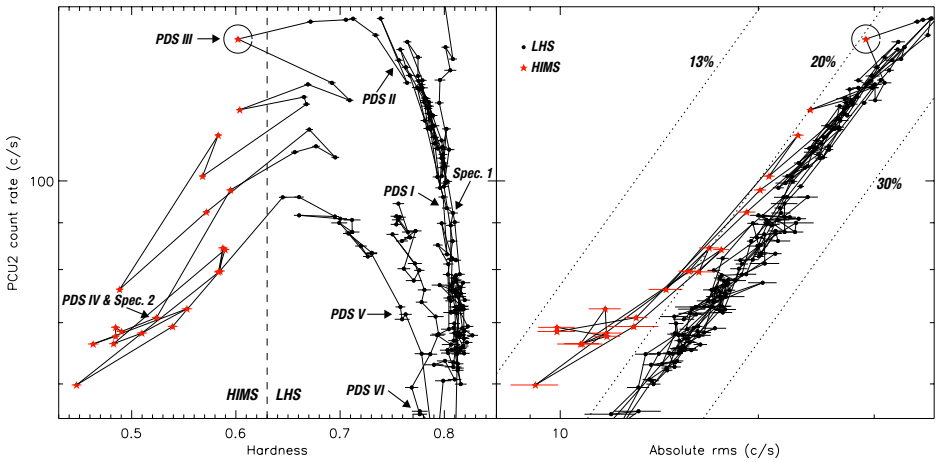

Figure 8.3: Zoom on the areas of the HID and the RID (left-hand and right-hand side, respectively) marked by the black points in Figure 8.1. Black-filled circles and red stars represent LHS and HIMS observations, respectively. In the HID the vertical dashed line separates the LHS from the HIMS. In the RID the dotted lines have been drawn at 30%, 20% and 13% fractional rms levels. In both panels a circle marks the first observation in the HIMS (Obs. ID 93105-02-58-00, on 2009-11-28). In the HID, small arrows point the observations used to extract the PDS that are shown in Figure 8.6, as well as the energy spectra in Figure 8.10.

8.1.1 Swift J1753.5-0127

Swift J1753.5-0127 was discovered in the hard X-ray band with the Burst Alert Telescope (BAT) aboard Swift on 2005 May 30 (Palmer et al. 2005). After the discovery, the source flux reached a peak of 200 mCrab on 2005 July 9 in the All Sky Monitor (ASM) on board the Rossi X-ray timing explorer satellite (RXTE). Subsequently the flux started decreasing and then stalled at a level of $\sim$20 mCrab (2-20 keV) for more than $\sim$ 6 months. This is an unusual behaviour for a transient, but even more unusual is the subsequent shallow flux rise which has been ongoing since roughly June 2006, with a steeping on June 2008 (Krimm et al. 2008), followed by a variable trend (see Figure 8.1, right-hand panel). The source did not return to quiescence and at the moment of writing this paper it is still active. Although its X-ray spectral hardness has not remained constant (Zhang et al. 2007, Ramadevi & Seetha 2007, Negoro et al. 2009), no state transition to the intermediate states or to the HSS has been reported so far, suggesting that Swift J1753.5-0127 has always been in the LHS during the whole outburst (Soleri et al. 2010). The mass of the compact object in the binary has not been dynamically measured. However, the strongest hint that the system harbours a black hole comes from the hard power-law tail in the X/γ-ray energy spectrum up to $\sim$600 keV, detected with INTEGRAL (Cadolle Bel et al. 2007) as no neutron star low-mass X-ray binary has ever been detected above $\sim$ 200 keV (see e.g. Falanga

et al. 2007).

Swift J1753.5-0127 is certainly peculiar and interesting for a number of reasons. First of all, the radio and infrared counterpart of its jet are fainter than expected from the two empirical correlations mentioned above (Soleri et al. 2010). This suggests that the bulk of the gravitational potential energy liberated by the accretion flow is not channeled into the jet and it is possibly radiated efficiently (Coriat et al. 2011), at variance with what expected for BHCs in the LHS (e.g. Fender et al. 2003).

Secondly, it would be the BHC with the second shortest orbital period, as claimed by Zurita et al. (2008) and Durant et al. (2009), who reported a $\sim$3.2 hr modulation in the optical light curves. It would be reasonable to expect that the value of the orbital period (hence the size of the Roche lobe and the accretion disc) influences other macroscopic properties of BHCs, as for example the jet power. However, this has been tested by Soleri & Fender (2011), who showed that there is no obvious correlation between orbital period and radio/infrared jet power.

Here we study the evolution of the outburst of Swift J1753-0127, from its beginning to October 2010. We first describe the general features of the whole outburst, making use of two fundamental diagrams (§8.3.1) and then we focus on X-ray spectral and timing properties of the source during the "failed state transition", that took place between June 2009 and May 2010 (§8.3.2). The discussion and our conclusions are presented in §8.4 and §8.5, respectively.

8.2 Observations and data analysis

8.2.1 Light curve, HID and RID

We used all the 263 observations performed with the Proportional Counter Array (PCA) aboard RXTE until 2010-10-05 (Obs. ID 95105-01-35-01) to produce the light curve and the HID in Figure 8.1. For each observation, the background-subtracted count rate has been obtained from PCU2 data in the energy range 2-15 keV [in Standard 2 (STD2) data mode], after applying dead-time corrections. We defined the spectral hardness h as the ratio of counts in the energy bands 6.1-9.8 keV and 3.3-6.1 keV (PCU2 STD2 mode). Using the same method presented in Muñoz-Darias et al. (2011), we produced the RID presented in Figure 8.2, calculating the fractional rms in the frequency band 0.1-64 Hz (see Belloni & Hasinger 1990), for the energy range 2-15 keV. The absolute rms (x axis of the same diagram) has been computed by multiplying fractional rms by net count rate. Using the same method, we also obtained the rms using a soft and a hard band (2-6 keV and 6-15 keV, respectively). Throughout the paper, we will explicitly use the terminology "absolute rms" when referring to this quantity while we will refer to the fractional rms in all the other cases.

8.2.2 Timing analysis

We produced power density spectra for 67 RXTE observations performed between 2009-06-27 and 2010-07-28 (Obs. IDs 93105-02-36-00 and 95105-01-25-01, respectively; see the black points in Figure 8.1 and §8.3.2). Restriction to this interval is due to two reasons: firstly, we want to study the "failed transition" making use of complementary instruments, including detailed timing and spectral analysis (see also §8.2.3); secondly the rest of the outburst can be successfully described using the two fundamental diagrams mentioned above (HID and RID), giving us results in agreement with the literature for the initial phases of the outburst (see e.g. Zhang et al. 2007).
The fast Fourier transform PDS were extracted from segments of 128 s accumulated in all the PCA energy channels (0-249), with a Nyquist frequency of 4096 Hz. For every RXTE observation we averaged one PDS, rebinned it logarithmically and also subtracted the Poissonian noise. If two contiguous observations were performed within 24 hours, we averaged their power spectra together. The resulting PDS were normalized according to Leahy et al. (1983) and then converted to square fractional rms (Belloni & Hasinger 1990). The fitting was carried out using a combination of Lorentzians: each of them has been been described as an L_i, where i determines the type of component according to Belloni et al. (2002). Throughout the paper we will quote the frequency ν_{max} at which the Lorentzians attain their maximum in νP_ν representation and the quality factor Q (Belloni et al. 2002a), where $\nu_{max} = \nu_0(1 + 1/4Q^2)^{1/2}$ and $Q = \nu_0/2\Delta$. ν_0 is the Lorentzian centroid frequency and Δ is its half-width-at-half-maximum. Errors on fit parameters were determined using $\Delta\chi^2 = 1$. The fitting parameters are reported in Tables 8.2 and 8.2 in §8.5.

8.2.3 Spectral analysis

Here we describe the procedures adopted to extract and fit the energy spectra of Swift J1753.5-0127, from RXTE and Swift data. A complete log of the models used for the spectral fitting, as well as the most relevant fitting parameters, are reported in Tables 8.3 and 8.4 in the Appendix.

RXTE

We produced energy spectra from the same RXTE observations used for the timing analysis described in §8.2.2. We applied standard filters and extracted PCA spectra from STD2 data from PCU2. The data were background and dead-time corrected. We generated response matrices and produced the spectra in the energy range 4-40 keV, after applying 0.6% systematic error. The energy range has been reduced to 4-25 keV when the PCA spectra have been fitted together with Swift/XRT spectra. For the

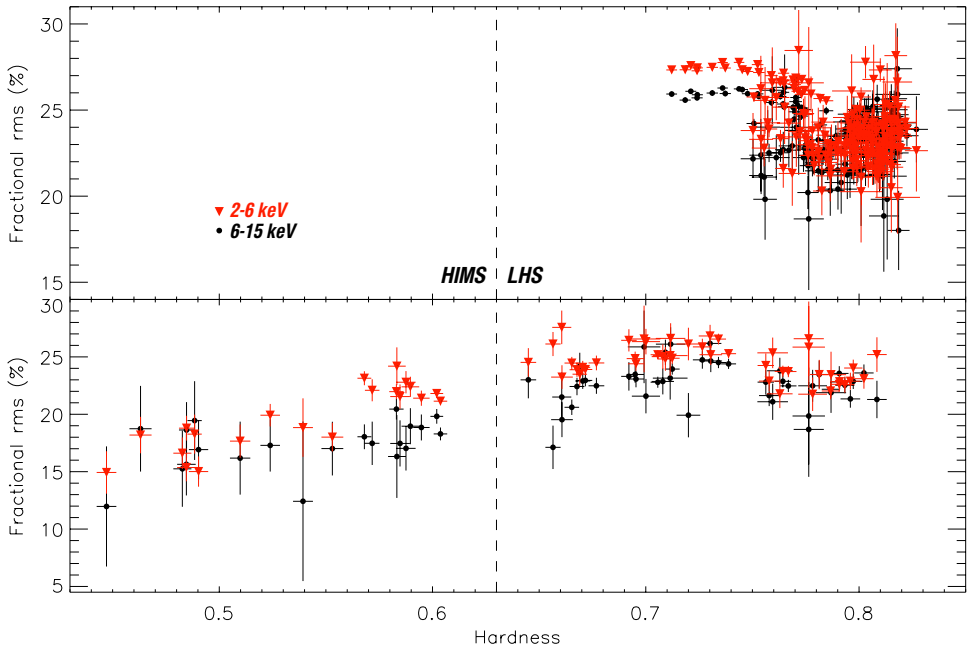

Figure 8.4: Hardness-rms diagram, using soft (2-6 keV, red-downward triangles) and hard (6-15 keV, black-filled circles) energy bands for computing the rms. The lower panel shows the observations marked by black circles in Figure 8.1 (the "failed transition"), the upper panel all the other observations (grey points in Figure 8.1). A vertical dashed line separates the LHS and the HIMS. Note the different scale on the y axis of the 2 panels.

observations performed before December 2009, we also extracted background and dead-time corrected spectra from the cluster B of the High Energy Timing Experiment (HEXTE aboard RXTE). On December 2009 HEXTE cluster B stopped rocking, hence we did not extract HEXTE spectra after that date. We fitted these spectra in the 20-200 keV energy range, after generating response matrices. No systematic error was applied.

Swift

We produced energy spectra from all the seven pointed Swift observations performed during the "failed transition" (see Table 8.4 in §8.5). All of them are quasi simultaneous (within one and a half day) to RXTE pointings. Two Swift observations (obs. IDs 00031232017 and 00031232018) have been taken quasi simultaneously to RXTE (Obs. ID 95105-01-16-00; the time difference is $\sim$ 24 hours and less than $\sim$ 11 hours, respectively), hence we decided to discard the observation with the largest temporal gap (obs. ID 00031232017). We processed the XRT data using *xrtpipeline* with standard quality cuts. Our data were all collected in windowed timing mode. We

extracted source and background spectra using circular regions with radii of ~ 30 and ~ 15 pixels, respectively. Exposure maps and ancillary response files were generated using *xrtexpomap* and *xrtmkarf*. The latest response matrix files (v12) were taken from the calibration database. We applied a systematic error of 2.5% (Campana et al. 2008) and we grouped the spectra to a minimum of 20 counts per bin. The XRT spectra were fitted in the 0.8-8 keV energy range.

Fitting procedures

We fitted the energy spectra using the standard XSPEC v11.3 fitting package (Arnaud 1996). For simultaneous RXTE and Swift observations (performed within ~ 36 hours) we combined the PCA+XRT spectra to fit them together. Unfortunately HEXTE data were available only for RXTE observations performed before December 2009 while Swift observed the source only in April and May 2010 (if we consider only the "failed transition"). In order to account for flux cross-calibration uncertainties, we multiplied the continuum model by a constant. All model parameters, except these multiplicative constants, were linked between the different instruments. When fitting the RXTE spectra alone, we fixed the interstellar absorption to the average column density value obtained by Hiemstra et al. (2009) ($N_H = 1.7 \times 10^{21}\mathrm{cm}^{-2}$) while we let it free to vary when including also Swift/XRT data. The RXTE spectra alone can be fitted using an absorbed broken (elbow-shaped) power law. However, when fitting RXTE+Swift spectra, a disc blackbody at low energies and a Gaussian emission line need to be added in order to obtain a statistically acceptable fit. The Gaussian component takes into account the escape peak of silicon at 1.9 keV (see the "XRT digest" webpage[1]). Errors on fit parameters were determined at 1σ confidence level.

8.3 Results

In this section we first describe the general behaviour of Swift J1753.5-0127 during the whole outburst using the X-ray light curve, HID and RID (§8.3.1), then we focus on the power and energy spectra of the source collected in the "failed transition" (black points in Figure 8.1; §8.3.2).

8.3.1 Fundamental diagrams

Figure 8.1 shows the X-ray HID and light curve of the outburst of Swift J1753.5-0127. At variance with the majority of the BHCs, the source did not follow the standard q-shaped pattern in the HID and it did not soften at its maximum flux in

[1] http://www.swift.ac.uk/xrtdigest.shtml#res

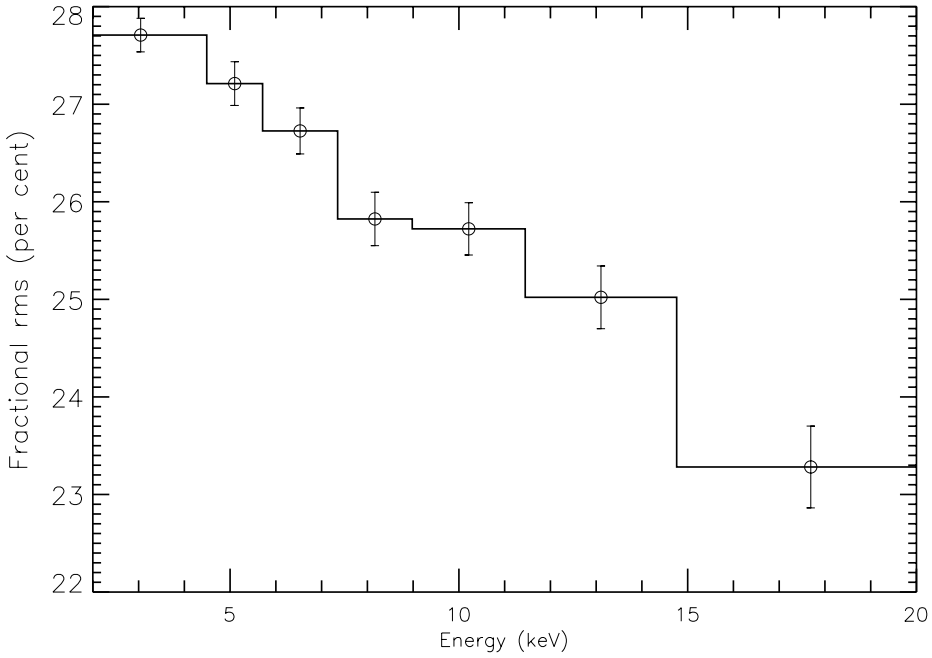

Figure 8.5: Rms spectrum of the RXTE observation performed on 2005-07-06 (obs. ID 91094-01-01-04), at the beginning of the outburst.

2005 (#2 in the HID). Its hardness actually increased from the outburst peak (#2) to its minimum (#3), in March 2006. After this point the the system re-brightened and softened again (#4, $h \sim 0.76$), following a variable trend in the light curve. A clear softening took place in July 2009 (#5, 6, 7), followed by a hardening at lower count rate (from #7 to #8). From #8 to #9 the source flux increased again, together with a weak softening (from $h \sim 0.78$ to $h \sim 0.75$).

RXTE started observing Swift J1753.5-0127 near the peak of its outburst (#1), when the source was in the LHS (e.g. Zhang et al. 2007). The RID in Figure 8.2 confirms the identification of the spectral state: after the first RXTE pointing (see the open circle), the system draws a line in the RID. This linear relation between rms and count rate, the so-called hard line, has already been observed in other BHCs (e.g. GX 339-4, Muñoz-Darias et al. 2011) and its presence is considered a typical signature of the LHS (see Uttley & McHardy 2001; Gleissner et al. 2004; Muñoz-Darias et al. 2011). In this initial phase the fractional rms decreases (from 27% to 24%) and the spectral hardness increases (from $h \sim 0.71$ to $h \sim 0.80$). Below a count rate of ~ 160 c/s (mid August 2005; day ~ 43 in the light curve), the source still follows a hard line, although the data points are scattered around it. The flux of Swift J1753.5-0127 keeps decreasing (along the hard line) until it reaches its minimum in March

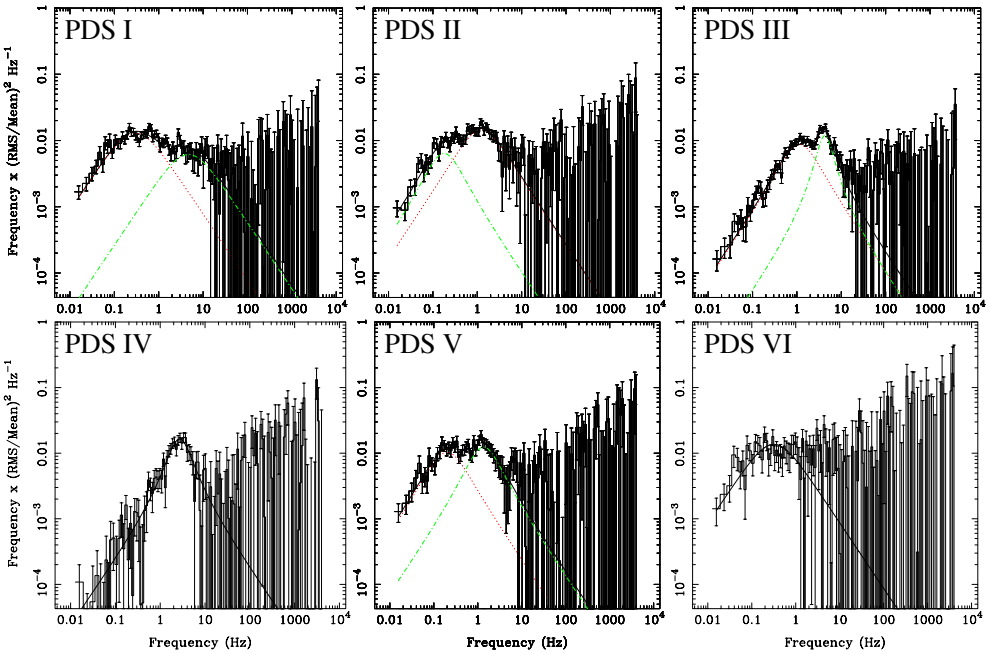

Figure 8.6: Fits to six power density spectra extracted in the "failed transition". All the Lorentzians, as well as the total fit function, have been plotted. PDS I, II, III, IV, V and VI correspond to observations 93105-02-37-00, 93105-02-48-00, 93105-02-58-00, 95105-01-12-00, 95105-01-23-00 and 95105-01-25-00, respectively. The position of these observations has been marked in the HID in Figure 8.3. PDS I, II, V and VI have been obtained in the LHS while PDS III and IV in the HIMS. In PDS I and VI the quality factor of the Lorentzians has been fixed to 0.

2006 (# 3 in Figure 8.1), when the fractional rms is $\sim$ 22%. After this point the flux is characterized by a variable trend, but the source remains on the hard line. From June 2009 (#5) the hardness decreases (not monotonically) and the count rate increases. Figure 8.3 shows a zoom of the HID and the RID on the soft excursion of Swift J1753.5-0127: on 2009-11-28 (big-open circle in both panels) the source does not fall on the hard line, its hardness drops to $h \sim 0.6$ and the fractional rms reaches level of 20%. Both hardness and count rate follow an oscillating (and correlated) behaviour until the system reaches the softest point of the whole outburst ($h \sim 0.45$), at the lowest count rate of the "soft excursion" ($\sim$ 60 c/s), on 2010-05-22 (Obs. ID 95105-01-16-00, #7 in Figure 8.1). The fractional rms decreases together with the count rate and the hardness, reaching the minimum values of the whole outburst ($\sim$ 14%), then Swift J1753.5-0127 starts hardening again (with the count rate ranging from $\sim$ 60 to $\sim$ 95 c/s), the fractional rms increases and the source joins the hard line. This is different from what has been reported by Muñoz-Darias et al. (2011) for GX 339-4: in this source, the return to the LHS (after the system has been in

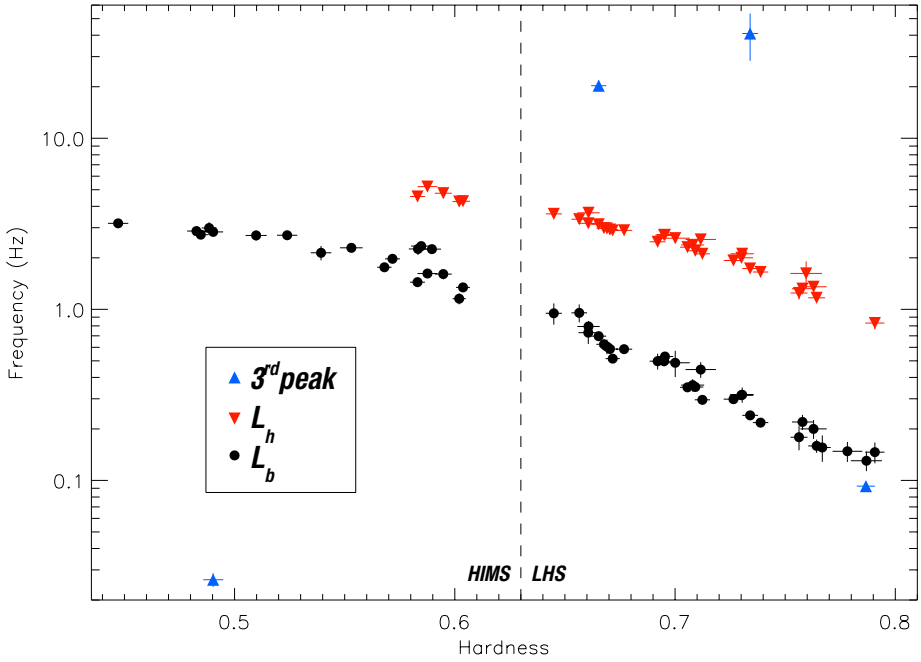

Figure 8.7: Frequency of the Lorentzians used to fit the power density spectra (see Tables 8.2 and 8.2) as a function of the spectral hardness. Only the Lorentzians in which the quality factor Q has been left free to vary are considered here. The black circles and the red upward triangles represent L_b and L_h, respectively. The upward blue triangles represent the third Lorentzian possibly identified either with L_{b2} or L_l (when its frequency is lower or higher than ν_b, respectively). The vertical-dashed line separates the LHS from the HIMS.

the soft states) is characterized by a different linear relation between the rms and the flux than in the LHS, called adjacent hard line. From Figure 8.3 one can see that all the observations marked by red stars (on the left-hand side of the dashed line in the HID) are visually detached from the hard line in the RID, although a handful of points might not follow this framework since their location can not be unambiguously determined (e.g. see the stars in the RID with a count rate of $\sim$ 80 c/s). Following Muñoz-Darias et al. (2011) and Muñoz-Darias et al. (2011) we identify the points that do not fall on the hard line (the red stars) as HIMS observations. This will be motivated in the discussion section (§8.4), in which we will also show that the source has never been observed in the SIMS. Considering that, despite the softening and the subsequent hardening described above, no transition to the soft states (either SIMS or HSS) has been observed in Swift J1753.5-0127, we will refer to this soft excursion as the "failed transition".

In Figure 8.4 we report the rms-hardness diagram for two different energy bands.

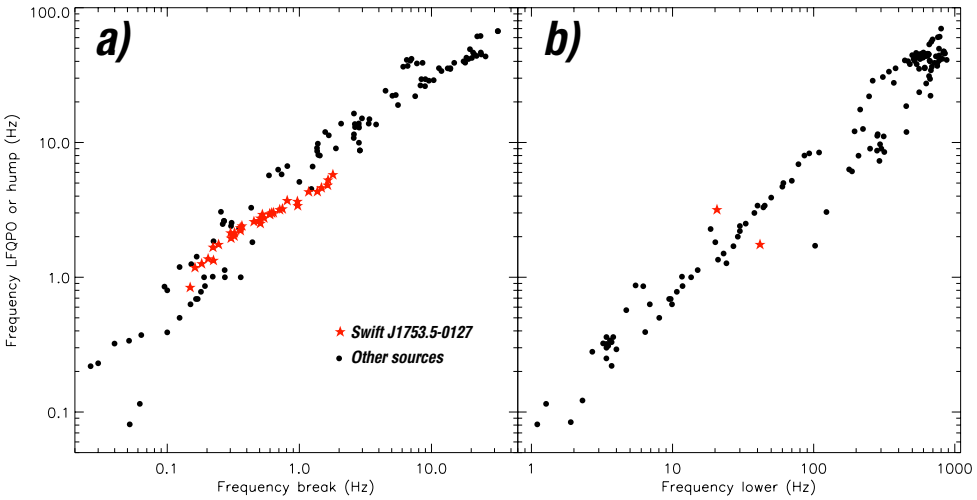

Figure 8.8: Frequency of the low-frequency QPO (ν_{LFQPO}) and of the hump (ν_h) as a function of the break frequency ν_b (panel *a*; WK relation) and as a function of the frequency of the "lower" Lorentzian ν_l (panel *b*; PBK relation). The plots have been adapted from Figure 11 and Figure 12 of Belloni et al. (2002a), respectively. The red stars represent the observations of Swift J1753.5-0127 in which both L_b and L_h are present (panel *a*) and in which the third Lorentzian and L_h are present (panel *b*). We reported only the fit components in which Q has been left free to vary.

During the first $\sim$ 33 days of the outburst, the rms features an inverted spectrum and in both bands the rms decreases together with the count rate. An example of rms spectrum from the initial phases of the outburst is shown in Figure 8.5 (from observation 91094-01-01-04): the spectrum is inverted, without any indication of flattening at low energies. Following Gierliński & Zdziarski (2005), we define inverted, flat and hard rms spectra the spectra in which the fractional rms at low energies is higher, similar to and lower than the rms at high energies, respectively. Although the majority of the BHCs in the LHS are characterized by flat rms spectra (see Gierliński & Zdziarski 2005; Muñoz-Darias et al. 2011; Muñoz-Darias et al. 2011), this type of behaviour has already been observed in some BHCs, e.g. XTE J1650-500 (Gierliński & Zdziarski 2005). After the first $\sim$ 33 days, the rms spectrum is consistent with being flat, however a slightly hard rms spectrum can not be discarded for some of the observations ($\sim$ 8) performed between $\sim$ 50 and $\sim$ 150 days after the beginning of the outburst. Given the lower number of counts and the worse statistics, we do not report other rms spectra. Our approach (calculating the rms for a hard and a soft band) does not give details of their shape, nevertheless it is sufficient to follow their general evolution. After day $\sim$ 150, the rms spectrum is always consistent with being flat or slightly inverted, both during LHS and HIMS observations (consistent with other BHCs; Gierliński & Zdziarski 2005, Belloni et al. 2011). From the bottom

panel of Figure 8.4 we can see that both the soft and the hard rms are correlated to the hardness during the "failed transition" (at least for $h \lesssim 0.75$).

8.3.2 The failed transition

In this section we present spectral and timing analysis of RXTE and Swift observations performed between 2009-06-27 and 2010-07-28. This interval is marked by black-filled circles in Figure 8.1. The best-fit parameters of the power density spectra, as well as the energy spectra are reported in the Appendix.

Power density spectra

We generally fit all the PDS using one or two Lorentzians, except for five observations in which a third Lorentzian is needed in order to get a statistically good fit. Figure 8.6 shows six power density spectra fitted with one or two Lorentzians, representative of the different phases and spectral states (LHS and HIMS) faced by the source during the "failed transition". Following van Straaten, van der Klis & Méndez (2003), if the Q-value of a Lorentzian goes to zero in the fit, we fix it to zero. Tables 8.2 and 8.2 show that there are 14 observations in which one or two Lorentzians feature a Q-value fixed to zero (as in PDS I and PDS VI in Figure 8.6). All these observations are either at the beginning or at the end of the interval and they are characterized by hardness $h \gtrsim 0.78$ and $h \gtrsim 0.76$ during the softening and the hardening, respectively. For the rest of the analysis we will only consider the Lorentzians in which the value of Q can be left free to vary.
In Figure 8.7 we plot the frequency of the Lorentzians as a function of hardness: two broad peaks can be identified, evolving in frequency with the hardness. Four power spectra have been fitted using a third Lorentzian, whose frequency does not follow any obvious path in the diagram. The first peak, represented by black circles, is characterized by a frequency that varies from $\nu \sim 0.15$ Hz at $h \sim 0.79$ to $\nu \sim 3.18$ Hz at the lowest hardness ($h \sim 0.45$) and it is always present. The second peak (downward red triangles) spans a slightly broader range in frequency (0.8-5.2 Hz) and, differently from the first one, it disappears below $h \sim 0.58$. PDS IV in Figure 8.6 represents an example of a power spectrum from an observation characterized by low h and fitted with one Lorentzian. The frequency of the third peak (upward blue triangles) is lower than the other peaks in two cases and higher in the other two.

Figure 8.8a shows the frequencies of the low-frequency QPO (ν_{LFQPO}) and of the hump (ν_h) for a number of black-hole and neutron star X-ray binaries in the hard states (commonly called WK correlation; Wijnands et al. 1999, Psaltis et al. 1999) as a function of the break frequency ν_b (black circles), defined according to Belloni et al. (2002a). Following Remillard et al. (2002), we identify L_{LFQPO} as the type-C QPO mentioned above. The plot also includes the data points for Swift J1753.5-0127

(red stars), obtained using the frequencies of the first two peaks described above. As one can see, the path of this source in the diagram overlaps to the one of the other systems, despite its (possibly) shallower slope. The higher frequency peak that we fit in the PDS of Swift J1753.5-0127 (read downward triangles in Figure 8.7) is broad (with $Q < 2$, except for two cases, see Table 8.2), and we can not identify as the low-frequency QPO commonly detected in the hard states. This suggests that during the "failed transition" no type-C QPO is detected. In several sources (e.g. 1E 1724-3045, GX 339-4) both L_{LFQPO} and L_h can be simultaneously present and in this case $\nu_h \gtrsim \nu_{LFQPO}$, although the difference is usually small. Following Belloni et al. (2002a), we will refer to the lower and the higher frequency broad peaks reported in Figure 8.8a as L_b (break) and L_h (hump), respectively.
The identification of the third peak (upward blue triangles in Figure 8.7 is less straightforward. Van Straaten et al. (2003) identified a new broadband-limited noise component L_{b2} appearing at frequency $\nu_{b2} \lesssim \nu_b$ in the neutron star 4U 1608-52, whose frequency correlates to the frequency of the "upper" Lorentzian L_u. In the PDS of Swift J1753.5-0127 we do not detect the L_u component, hence a direct test can not be provided. However, for the two cases in which the third Lorentzian has frequency lower than ν_b, we tentatively associate it with L_{b2}.
Figure 8.8b shows the frequencies of L_{LFQPO} and L_h as a function of the "lower" Lorentzian L_l (commonly called PBK relation; Psaltis et al. 1999). The black circles represent the sample of black hole and neutron stars used in Belloni et al. (2002a). We also included the two observations of Swift J1753.5-0127 in which we need a third Lorentzian with frequency higher than ν_h (red stars). These points fall close to but not on the path drawn by the other sources, suggesting that the third component needed to fit the power density spectra might be possibly (but not safely) identified with the "lower" Lorentzian L_l.

In Figure 8.9 we reported the quality factor and the rms of L_b and L_h as a function of the frequency (in the lower and upper panel, respectively). L_b is broad: its Q decreases as a function of the frequency below $0.3 - 0.4$ Hz while above 0.4 Hz it increases, without exceeding ~ 1. In the frequency range $\sim 0.8 - 1.2$ Hz, where both L_h and L_b are present, the quality factors follow the same dependency on the frequency and also feature similar values (given a certain frequency). Above $\nu \sim 1.2$ Hz, the Q of L_h keeps increasing, but it always remains below ~ 1.5 (even considering the large error bars). The rms of L_b increases with the frequency for $\nu \lesssim 0.3$ Hz, it is stable (in the range $\sim 15 - 22\%$) for $0.3 < \nu < 1.1$ Hz and then it decreases to $\sim 12\%$ between 1.1 Hz and 1.2 Hz. The rms of L_h is characterized by a similar behaviour as L_b (in the frequency range where they overlap) and then it decreases below 10% above $\nu \sim 1.4$ Hz.

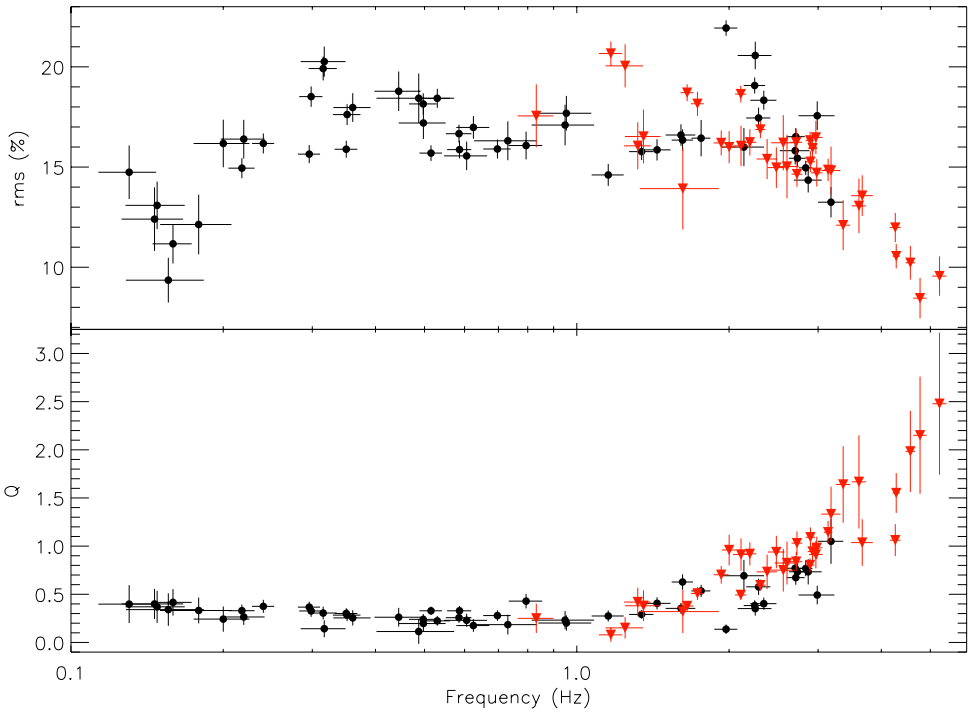

Figure 8.9: Evolution of the rms and the quality factor Q of L_b and L_h as a function of the frequency of the peak (top and bottom panel, respectively). Symbols are the same as in Figure 8.7.

Energy spectra

We fitted all the RXTE energy spectra using a simple model constituted by an absorbed broken (elbow-shaped) power law (*bknpower* in *xspec*; *wabs* for the absoprtion), both for the observations with PCA and HEXTE data and the observations with PCA data only (before and after December 2009, respectively). Spectrum 1 in Figure 8.10 is an example of a fit to the energy spectrum of observation 93105-02-36-00 in which both PCA and HEXTE data were available. For one observation (95105-01-05-00, performed when Swift J1753.5-0127 was in the HIMS) we were obtaining residuals at low energies, hence we decided to add a thermal component to the fit (*diskbb*). Although in this way we can get a statistically good fit and acceptable parameters (for the *bknpower*), the thermal component is not significant. Nevertheless, we decided to keep it, given the simplicity of the model and the good value of the χ^2. We also used an absorbed broken power law (leaving the absorption free to vary) to fit the energy spectra from the simultaneous RXTE and Swift observations (PCA+XRT). All these observations have been performed in the HIMS at low hardness $h \lesssim 0.59$. However, this model could not yield a satisfactory fit, leaving

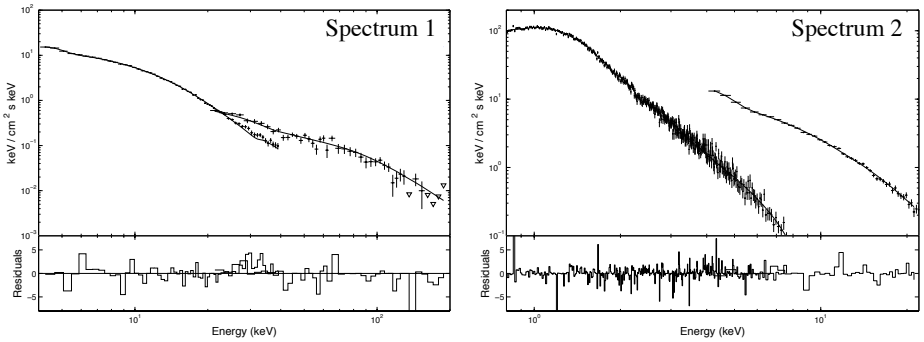

Figure 8.10: Examples of spectral fits and residuals resulted from observations taken during the "failed transition". The observations have been marked in the HID in Figure 8.3. *Spectrum 1:* fit to PCA and HEXTE spectra, from observation 93105-02-36-00. The triangles represents 3σ upper limits. *Spectrum 2:* fit to XRT and PCA spectra, from observations 00031232008 and 95105-01-12-00, respectively.

residuals at low energies. The fit can be significantly improved by adding a Gaussian emission line and a thermal component (*diskbb*) that account for an escape peak of silicon at ~ 1.9 keV and the soft residuals, respectively. In three RXTE+Swift spectra (see Table 8.4), the disc blackbody is not significant but the component is needed in order to get an acceptable fit (as discussed above for 95105-01-05-00). Spectrum 2 in Figure 8.10 is an example of a fit to the energy spectra of XRT+PCA observations (Obs. IDs 00031232008 and 00031232010). The best fit parameters (except for the Gaussian emission line at ~ 1.9 keV), as well as the values of the χ^2, are reported in Tables 8.3 and 8.4.

Figure 8.11 shows the evolution of the parameters of the broken power law for all the spectral fits. Γ_1 and Γ_2 are the power law photon indices before and after the break, respectively. From the lower panel one can see that Γ_1 increases from ~ 1.65 to ~ 2.0 in the first 150 days, then it is rather variable for ~ 185 days before decreasing again to its initial level during the next ~ 95 days. All the observations with $\Gamma_1 > 2.08$ (above the horizontal-dashed line) belong to the HIMS (see §8.3.1), the only exception being the first point in the third HIMS interval (HIMS epochs have been coloured in grey).

The value of the energy break E_{break} is always in the range $9 - 15$ keV, except for one point which has a lower value. At variance with the photon index Γ_1, no clear trend is observed: the spectral states can not be associated with different values of E_{break}. The top panel of Figure 8.11 shows the behaviour of the photon index of the broken power law after the energy break, Γ_2. This parameter is always in the interval $1.4 - 1.85$, except for the point (mentioned above) with value of E_{break} out of the range $9 - 15$ keV. From Figure 8.12 we can see that Γ_2 and Γ_1 seem to be corre-

lated (despite a large scatter) and follow similar trend. The slope of the correlation becomes shallower at $\Gamma_1 \gtrsim 2$: this can be inferred by looking at the positions of the points and the dashed line, that has been drawn for $\Gamma_2 = \Gamma_1$. It is worth to mention that the possible correlation between Γ_2 and Γ_1 do not always hold: for example during the third HIMS epoch (days $\sim 230 - 260$) the two parameters have an opposite behaviour.
In five PCA+XRT spectral fits the thermal component is significant above 3σ. For all these HIMS spectra, the temperature of the *diskbb* lies in the range $0.30 - 0.42$ keV, slightly lower than the values usually observed in other BHCs in the HIMS (see e.g. Motta et al. 2009 and Muñoz-Darias et al. 2011). The associated inner radius R_{in} (for a distance to the source of 8 kpc, Soleri et al. 2010) varies between 66 km and 144 km. The dependence of R_{in} on the inclination on the line of sight θ, yet poorly constrained, still needs to be taken into account (see Table 8.4; see also Hiemstra et al. 2009, Reis et al. 2009 and Reynolds et al. 2010).

8.4 Discussion

Despite several years of observations at different wavelengths, it is difficult to explain the morphology of the exceptionally long outburst of Swift J1753.5-0127 (still ongoing at the moment of writing this manuscript) in the same framework as the majority of the transient BHCs. Our observing campaign with RXTE and Swift provided important information about its evolution, showing that the source did not go to the soft states and allowing us to make comparisons with other (classes of) sources.

The combined use of the HID and the RID is fundamental to identify the source states and determine the moment of state transitions. If we compare the RID of Swift J1753.5-0127 and GX 339-4 (Muñoz-Darias et al. 2011), we see that both sources draw a hard line. However, the former features a lower fractional rms than the latter. It is interesting to note that Swift J1753.5-0127, at the beginning of its activity (when $h \lesssim 0.78$ and the count rate is above ~ 160 c/s), features the highest fractional rms of the whole outburst (between 24% and 27%). At variance with the majority of the BHCs in the LHS (Belloni 2010), the fractional rms anticorrelates with the spectral hardness h and correlates with the count rate. This suggests that the value of h (lower than in stages of the outburst in which $h \sim 0.8$) was not an indication of an approaching spectral transition to the HIMS. During these initial phases the rms spectrum is inverted, without any indication of flattening at low energies (see the rms spectrum in Figure 8.5). Although most of the BHCs in the LHS feature flat spectra, inverted spectra have already been observed in some sources (XTE J1650-500, see Figure 5 in Gierliński & Zdziarski 2005). Zdziarski et al. (2002) and Gierliński & Zdziarski (2005) explained this type of spectrum by considering a seed photon input to the Comptonizing corona with variable energy, that causes a pivoting of the energy

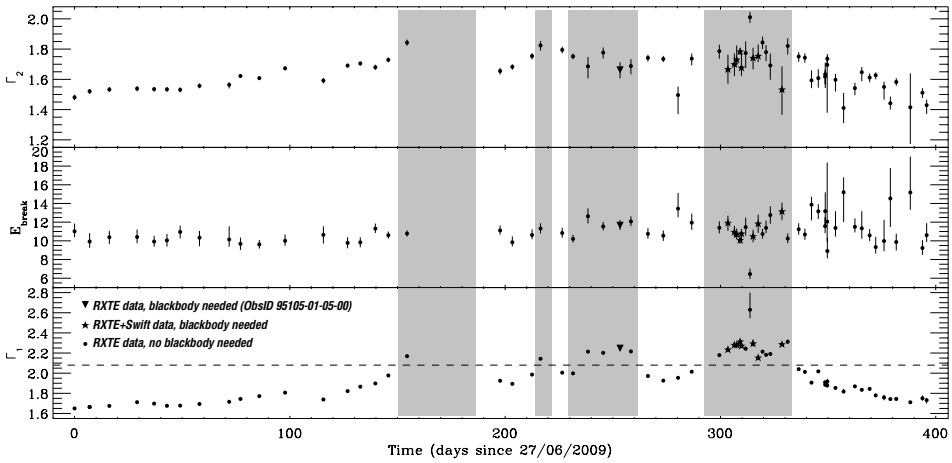

Figure 8.11: Evolution of the three parameters of the broken power law used to fit the energy spectra in Tables 8.3 and 8.4. The grey areas mark HIMS epochs. The horizontal dashed line in the lower panel separates LHS observations from HIMS observations (below and above the line, respectively). The line is traced at $\Gamma_1 = 2.08$.

spectrum around $\sim 20 - 50$ keV and a decline in fractional rms above ~ 5 keV. The absence of a flattening suggests that the disc from which the seed photons originates is very cold (a disc with $kT \sim 0.7$ keV would give a flattening in the rms spectrum below ~ 2 keV, Gierliński & Zdziarski 2005). In §8.3.2 we showed that an absorbed broken power law is sufficient to fit all the spectra from the observations in the LHS (at least during the "failed transition") and even in the softest part of the HIMS the disc is slightly colder than in other BHCs in this state.

Chiang et al. (2010) analysed Swift and RXTE observations of Swift J1753.5-0127 performed when the source was in the LHS, between 2005 July and 2007 July. They found that a thermal component *diskbb* is needed to fit the energy spectra, with temperature below ~ 0.25 keV. These results confirm that the disc is indeed too cold to produce a flat rms spectrum at low energies.

After the first ~ 33 days the rms spectrum changes and becomes, for the rest of the outburst, consistent with being either flat or slightly inverted (except for ~ 8 observations, see §8.3.1), independently on whether the source is in the LHS or in the HIMS. Flat rms spectra correspond to a situation in which the entire energy spectrum (dominated by a Comptonizing component) varies in normalization (luminosity) but not in spectral shape (except possibly the high energy cut-off).

Muñoz-Darias et al. (2011) showed that in three outbursts of GX 339-4, the transition from the LHS to the HIMS is associated to clear changes in the RID, namely the source leaves the hard line and moves to the left-hand side of the diagram along another track. This change in the RID is associated to the drop in the infrared flux previously reported by Homan et al. (2005) for one of the outbursts, considered a

signature of the state transition. Figure 8.1 shows that, after $\sim$ 4 years from the beginning of the outburst, a spectral softening begins, bringing Swift J1753.5-0127 below its initial hardness level. In Figure 8.3 we can see that there is a number of points that, at a visual inspection, do not fall on the hard line. Differently from GX 339-4, these points do not follow a precise path in the RID but they are all located on the left-hand side of the hard line, at lower fractional rms. However, they all feature a spectral hardness $h \lesssim 0.63$. For this reasons we identify these points as HIMS observations. It is also worth pointing out that, differently from GX 339-4, several transitions from the LHS to the HIMS (and vice versa) take place, hence the sources leaves and joins the hard line several times. The use of both the HID and the RID is fundamental to determine the spectral state: in the right-hand panel of Figure 8.3 one can see that, at a count rate of $\sim$ 80 c/s and absolute rms above $\sim$ 20 c/s there are two points for which it is difficult to determine whether they fall on the hard line or not. However, in the HID, their spectral hardness is $h > 0.7$, strongly suggesting that they represent LHS observations. It would be interesting to test whether the transition from the LHS to the HIMS matches with broad-band spectral changes, in turn associated with a different disc/jet coupling (as found in GX 339-4 by Homan et al. 2005). Soleri et al. (2010) and Miller-Jones et al. (2011) reported on X-ray/radio and radio observations of Swift J1753.5-0127 performed in 2009 but unfortunately all of them have been taken before the first transition to the HIMS, hence they can not be used for our purposes.

In §8.3.2 we showed that in the LHS, the features of the power density spectra, as well as the energy spectra, are in agreement with those usually seen in other BHCs in this state. As expected, the transition to the HIMS is smooth (Belloni 2010), without abrupt changes of the spectral and timing properties. A cold disc component appears but it is only detected during the softest phases of the "failed transition" when both RXTE and Swift observed the source.

It is interesting to note that no type-C QPO appears during the "failed transition", both in the LHS and in the HIMS. Its presence however has been reported during the initial months of the outburst by Zhang et al. (2007) and Ramadevi & Seetha (2007), who found a QPO with properties compatible with the type C. For clarity, we notice that both papers do not adopt this nomenclature to classify low-frequency QPOs. Although its presence is considered a signature of the HIMS, a type-C QPO has not been detected in this state also in the BHC Cyg X-1 (Pottschmidt et al. 2003). In GX 339-4 (in the data set of Nowak et al. 2002 used to produce Figure 11 in Belloni et al. 2002) either both L_{LFQPO} (i.e. the type-C QPO) and L_h are present in the PDS or only L_h, further suggesting that the absence of the type-C QPO in the hard states is uncommon but not unreported. During the softest part of the "failed transition", the fractional rms decreases to $\sim 14\%$, close to (but still above) the typical rms levels of

the transition to the SIMS, that in the BHCs MAXI J1659-152 and GX 339-4 happens in the rms range $\sim 10 - 13\%$ and at $\sim 10\%$ rms, respectively (Muñoz-Darias et al. 2011, Muñoz-Darias et al. 2011). Considering that there are no abrupt changes of the properties of the PDS and that no type-B QPO is detected, we can safely state that the system did not go to the SIMS. Motta et al. (2010) studied the 2008 outburst of the BHC H 1743-322, in which the source, as Swift J1753.5-0127, has been observed only in the hard states. Although the type-C QPO appears in the HIMS, in the softest observation the PDS shows no QPO and the fractional rms is $\sim 10\%$, similar to the softest observations of Swift J1753.5-0127. However the softest energy spectra of H 1743-322 in the HIMS feature a thermal component with temperature ~ 0.7 keV, higher than in Swift J1753.5-0127. Belloni et al. (2011) recently showed that that the rms spectra of GX 339-4 are either inverted or hard in the HIMS, depending on whether the source was observed close to the transition from the LHS or to the SIMS, respectively. These results suggest that Swift J1753.5-0127 did not arrive to the immediate vicinity of the transition to the SIMS.

PDS	Obs. ID	Fit function	χ^2/d.o.f.	ν_b (Hz)	rms (%) $\nu_b - 100\nu_b$	rms (%) $100\nu_b - 1000\nu_b$	ratio rms
			Black hole candidates				
			Swift J1753.5-0127				
a)	93105-02-52-00	2 Lorentzians	175/116	0.16 ± 0.01	21.52 ± 0.21	7.82 ± 1.03	2.75 ± 0.36
			XTE J1550-564				
b)	50137-02-05-01	7 Lorentzians	511/414	0.15 ± 0.02	30.38 ± 0.06	10.41 ± 0.14	2.92 ± 0.04
			Neutron stars				
			4U 1705-44				
c)	40034-01-04-05	3 Lorentzians	85/97	0.22 ± 0.02	23.36 ± 0.25	14.27 ± 0.93	1.64 ± 0.11
			4U 1608-52				
d)	93408-01-02-02	3 Lorentzians	100/98	0.14 ± 0.02	16.77 ± 0.33	13.47 ± 1.11	1.25 ± 0.11
e)	93408-01-08-02	3 Lorentzians	74/98	0.18 ± 0.03	18.16 ± 0.25	12.63 ± 0.92	1.44 ± 0.11
f)	93408-01-25-01	1 broken power law	81/102	0.16 ± 0.05	19.72 ± 0.41	14.57 ± 1.38	1.35 ± 0.13

Table 8.1: List of RXTE observations used to compare the power spectra of BHCs and neutron stars. The letters in the first column can be used to identify the power spectra in Figure 8.13. The Table also shows the values of the χ^2 and the degrees of freedom, the break frequency ν_b, the rms in two frequency intervals and the ratio between the rms in the intervals $\nu_b - 100\nu_b$ and $100\nu_b - 1000\nu_b$. More details on the analysis of these PDS are reported in §8.4.1.

On 2010-05-24 (Obs. ID 95105-01-16-00), Swift J1753.5-0127 starts hardening and rapidly joins the hard line after five days. No adjacent hard line is seen in the RID, supporting the idea that its presence is a consequence of the passage of the source through the soft states. Considering the possibility that the presence of an adjacent hard line might be associated with the re-appearance of the jet after its quenching in the soft states (at least in GX 339-4; Muñoz-Darias et al. 2011), sources in which the jet gives a low contribution to the total energy output of the system (as Swift J1753.5-0127; see Soleri et al. 2010 and Soleri & Fender 2011) are good candidates to test this possibility, if observed in a "normal" outburst.

8.4.1 The nature of the compact object

Despite several years of observations at different wavelengths, the nature of the compact object in Swift J1753.5-0127 (black hole or neutron star) remains uncertain, although evidence points towards a black hole, as already mentioned in §8.1.1. The results that we obtained from spectral and timing analysis of the "failed transition" are also consistent with a black-hole binary in the hard states, even though they do not constitute a solid proof. The correlation between the photon indices of the broken power law used to fit the energy spectra (see Figure 8.12) probably reflects trends in the continuum of spectral shapes of the source: the energy spectra evolve smoothly between the LHS and the HIMS. Interestingly, a similar correlation (with a lower scatter) has already been reported by Wilms et al. (2006) in Cyg X-1, who analysed ~ 200 RXTE observations performed during 1999 and 2004. Cyg X-1 is a dynamically confirmed persistent black hole (Herrero et al. 1995) which spends most of its time in the LHS, with frequent transitions to the HIMS. Its behaviour shows several similarities with Swift J1753.5-0127, at least during the "failed transition": they both go through frequent transition from the LHS to the HIMS (and vice versa), they both lack a type-C QPO in their PDS and they show a similar correlation between the photon indices of the broken power law. This is far from being a proof that Swift J1753.5-0127 contains a black hole, nevertheless, it can be considered another hint towards this direction.

Sunyaev & Revnivtsev (2000) analysed a sample of 9 BHCs and 9 neutron stars in the hard state and noted that the former demonstrate a stronger decline in the power spectra at frequencies higher than 10-50 Hz than the latter. Although the properties of the aperiodic variability can give useful hints on the nature of the compact object, they need to be examined extremely carefully: Linares et al. (2007) for example showed that several features of the PDS of the accreting millisecond X-ray pulsar IGR J00291+5934 (e.g. very high rms, $\sim 50\%$) are more typical of BHCs in the LHS, rather than the majority of the neutron stars.
Here we compare one power spectrum of Swift J1753.5-0127 in the LHS with spectra from a dynamically confirmed black hole (XTE J1550-564, Orosz et al. 2002) and

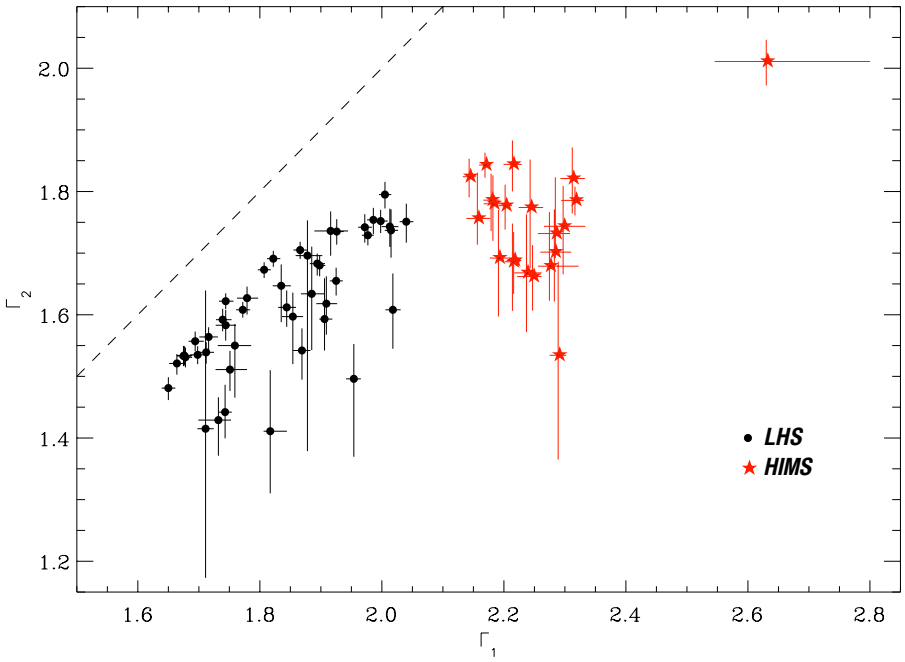

Figure 8.12: Correlation between the photon indices of the broken power law component before and after the energy break (Γ_1 and Γ_2, respectively), for all the spectral fits in Figure 8.11. The dashed line corresponds to $\Gamma_1 = \Gamma_2$. LHS and HIMS points are represented with black circles and red stars, respectively.

two secure neutron star atoll sources (4U 1705-44 and 4U 1608-52) in the hard (island) state (see Remillard & McClintock 2006 and references therein). A systematic study of the differences between the power spectra of BHCs and neutron star would require the use of a large sample of sources and is beyond the scope of this paper. The purpose of our exercise is to obtain some more information about the compact object in Swift J1753.5-0127 and is not to establish a method to distinguish black holes from neutron stars. In order to have a criterion to compare PDS from different sources in the hard state, we only considered power spectra with similar break frequency ν_b (within a factor 1.6). Table 8.1 reports a list with the observations taken into account. All the power spectra have been extracted following the procedure presented in §8.2.2, with the only difference being that intervals of 256 s have been used to accumulate the spectra of 4U 1705-44 and 4U 1608-52.

The power spectra are shown in Figure 8.13. All the PDS have been fitted using a combination of Lorentzians (as described in §8.2.2), except for the last power spectrum of 4U 1608-52, which can be successfully fitted using a broken power law function. For each power spectrum, we calculated the fractional rms in two frequency

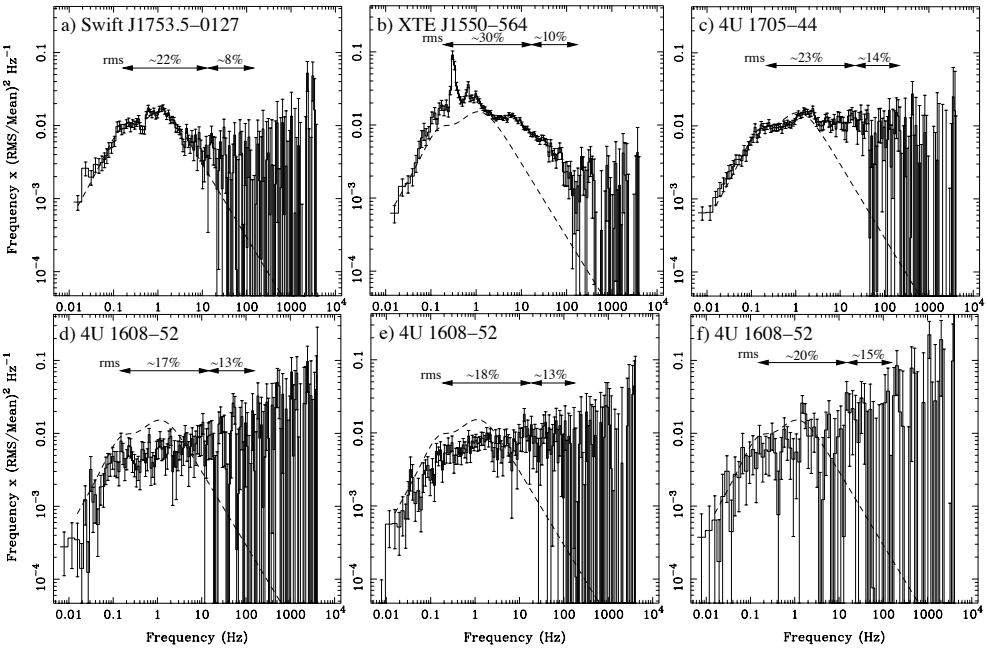

Figure 8.13: Power density spectra extracted from the RXTE observations listed in Table 8.1. In all the panels, the dashed line represents the best fitting function to the power spectrum of Swift J1753.5-0127 reported in panel a).

intervals, using as extremities multiples of the break frequency ν_b. The values of the χ^2, as well as the break frequencies and the rms are reported in Table 8.1. We also show the ratio between the fractional rms in the frequency intervals $\nu_b - 100\nu_b$ and $100\nu_b - 1000\nu_b$. Neutron stars have a smaller drop in rms at high frequencies than BHCs: a drop by a factor of $1.3 - 1.6$ in neutron stars and by a factor 2.9 in the black hole XTE J1550-564, whereas Swift J1753.5-0127 shows a 2.8 factor drop. The difference is already evident inspecting Figure 8.13, in which the power spectra in our sample have been overplotted to the best fitting function to the spectrum of Swift J1753.5-0127. Bearing in mind that this exercise is far from being a systematic study, our result is a further hint that Swift J1753.5-0127 harbours a black hole.

8.4.2 Swift J1753.5-0127: a peculiar outburst

The outburst of Swift J1753.5-0127 is certainly interesting under a number of aspects. Despite the properties of the LHS and the HIMS seem rather ordinary in comparison to the other BHCs, the source features a peculiar behaviour. First of all, it belongs to the group of sources that stayed in the hard states during the whole outburst. Obviously it would be interesting to find a characteristic systematically associated with hard outbursts. Soleri & Fender (2011) investigated whether the type of outburst

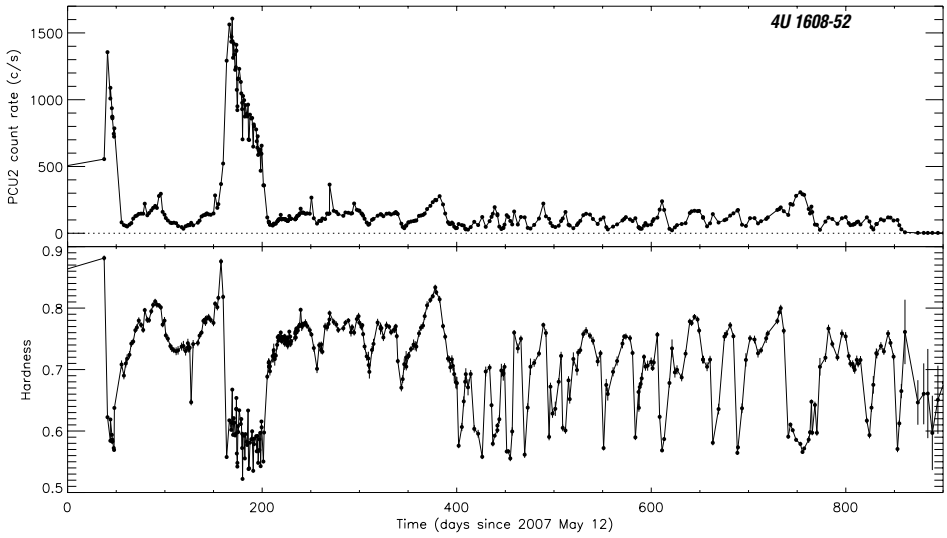

Figure 8.14: RXTE/PCA light curve and hardness curve of the neutron star 4U 1608-52 (top and bottom panels, respectively), from 2007 May 12. Every point represent one RXTE observation. The count rate has been obtained in the energy range 3.3-20.2 keV, the hardness is the ratio between the count rate in the energy bands 9.8-6.1 keV and 3.3-6.1 keV. The horizontal dotted line in the light curve marks a count rate of 0 c/s.

("normal" or hard) can influence the radio loudness of the source. Although it is not clear why some sources are "radio quiet" (i.e. they are fainter in radio than expected from the X-ray/radio correlation found by Gallo et al. (2003), see §8.1), it has been proposed that "radio quiet" sources could be characterized by a radiatively efficient accretion flow even in the LHS (Coriat et al. 2011). This suggests that the mechanisms responsible for the state transition might also be slightly different in these systems, given the different properties of the accretion flow. However, hard outbursts are not a prerogative of "radio quiet" sources (Soleri & Fender 2011) and "radio quiet" systems that had "normal" outbursts have also been observed (e.g. XTE J1720-318, Brocksopp et al. 2005).

The idea of a connection between hard outbursts and BHCs with short orbital period is also intriguing. Soleri et al. (2010) pointed out that three of the four known BHCs with the shortest orbital periods (Swift J1753.5-0127, XTE J1118+480 and GRO J0422+32) only had hard outbursts. However, hard outbursts do not seem to be a prerogative of short period systems: for instance XTE J1550-564 had a hard-only outburst and its orbital period is ~ 1.54 days; Orosz et al. 2011). Interestingly, the BHC with the shortest orbital period, MAXI J1659-152 (2.4 hr, as claimed by Kuulkers et al. 2011) certainly featured a transition to the SIMS in its outburst (Muñoz-Darias et al. 2011) but there is debate on whether it made it to the HSS (Kalamkar

et al. 2011, Muñoz-Darias et al. 2011). This last results suggest that a short orbital period could be a property sufficient to produce hard outbursts, although conclusive evidence is missing. Yu & Yan (2009) studied the outburst of a sample of BHCs using RXTE/ASM and Swift/BAT and showed that the luminosity at which the transition from the hard to the soft states happens is correlated to peak luminosity of the HSS, as well as to the derivative of the luminosity around the hard-to-soft transition (in other words the rate of change of the luminosity). In this framework, the correlations could define two transition regimes, in which the hard-to-soft state transition is allowed. Moreover, it has been recently shown that the peak luminosity of an outburst correlates to the orbital period of the binary system (Wu et al. 2010). This might suggest that short orbital period BHCs remain in the hard states because their derivative of the luminosity is too high, hence they do not fall into the transition regime mentioned above. Although this could explain why Swift J1753.5-0127 did not go to the soft states during the initial phases of the outburst, this can not explain the "failed transition", when the variations of the source count rate (and consequently the luminosity of the system) were smaller, suggesting that this approach is too simple to reveal the nature of hard state outbursts (see Yu & Yan 2009).
Another (speculative) explanation is that in short period system, the accretion disc can not extend to the vicinity of the innermost stable orbit, preventing the ejection of the geometrically thick accretion flow (e.g. the corona) and the transition to the soft states. Such thick accretion flow is often considered fundamental for the formation of a jet (Livio et al. 1999; Meier 2001). Swift J1753.5-0127 has a cold accretion disc, in agreement with this idea, however it is also features a faint jet, suggesting that the thick accretion flow close to the accreting object is not dominant or has different radiative properties than in other sources.

A second interesting aspect concerns the morphology of the X-ray light curve, namely the long period at low and slowly increasing flux that took place after the end of the initial flare and lasted more than two years. Although such behaviour is uncommon, it is already been observed in other X-ray binaries. In Figure 8.14 we report the X-ray light curve and hardness curve of the neutron star X-ray binary 4U 1608-52, obtained with RXTE/PCA for a period of ~ 900 days from 2007 May 12. The count rate and the hardness have been extracted from PCU2 data, following identical procedures to those presented in §8.2, except for the use of a slightly different energy band for the count rate (see the caption). This source usually undergoes regular outbursts, spaced out by periods of quiescence in which the PCA count rate is consistent with zero. In Figure 8.14 two outbursts of 4U 1608-52 appear, a short one in the day interval $\sim 50 - 150$ and a longer one between day ~ 150 and ~ 210. In between the two outbursts and after the second one, the system goes into prolonged low-flux phases (the second one lasts approximately 650 days) in which its hardness is higher than during the outbursts, implying that the source was not in

quiescence but in a low-flux and hard state. The behaviour of Swift J1753.5-0127 and 4U 1608-52 is reminiscent of those observed in a class of cataclysmic variables, the so-called Z Camelopardalis (Z Cam). These sources undergo regular outbursts like other subgroups of dwarf novae, followed by periods of standstills (that can last from weeks to months), in which their optical luminosity remains constant at a level close to, but slightly below, the peak of the outburst. King & Cannizzo (1998) suggested that standstills occur because in the Z Cam the mass transfer rate from the companion star is always very close to the critical mass transfer that ensures stability of disc accretion onto the compact object. The end of standstills could be due to the presence of sunspots on the star surface close to the Lagrangian point L1, where the mass transfer happens (see King & Cannizzo 1998 for the details). Haswell & King (2001) suggested that neutron star X-ray binaries with short orbital period ($\lesssim$ 10 hours, as the majority of the cataclysmic variables) could also feature standstills, given their high mass transfer. As an example they mention the neutron star EXO 0748-678, that has been active for decades after its discovery in 1985, suggesting that the system entered a particularly long standstill phase, possibly prolonged by the irradiation from the compact object.
The light curve in Figure 8.1 shows that an equivalent of a standstill also follows the initial flare of Swift J1753.5-0127, with X-ray flux approximately 13 times lower than at the peak of the outburst (at its minimum in 2006 March, Soleri et al. 2010). The similarity between Swift J1753.5-0127 and Z Cam systems is strenghtened by the low orbital period of the former ($\sim$ 3.2 hours), similar to those typically found in cataclysmic variables.

8.5 Conclusions

We performed X-ray timing and spectral analysis of the BHC Swift J1753.5-0127 during its long outburst, still ongoing at the moment of writing this manuscript. We studied the general evolution of the outburst making use of the rms-intensity diagram and the hard-intensity diagram, obtained with RXTE. The source spent most of its time in the hard state and, more than 4 years after the beginning of the outburst, moved to the hard-intermediate state. At variance with the majority of the transient black holes, the transition to the soft states failed and the system came back to the hard state after a few months. We also followed in detail this complex state transition by means of the analysis of the power spectra and energy spectra, using both RXTE and the Swift satellite. Although the majority of the black hole candidates passes through the soft states during an outburst, several sources do not do it. It is difficult to find a property that can be unambiguously associated to hard outbursts. The fact that a source has a short orbital period ($\lesssim$ 5 hours) could be a condition sufficient but not necessary to inhibit the transition to the soft states, although recent results from

the black hole MAXI J1659-162 might weaken this possibility.

The properties of the hard states featured by Swift J1753.5-0127 are consistent with the majority of the black holes in this states, except for a few uncommon characteristics, as the absence of a type-C QPO in the power spectra of the hard-intermediate state, that nevertheless has already been reported in other sources.

Despite the properties of the hard states being fairly ordinary, the morphology of the outburst is peculiar, both in terms of length (more than ~ 6 years) and shape of the X-ray light curve, given the prolonged period at low flux that followed the initial flare. Although such phases are rare (but not unobserved) in low-mass X-ray binaries, they are very common in cataclysmic variables, namely in the Z Camelopardalis sources, which often undergo standstills characterized by an approximately constant luminosity. Given its short orbital period, similar to those typically found in cataclysmic variables, it is not unexpected that Swift J1753.5-0127 behaves similarly.

Although conclusive evidence is missing, the high-energy tail in the energy spectra of Swift J1753.5-0127 constitutes the strongest hint that the binary harbours a black hole. Here we bring further clues in this direction: first of all, the photon indices of the broken power law used to fit the energy spectra seem to be correlated (despite a large scatter), as already reported for a dynamically confirmed BHC, Cyg X-1. Secondly, we showed that the drop in rms at high frequencies (above 100 times the break frequency) is higher than in two neutron star systems and similar to a dynamically confirmed black hole XTE J1550-564. We stress that this result should be considered carefully, and a systematic investigation on more source about the validity of this method is necessary. Nevertheless, we can consider it as a further hint, in agreement with the evidence already reported.

Acknowledgments

PS acknowledges support from NWO (Netherlands Foundation for Scientific Research). We thank Andrea Sanna, Andrew King and Chris Done for useful discussion. The authors also thank the Principal Investigator of the Swift mission, Neil Gehrels, for approving and scheduling the Swift ToO (Target of Opportunity). Partially funded by the Spanish MEC under the Consolider-Ingenio 2010 Program grant CSD2006-00070: 'First Science with the GTC'(http://www.iac.es/consolider-ingenio-gtc/). SM and TB acknowledge support from grant INAF-ASI I/009/10/0. The research leading to these results has received funding from the European Community's Seventh Framework Programme (FP7/2007-2013) under grant agreement number ITN 215212 "Black Hole Universe". ML acknowledges support from a NWO Rubicon fellowship. This research has made use of data obtained through the High Energy Astrophysics Science Archive Research Center Online Service, provided by the NASA (National Aeronautics and Space Administration) Goddard space

flight center.

Appendix A: Timing and spectral analysis

Here we report five tables in which we show the best fitting parameters of the power density spectra as well as the energy spectra for the observations performed during the “failed transition”.

Table 8.2: Fit parameters of the power density spectra extracted from the 67 RXTE observations marked by black-filled circles in Figure 8.1. The details on the extraction of the spectra and on the fitting procedures are described in §8.2.2 and §8.3.2. For each observation, the table shows the frequency ν_{max}, the quality factor Q and the rms of two Lorentzian components, L_b and L_h. The values of the χ^2 and the degrees of freedom are also reported.

		L_b			L_h			
Obs. ID	Date	ν_b (Hz)	Q_b	rms$_b$ (%)	ν_h (Hz)	Q_h	rms$_h$ (%)	χ^2/d.o.f.
93105-02-36-00	2009-06-27	0.17 ± 0.05	0	15.68 ± 2.40	0.90 ± 0.31	0	18.01 ± 1.88	145/118
93105-02-37-00	2009-07-04	0.30 ± 0.02	0	20.18 ± 0.40	4.67 ± 0.98	0	13.90 ± 0.56	120/118
93105-02-38-00	2009-07-13	0.36 ± 0.04	0	19.24 ± 0.79	2.90 ± 0.96	0	12.36 ± 1.03	130/118
93105-02-40-00	2009-07-26	0.62 ± 0.04	0	20.42 ± 0.33	11.07 ± 3.52	0	10.47 ± 0.79	121/115[a]
-[b]		0.093 ± 0.002	1.30 ± 0.50	6.77 ± 0.82				
93105-02-41-00	2009-08-03	0.42 ± 0.03	0	20.79 ± 0.45	4.51 ± 1.11	0	12.02 ± 0.67	116/118
93105-02-42-00	2009-08-09	0.24 ± 0.06	0	16.74 ± 2.06	1.30 ± 0.76	0	14.51 ± 2.15	159/118
93105-02-43-00	2009-08-15	0.42 ± 0.03	0	20.87 ± 0.55	3.86 ± 1.24	0	11.64 ± 0.84	164/118
93105-02-44-00	2009-08-24	0.15 ± 0.02	0.40 ± 0.16	12.40 ± 1.59	0.83 ± 0.07	0.25 ± 0.15	17.55 ± 1.57	105/114[c]
-[d]		12.08 ± 4.88	0	11.42 ± 0.89				
93105-02-46-00	2009-09-07	0.46 ± 0.06	0	19.43 ± 1.11	3.78 ± 1.56	0	13.15 ± 1.34	120/118
93105-02-47-00	2009-09-12	0.16 ± 0.03	0.34 ± 0.17	9.36 ± 1.12	0.96 ± 0.06	0	20.93 ± 0.48	166/117
93105-02-48-00	2009-09-21	0.18 ± 0.03	0.33 ± 0.13	12.13 ± 1.49	1.25 ± 0.11	0.16 ± 0.11	20.05 ± 1.07	127/116
93105-02-50-00	2009-10-03	0.22 ± 0.01	0.33 ± 0.06	14.95 ± 0.50	1.65 ± 0.05	0.38 ± 0.05	18.71 ± 0.42	132/116
93105-02-52-00	2009-10-21	0.16 ± 0.01	0.42 ± 0.14	11.17 ± 0.98	1.17 ± 0.06	0.08 ± 0.07	20.66 ± 0.60	175/116
93105-02-54-00	2009-11-01	0.24 ± 0.01	0.37 ± 0.07	16.18 ± 0.50	1.73 ± 0.05	0.51 ± 0.07	18.16 ± 0.60	110/113[c]
-[d]		40.93 ± 12.59	0.16 ± 0.98	10.72 ± 1.42				
93105-02-55-00	2009-11-07	0.30 ± 0.01	0.37 ± 0.06	15.65 ± 0.45	2.11 ± 0.05	0.49 ± 0.05	18.64 ± 0.42	133/116
93105-02-56-00	2009-11-14	0.35 ± 0.02	0.30 ± 0.05	15.89 ± 0.43	2.31 ± 0.05	0.59 ± 0.06	16.87 ± 0.43	156/116
93105-02-57-00	2009-11-20	0.52 ± 0.03	0.33 ± 0.04	15.70 ± 0.39	2.89 ± 0.06	0.80 ± 0.07	16.33 ± 0.43	121/116
93105-02-58-00	2009-11-28	1.15 ± 0.08	0.27 ± 0.06	14.61 ± 0.54	4.26 ± 0.10	1.06 ± 0.17	11.98 ± 0.73	141/116
93105-02-39-00	2010-01-11	0.50 ± 0.05	0.20 ± 0.08	17.20 ± 0.80	2.48 ± 0.09	0.94 ± 0.17	14.97 ± 1.01	135/116
93105-02-45-00	2010-01-16	0.35 ± 0.02	0.28 ± 0.06	17.62 ± 0.52	2.20 ± 0.07	0.92 ± 0.12	16.23 ± 0.66	122/116
93105-02-49-00	2010-01-25	0.61 ± 0.06	0.23 ± 0.07	15.56 ± 0.71	2.97 ± 0.09	0.91 ± 0.14	16.48 ± 0.83	129/116
93105-02-51-00	2010-01-29	1.34 ± 0.07	0.29 ± 0.04	15.77 ± 0.42	4.28 ± 0.07	1.55 ± 0.21	10.55 ± 0.61	154/116

Continued on next page

Table 8.2 – continued from previous page

		L_b			L_h			
Obs. ID	Date	ν_b (Hz)	Q_b	rms$_b$ (%)	ν_h (Hz)	Q_h	rms$_h$ (%)	χ^2/d.o.f.
95105-01-01-00	2010-02-08	0.70 ± 0.04	0.28 ± 0.05	15.90 ± 0.47	3.14 ± 0.06	1.14 ± 0.12	14.86 ± 0.56	138/113[c]
-[d]		20.28 ± 1.41	2.53 ± 1.67	5.76 ± 1.06				
95105-01-02-00	2010-02-13	0.62 ± 0.05	0.18 ± 0.07	16.98 ± 0.56	2.98 ± 0.08	0.98 ± 0.12	14.71 ± 0.68	145/116
95105-01-03-00	2010-02-20	1.76 ± 0.08	0.53 ± 0.06	16.44 ± 0.91	5.71[e]	0.57 ± 0.37	11.10 ± 1.99	97.9/94
95105-01-04-00	2010-02-27	1.44 ± 0.09	0.41 ± 0.06	15.86 ± 0.53	4.57 ± 0.10	1.98 ± 0.42	10.22 ± 0.84	117/116
95105-01-05-00	2010-03-07	2.99 ± 0.24	0.49 ± 0.10	17.56 ± 0.72	-[f]	-	-	118/119
95105-01-06-00	2010-03-12	1.97 ± 0.10	0.14 ± 0.05	21.93 ± 0.39	-[f]	-	-	154/119
95105-01-07-00	2010-03-20	0.59 ± 0.03	0.33 ± 0.05	15.87 ± 0.44	2.93 ± 0.06	0.94 ± 0.09	15.94 ± 0.50	124/116
95105-01-08-00	2010-03-27	0.53 ± 0.03	0.22 ± 0.05	18.43 ± 0.48	2.72 ± 0.07	1.03 ± 0.12	14.65 ± 0.63	119/116
95105-01-09-00	2010-04-03	0.59 ± 0.03	0.26 ± 0.05	16.66 ± 0.45	2.90 ± 0.06	1.09 ± 0.10	15.26 ± 0.53	132/116
95105-01-10-00	2010-04-10	0.95 ± 0.11	0.20 ± 0.08	17.68 ± 0.87	3.36 ± 0.11	1.64 ± 0.40	12.10 ± 1.24	109/116
95105-01-11-00	2010-04-22	1.61 ± 0.11	0.35 ± 0.06	16.60 ± 0.54	4.77 ± 0.14	2.15 ± 0.61	8.46 ± 1.01	162/116
95105-01-12-00	2010-04-26	2.71 ± 0.11	0.67 ± 0.07	16.52 ± 0.44	-[f]	-	-	124/119
95105-01-12-02[g]	2010-04-29	2.84 ± 0.09	0.77 ± 0.08	14.96 ± 0.35	-[f]	-	-	118/116 [a]
-[b]		0.026 ± 0.002	0.78 ± 0.17	7.47 ± 0.42				
95105-01-12-01[h]								
95105-01-13-00[g]	2010-05-02	2.73 ± 0.10	0.73 ± 0.09	15.44 ± 0.44	-[f]	-	-	103/119
95105-01-13-03[h]								
95105-01-13-02	2010-05-05	2.29 ± 0.13	0.58 ± 0.08	17.45 ± 0.52	-[f]	-	-	108/119
95105-01-14-03	2010-05-07	2.70 ± 0.18	0.77 ± 0.13	15.82 ± 0.69	-[f]	-	-	111/119
95105-01-14-00	2010-05-08	2.87 ± 0.18	0.73 ± 0.13	14.35 ± 0.62	-[f]	-	-	97/119
95105-01-14-01	2010-05-10	2.25 ± 0.11	0.38 ± 0.05	19.07 ± 0.40	-[f]	-	-	111/119
95105-01-14-02	2010-05-12	2.25 ± 0.17	0.35 ± 0.07	20.57 ± 0.69	-[f]	-	-	100/119
95105-01-15-00	2010-05-14	1.62 ± 0.08	0.63 ± 0.08	16.35 ± 0.53	5.21 ± 0.17	2.48 ± 0.74	9.56 ± 0.98	107/116
95105-01-15-01	2010-05-16	2.34 ± 0.14	0.40 ± 0.06	18.33 ± 0.47	-[f]	-	-	122/119
95105-01-16-00	2010-05-22	3.18 ± 0.18	1.05 ± 0.23	13.25 ± 0.76	-[f]	-	-	150/119
95105-01-16-01	2010-05-24	2.14 ± 0.21	0.69 ± 0.17	16.00 ± 0.95	-[f]	-	-	100/119
95105-01-17-00	2010-05-29	0.95 ± 0.13	0.23 ± 0.09	17.10 ± 1.01	3.61 ± 0.12	1.67 ± 0.48	13.06 ± 1.36	126/116

Continued on next page

Table 8.2 – continued from previous page

		L_b			L_h			
Obs. ID	Date	ν_b (Hz)	Q_b	rms$_b$ (%)	ν_h (Hz)	Q_h	rms$_h$ (%)	χ^2/d.o.f.
95105-01-17-01	2010-06-01	0.73 ± 0.10	0.19 ± 0.10	16.31 ± 0.97	3.18 ± 0.14	1.33 ± 0.28	14.83 ± 1.19	144/116
95105-01-18-00	2010-06-04	0.50 ± 0.03	0.24 ± 0.06	18.15 ± 0.53	2.72 ± 0.08	0.84 ± 0.10	16.24 ± 0.65	115/116
95105-01-18-01	2010-06-07	0.79 ± 0.06	0.43 ± 0.08	16.07 ± 0.70	3.67 ± 0.18	1.04 ± 0.24	13.57 ± 1.01	109/116
95105-01-19-00[g]	2010-06-11	0.49 ± 0.09	0.11 ± 0.13	18.43 ± 1.23	2.60 ± 0.14	0.82 ± 0.22	15.03 ± 1.58	106/116
95105-01-19-01[h]								
95105-01-19-02[g]	2010-06-12	0.44 ± 0.05	0.26 ± 0.10	18.78 ± 0.99	2.56 ± 0.14	0.75 ± 0.22	16.21 ± 1.38	100/116
95105-01-19-03[h]								
95105-01-19-04[i]	2010-06-15							
95105-01-20-00	2010-06-19	0.30 ± 0.02	0.33 ± 0.06	18.51 ± 0.51	1.93 ± 0.07	0.70 ± 0.09	16.20 ± 0.62	164/116
95105-01-20-01	2010-06-24	0.36 ± 0.03	0.25 ± 0.08	17.97 ± 0.71	2.38 ± 0.11	0.73 ± 0.18	15.40 ± 1.00	97/116
95105-01-21-00	2010-06-28	0.32 ± 0.03	0.14 ± 0.09	20.26 ± 0.75	2.11 ± 0.08	0.91 ± 0.17	16.06 ± 1.01	117/116
95105-01-21-01	2010-07-01	0.32 ± 0.02	0.31 ± 0.07	19.91 ± 0.59	2.00 ± 0.07	0.96 ± 0.16	15.99 ± 0.80	114/116
95105-01-22-00	2010-07-04	0.22 ± 0.02	0.26 ± 0.08	16.39 ± 0.96	1.32 ± 0.08	0.42 ± 0.15	16.06 ± 1.17	121/116
95105-01-22-01	2010-07-08	0.28 ± 0.05	0	16.96 ± 1.48	1.62 ± 0.29	0.32 ± 0.22	13.92 ± 2.04	135/117
95105-01-23-00	2010-07-11	0.20 ± 0.03	0.24 ± 0.13	16.18 ± 1.19	1.35 ± 0.11	0.38 ± 0.16	16.53 ± 1.34	109/116
95105-01-23-01	2010-07-14	0.15 ± 0.02	0.37 ± 0.17	13.09 ± 1.18	1.06 ± 0.16	0	17.18 ± 0.83	131/117
95105-01-24-00	2010-07-20	0.13 ± 0.02	0.40 ± 0.20	14.74 ± 1.33	1.08 ± 0.29	0	16.50 ± 1.02	131/117
95105-01-25-00	2010-07-26	0.32 ± 0.05	0	20.70 ± 0.71	-[d]	-	-	118/120
95105-01-25-01	2010-07-28	0.18 ± 0.02	0	21.01 ± 0.63	-[d]	-	-	111/120

[a] A third Lorentzian with frequency $\nu < \nu_b$ was used to obtain a satisfactory fit. The values of its parameters are reported at the following line.

[b] This component has been used to fit the power spectrum of the observation at the previous line. It can be possibly identified with L_{b2}.

[c] A third Lorentzian with frequency $\nu > \nu_h$ was used to obtain a satisfactory fit. The values of its parameters are reported at the following line.

[d] This component has been used to fit the power spectrum of the observation at the previous line. It can be possibly identified with L_l.

[e] The frequency ν_h has been fixed in order to fit L_h.

[f] L_h is not needed in this fit.

[g] This observation and the following one have been performed within 24 hours, hence power spectra have been averaged and fitted together.

[h] This observation and the previous one have been performed within 24 hours, hence power spectra have been averaged and fitted together.

[i] The PDS extracted from this observation can not be fitted because of a spike in the light curve of PCU0.

Table 8.3: Best-fitting parameters of 59 energy spectra extracted from RXTE observations performed during the "failed transition" (see §8.3.2). The details on the extraction of the spectra and on the fitting procedures are described in §8.2.3 and §8.3.2. For all the observations performed before December 2009 we made use of PCA and HEXTE data (until Obs. ID 93105-02-58-00) while for the remaining observations only PCA data were available. Here we report the value of the parameters of the broken power law used to fit the spectra.

Obs. ID	χ^2/d.o.f.	Γ_1	E_{break}	Γ_2
PCA & HEXTE				
93105-02-36-00	122/104	1.65 ± 0.01	$11.02^{+0.83}_{-0.63}$	1.48 ± 0.02
93105-02-37-00	118/104	1.67 ± 0.01	$9.92^{+0.90}_{-0.67}$	1.52 ± 0.02
93105-02-38-00	87/104	1.68 ± 0.01	$10.39^{+0.68}_{-0.74}$	1.53 ± 0.02
93105-02-40-00	130/104	1.71 ± 0.01	$10.41^{+0.80}_{-0.67}$	1.54 ± 0.03
93105-02-41-00	97/104	1.69 ± 0.01	$9.93^{+0.62}_{-0.55}$	$1.54^{+0.01}_{-0.02}$
93105-02-42-00	86/104	1.68 ± 0.01	$10.05^{+0.68}_{-0.67}$	1.53 ± 0.02
93105-02-43-00	114/104	1.68 ± 0.01	$10.95^{+0.67}_{-0.70}$	1.53 ± 0.02
93105-02-44-00	107/104	1.69 ± 0.01	$10.34^{+0.72}_{-0.91}$	1.56 ± 0.02
93105-02-46-00	94/104	1.72 ± 0.02	$10.14^{+1.42}_{-0.77}$	1.56 ± 0.02
93105-02-47-00	122/104	1.74 ± 0.01	9.69 ± 0.66	1.62 ± 0.01
93105-02-48-00	116/104	1.77 ± 0.01	$9.62^{+0.47}_{-0.45}$	1.61 ± 0.01
93105-02-50-00	130/104	1.81 ± 0.01	$10.00^{+0.68}_{-0.53}$	1.67 ± 0.01
93105-02-52-00	132/104	1.74 ± 0.01	$10.64^{+0.92}_{-0.93}$	1.59 ± 0.02
93105-02-54-00	80/104	1.82 ± 0.01	$9.78^{+0.61}_{-0.58}$	1.69 ± 0.01
93105-02-55-00	129/104	1.87 ± 0.01	$9.84^{+0.55}_{-0.53}$	1.71 ± 0.01
93105-02-56-00	141/104	1.90 ± 0.01	$11.31^{+0.53}_{-0.48}$	1.68 ± 0.02
93105-02-57-00	115/104	1.98 ± 0.01	$10.60^{+0.40}_{-0.37}$	1.73 ± 0.02
93105-02-58-00	128/104	2.17 ± 0.01	$10.78^{+0.33}_{-0.31}$	1.84 ± 0.02

Continued on next page

Table 8.3 – continued from previous page

Obs. ID	χ^2/d.o.f.	Γ_1	E_{break}	Γ_2
PCA only				
93105-02-39-00	48/60	1.93 ± 0.01	$11.11^{+0.53}_{-0.46}$	1.66 ± 0.02
93105-02-45-00	72/60	1.89 ± 0.01	$9.85^{+0.62}_{-0.44}$	1.68 ± 0.02
93105-02-49-00	62/60	1.99 ± 0.01	$10.62^{+0.60}_{-0.45}$	1.75 ± 0.02
93105-02-51-00	78/60	2.14 ± 0.01	$11.32^{+0.57}_{-0.51}$	1.82 ± 0.03
95105-01-01-00	61/60	2.01 ± 0.01	$10.84^{+0.56}_{-0.49}$	1.80 ± 0.02
95105-01-02-00	61/60	2.00 ± 0.01	$10.21^{+0.44}_{-0.38}$	1.75 ± 0.02
95105-01-03-00	89/60	2.21 ± 0.01	$12.64^{+0.84}_{-0.77}$	$1.69^{+0.06}_{-0.08}$
95105-01-04-00	73/60	2.20 ± 0.01	$11.54^{+0.49}_{-0.41}$	$1.78^{+0.03}_{-0.04}$
95105-01-05-00[a]	72/58	$2.25^{+0.01}_{-0.03}$	$11.65^{+0.58}_{-0.48}$	$1.66^{+0.05}_{-0.06}$
95105-01-06-00	65/60	2.22 ± 0.01	$12.08^{+0.55}_{-0.50}$	1.69 ± 0.05
95105-01-07-00	61/60	1.97 ± 0.01	$10.75^{+0.61}_{-0.52}$	1.74 ± 0.02
95105-01-08-00	43/60	1.93 ± 0.02	$10.56^{+0.55}_{-0.56}$	1.74 ± 0.02
95105-01-09-00	66/60	1.95 ± 0.01	$13.45^{+1.69}_{-0.92}$	$1.50^{+0.13}_{-0.06}$
95105-01-10-00	64/60	2.02 ± 0.01	$11.95^{+0.96}_{-0.77}$	$1.74^{+0.03}_{-0.04}$
95105-01-11-00	83/60	2.18 ± 0.01	$11.40^{+0.69}_{-0.61}$	$1.79^{+0.04}_{-0.05}$
95105-01-13-02	52/60	2.24 ± 0.02	$11.47^{+1.02}_{-0.91}$	$1.77^{+0.08}_{-0.10}$
95105-01-14-03	68/60	$2.63^{+0.17}_{-0.08}$	$6.45^{+0.58}_{-0.53}$	2.01 ± 0.04
95105-01-14-02	49/60	$2.21^{+0.02}_{-0.01}$	$10.73^{+0.55}_{-0.48}$	1.84 ± 0.04
95105-01-15-00	41/60	2.18 ± 0.02	$11.39^{+0.78}_{-0.56}$	$1.78^{+0.05}_{-0.06}$
95105-01-15-01	45/60	$2.19^{+0.02}_{-0.01}$	$12.76^{+0.95}_{-0.93}$	$1.69^{+0.08}_{-0.09}$
95105-01-16-01	56/60	2.31 ± 0.02	$10.26^{+0.55}_{-0.50}$	$1.82^{+0.05}_{-0.06}$
95105-01-17-00	35/60	2.04 ± 0.01	$11.24^{+0.59}_{-0.65}$	1.75 ± 0.03

Continued on next page

Table 8.3 – continued from previous page

Obs. ID	χ^2/d.o.f.	Γ_1	E_{break}	Γ_2
95105-01-17-01	55/60	2.01 ± 0.01	$10.68^{+0.63}_{-0.57}$	1.74 ± 0.03
95105-01-18-00	48/60	1.91 ± 0.01	$13.87^{+0.85}_{-1.67}$	$1.59^{+0.07}_{-0.05}$
95105-01-18-01	43/60	2.02 ± 0.01	$13.16^{+0.76}_{-0.83}$	1.61 ± 0.06
95105-01-19-00	53/60	1.91 ± 0.02	$11.57^{+0.95}_{-0.75}$	$1.62^{+0.04}_{-0.05}$
95105-01-19-01	47/60	1.89 ± 0.02	$13.17^{+2.03}_{-1.78}$	$1.63^{+0.08}_{-0.09}$
95105-01-19-02	52/60	$1.88^{+0.02}_{-0.03}$	$12.06^{+6.33}_{-2.13}$	$1.70^{+0.06}_{-0.32}$
95105-01-19-03	44/60	$1.92^{+0.03}_{-0.04}$	$8.91^{+1.41}_{-0.78}$	$1.74^{+0.03}_{-0.04}$
95105-01-19-04	68/60	1.85 ± 0.02	$11.38^{+1.79}_{-0.93}$	$1.60^{+0.04}_{-0.08}$
95105-01-20-00	66/60	$1.82^{+0.03}_{-0.01}$	$15.20^{+1.61}_{-3.19}$	1.41 ± 0.10
95105-01-20-01	38/60	1.87 ± 0.01	$11.50^{+0.91}_{-0.60}$	$1.54^{+0.04}_{-0.05}$
95105-01-21-00	39/60	$1.84^{+0.02}_{-0.01}$	$11.34^{+1.84}_{-1.12}$	$1.65^{+0.03}_{-0.06}$
95105-01-21-01	37/60	$1.84^{+0.02}_{-0.01}$	$10.59^{+0.68}_{-0.61}$	1.61 ± 0.03
95105-01-22-00	54/60	1.78 ± 0.02	$9.34^{+1.09}_{-0.71}$	$1.63^{+0.02}_{-0.03}$
95105-01-22-01	57/60	1.76 ± 0.03	$9.98^{+2.27}_{-1.09}$	$1.55^{+0.03}_{-0.08}$
95105-01-23-00	40/61	1.74 ± 0.01	$14.54^{+3.26}_{-3.06}$	1.44 ± 0.04
95105-01-23-01	53/61	1.74 ± 0.02	$9.87^{+0.89}_{-0.90}$	1.58 ± 0.02
95105-01-24-00	41/60	1.71 ± 0.01	$15.18^{+3.83}_{-1.86}$	$1.42^{+0.22}_{-0.24}$
95105-01-25-00	52/60	$1.75^{+0.03}_{-0.02}$	$9.23^{+0.84}_{-0.73}$	1.51 ± 0.03
95105-01-25-01	49/60	$1.73^{+0.02}_{-0.03}$	$10.60^{+1.29}_{-0.72}$	$1.43^{+0.04}_{-0.06}$

[a] A disc-blackbody component (*diskbb* with temperature $kT = 0.41^{+0.11}_{-0.06}$ keV) needs to be added in order to get a statistically acceptable fit, even if it is not significant abobe 3σ.

Table 8.4: Best-fitting parameters of 8 energy spectra from simultaneous RXTE/PCA plus Swift/XRT observations performed during the "failed transition" (see §8.3.2). The details on the extraction of the spectra and on the fitting procedures are described in §8.2.3 and §8.3.2. Here we report the value of the parameters of the absorption N_H, the thermal component *diskbb* and the broken power law used to fit the spectra.

Obs. ID		Component:	*wabs*	*diskbb*		*bknpower*		
RXTE	Swift	χ^2/d.o.f.	N_H^{a}	kT (keV)	$R_{in}^{b}\sqrt{cos\,\theta}$	Γ_1	E_{break}	Γ_2
95105-01-12-00	00031232008	357/426	$0.283^{+0.014}_{-0.004}$	$0.273^{+0.006}_{-0.007}$	-[c]	2.24 ± 0.02	$11.95^{+0.74}_{-0.88}$	$1.67^{+0.09}_{-0.10}$
95105-01-12-02	00031232009	389/426	$0.178^{+0.007}_{-0.010}$	$0.415^{+0.004}_{-0.011}$	66^{+5}_{-3}	$2.28^{+0.03}_{-0.02}$	$10.97^{+0.62}_{-0.55}$	$1.70^{+0.07}_{-0.08}$
95105-01-12-01	00031232009	386/426	$0.18^{+0.02}_{-0.01}$	$0.41^{+0.01}_{-0.04}$	67^{+24}_{-4}	$2.28^{+0.02}_{-0.03}$	$10.71^{+0.60}_{-0.52}$	$1.73^{+0.09}_{-0.04}$
95105-01-13-00	00031232010	381/426	$0.272^{+0.010}_{-0.009}$	$0.32^{+0.03}_{-0.02}$	-[c]	$2.32^{+0.01}_{-0.02}$	$10.10^{+0.23}_{-0.38}$	1.79 ± 0.02
95105-01-13-03	00031232011	397/426	$0.209^{+0.006}_{-0.016}$	0.36 ± 0.02	94^{+13}_{-9}	$2.27^{+0.05}_{-0.02}$	$10.81^{+0.46}_{-0.73}$	$1.68^{+0.09}_{-0.06}$
95105-01-14-00	00031232013	398/426	0.20 ± 0.02	0.34 ± 0.02	106^{+23}_{-13}	$2.30^{+0.04}_{-0.03}$	$10.51^{+0.69}_{-0.66}$	$1.74^{+0.07}_{-0.08}$
95105-01-14-01	00031232014	326/426	$0.21^{+0.03}_{-0.01}$	$0.32^{+0.03}_{-0.04}$	-[c]	2.16 ± 0.02	$11.86^{+0.95}_{-1.01}$	$1.76^{+0.07}_{-0.04}$
95105-01-16-00	00031232018	369/426	0.23 ± 0.01	$0.303^{+0.013}_{-0.007}$	144^{+20}_{-16}	2.29 ± 0.01	$13.18^{+0.91}_{-0.97}$	$1.53^{+0.15}_{-0.17}$

[a] The values of N_H are in units of $\times 10^{22}\mathrm{cm}^{-2}$.

[b] The inner disc radius (in kilometres) is related to the normalization K of the *diskbb* component in this way: $R_{in} = \frac{D_{10}}{\sqrt{cos\,\theta}} \times \sqrt{K}$, where θ is the disc inclination on the line of sight and D_{10} is the distance to the source (in units of 10 kpc). Following Soleri et al. (2010), we consider a distance to Swift J1753.5-0127 of 8 kpc.

[c] For this fit the disc-blackbody component is not significant above 3σ (but it is needed in order to get a statistically acceptable fit), hence we do not calculate R_{in}.

9 The hard state of black hole candidates: XTE J1752-223

Teo Muñoz-Darias, Sara E. Motta, Devraj Pawar, Tomaso M. Belloni, Sergio Campana, Dipankar Bhattacharya

Monthly Notices of the Royal Astronomical Society, 2009, 404, 94

Abstract

We present a two-day long RXTE observation and simultaneous Swift data of the bright X-ray transient XTE J1752-223. Spectral and timing properties were stable during the observation. The energy spectrum is well described by a broken power-law with a high energy cut-off. A cold disc (~ 0.3 keV) is observed when Swift/XRT data are considered. The fractional rms amplitude of the aperiodic variability (0.002–128 Hz) is $48.2 \pm 0.1\%$ and it is not energy dependent. The continuum of the power density spectrum can be fitted by using four broad-band Lorentzians. A high frequency (~ 21 Hz) component and two weak QPO-like features are also present. Time-lags between soft and hard X-rays roughly follow the relation $\Delta t \propto \nu^{-0.7}$, with delays dropping from ~ 0.5 (0.003 Hz) to ~ 0.0015 ($\geq$10 Hz) seconds. Our results are consistent with XTE J1752-223 being a black-hole candidate, with all timing and spectral components very similar to those of Cyg X-1 during its canonical hard state.

9.1 Introduction

Black hole X-ray transients (BHT) represent the majority of the black hole binary (BHB) population known so far. These systems spend most of their lives in quiescence, displaying luminosities too low to be detected by X-ray all-sky monitors (see e.g. Garcia et al. 1998). However, they also undergo outburst events in which they become as bright as persistent sources, allowing their discovery. During these episodes, both the spectral and the time variability properties of BHTs vary dramatically, yielding the so-called "states". There is still much discussion about how many different states there are, and their correspondence with different physical conditions (see e.g. Belloni 2010 for a general description), but the presence of a $hard$ state (historically known as *low/hard*; LHS) at the begining of the outburst which evolves towards a $soft$ state (*high/soft*; HSS) is widely accepted. The LHS, also associated with the last part of the outburst, is characterized by a power-law dominated energy spectrum with a power-law index of ~ 1.6 (2–20 keV band). A high energy cut-off ($\sim$ 60–200 keV; Wilms et al. 2006; Motta et al. 2009) is observed and aperiodic variability with a fractional root mean square amplitude (rms) above 30% is seen. The energy spectrum is softer during HSS, being dominated by a thermal disc black body component. However, a hard tail up to $\sim$ 1 MeV is present (Grove et al. 1998). The rms associated with the aperiodic variability drops until 1% or less. These two "canonical" states were first proposed to describe the behaviour of the prototypical BHB Cyg X-1.

XTE J1752-223 was discovered by the *Rossi X-ray Timing Explorer* (RXTE) on October 23, 2009 (Markwardt et al. 2009). The source showed a 2–10 keV flux of

Spectral parameter	Value
Absorption (10^{22} atoms cm^{-2})	$0.72^{+0.01}_{-0.04}$
$T_{\rm in}$ (keV)	0.313 ± 0.007
Diskbb norm.	$(1.027 \pm 0.001) \times 10^6$
Γ_1	1.471 ± 0.008
$E_{\rm break}$ (keV)	10.2 ± 0.4
Γ_2	1.24 ± 0.01
PL. norm. (photons keV^{-1}cm^{-2}s^{-1})	$44.7^{+0.5}_{-0.6}$
High energy cut-off (keV)	133^{+6}_{-5}

Table 9.1: Spectral parameters for XRT+PCA+HEXTE spectra. Absorption is the equivalent Hydrogen column. $T_{\rm in}$ is the temperature at inner disc radius. Diskbb norm. is the normalisation of the *diskbb* component defined as $(\frac{R_{in}/{\rm km}}{D/10\ {\rm kpc}})^2 cos\Theta$, where $R_{\rm in}$ is the inner disc radius (km), D is the distance to the source (kpc) and Θ is the inclination angle of the disc. Γ_1 and Γ_2 are the power-law photon indexes. $E_{\rm break}$ is the break energy. PL norm. is the power-law normalisation at 1 keV.

30 mCrab. Significant similarities with the typical properties of BHT during the LHS were soon noticed by Markwardt et al. (2009) and Shaposhnikov et al. (2009). A bright optical counterpart was detected (Torres et al. 2009), showing in the optical spectrum a broad Hα emission line ($FWHM \sim 750$ km s^{-1}) typical of accreting binaries (Torres et al. 2009). A radio counterpart with a spectrum consistent with that of a compact jet, as expected for LHS, was also reported by Brocksopp et al. (2009). All these properties triggered a daily monitoring by RXTE in order to follow up the outburst evolution. In this paper we present spectral and time variability analysis of XTE J1752-223 using an unusually long, almost continuous observation (~ 116 ks) performed by RXTE during 26th, 27th and 28th October 2009 (MJD 55130-55132). The quality of this data set allows us to perform a detailed study of this source and compare its general behaviour with that shown by the prototypical BHB Cyg X-1 during LHS.

9.2 Observations

We analyse a ~ 116 ks observation of XTE J1752-223 interrupted only by satellite-related gaps. This corresponds to RXTE archive observations identifiers 94044–07–01–00, 94044–07–01–01, 94044–07–01–02 and 94331–01–01–00, 94331–01–01–02 that were performed between October 26 (15:03 UT) and 29 (20:50 UT), 2009. A total of 35 one-orbit pointings were used. For comparison we have also analysed a ~ 15 ks RXTE observation of Cyg X-1 (94121–01–08–00) starting on April 12, 2009 (02:15 UT). This observation was chosen because it is the longest observation of Cyg X-1 performed recently with RXTE and the instrument response is expected to be similar to that for the XTE J1752-223 data.

The variability study presented in this paper is based on data from the *Proportional Counter Array* (PCA). For XTE J1752-223 the data are in the mode E_125us_64M_0_1s which covers the PCA effective energy range (2-60 keV) with 64 bands. However only PCA channels 0–35 (2–15 keV) were used in the analysis. For Cyg X-1 we selected the modes SB_125us_0_13_1s and SB_125us_0_13_1s that cover the 2–15 keV band used for the analysis of XTE J1752-223. For both objects the time resolution is 122μs.

The PCA Standard 2 mode (STD2) was used for spectral analysis. It covers the 2–60 keV energy range with 129 channels. From the data, we extracted hardness (h), defined as the ratio of counts in STD2 channels 11–20 (6.1–10.2 keV) and 4-10 (3.3–6.1 keV). Using this definition we find similar average values of $h = 0.887 \pm 0.002$ for XTE J1752-223 and $h = 0.821 \pm 0.003$ for Cyg X-1, both in the range expected for LHS. Energy spectra from the PCA and *High Energy X-ray Timing Experiment* (HEXTE) instruments (background and dead-time corrected) were extracted for each observation using the standard RXTE software within HEASOFT V. 6.7. For our

spectral fitting, only Proportional Counter Unit 2 from the PCA and Cluster B from HEXTE were used. In order to account for residual uncertainties in the instrument calibration a systematic error of 0.6% and 1% was added to the PCA and HEXTE spectra, respectively. All the observations were averaged in a single spectrum after a preliminary spectral analysis where no significant spectral variability across the pointings was found.
To extend our energy coverage down to 0.5 keV we also made use of snapshot *Swift X-ray Telescope* (XRT) observations collected within 26-28 Oct 2009. In particular, we use observation numbers 00031532001, 00031532002 and 00031532003 (3.2 ks of data). They were carried out in Windowed Timing (WT) mode, due to the brightness of the source. In WT mode a 1D image is obtained by reading data compressed along the central 200 pixels in a single row. The XRT data were reprocessed with standard procedures (xrtpipeline V. 0.12.3 within HEASOFT V. 6.7). We extracted source events in a circular region with radius 20 pixels centred on source. Ancillary response files were generated with the XRTMKARF task, accounting for CCD defects, vignetting, and point-spread function corrections. Given the relatively high interstellar absorption and source count rate, we prefer also to select photons based on their grade, allowing only for single-pixel events. This provides a clearer spectrum and a higher spectral resolution. The source is very bright: since within the energy range considered the background contributes less than 1%, we did not correct for the background. After verification of comparable spectra in the three observations, we summed the data into a single spectrum, creating the corresponding *arf* file. During the fit we used the response file swxwt0s6_20070901v011.rmf appropriate for single pixel events and for the new XRT substrate voltage (6 V).

9.3 Data analysis

The analysis of the energy spectrum, power density spectrum (PDS), rms spectrum and time-lags is presented here. They have been performed making use of XSPEC and custom timing software running under IDL.

9.3.1 Spectral analysis

In order to perform a broad band spectral analysis, *Swift*/XRT (0.5-7.0 keV), PCA (4-20 keV) and HEXTE (20-200 keV) spectra were combined. XSPEC V. 12.5.1 was used to fit the spectra. We started by trying a one-component model, either a cut-off-power-law (*cutoffpl* in XSPEC) or a black body disc (*diskbb* in XSPEC), without success. In the same way, a clear residual in the soft part of the spectrum is observed when using a simple combination of these two models (i.e. *cutoffpl* + *diskbb*).
Nowak et al. (2005) showed that the energy spectra of BHB can be empirically de-

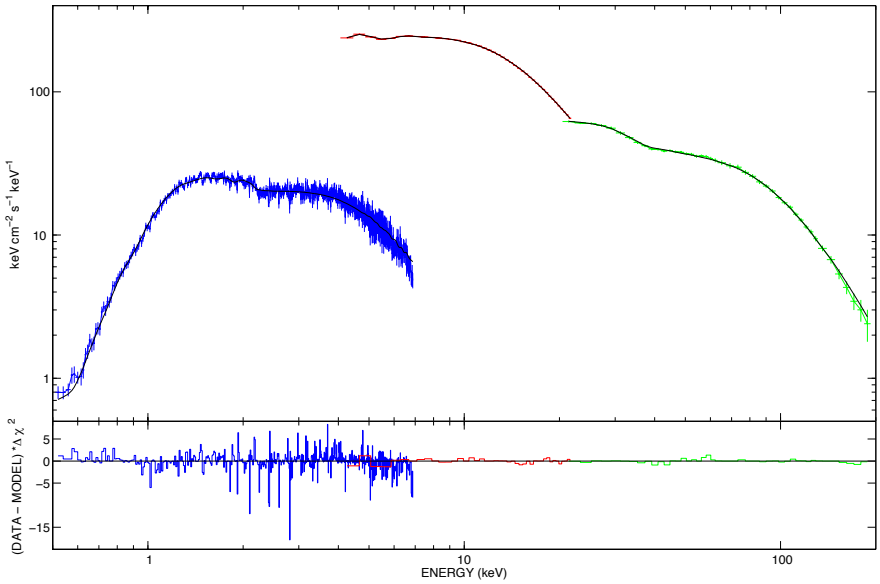

Figure 9.1: Our best fit to the combined XRT, PCA and HEXTE spectrum of XTE J1752-223. The model used consist of an interstellar absorption component, two Gaussian lines, a multicolour black-body disc, a broken power-law and a high energy cut-off (see text). Top panel: XRT, PCA and HEXTE spectra. Bottom panel: residuals plotted as signed contribution to the chi square.

scribed by an absorbed broken power-law with an exponential cut-off. Following this, we substituted the power-law component by a broken power-law component (*bknpower* in XSPEC). We also found that a high energy cut-off component (*highecut* in XSPEC) with a typical folding energy of $\sim$ 130 keV clearly improves the fit and better describes the spectrum. A broad ($FWHM \sim 2.8$ keV) iron emission line with centroid energy fixed at 6.4 keV was also needed in order to obtain acceptable fits. The iron line has an equivalent width of 53.5 eV. Finally, the addition of a narrow Gaussian component at $\sim$ 2 keV was also required in order to account for unphysical residuals in the XRT spectrum. To account for cross-calibration problems, a variable multiplicative constant for the PCA and HEXTE spectra (as compared to XRT) was added to the fits. $\chi^2_{\rm red}$ = 1.13 for 653 degrees of freedom (dof) was finally obtained. No additional reflection component is required to obtain a good fit. We derive an equivalent Hydrogen column value of $N_{\rm H} = (0.72^{+0.01}_{-0.04}) \times 10^{22}$ atoms cm^{-2}. The fit for the XRT+PCA+HEXTE spectrum is shown in Fig. 9.1. The spectral parameters obtained are listed in Table 9.1. We also tried to fit the spectra using more sophisticated Comptonization models (*comptt*, *pexrav*) but the result was statistically worse than the obtained by using the model described above. *comptt* and *comptt*+reflection

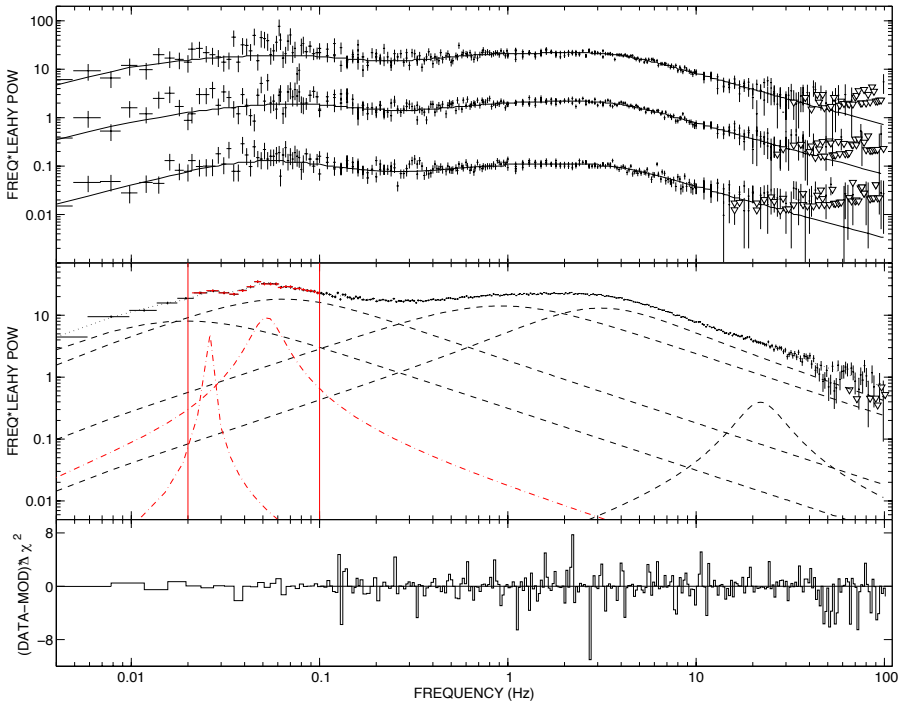

Figure 9.2: PDS fits. Top panel: arbitrarily re-scaled PDS spectra for 3 different one-orbit observations (2/35, 16/35, 33/35) and their corresponding best fits (solid line). Triangles are 3σ upper limits. Middle panel: fit of the average PDS. The four main components and the high frequency Lorentzian are shown in black, dashed lines. The (red) dotted-dashed lines correspond to the extra components added in the 0.02–0.1 Hz interval (see text). Bottom panel: residuals plotted as signed contribution to the chi square.

do not provide a valid fit and for *pexrav* we obtain $\chi^2_{\rm red} = 1.26$. for 650 dof.
The broad band spectrum of XTE J1752-223 is consistent with the source being a BHT in LHS. Its energy spectrum is dominated by a broken power-law component with photon indexes ~ 1.2 and ~ 1.5 and break energy ~ 10 keV. This is in agreement with the analysis performed by Wilms et al. (2006) on Cyg X-1 (see section 9.4). We also note that, in contrast to Shaposhnikov et al. (2009), we do not need a disc component to fit the RXTE spectra. Only the addition of the XRT spectrum evidences that a disc component is necessary to achieve a good fit.

9.3.2 Power density spectrum

Power density spectra (PDS) for each one-orbit pointing were computed using the same procedure outlined in Belloni et al. (2006). We used stretches 512 s long and

Lorentzian	Frequency (Hz)	Q	rms (%)
L_0	$0^{+0.001}$	$0^{+0.28}$	27.3 ± 0.7
L_1	0.014 ± 0.002	0.114 ± 0.012	36.5 ± 0.3
L_2	0.07 ± 0.01	0.04 ± 0.01	34.7 ± 0.2
L_3	1.57 ± 0.02	0.291 ± 0.005	26.3 ± 0.1
L_4	21.1 ± 1.9	1.7 ± 0.5	2.3 ± 0.2
eL_1	$0.0256^{+0.0002}_{-0.0006}$	unconstrained	3.7 ± 0.8
eL_2	0.051 ± 0.002	2.7 ± 0.6	8.9 ± 0.6

Table 9.2: Fit parameters for the broad Lorentzians, the high frequency Lorentzian ($L_{0,1,2,3,4}$; dashed line in Fig. 9.2) and the extra ones added in the 0.02–0.1 Hz region ($eL_{1,2}$; dotted-dashed line in Fig. 9.2).

energy channels STD2 0–31 (2–15 keV). PDS were fitted with XSPEC V.11. As for energy spectra we find that the shape of PDSs is almost constant during the whole observation, with it being possible to fit them by using 4 broad Lorentzians. Following Belloni et al. (2002), one of this components is centred at zero frequency and it is kept frozen. To illustrate this, three one-orbit PDS (orbits 2, 16, 33) are shown in the upper panel of Fig. 9.2. In these fits we notice the presence of residuals in the $\sim$ 0.02–0.1 Hz band. This extra component appears to vary between different orbits and can not be fitted by adding an extra narrow Lorentzian. In a second step, an average PDS was created (see lower panel in Fig. 9.2). This PDS has a S/N ratio much higher than the previous ones, allowing a more accurate fit. We initially excluded the region 0.02–0.1 Hz and fitted with four Lorentzians. We find that these four broad components describe well the continuum of the average PDS. We obtain $\chi^2_{\rm red}$ =1.26 for 265 dof. Given the high signal-to-noise of the PDS it was not possible to fit all its wiggles and get a lower value for $\chi^2_{\rm red}$. In order to properly fit the 0.02–0.1 Hz region two extra components are required (dot-dashed lines in Fig. 9.2). Moreover a weak, high frequency ($\sim$ 21 Hz) component not visible in the one-orbit PDSs appears in the average spectra. In conclusion, seven Lorentzians are used, yielding $\chi^2_{\rm red}$ =1.28 for 281 dof (see lower panel in Fig. 9.2). Table 9.2 shows the parameters obtained from the fit. eL_1 and eL_2 with $Q > 2$ are probably related with weak quasi periodic oscillations (QPOs; see Belloni et al. 2002). The total rms in the 0.002–128 Hz band is $48.2 \pm 0.1\%$.

9.3.3 The spectrum of the fractional rms

In order to study the energy dependence of the rms we calculated it for seven energy bands within the range 2–20 keV. Average PDS corresponding to the STD2 channels 0–6 (2–4.5 keV), 7–9 (4.5–5.7 keV), 10–13 (5.7–7.3 keV), 14–17 (7.3–9 keV), 18–23 (9–11.4 keV), 24–31 (11.4–14.8 keV) and 32–45 (14.8-20.6 keV) were used to

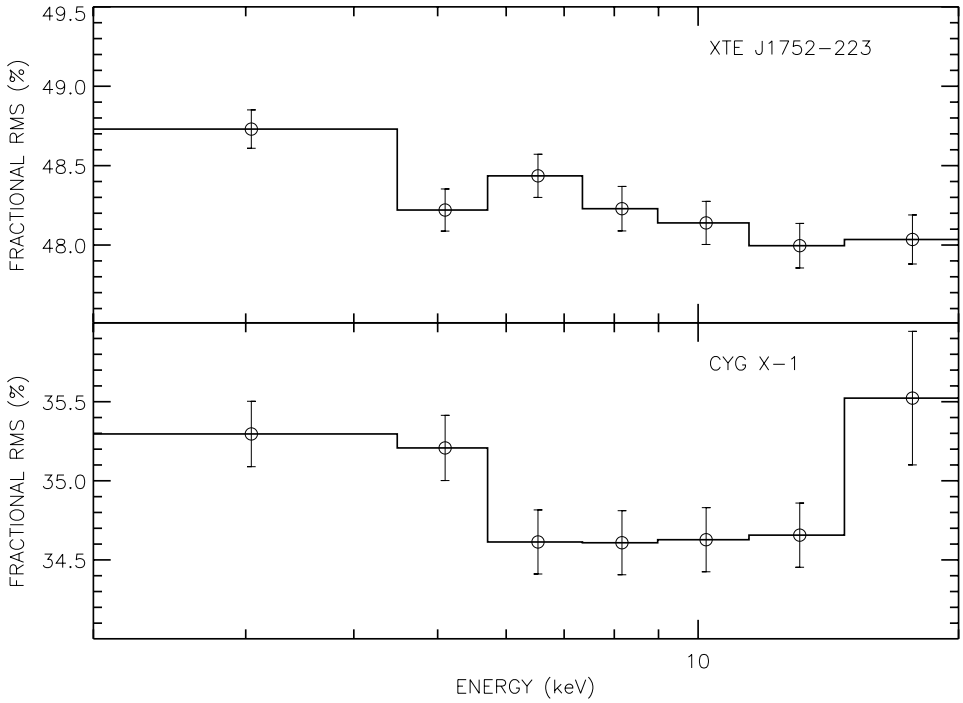

Figure 9.3: Rms spectra for XTE J1752-223 and Cyg X-1 (0.002–128 Hz).

compute the rms spectra (i.e. fractional rms vs. energy; see e.g. Vaughan et al. 2003, Gierliński & Zdziarski 2005). In Fig. 9.3 we show our results for both XTE J1752-223 and Cyg X-1 within the 0.002–128 Hz band. We find that in both sources the fractional rms is almost independent of energy. We measure a rms of ∼48% for XTE J1752-223 and $\sim 35\%$ for Cyg X-1. This difference is consistent with the hardness-rms correlation generally observed in BHT (e.g. Belloni 2010). We have also tried other frequency bands (e.g. 0.04–5, 10–128 Hz) always obtaining flat rms spectra.

9.3.4 Time-lags

We have computed time-lags between soft and hard variability (see e.g. Casella et al. 2004). Following Pottschmidt et al. (2000), we have used the energy ranges $\sim$ 2–4 keV and $\sim$ 8–13 keV for the soft and hard bands, corresponding to the STD2 channels 0–5 and 15–27, respectively. Fast Fourier transforms of each band were computed and cross spectra were produced. Here, a positive lag means hard variability lagging soft variability. The obtained time-lags (Δt) as a function of the frequency (ν) are shown in Fig. 9.4 (black circles). Thanks to the quality of the data, we are able to cover the frequency range 0.003–30 Hz obtaining accurate time-lags determinations in most of the cases. Our results are in agreement with the relation ($\Delta t \propto \nu^{-0.7}$)

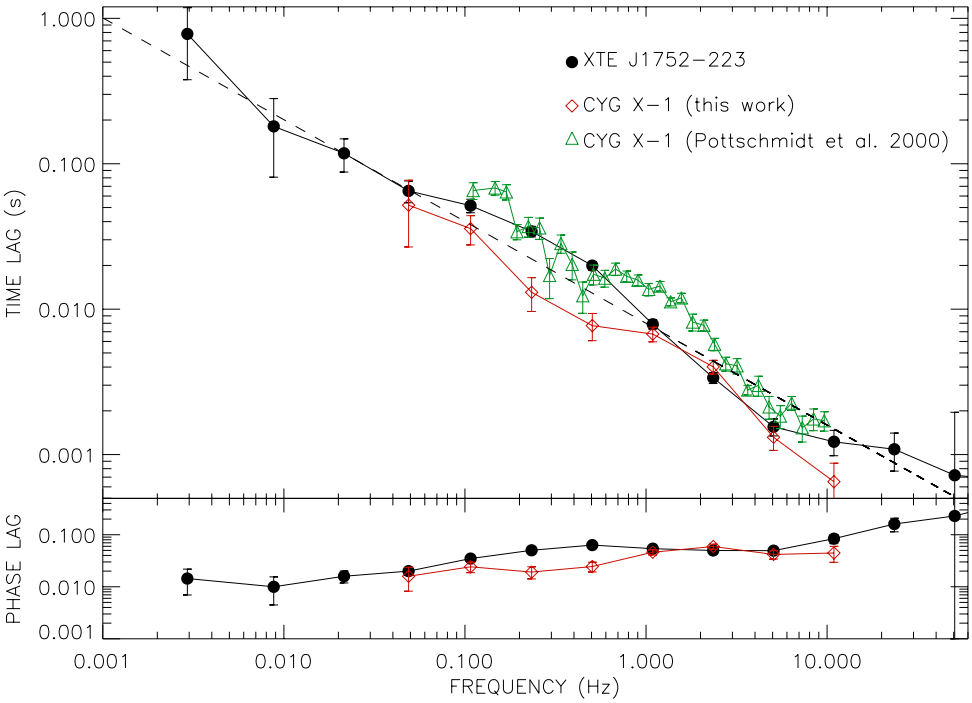

Figure 9.4: Top panel: time-lag vs. frequency for XTE J1752-223 (black circles). For Cyg X-1 we over-plot the time-lags we find during the LHS observation we have analysed (open diamonds) and those found by Pottschmidt et al. (2000) also during LHS (open triangles). The dashed line shows the relation $\Delta t \propto \nu^{-0.7}$ previously observed in Cyg X-1 (e.g. Nowak et al. 1999). Bottom panel: corresponding phase lags.

observed in Cyg X-1 (e.g. Nowak et al. 1999; dashed line in Fig. 9.4). We find that time-lag drops from $\sim$ 0.4–1 s for 0.003 Hz to $\sim$ 0.0015 s above 10 Hz. Evidences for a maximum delay are not found in the frequency range considered in this work. In Fig. 9.4 we also show the time-lags obtained for Cyg X-1 by Pottschmidt et al. (2000) (open triangles). Although they only cover the range $\sim$ 0.1–10 Hz, the same trend is observed. We also include time-lags obtained from the Cyg X-1 observation analysed in this paper (open diamonds). The shape of the time-lag distribution is the same as the obtained by Pottschmidt et al. (2000), but it is slightly re-scaled to smaller delays. This effect can be real or just be due to small changes in the energy bands used to compute the time-lags (e.g. changes in the sensitivity of the detectors). As shown in previous works (e.g. Nowak et al. 1999) time-lags increase when the difference between the energy bands considered does. For instance, if we use the energy range 14–45 keV (STD2 30–75) as the hard band, the higher delay observed for XTE J1752-223 is $\geq$ 0.6 s.

9.4 Discussion

We have performed a general analysis of XTE J1752-223 by looking at the spectral and timing properties of this recently discovered source. For a more complete understanding of the overall behaviour of the system we have also made use of rms spectra and time-lags. We have analysed a very long RXTE observation which provides high S/N data and therefore an accurate determination of the different parameters has been possible.

- The combination of Swift (XRT) and RXTE (PCA+HEXTE) data have allowed us to fit the energy distribution of XTE J1752-223 over the broad energy range 0.5-200 keV. The RXTE spectrum of the system is power-law dominated, the best fits being obtained by using a broken power-law model with photon indices $\Gamma_1 \sim 1.5$ and $\Gamma_2 \sim 1.2$. It is remarkable that this is also the model which best reproduce the energy spectra of the canonical BHB Cyg X-1 (Wilms et al. 2006). These authors monitored the source during five years finding interesting correlations between Γ_1 and Γ_2 but also between $(\Gamma_1 - \Gamma_2)$ and Γ_1. The values we found for XTE J1752-223 lie on both correlations but correspond to a state slightly harder than the hardest reported by Wilms et al. (2006). On the other hand, the difference between spectral indices ($\Gamma_1 - \Gamma_2 \sim 0.23$) and high energy cut-off ($\sim$ 133 keV) are in agreement with those measured for Cyg X-1 during LHS. The latter is also consistent with values found in classical BHT like GX 339-4 (Motta et al. 2009) or GRO J1655-40 (Joinet et al. 2008) during LHS. The RXTE spectrum of XTE J1752-223 does not require of a disc component to get a good fit, but the disc becomes evident when adding the Swift data. Our analysis reveals the presence of a cold disc with an inner radius temperature of ~ 0.3 keV. From the disc black-body normalization component (see Mitsuda et al. 1984) it is possible to derive the value of the inner radius of the accretion disc. In particular, assuming a distance in the range 2-8 kpc, a $10\ \mathrm{M}_{\odot}$ BH and an inclination $\leq 70^{\circ}$ (eclipses have not been observed) we find an inner disc radius in the range 9–43 gravitational radii. Using the same distance interval we derive a luminosity (0.5-200 keV) of $2.5 - 40 \times 10^{36}$ erg s^{-1}.

- The continuum of the PDS of XTE J752-322 can be described by four broad Lorentzians ($L_{0,1,2,3}$) with rms above 25%, a high frequency Lorentzian (L_4) and two QPO-like features ($eL_{1,2}$). This is very similar to the found on Cyg X-1 by Pottschmidt et al. (2003) during some of the LHS epochs they analyse. Associating L_0 with the low frequency power-law component they used, one is tempted to match the other components ($L_{1,2,3,4}$) one-to-one. For Cyg X-1 the Lorentzians have lower rms values and higher frequencies, which is consistent with XTE J752-322 being in a harder state. We note that in both cases $L_{1,2,3}$ show large rms values whereas the high frequency Lorentzian (L_4) present in

both studies is much weaker. On the other hand, frequency ratios are different. Pottschmidt et al. (2003) report $\nu_2/\nu_1 \sim$ 6–9, $\nu_3/\nu_1 \sim$ 25–35, $\nu_4/\nu_1 \sim$ 80–200, $\nu_3/\nu_2 \sim$ 3–4, $\nu_4/\nu_2 \sim$ 11–25, $\nu_4/\nu_3 \sim$ 4–6 whereas we find 5.2 ± 0.9, 110 ± 11, 1483 ± 198, 21 ± 3, 285 ± 48 and 13 ± 1, respectively. The ratios might be affected by the different definition of L_0 adopted in both works (Lorentzian/power-law). We have tried to fit our average PDS with a power-law, which results very flat, instead of L_0. Significant variations on frequency are only observed for L_1 (i.e. ν_1). We also note that weak QPOs like the ones we detect in the 0.02–0.1 Hz band (i.e. $eL_{1,2}$) are also detected by Pottschmidt et al. (2003) in Cyg X-1. Again, their frequencies are slightly higher (0.1–1 Hz) than those we observe in XTE J1752-223.

- Rms spectra tell us how variability depends on the energy band considered. Their shape and comparison with energy spectra also provides clues on the origin of the observed variability (e.g. Wilkinson & Uttley 2009). Previous works have studied the shape of rms spectra during different states in several BHT (see e.g. Gierliński & Zdziarski 2005 for a general description). In particular, two different rms spectral shapes have been observed during LHS: flat (e.g. XTE J1550-564) and smoothly decreasing with energy (e.g. XTE J1650-500). In this paper we show that the 2-20 keV rms spectrum of XTE J1752-223 is flat within 1%. The same behaviour is observed in the LHS observation of Cyg X-1 that we have analysed. This is expected if the variability is produced by changes in the normalization of the entire spectrum, but keeping the spectral shape constant. For the case of XTE J1752-223 (and Cyg X-1), where no disc component is present in the RXTE spectrum, our results are consistent with variability being due by variations in the normalization of the Comptonization (power-law) component. Gierliński & Zdziarski (2005) also discuss possible features caused by reflection components in the rms spectrum. For the case in which reflection and continuum components are not correlated, they predict the presence of $\sim 2-5\%$ absorption features in the rms spectra. These features are not detected in our rms spectrum. We note that this is consistent with our spectral fitting (it does not require a reflection component), although the broken power-law shape mimics the effect of reflection (Wilms et al. 2006).

- Time-lags between soft and hard photons are expected in Comptonized spectra as a result of the different number of scatterings that they undergo. In this framework, one expect hard variability delayed relative to soft variability. This is observed in XTE J1752-223, being the time-lag a function of the frequency. We find that our measurements are well described by $\Delta t \propto \nu^{-0.7}$. However, we note that this is only a qualitative description of the time-lags since clear deviations are observed. Clear flattenings suggesting a maximum or minimum

delay are not observed in our data, but above 10 Hz our results are consistent with $\Delta t \sim 0.0015$ s. This is in agreement with what it has been observed in Cyg X-1 (e.g. Nowak et al. 1999, Pottschmidt et al. 2000). The highest delay we observe is $\gtrsim 0.5$ s. However, our frequency coverage extends down to 0.003 Hz, and our highest lag is one order of magnitude larger that the highest found by the cited works (~ 0.05 s at 0.1 Hz). As noticed by Nowak et al. (1999) a ~ 0.05 s delay is difficult to be reproduced by either Comptonization models, sound speed propagation or gravitational free fall, unless the length scales involved were very large ($\sim 10^3$ gravitational radii). For XTE J1752-223 the highest delay ($\gtrsim 0.5$ s) yields a characteristic length of $\sim 10^4$ gravitational radii and there is no evidence to discard higher lags at frequencies lower than 0.003 Hz. These large lags require of either, those long length scales or low propagation velocities ($< 0.001c$) difficult to be reproduced by the current theoretical models (e.g. ADAF). Alternative scenarios show that time-lags are expected for pivoting power law emission (Körding & Falcke 2004). Kazanas et al. (1997) and Pottschmidt et al. (2000) suggest that they can be related with the accretion disc or outflows, respectively. Our results favour these latter scenarios in which time-lags are not purely created by Comptonization processes within the corona.

9.5 Conclusions

An unusually long RXTE observation of the X-ray transient XTE J1752-223 is presented in this paper. The quality of the data have allowed us to obtain high S/N energy spectrum, PDS, rms spectrum and time-lags for this new source. All the obtained results are consistent with a black hole binary in the hard state. In particular, we find a behaviour similar to that exhibited by Cyg X-1 during hard state, but XTE J1752-223 happens to be in a slightly harder state. However, we note that there are two important differences between these two systems: Cyg X-1 is so far a persistent black hole binary and it harbours a high-mass companion. XTE J1752-223 is a transient and probably harbours a low-mass donor. Future multi-wavelength campaigns will probably provide new clues to the fundamental properties of this new black hole candidate.

Acknowledgments

The research leading to these results has received funding from the European Community's Seventh Framework Programme (FP7/2007-2013) under grant agreement number ITN 215212 "Black Hole Universe". SM and TB acknowledge support to the ASI grant I/088/06/0. TMD, SM, TB and DP acknowledge hospitality during their visits to IUCAA (Pune).

10 The black hole candidate MAXI J1659-152: spectral and timing analysis during its 2010 outburst

Teo Muñoz-Darias, Sara E. Motta, Tomaso M. Belloni, Holger Stiele

Monthly Notices of the Royal Astronomical Society, 2011, 415, 292

Abstract

We present a comprehensive spectral-timing study of the black hole candidate MAXI J1659-152 during its 2010 outburst. We analysed 65 RXTE observations taken along this period and computed the fundamental diagrams commonly used to study black hole transients. We fitted power density and energy spectra and studied the evolution of the spectral and timing parameters along the outburst. We discuss the evolution of the variability observed at different energy bands on the basis of the relative contribution of the disc and hard components to the energy spectrum of the source. We conclude that hard emission accounts for the observed fast variability, it being strongly quenched when type-B oscillations are observed. We find that both disc and hard emission are responsible for local count-rate peaks until the system reaches the soft state. From that point, the peaks are only observed in the hard component, whereas the thermal component drops monotonically probably following the accretion rate decrease. We have also computed time-lags between soft and hard X-ray variability confirming that lags are larger during the hard-to-soft transition than during the hard state.

10.1 Introduction

Black hole X-ray transients (BHT) spend most of their lives in quiescence, displaying luminosities too low to be detected by X-ray all-sky monitors (see e.g., Garcia et al. 1998). They are discovered during outburst events in which their X-ray luminosity increases by several orders of magnitude and their spectral and time variability properties change with time. This leads to the definition of the so-called 'states'. There is still much discussion about how many different states there are (van der Klis 2006; Belloni 2010 for recent reviews), but X-ray observations have made clear the presence of a $hard$ state (historically known as *low/hard*; LHS) at the beginning of the outburst, which evolves towards a $soft$ state (*high/soft*; HSS). The LHS is also observed at the end of the outburst and it is characterized by a power-law dominated energy spectrum with a power-law index of ~ 1.6 (2–20 keV band). This power-law component is though to arise from a 'corona'of hot electrons, where softer seed photons coming from an accretion disc are up-Comptonized (e.g., Gilfanov 2010 for a review). Compact radio jets are observed during the LHS (see e.g., Fender 2006) and synchrotron emission could also account for the high energy emission during this stage of the outburst (Markoff et al. 2001). Aperiodic variability with a fractional root mean square amplitude (rms) above 30% is also seen. It is almost energy independent (Gierliński & Zdziarski 2005) and sharply correlated with flux (Gleissner et al. 2004; Muñoz-Darias et al. 2011).

The high energy spectrum softens during HSS since a thermal disc black-body component becomes dominant. The rms drops below 5 per cent and a much more scattered rms-flux correlation is observed (see Muñoz-Darias et al. 2011 for the evolution of the long term rms-flux relation along the outburst). The situation is more complex in between these two 'canonical' states. A hard-to-soft transition at high flux is generally observed on relatively short time scales (hours/days) as compared to those seen for the canonical states (weeks/months). During this transition, both timing and spectral properties change dramatically, leading to 'intermediate' states. Homan et al. (2005) and Belloni (2005) identify two additional states, the hard-intermediate state (HIMS) and the soft-intermediate state (SIMS) based on spectral and timing properties (see Wijnands et al. 1999, Casella et al. 2004 and Casella et al. 2005 for different types of quasi periodic oscillations (QPOs)). In this paper we would follow this classification (see McClintock & Remillard 2006 for an alternative classification and Motta et al. 2009 for a comparison). The count-rate drops considerably during the HSS and a final soft-to-hard transition towards quiescence is usually observed. Whereas the main properties of the LHS and HSS are known and have been studied in many sources finding a relatively homogeneous behaviour, the study of the whole outburst evolution and state-transitions has proven more elusive and very different behaviours have been reported depending on the system.

MAXI J1659-152 was discovered independently by Swift/BAT (GRB 100925A; Mangano et al. 2010) and MAXI/GSC (Negoro et al. 2010) on September 25, 2010. A variable optical counterpart was soon detected (Marshall 2010; Jelinek et al. 2010; Russell et al. 2010), showing broad, double-peak emission lines ($FWHM \sim 2000$ $\mathrm{km\,s^{-1}}$) typical of accreting binaries (de Ugarte Postigo et al. 2010). The source was detected in radio with a linear polarization level of $\sim 23\%$ (van der Horst et al. 2010), submillimetres (de Ugarte Postigo et al. 2010) and near infrared (D'Avanzo et al. 2010) wavelengths. At high energies MAXI J1659-152 was also observed by the *Rossi X-ray timing explorer* (RXTE) and the XMM and INTEGRAL observatories (Kuulkers et al. 2010; Vovk et al. 2010). RXTE observations performed 3 days after the discovery revealed strong similarities with the typical timing properties of BHT during the HIMS (citealtKalamkar2011) indicating that MAXI J1659-152 is a black hole candidate. This was confirmed by the subsequent transitions to the SIMS and HSS observed on October 12 (Belloni et al. 2010) and October 17 (Shaposhnikov & Kazutaka 2010), respectively. After a short (15 days) stay in soft states, a new transition to the HIMS was observed (Muñoz-Darias et al. 2010a). X-ray dips with a recurrent period of 2.41 hours have been detected in MAXI J1659-152, pointing to a high orbital inclination and suggesting that MAXI J1659-152 is the black hole binary with the shortest orbital period (Kuulkers et al. 2010; Belloni et al. 2010; Kuulkers et al. 2011). Here, we study in detail the evolution of the spectral and timing properties of the source along the 2010 outburst until observations were interrupted due to Sun constraints. We focus on the evolution of the variability during the hard-to-soft and soft-to-hard transitions and how it is related to the relative contribution of the various components present in the energy spectra.

10.2 Observations

We analyse 65 RXTE observations of MAXI J1659-152 performed within September 28, 2010 and November 11, 2010.
The variability study presented in this paper is based on data from the *Proportional Counter Array* (PCA). For some observations the mode GoodXenon1_2s was used but most of the data are in the mode E_125us_64M_0_1s, which covers the PCA effective energy range (2-60 keV) with 64 bands. Power density spectra (PDS) for each observation were computed following the procedure outlined in Belloni et al. (2006). We used stretches 16 s long and PCA channels 0–35 (2–15 keV).

The PCA Standard 2 mode (STD2) was used for the spectral analysis. It covers the 2–60 keV energy range with 129 channels. From the data, we extracted hardness (h), defined as the ratio of counts in STD2 channels 11–20 (6.1–10.2 keV) and 4-10 (3.3–6.1 keV). Energy spectra from the PCA (background and dead-time corrected) were

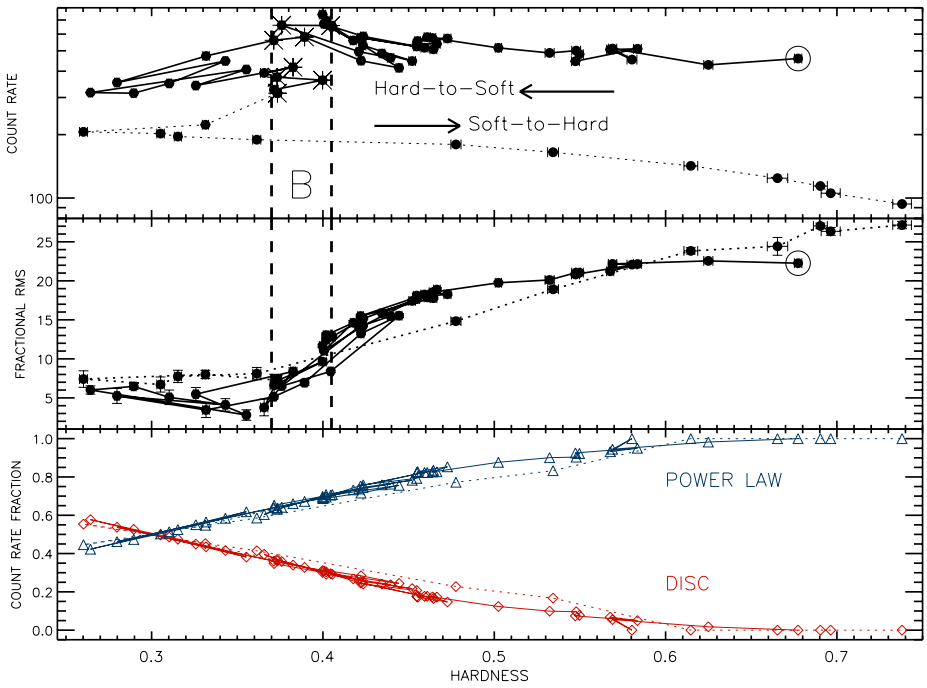

Figure 10.1: Upper panel: hardness-intensity diagram obtained using all the RXTE observations available. Intensity correspond to the count rate within the STD2 channels 0–31 (2–15 keV) and hardness is defined as the ratio of counts in 11–20 (6.1–10.2 keV) and 4-10 (3.3–6.1 keV) STD2 channels. Each point corresponds to an entire observation. Observations with a star correspond to those with a type-B QPO in the PDS. Solid line joins consecutive observations starting from observation #1 (big, open circle). Observations taken after the last type-B QPO are joined by a dotted line. Dashed lines delimit the range in hardness where these oscillation are detected. Middle panel: corresponding hardness-rms diagram within the 0.1–64 Hz frequency band. Lower panel: corresponding power-law (open triangles) and disc (open diamonds) relative contributions to the observed count rate (see Sect. 10.3.2).

extracted for each observation using the standard RXTE software within HEASOFT V. 6.7. For the spectral fitting, Proportional Counter Unit 2 was solely used. In order to account for residual uncertainties in the instrument calibration a systematic error of 0.6% was added to the spectra[1].

[1]See http://www.universe.nasa.gov/xrays/programs/rxte/pca/doc/rmf/pcarmf-11.7/ for a detailed discussion on the PCA calibration issues.

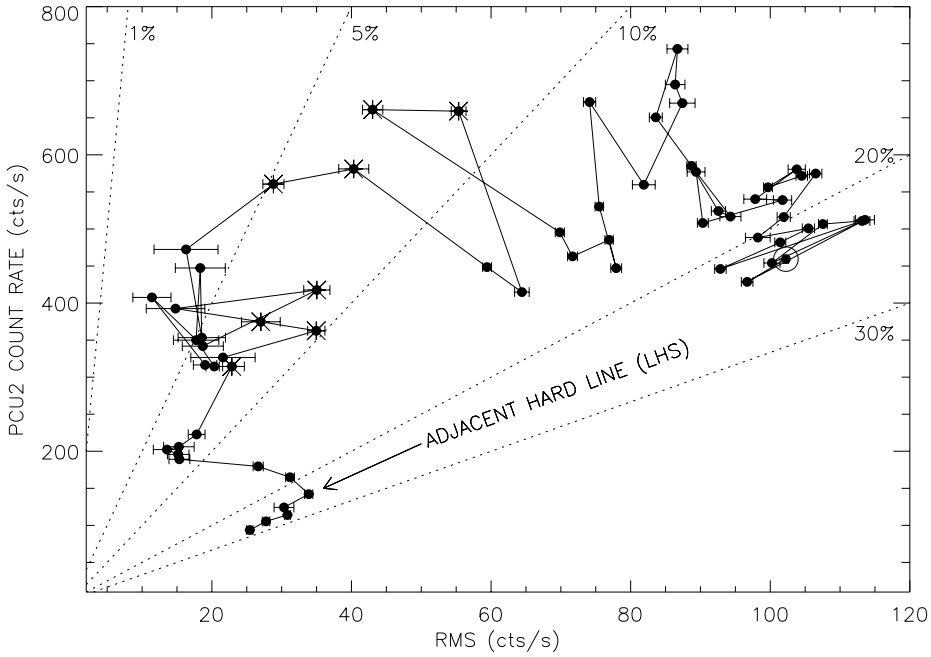

Figure 10.2: Rms-intensity diagram obtained following Muñoz-Darias et al. (2011). Each point corresponds to an entire observation. A solid line joins consecutive observations starting from observation #1 (big, open circle). Stars correspond to observations with a type-B QPO in the PDS. Dotted lines represent the 1, 5, 10, 20 and 30 per cent fractional rms levels.

10.3 Analysis and results

We computed the fundamental diagrams commonly used for the study of BHT and performed fits to the energy spectra and PDS. The QPOs present in the PDS have been classified following Casella et al. (2005). Finally, we have also measured time-lags between soft and hard variability for the only observation long enough to perform this analysis.

10.3.1 Fundamental diagrams

As a first step of the analysis, we computed the hardness-intensity and the hardness-rms diagrams (HID and HRD), which are presented in the upper and middle panels of Fig.10.1, respectively. The fractional rms was computed within the frequency band 0.1–64 Hz following Belloni & Hasinger (1990). We have also computed the rms-intensity diagram (RID) presented in Fig. 10.2 following Muñoz-Darias et al. (2011). Rms values obtained by using a soft (2–6 keV) and a hard (6–15 keV) band are shown in the upper panel of Fig. 10.3 as open and filled circles, respectively. The compar-

ison between the rms observed in these two bands is effectively a rms spectrum of two energy bins. This is enough to get a reliable estimation of the energy spectrum of the variability even when the count rate is low. The latter results in large error bars if using narrow energy bands. This method allows us to infer whether the rms spectrum is flat, hard or inverted (i.e. more variability at low energies) for each observation. For a more detailed comparison, we show in Fig. 10.4 three rms spectra corresponding to observations taken along the hard-to-soft transition. They are obtained using six energy bands and give results consistent with those that can be extracted from the upper panel of Fig. 10.3.

The source describes in the HID the standard q-shaped pattern moving from observation #1 (open, big circle in Fig. 10.1) in the counter clockwise direction. However, the initial flux rise was not observed by RXTE and, as pointed out by Kalamkar et al. 2011, the first RXTE observation already correspond to the HIMS. This is confirmed by the fact that no hard line (i.e. sharp, linear rms-flux relation; Muñoz-Darias et al. 2011) is observed in the RID. After $\sim$ 16 days in the HIMS, where the count rate peak is observed, type-B QPOs are seen in the PDS, indicating the system is in the SIMS. Once this state is reached, fast transitions are observed between the SIMS and the HSS. A hard excursion to the HIMS between two soft excursions is observed. After an important decrease in count rate the system reaches the softest (observed) point of the outburst and a soft-to-hard transition is seen. The following can be outlined after a detailed study of the fundamental diagrams:

- The rms decreases monotonically during the first HIMS observations. The corresponding PDS show strong type-C QPOs typical of this state. As usually observed in BHT, a fast decrease in rms is observed during the transition between the HIMS and the SIMS. All the type-B QPOs are observed within $h \sim 0.40$–0.37 (see dashed lines in Fig. 10.1) and a minimum in rms is observed at $h \sim 0.35$. From that point, rms increases with softening. This trend is not observed during the second soft excursion and the soft-to-hard transition (dotted line in Fig. 10.1), but a constant rms $\sim 8\%$ value is seen until the system reaches again the HIMS. As far as we know, this clear break in the hardness-rms relation widely observed in BHT has not been reported before (however see discussion in Sect. 10.4). The above behaviour is present in both, soft and hard energy bands (Fig. 10.3), but it is much more prominent in the hard channels.

- During the first observation, the rms shows an almost flat energy spectrum (see upper panel in Fig. 10.4), consistent with what is observed in early HIMS observations in other systems (see e.g., Gierliński & Zdziarski 2005). Less variability is observed in the soft band as the system gets soft, but in contrast

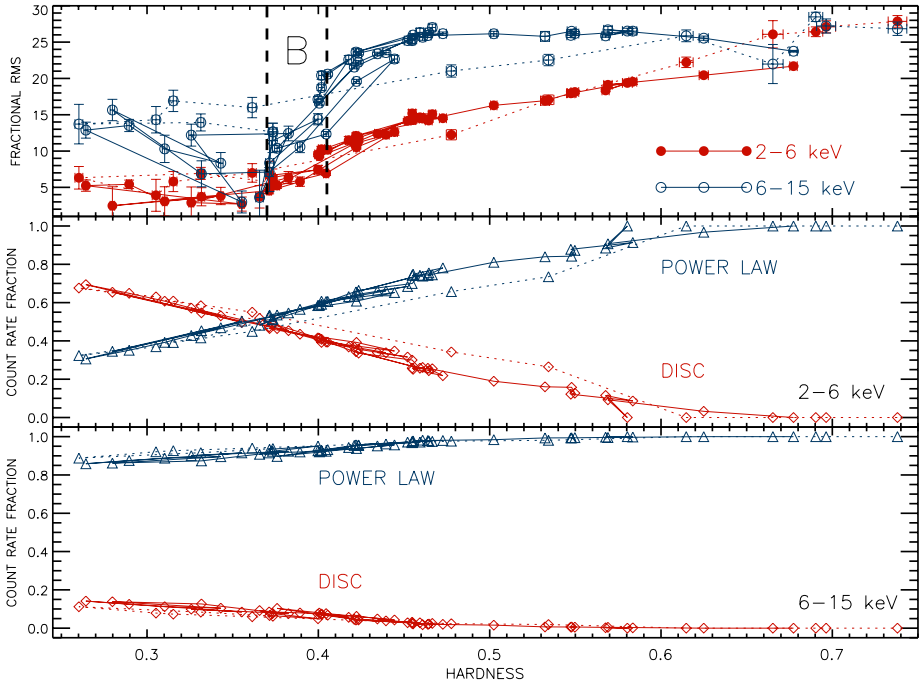

Figure 10.3: Upper panel: hardness-rms diagrams obtained by using soft (STD2 0-9; 2-6 keV) and hard (STD2 10-31; 6-15 keV) energy bands for computing rms, respectively. Dotted and dashed lines represent the same as in Fig.10.1. Middle and lower panels: power-law (open triangles) and disc (open diamonds) contribution to the observed count rate within the above bands.

with what is usually observed (see e.g., Muñoz-Darias et al. 2011 for the case of GX 339-4), the hard rms slightly increases during the HIMS (middle panel in Fig. 10.4). The rms drops abruptly from the last HIMS observation to the softer SIMS observations. In the hard band, rms fades from $\sim$ 20% to 4% within the narrow range of hardness where type-B QPOs are observed (dotted lines in Fig. 10.1 and Fig. 10.3). The rms minimum at $h \sim 0.35$ is observed in both hard and soft bands, being the rms spectra flat again (see upper panel in Fig. 10.3 and lower panel in Fig. 10.4). Between $h \sim 0.25$–0.35 we see again much more variability at high energies (upper panel in Fig. 10.3). Hard rms spectra are observed during the soft-to-hard transition until they become flat or slightly inverted. This behaviour is typical of the LHS (Gierliński & Zdziarski 2005; Muñoz-Darias et al. 2011) and it is observed in the last four RXTE observations.

- No hard line is observed in the RID (Fig. 10.2). The adjacent hard line seems

to be obeyed by the last four RXTE observations, when a flat/inverted rms spectrum are observed, confirming that they correspond to the LHS. We note that this HIMS-LHS transition, which is not obvious when looking at the HID, is sharply marked in the RID. As seen in GX 339-4, type-B QPOs are localized in the $\sim$ 5–10% region of the RID. This 10% line seems to divide precisely HIMS and SIMS observations; as an example, observation 95108-01-21-00 with a very late HIMS PDS (low coherent Type C QPO) has a rms of 11%. The $\sim 5\%$ border is not so sharp, especially at count rates $\lesssim 350$ cts s^{-1} where some observations without a type B QPO cross this line. This is due to (i) fast transitions between the HSS and SIMS in the region around $\sim$ 350 cts s^{-1}, which results in hybrid observations (see also Muñoz-Darias et al. 2011), and (ii) the already mentioned break of the usual hardness-rms correlation during the two soft excursions observed. This results in HSS observations with rms $\geqslant 5\%$ and around $\sim 15\%$ in the hard band. Indeed, a clear soft branch (rms $\sim$ 1–5 per cent) is not present in the RID.

Finally we show the RXTE light-curve (2–15 keV) during the outburst in Fig. 10.5. SIMS and HSS epochs have been marked with light and dark grey bands, respectively. The thick solid line represents the transition to the LHS.

10.3.2 Spectral evolution

We have performed a spectral fitting of the 65 observations analysed in this paper. Energy spectra have been fitted within the band $\sim$ 4–22 keV, where RXTE/PCU offers its maximum throughput and spectral calibration is reliable (see e.g., Jahoda et al. 2006). We have used XSPEC V 11.3.2. Given the multitude of spectral models available, we tested several ones in a first approach. This method has been already adopted for other sources (e.g., GX 339-4, Nowak et al. 2002; Cyg X-1, Wilms et al. 2006).

We started with models of one single component, either a cutoff power law or a multicolor disk blackbody. Neither of them could fit the spectra. In order to obtain good fits and acceptable parameters, a model consisting of a simple power-law plus a multi-color disk-blackbody component was used. No high energy cut-off associated to the powerlaw component was needed for any of the observations, as expected from the energy range considered ($\leq$ 22 keV; e.g., Motta et al. 2009, Miyakawa et al. 2008). A Gaussian emission line with a centroid constrained between 6.4 and 6.8 keV was also needed. A hydrogen column density was used (`wabs` in XSPEC), with N_H frozen to $3 \times 10^{21} cm^{-2}$, the value derived from *Swift*/XRT (Kennea et al. 2010). The addition of an iron edge did not significantly improve the fits. No evident residuals due to reflection features were evident apart from the iron line, thus no additional reflection component was needed to describe the data. In a second step, we tried to

fit the spectra using more sophisticated Comptonization models (*comptt*, *pexrav*) but the result was not statistically better than that obtained by using the model described above. Using *comptt* and *pexrav* we obtain a value of the χ^2_{red} higher than that obtained with the powerlaw+diskbb model. We conclude that a empirical simple model constituted by a powerlaw+diskbb is sufficient to describe the data. In Fig. 10.6 we present the evolution of the main spectral parameters along the outburst evolution. Our results are consistent with a constant inner disc radius[2] around ~ 40 km (assuming an orbital inclination of 70 degrees), showing a possible decrease at the end of the outburst. We find an inner disc temperature in the range 0.6-0.9 keV, consistent with the values usually observed in BHT (see e.g., Motta et al. 2009).
The photon index of the power-law component increases from ~ 1.9 during the first HIMS observation to ~ 2.3 during the soft states. This value is lower than those usually observed in BHT during soft states. The photon index decreases again during the final soft-to-hard transition where values around ~ 1.7 are reached during the LHS observations. The main spectral parameters obtained for each of the observation are shown in Tab. 10.1. From this table (see also Fig. 10.6) it is clear that our constraints on the disc parameters are sometimes poor. This is expected since by using PCA data we are only able to see the high energy part of the disc black body component above the Wien peak. It is also known that, even if the the `diskbb` model provides a good description of the thermal component, the derived spectral parameters should not be interpreted literally (see e.g. Remillard & McClintock 2006). However, we note that this thermal component is clearly present in the data and well described by the model we use. Hereafter we focus on the contribution of this thermal component to the total flux rather than in the evolution of single disc parameters to which our study is less sensitive.
The fractional contribution to the observed count-rate associated with the disc and the power-law component are shown in the lower panel of Fig. 10.1 (2-15 keV), and in the middle and lower panels of Fig. 10.3 (2-6 keV and 6-15 keV). The following is noted by comparing these results with the hardness and rms evolution:

- During the LHS and the HIMS ($h > 0.4$; see Fig. 10.1) the rms is well correlated with the power-law contribution to the total count-rate and anti-correlated with the disc contribution. The fact that within $0.41 \leqslant h \leqslant 0.58$ we see a higher rms during the hard-to-soft transition than during the soft-to-hard (dotted line) can be also explained in terms of power-law contribution to the observed count rate. The same conclusion can be extracted from Fig. 10.3 when the soft (2-6 keV) and hard bands (6-15 keV) are considered.

- During the SIMS ($0.37 \leq h \leq 0.40$) the situation is different. The rms de-

[2]The normalization for the `diskbb` component is defined as $(\frac{R_{in}/km}{D/10kpc})^2 cos\Theta$, where R_{in} is the inner disc radius (km), D is the distance to the source (kpc) and Θ is the inclination angle of the disk.

creases drastically, much faster than power-law contribution decreases. This becomes even more evident when we look at the hard band in Fig. 10.3, which is clearly power-law dominated. There is no observation within this hardness band during the soft-to-hard transition, but if we consider the closest two observations at both sides of the SIMS it seems probable that during this back transition there is more variability and less power-law contribution than during the hard-to-soft transition.

- In the HSS ($h < 0.37$) the behaviour is complex. During the first soft excursion, when count-rate is above ~ 300, the rms increases with softening, i.e. with disc contribution. However from Fig. 10.3 it is clear that in the hard band (power-law dominated) the rms is larger than in the soft band (disc dominated) with the exception of the points very close to the SIMS, where energy spectrum of the rms is flat. During the second soft excursion (count-rate lower than ~ 300) the rms is constant and higher than that observed in the first soft excursion, especially in the points close to the SIMS. The power-law contribution slightly increases as compared to the previous soft excursion and there is much more variability in the hard band than in the soft band. By comparing the two soft excursions it is clear that we see very different variability levels in correspondence with rather similar power-law and disc relative contributions. We note that this second soft excursion at lower count rate and higher rms occurs right after the last type-B QPO is observed.

Using the results from the spectral fits we computed the absolute count-rates associated with the disc and the power-law (2–15 keV). We have over-plotted them in Fig. 10.5. Only during the HSS epochs (dark grey bands) the disc dominates the observed count-rate. As seen in other systems the disc is not observed within the XTE/PCU band at the beginning and at the end of the outburst (e.g., Motta et al. 2009).
We also note that all the wiggles present in the light-curve are observed in both components until the system reaches the HSS for the first time. From that point onwards (day ~ 21), the count-rate associated with the disc decreases monotonically, probably following the accretion rate, and the wiggles observed in the light-curve are solely caused by variations in the power-law count rate.

10.3.3 Quasi periodic oscillations

Together with the timing analysis on the evolution of the rms along the outburst and its energy dependence, we have also studied the evolution of the main QPO properties. In table 10.2 we present the fits for the 43 PDS in which Type-C QPOs were observed and the 9 PDS with a type-B QPO. Only in one observation (95118-01-06-00) we see a possible type-A QPO, although its significance is low and we will not consider it in our analysis. PDS fitting was carried out with the standard XSPEC

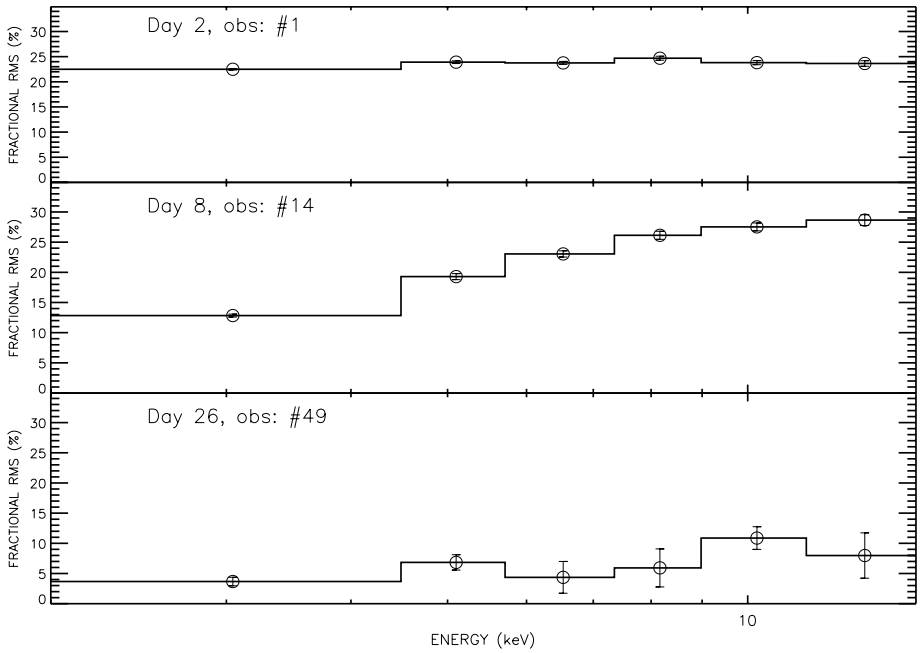

Figure 10.4: Rms spectra calculated for STD2 channels 0–6 (2–4.5 keV), 7–9 (4.5–5.7 keV), 10–13 (5.7–7.3 keV), 14–17 (7.3–9 keV), 18–23 (9–11.4 keV) and 24–31 (11.4–14.8 keV). They cover gradually the behaviour observed during the hard-to-soft transition within the first 49 observations. T_0 corresponds to MJD 55465.

fitting package by using a one-to-one energy-frequency conversion and a unit response. Following Belloni et al. (2002), we fitted the noise components with three Lorentzians, one zero-centred and other two centred at a few Hz. The QPOs were fitted with one Lorentzian each, only occasionally needing the addition of a Gaussian component to better approximate the shape of the narrow peaks and to reach values of reduced χ^2 close to 1. The behaviour of both Type-B and Type-C QPOs is similar to that observed in other BHT (see e.g., Belloni 2010). We see the type-C frequency increasing with hardness, whereas type-B are always observed within the frequency range $\sim$ 2–4 Hz.

Following Casella et al. (2004) and Motta et al. (2011 in prep.) we have plotted total rms as a function of the QPO frequency (Fig. 10.7). As it was found in those works, Type-C QPOs follow a clear negative correlation. This correlation seems to saturate around $\sim$ 7.5 Hz. Interestingly, if we only consider the Type-C QPOs observed during the soft-to-hard transition (open circles in Fig. 10.7) a slightly higher slope is observed in the correlation.

Type-B QPOs are unequivocally separated from Type-C using the rms-frequency rep-

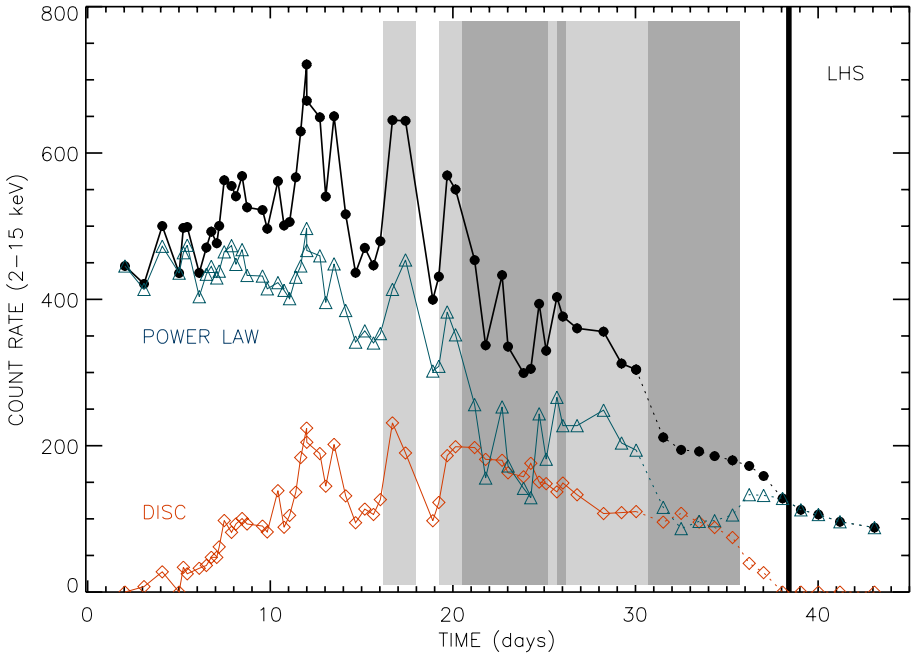

Figure 10.5: Light-curve of the system along the outburst within the band 2-15 keV (STD2 0-31). Count rates associated with the disc and power-law components are shown as open diamonds and open triangles, respectively. SIMS epochs are coloured in light grey, whereas the dark grey regions correspond to the HSS. T_0 corresponds to MJD 55465.

resentation and they are solely observed when the rms is ≤ 10 per cent.

10.3.4 Time-lags

Time-lags between soft and hard variability were computed for the first observation (95358-01-02-00), the only one long enough for this purpose. Following Pottschmidt et al. (2000) we used the energy ranges $\sim$ 2–4 keV and $\sim$ 8–13 keV for the soft and hard bands. They corresponds to the STD2 channels 0–5 and 15–27, respectively. Fast Fourier transforms of each band were computed and cross spectra produced. A positive lag means hard variability lagging soft variability. The obtained time-lags (Δt) as a function of frequency (ν) are shown in Fig. 10.8 (black circles). As observed in previous works, the time-lag decreases with frequency within the 0.1-10 Hz band to which we are sensitive. Pottschmidt et al. (2000) noted that in Cyg X-1 the time-lags were larger during the transition between hard and soft states as compared to those observed in the canonical states. The system was in the HIMS during observation #1 and in agreement with the above work the lags we measure are larger than those typically observed in BHT during LHS. For a direct compari-

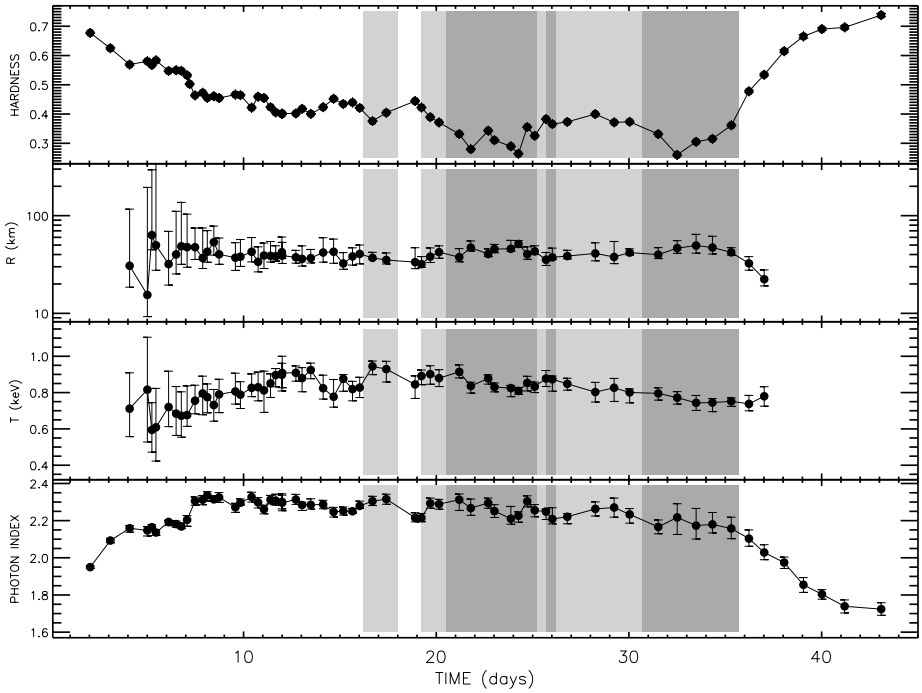

Figure 10.6: Evolution of the hardness and the main spectral parameters during the outburst. R corresponds to the inner disc radius and T to its temperature. SIMS epochs are coloured in light grey, whereas the dark grey regions correspond to the HSS. T $_0$ corresponds to MJD 55465.

son we have computed time-lags for a LHS observation (diamonds in Fig.10.8) and two HIMS observations at the same hardness (triangles in Fig.10.8) and same fractional rms (open circles in Fig.10.8) corresponding to the 2007 outburst of GX 339-4. Whereas the time-lags corresponding to the LHS observation follows the relation $\Delta t \sim 0.009 \times \nu^{-0.7}$ (dashed line in Fig.10.8), consistent with the one observed in other systems during that state (see e.g., Muñoz-Darias et al. 2011 for Cyg X-1 and XTE1752-223) a normalization at least two times bigger (~ 0.02; dashed line in Fig.10.8) is needed to account for the time-lags observed in MAXI J1659-152. We note that deviations from the power-law seems to be present at low frequencies.

10.4 Discussion

The evolution of MAXI J1659-152 during its 2010 outburst is consistent with that usually observed in black hole transients. The hardness-intensity, rms-hardness and rms-intensity diagrams are rather typical, with a hard-to-soft transition, a flux decay during a soft (accretion disc dominated) state and a final soft-to-hard transition to-

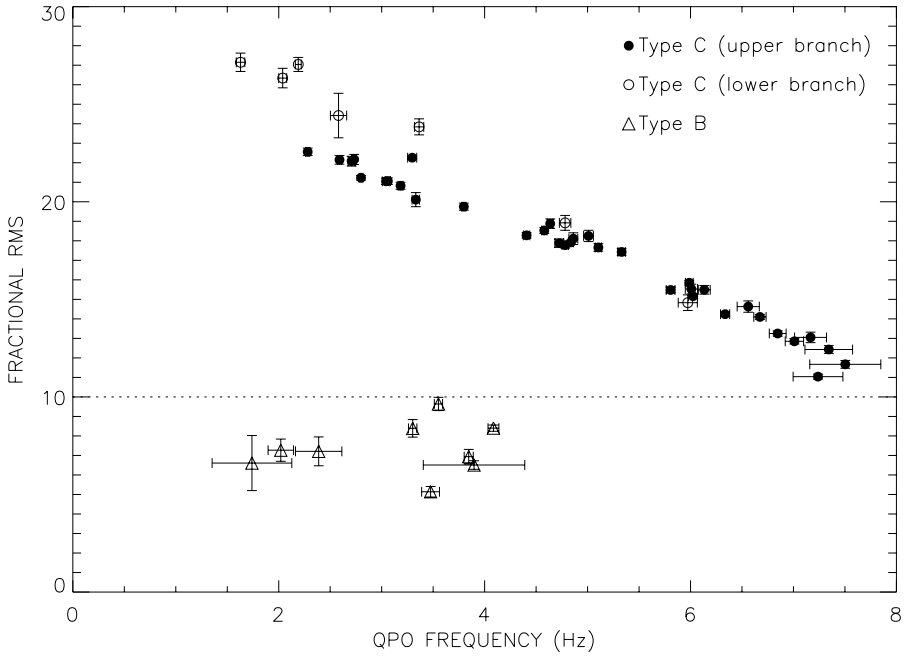

Figure 10.7: Total fractional rms (0.1–64 Hz) as a function of the QPO frequency. Type-C observed during the hard-to-soft and soft-to-hard transitions are marked with a filled and an open circle, respectively. Open triangles correspond to Type-B QPOs, which do not follow the correlation observed for the type-C and are solely observed when the rms is ≤ 10 per cent (dotted line).

ward the quiescence. Variability is in general correlated with hardness. Its energy spectrum is hard during the HIMS and the HSS and flat during the LHS.
If we compare the hardness values with those observed in other systems, we see that MAXI J1659-152 has a rather hard spectrum. This is clear when looking at the spectral parameters that we obtain from the black-body disc + power-law model that fits its energy spectrum. Whereas the disc parameters are within the standard range for a black hole, the power-law index is never higher than ~ 2.3 . This can be understood in terms of the high orbital inclination needed to explain the dips observed in the light-curve of the system. As discussed in Motta & Belloni (2010) for the case of the 2009 ourburst of H 1743-322, assuming that the power-law is arising from a spherical corona and the thermal emission from a thin disc, a hard outburst could be observed in high inclination systems. However, we note that the same system can reach different softening levels (e.g., H1743-322 see also McClintock et al. 2009) during different outburst. This shows that other factors, probably related with the available accreting fuel, should play a role.

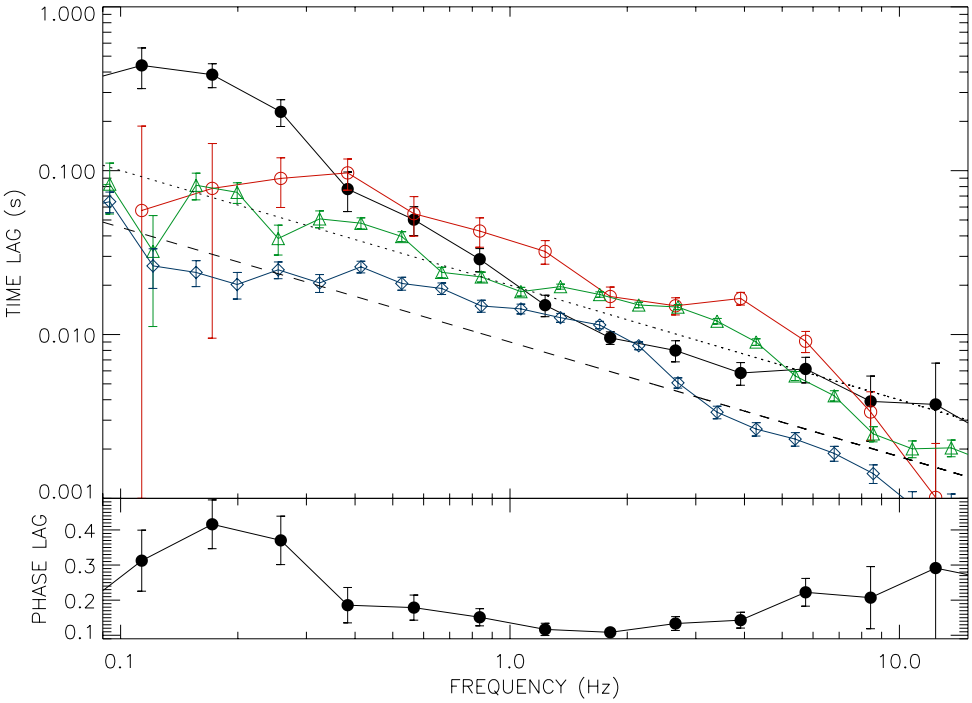

Figure 10.8: Top panel: time-lag vs. frequency for MAXI J1659-152 (black circles). For GX 339-4 we over-plot the time-lags we find during the LHS observation we have analysed (open diamonds) and two HIMS observations at the same hardness (open triangles) and same fracional rms (open circles). The dashed line shows the relation $\Delta t = 0.009 \times \nu^{-0.7}$ consistent with what is observed during the LHS. The dotted line shows the relation $\Delta t = 0.02 \times \nu^{-0.7}$, which seems more appropriate for HIMS observations.

The rms values observed during some stages of the outburst are similar to those observed in other systems. We see rms close to $\sim$ 30 per cent in the LHS, rms $>$ 10 per cent in the HIMS and $5\% \leq$ rms $\leq 10\%$ in the SIMS. In the HSS we see rms higher than usual, the minimun being $\sim$ 3 per cent. In the softest observation rms is $\sim$ 8 per cent, much higher than usually observed in BHT. Assuming that much less variability is coming from the disc than from the power-law, a high orbital inclination could in principle explain this behaviour values since we observe less disc photons diluting power-law variability.

Many of the observed rms values could be explained by solely assuming that the power-law component accounts for the observed variability whereas disc emission varies very little and dilutes power-law variability. Assuming that disc emission does not vary more than the minimum observed rms ($\sim$ 3 per cent) we can roughly recover the rms values we see in the hard states by correcting from the relative contribution of each component along the HIMS. A similar behaviour was reported by Shaposhnikov

et al. 2010 during the hard-to-soft transition in the BH candidate XTE J1752-223. As discussed by these authors, this can be understood in terms of variability arising from the Comptonization corona which dominates the LHS, whereas a more stable disc emission starts to contribute significantly to the soft emission during the transition. We note that both a recessing corona resulting in a progressive exposing of the innermost region of the accretion flow, and a truncated disk with an inner radius moving inwards during the transition are able to explain the observations.

Variability fades dramatically during the SIMS. Fig. 10.3 shows that this is the result of a much less variable power-law emission. We see a jump in the hard rms (6-15 keV), which drops from ~ 20 to ~ 7 per cent whereas the contribution of the power-law to the total count rate decreases just a little in a monotonic way. This is only observed during the hard-to-soft transition. During the back transition to quiescence the variability level seems much higher even if the power-law contribution is lower. We note that when BHTs cross the SIMS during the hard-to-soft transitions at high flux, relativistic jet ejections are observed (see e.g. Fender 2006 and Fender et al. 2009). As far as we know they have not been seen during the soft-to-hard transition. Thus, the fact that the physical mechanism responsible for power-law variability is removed could be related to the jet ejection. This can be explained if the variability is produced on the base of the jet, since compact radio emission is observed in BHT during the LHS and the HIMS. However, jet emission should not be present in the HSS, when we clearly see power-law variability. More than one variability component is needed for that model to work.

The evolution of the rms during the HSS is at odds with what is usually observed. In the HRD we see fractional rms increasing with softening at high count rate (first soft excursion) and hardness independent rms at lower fluxes (second soft excursion). The minimum in rms is observed close to the SIMS, and power-law and disc variabilities are consistent with ~ 3 per cent fractional rms. Thus, the $\sim$ 20–25 per cent power-law variability observed at the end of the HIMS almost disappear after crossing the SIMS. This cannot be explained in terms of an increase of the disc contribution. Indeed, the RID shows that absolute (i.e. non fractional) rms fades dramatically from the HIMS to the HSS. Power-law variability is recovered when the system softens and especially when the total count rate drops after the last type-B QPO is observed. If we associate type-B QPOs with jet ejections (e.g., Soleri et al. 2008;Fender et al. 2009), we see rms increasing when the system abandons the region where they are observed and when the type-B/jet mechanism is suppressed. Belloni (2005) observed a similar behaviour during the hard-to-soft transition in GX 339-4 (see also Fender et al. 2009 for XTE J1859+226 and XTE J1550-564). They find similar (2–3%) variability levels in observations showing type-A QPOs, which have hardness values softer but close to those observed in type-B observations. The rms rises for a while after the observations with a type-A and fades again during the softest observations.

GX 339-4 crosses the same region with higher rms during the soft-hard-transition. In MAXI J1659-152 we see a possible type-A QPO only in one observation, although its significance is low and it is observed in one of the softest observations (i.e. with higher rms). However, statistics are much lower in this case than for GX 339-4 and it could be the case that we are not sensitive enough to detect those type-A or that they are not present for other reasons. Assuming that these low rms observations of MAXI J1659-152 after the type-B region correspond to those with type-A in GX 339-4, the behaviour of the two sources is similar with the exception of the final softening and variability decrease observed in GX 339-4 (see Fig. 10 in Belloni 2005). The latter can be explained by the fact that a strong disc dominated soft state is missing in MAXI J1659-152. As discussed above, this can be understood in terms of the high orbital inclination of the system. In addition or alternatively to this, we should take into account that the orbital period proposed for this system (Kuulkers et al. 2010; Belloni et al. 2010) is much sorter than the one of GX 339-4. This should favour a shorter outburst (as observed) and it could have also an effect on the properties of the steady optically thick accretion flow expected to dominate during soft states.

Only type-C and type-B QPOs are observed in MAXI J1659-152. Apart from their intrinsic differences noted in Casella et al. (2005), they are clearly separated using a frequency-fractional rms representation. Whereas type-C follow a clear correlation, type-B are clearly outside this correlation, showing a roughly constant rms as function of the frequency. This has been observed by Casella et al. (2004) and Motta et al. (2011 in prep.) for the cases of XTE J1859+226 and GX 339-4, respectively.

Jet ejections are known to be connected to flux peaks (Fender et al. 2004) and to HIMS/SIMS transitions (i.e. type-B QPOs Soleri et al. 2008; Fender et al. 2009). There are known exceptions, as the case of the strong X-ray flux peak of the 1998/1999 outburst of XTE J1550-564, where a jet ejection $\sim$4 days after the peak was observed before the transition to the soft states (Hannikainen et al. 2001; Corbel et al. 2002). In MAXI J1659-152, type-B QPOs are found in correspondence with local count rate peaks (see light grey bands in Fig. 10.5), especially at high fluxes. However, the absolute count rate peak is observed before the transition to the SIMS (Fig. 10.5) and from that point radio emission is observed to quench (van der Horst et al. 2010). No QPO is observed in that observation (either type-B or C) and the rms is that expected for the HIMS. Similar behaviour is seen in the already mentioned very bright observation of XTE J1550-564, although weak QPOs are present in this case. We expect that multi-wavelength studies performed during this outburst of MAXI J1659-152 will be able to discuss our results in light of the detection or non-detection of relativistic jet emission during the observed X-ray count rate peaks. A possible scenario in which both, jet ejections and HIMS/SIMS transitions are related to flux peaks but not between each others cannot be ruled out.

It is also remarkable that once the system reaches the HSS all the wiggles and flux

peaks present in the light-curve seem related to variations in the power-law emission whereas the disc emission decreases monotonically. This is not observed before the first HSS observation and it is probably connected with the formation of a steady accretion disc during the HSS. Our study suggests that all the scatter usually observed during HSS in the hard-intensity diagrams and rms-intensity diagrams of BHT (see e.g., Dunn et al. 2010) is due to a change in the relative contribution of the power-law, whereas disc emission drops monotonically probably following the accretion rate decrease.

We have measured time-lags between soft and hard emission finding a similar frequency dependence time-lag distribution than that already observed in other BHT during hard states (Nowak et al. 1999; Pottschmidt et al. 2000; Muñoz-Darias et al. 2011). The observation in which it was possible to perform this study belongs to the HIMS, and by comparing with the case of GX 339-4 we obtain results in agreement with those reported by Pottschmidt et al. (2000) in Cyg X-1. In the hard-to-soft transition lags are higher than in the LHS. As discussed in the above works and extensively in Nowak et al. (1999), both the time-lags measured in several systems and the observed time-lag evolution cannot be explained by purely Comptonization models, and alternative scenarios (see e.g., Kazanas et al. 1997; Körding & Falcke 2004) should be further explored.
Finally, we note that by the time we submitted the last revised version of this manuscript another paper based on RXTE analysis on the same source has been accepted for publication (Kalamkar et al. 2011). It is focussed on identifying the black hole nature of the source and according to arXiv was submitted about the same date than this work.

10.5 Conclusions

We have performed an X-ray spectral and timing analysis of the black hole candidate MAXI J1659-152 during its first observed outburst. The outburst evolution of the system is similar to that previously observed in other black hole candidates, although it presents clear peculiarities especially in what regards to the evolution of the fast variability and its energy dependence. We have discussed this behaviour on the basis of the spectral decomposition we have performed. Complementary results obtained through multi-wavelengths campaigns of the present and forthcoming outbursts of this source will result in a deeper understanding of the behaviour observed in this source and of the accretion process taken place in black hole binaries.

Acknowledgments

The research leading to these results has received funding from the European Community's Seventh Framework Programme (FP7/2007-2013) under grant agreement number ITN 215212 "Black Hole Universe". SM and TB acknowledge support to the ASI grant I/088/06/0.

Table 10.1: Spectral parameters derived from the best fit for each observation. A model consisting of a power-law, a multi-color disk-blackbody and a Gaussian emission line with a centroid constrained between 6.4 and 6.8 keV was used. Fluxes (erg s^{-1} cm^{-2}) are computed within the band 4-22 keV.

Obs. Num.	MJD	Obs. ID	χ^2_{red}	kT (keV)	R (km)	Γ	Disc flux	Powerlaw flux
1	55467.0	95358-01-02-00	0.66	–	31^{+86}_{-12}	$1.95^{+0.01}_{-0.01}$	0.00E+00	4.87E-09
2	55468.1	95358-01-02-01	1.57	$0.40^{+2.55}_{-0.40}$	15^{+179}_{-6}	$2.09^{+0.01}_{-0.01}$	5.28E-12	4.26E-09
3	55469.1	95358-01-02-02	0.61	$0.71^{+0.20}_{-0.15}$	63^{+232}_{-19}	$2.16^{+0.01}_{-0.02}$	7.50E-11	4.72E-09
4	55470.0	95108-01-01-00	1.01	$0.82^{+0.29}_{-0.29}$	50^{+303}_{-22}	$2.15^{+0.02}_{-0.03}$	7.12E-11	4.29E-09
5	55470.2	95358-01-03-00	0.82	$0.59^{+0.15}_{-0.12}$	32^{+37}_{-12}	$2.16^{+0.01}_{-0.01}$	6.73E-11	4.62E-09
6	55470.5	95108-01-02-00	0.84	$0.61^{+0.21}_{-0.19}$	40^{+71}_{-15}	$2.14^{+0.01}_{-0.02}$	5.18E-11	4.78E-09
7	55471.1	95358-01-03-01	0.60	$0.72^{+0.20}_{-0.11}$	49^{+88}_{-17}	$2.19^{+0.01}_{-0.02}$	8.99E-11	3.97E-09
8	55471.5	95108-01-03-00	1.08	$0.68^{+0.15}_{-0.12}$	48^{+56}_{-18}	$2.18^{+0.02}_{-0.02}$	9.28E-11	4.29E-09
9	55471.8	95108-01-04-00	1.03	$0.67^{+0.13}_{-0.12}$	48^{+27}_{-12}	$2.17^{+0.02}_{-0.01}$	1.18E-10	4.42E-09
10	55472.1	95108-01-05-00	0.84	$0.68^{+0.16}_{-0.06}$	37^{+38}_{-8}	$2.20^{+0.02}_{-0.03}$	1.18E-10	4.20E-09
11	55472.2	95358-01-03-02	1.05	$0.73^{+0.04}_{-0.04}$	40^{+9}_{-6}	$2.26^{+0.01}_{-0.01}$	1.96E-10	4.20E-09
12	55472.5	95108-01-06-00	0.49	$0.76^{+0.09}_{-0.07}$	43^{+28}_{-9}	$2.31^{+0.02}_{-0.02}$	2.90E-10	4.34E-09
13	55472.9	95108-01-07-00	0.81	$0.80^{+0.10}_{-0.12}$	53^{+25}_{-14}	$2.31^{+0.02}_{-0.03}$	2.60E-10	4.40E-09
14	55473.1	95108-01-08-00	0.92	$0.77^{+0.07}_{-0.09}$	40^{+19}_{-8}	$2.34^{+0.02}_{-0.03}$	2.86E-10	4.12E-09
15	55473.5	95108-01-09-00	0.82	$0.73^{+0.09}_{-0.09}$	37^{+16}_{-10}	$2.31^{+0.02}_{-0.01}$	2.84E-10	4.35E-09
16	55473.7	95108-01-10-00	0.90	$0.79^{+0.08}_{-0.10}$	38^{+19}_{-8}	$2.33^{+0.03}_{-0.03}$	2.94E-10	4.00E-09
17	55474.6	95108-01-11-00	0.63	$0.81^{+0.10}_{-0.07}$	43^{+17}_{-9}	$2.27^{+0.02}_{-0.03}$	2.93E-10	4.09E-09
18	55474.8	95108-01-12-00	1.00	$0.79^{+0.07}_{-0.08}$	34^{+14}_{-7}	$2.30^{+0.02}_{-0.01}$	2.59E-10	3.88E-09
19	55475.4	95108-01-13-00	0.59	$0.83^{+0.08}_{-0.05}$	39^{+13}_{-10}	$2.33^{+0.03}_{-0.03}$	4.65E-10	3.91E-09
20	55475.8	95108-01-14-00	0.58	$0.83^{+0.08}_{-0.07}$	39^{+16}_{-5}	$2.30^{+0.03}_{-0.03}$	2.99E-10	3.86E-09

Continued on next page

Table 10.1 – continued from previous page

Obs. Num.	MJD	Obs. ID	χ^2_{red}	kT (keV)	R (km)	Γ	Disc flux	Powerlaw flux
21	55476.1	95108-01-15-00	0.91	$0.81^{+0.11}_{-0.12}$	38^{+11}_{-4}	$2.26^{+0.02}_{-0.02}$	3.44E-10	3.82E-09
22	55476.4	95108-01-16-00	0.60	$0.85^{+0.05}_{-0.08}$	42^{+18}_{-6}	$2.31^{+0.02}_{-0.02}$	4.75E-10	4.00E-09
23	55476.7	95108-01-17-00	0.85	$0.90^{+0.04}_{-0.06}$	39^{+14}_{-7}	$2.31^{+0.03}_{-0.02}$	6.82E-10	4.15E-09
24	55477.0	95108-01-18-00	1.31	$0.90^{+0.06}_{-0.09}$	37^{+7}_{-5}	$2.30^{+0.04}_{-0.04}$	8.33E-10	4.64E-09
25	55477.0	95108-01-18-01	0.91	$0.91^{+0.09}_{-0.08}$	36^{+13}_{-6}	$2.30^{+0.04}_{-0.04}$	7.71E-10	4.37E-09
26	55477.7	95108-01-19-00	0.97	$0.91^{+0.04}_{-0.05}$	37^{+8}_{-4}	$2.31^{+0.03}_{-0.03}$	7.14E-10	4.27E-09
27	55478.0	95108-01-20-00	1.05	$0.88^{+0.06}_{-0.08}$	42^{+18}_{-9}	$2.28^{+0.02}_{-0.03}$	5.25E-10	3.73E-09
28	55478.5	95108-01-21-00	0.92	$0.92^{+0.04}_{-0.05}$	43^{+15}_{-10}	$2.29^{+0.03}_{-0.02}$	7.76E-10	4.22E-09
29	55479.1	95108-01-22-00	0.66	$0.82^{+0.07}_{-0.06}$	32^{+10}_{-4}	$2.29^{+0.02}_{-0.02}$	4.39E-10	3.62E-09
30	55479.7	95108-01-23-00	0.62	$0.78^{+0.09}_{-0.06}$	38^{+9}_{-7}	$2.25^{+0.02}_{-0.03}$	2.93E-10	3.27E-09
31	55480.2	95108-01-24-00	0.72	$0.88^{+0.02}_{-0.07}$	41^{+10}_{-8}	$2.25^{+0.02}_{-0.02}$	4.09E-10	3.41E-09
32	55480.7	95108-01-25-00	1.41	$0.82^{+0.04}_{-0.06}$	37^{+5}_{-1}	$2.25^{+0.02}_{-0.01}$	3.52E-10	3.26E-09
33	55481.0	95108-01-26-00	1.30	$0.83^{+0.06}_{-0.05}$	35^{+6}_{-3}	$2.28^{+0.03}_{-0.01}$	4.24E-10	3.33E-09
34	55481.7	95108-01-27-00	0.77	$0.94^{+0.03}_{-0.05}$	33^{+14}_{-5}	$2.30^{+0.03}_{-0.02}$	9.11E-10	3.86E-09
35	55482.4	95108-01-28-00	0.83	$0.93^{+0.04}_{-0.07}$	32^{+6}_{-2}	$2.32^{+0.03}_{-0.03}$	7.35E-10	4.21E-09
36	55483.9	95108-01-30-00	0.91	$0.84^{+0.05}_{-0.08}$	38^{+9}_{-5}	$2.22^{+0.03}_{-0.02}$	3.36E-10	2.94E-09
37	55484.2	95118-01-01-00	0.45	$0.89^{+0.03}_{-0.05}$	42^{+7}_{-6}	$2.21^{+0.02}_{-0.02}$	4.52E-10	3.00E-09
38	55484.7	95118-01-01-01	0.81	$0.90^{+0.05}_{-0.06}$	38^{+8}_{-4}	$2.29^{+0.03}_{-0.03}$	6.97E-10	3.59E-09
39	55485.1	95118-01-02-00	0.67	$0.88^{+0.05}_{-0.05}$	47^{+8}_{-4}	$2.29^{+0.03}_{-0.03}$	7.21E-10	3.31E-09
40	55486.2	95118-01-03-01	0.59	$0.91^{+0.04}_{-0.03}$	41^{+5}_{-2}	$2.31^{+0.03}_{-0.06}$	7.50E-10	2.38E-09
41	55486.8	95118-01-03-00	0.93	$0.84^{+0.02}_{-0.04}$	46^{+5}_{-4}	$2.27^{+0.05}_{-0.04}$	6.18E-10	1.48E-09
42	55487.7	95118-01-04-00	0.88	$0.88^{+0.02}_{-0.03}$	46^{+10}_{-3}	$2.29^{+0.03}_{-0.03}$	6.52E-10	2.37E-09
43	55488.0	95118-01-05-00	1.08	$0.83^{+0.02}_{-0.03}$	51^{+4}_{-4}	$2.25^{+0.04}_{-0.03}$	5.51E-10	1.65E-09

Continued on next page

Table 10.1 – continued from previous page

Obs. Num.	MJD	Obs. ID	χ^2_{red}	kT (keV)	R (km)	Γ	Disc flux	Powerlaw flux
44	55488.9	95118-01-05-01	0.72	$0.82^{+0.01}_{-0.05}$	40^{+8}_{-5}	$2.21^{+0.07}_{-0.03}$	5.27E-10	1.38E-09
45	55489.3	95118-01-06-00	1.20	$0.81^{+0.02}_{-0.02}$	43^{+6}_{-3}	$2.23^{+0.02}_{-0.03}$	5.75E-10	1.25E-09
46	55489.7	95118-01-06-01	1.26	$0.85^{+0.04}_{-0.04}$	35^{+7}_{-4}	$2.30^{+0.03}_{-0.03}$	5.25E-10	2.27E-09
47	55490.1	95118-01-07-01	1.12	$0.83^{+0.03}_{-0.03}$	37^{+9}_{-2}	$2.26^{+0.03}_{-0.04}$	5.02E-10	1.73E-09
48	55490.7	95118-01-07-00	1.33	$0.88^{+0.04}_{-0.04}$	39^{+6}_{-2}	$2.25^{+0.01}_{-0.04}$	4.95E-10	2.55E-09
49	55491.0	95118-01-08-00	0.50	$0.87^{+0.02}_{-0.07}$	41^{+12}_{-7}	$2.21^{+0.06}_{-0.03}$	5.36E-10	2.22E-09
50	55491.8	95118-01-09-00	0.98	$0.85^{+0.03}_{-0.03}$	38^{+17}_{-5}	$2.22^{+0.02}_{-0.04}$	4.62E-10	2.21E-09
51	55493.3	95118-01-10-00	1.78	$0.80^{+0.05}_{-0.05}$	42^{+4}_{-2}	$2.26^{+0.04}_{-0.04}$	3.47E-10	2.37E-09
52	55494.2	95118-01-11-00	0.85	$0.83^{+0.05}_{-0.08}$	40^{+7}_{-4}	$2.27^{+0.05}_{-0.05}$	3.65E-10	1.93E-09
53	55495.0	95118-01-12-00	0.62	$0.80^{+0.02}_{-0.06}$	47^{+9}_{-5}	$2.23^{+0.03}_{-0.05}$	3.54E-10	1.87E-09
54	55496.5	95118-01-13-00	0.86	$0.80^{+0.03}_{-0.04}$	49^{+15}_{-8}	$2.17^{+0.04}_{-0.04}$	3.05E-10	1.15E-09
55	55497.5	95118-01-14-00	0.76	$0.77^{+0.03}_{-0.04}$	47^{+14}_{-7}	$2.22^{+0.07}_{-0.09}$	3.30E-10	8.43E-10
56	55498.5	95118-01-15-00	0.58	$0.74^{+0.04}_{-0.04}$	42^{+5}_{-3}	$2.17^{+0.09}_{-0.07}$	2.77E-10	9.58E-10
57	55499.3	95118-01-15-01	0.57	$0.74^{+0.02}_{-0.05}$	32^{+6}_{-5}	$2.18^{+0.06}_{-0.05}$	2.57E-10	9.65E-10
58	55500.3	95118-01-16-00	0.77	$0.75^{+0.02}_{-0.03}$	22^{+5}_{-3}	$2.16^{+0.06}_{-0.05}$	2.20E-10	1.05E-09
59	55501.2	95118-01-16-01	0.87	$0.74^{+0.05}_{-0.04}$	37^{+138}_{-14}	$2.10^{+0.05}_{-0.04}$	1.13E-10	1.36E-09
60	55502.0	95118-01-17-00	0.90	$0.78^{+0.05}_{-0.05}$	37^{+138}_{-14}	$2.03^{+0.04}_{-0.04}$	8.23E-11	1.40E-09
61	55503.1	95118-01-17-01	0.99	–	37^{+138}_{-14}	$1.97^{+0.03}_{-0.03}$	0.00E+00	1.39E-09
62	55504.1	95118-01-18-00	0.80	–	37^{+138}_{-14}	$1.85^{+0.04}_{-0.04}$	0.00E+00	1.29E-09
63	55505.0	95118-01-19-00	1.48	–	37^{+138}_{-14}	$1.80^{+0.02}_{-0.03}$	0.00E+00	1.25E-09
64	55506.2	95118-01-20-00	1.22	–	37^{+138}_{-14}	$1.74^{+0.03}_{-0.04}$	0.00E+00	1.17E-09
65	55508.1	95118-01-21-00	0.85	–	37^{+138}_{-14}	$1.72^{+0.03}_{-0.03}$	0.00E+00	1.08E-09

Table 10.2: Best fit for the central peak of the QPO detected during the whole outburst. The noise components were fitted with three Lorentzian shapes, one zero-centred and other two centred at a few Hz. The QPOs were fitted with one Lorentzian each. Rms is the total, fractional rms (i.e. all the PDS components) within the band 0.1-64 Hz.

Observation ID	Frequency (Hz)	Width (Hz)	Normalization	rms (%)
95358-01-02-00	3.30 ± 0.04	0.53 ± 0.32	1 ± 1	22.3 ± 0.1
95358-01-02-01	2.28 ± 0.02	0.38 ± 0.07	14 ± 1	22.6 ± 0.2
95358-01-02-02	5.5 ± 0.2	0.77 ± 0.61	1.3 ± 0.7	22.2 ± 0.3
95108-01-01-00	2.71 ± 0.03	0.32 ± 0.08	11 ± 2	22.1 ± 0.3
95358-01-03-00	2.80 ± 0.02	0.34 ± 0.05	11.6 ± 1.2	21.2 ± 0.1
95108-01-02-00	5.3 ± 0.1	0.61 ± 0.36	1.0 ± 0.6	22.2 ± 0.2
95358-01-03-01	3.18 ± 0.02	0.41 ± 0.09	11 ± 2	20.8 ± 0.2
95108-01-03-00	3.04 ± 0.04	0.37 ± 0.15	11 ± 4	21.1 ± 0.2
95108-01-04-00	3.06 ± 0.03	0.34 ± 0.09	25 ± 5	21.1 ± 0.2
95108-01-05-00	3.33 ± 0.04	0.32 ± 0.16	5 ± 2	20.1 ± 0.4
95358-01-03-02	3.80 ± 0.02	0.45 ± 0.07	5.8 ± 0.7	19.8 ± 0.2
95108-01-06-00	4.58 ± 0.03	0.50 ± 0.08	11 ± 1	18.5 ± 0.2
95108-01-07-00	4.41 ± 0.03	0.54 ± 0.10	18 ± 2	18.3 ± 0.1
95108-01-08-00	4.84 ± 0.02	0.54 ± 0.07	9.0 ± 0.9	17.9 ± 0.1
95108-01-09-00	4.72 ± 0.04	0.53 ± 0.15	5 ± 1	17.9 ± 0.2
95108-01-10-00	4.86 ± 0.04	0.47 ± 0.14	4.1 ± 0.8	18.1 ± 0.3
95108-01-11-00	4.64 ± 0.03	0.42 ± 0.10	4.9 ± 0.8	18.9 ± 0.2
95108-01-12-00	4.78 ± 0.03	0.57 ± 0.10	10 ± 2	17.8 ± 0.2
95108-01-13-00	6.13 ± 0.06	0.79 ± 0.24	2.8 ± 0.6	15.5 ± 0.2
95108-01-14-00	5.01 ± 0.05	0.56 ± 0.16	4.2 ± 1.0	18.3 ± 0.3

Continued on next page

Table 10.2 – continued from previous page

Observation ID	Frequency (Hz)	Width (Hz)	Normalization	rms (%)
95108-01-15-00	5.10 ± 0.03	0.60 ± 0.11	3.9 ± 0.4	17.7 ± 0.2
95108-01-16-00	6.02 ± 0.04	0.88 ± 0.16	6.6 ± 0.9	15.2 ± 0.1
95108-01-17-00	7.01 ± 0.09	0.98 ± 0.32	3.3 ± 0.8	12.9 ± 0.1
95108-01-18-00	7.5 ± 0.3	0.78 ± 1.28	1 ± 1	11.7 ± 0.2
95108-01-18-01	7.3 ± 0.2	1.01 ± 0.63	2 ± 1	12.4 ± 0.2
95108-01-19-00	7.2 ± 0.2	0.69 ± 0.55	1.0 ± 0.5	13.1 ± 0.3
95108-01-20-00	6.6 ± 0.1	0.79 ± 0.30	1.7 ± 0.5	14.6 ± 0.3
95108-01-21-00	7.2 ± 0.2	1.18 ± 0.74	1.3 ± 0.7	11.0 ± 0.1
95108-01-22-00	6.34 ± 0.04	0.63 ± 0.11	3.1 ± 0.4	14.2 ± 0.1
95108-01-23-00	5.33 ± 0.04	0.57 ± 0.12	5.6 ± 0.8	17.4 ± 0.2
95108-01-24-00	5.99 ± 0.04	0.69 ± 0.11	4.1 ± 0.5	15.9 ± 0.1
95108-01-25-00	5.81 ± 0.04	0.60 ± 0.13	4.1 ± 0.6	15.5 ± 0.2
95108-01-26-00	6.67 ± 0.06	0.81 ± 0.19	2.6 ± 0.6	14.1 ± 0.1
95108-01-27-00	3.90 ± 0.49	0.49 ± 0.03	2.8 ± 0.1	6.5 ± 0.2
95108-01-28-00	4.09 ± 0.05	0.60 ± 0.13	2.1 ± 0.3	8.4 ± 0.2
95108-01-30-00	6.01 ± 0.06	0.56 ± 0.17	1.3 ± 0.3	15.5 ± 0.3
95118-01-01-00	6.85 ± 0.08	0.81 ± 0.23	1.6 ± 0.4	13.3 ± 0.1
95118-01-01-01	3.85 ± 0.04	0.53 ± 0.11	1.7 ± 0.3	6.9 ± 0.4
95118-01-02-00	3.47 ± 0.09	1.21 ± 0.28	2.0 ± 0.3	5.1 ± 0.3
95118-01-06-00	6.77 ± 0.85	5.12 ± 2.87	1.5 ± 0.5	6.0 ± 0.5
95118-01-07-00	3.30 ± 0.04	0.48 ± 0.12	1.5 ± 0.3	8.4 ± 0.5
95118-01-09-00	2.39 ± 0.23	1.37 ± 0.96	1.4 ± 0.9	7.2 ± 0.7
95118-01-10-00	3.55 ± 0.04	0.37 ± 0.09	2.9 ± 0.5	9.6 ± 0.3

Continued on next page

Table 10.2 – continued from previous page

Observation ID	Frequency (Hz)	Width (Hz)	Normalization	rms (%)
95118-01-11-00	1.74 ± 0.39	1.07 ± 1.39	0.8 ± 0.7	6.6 ± 1.4
95118-01-12-00	2.02 ± 0.12	0.65 ± 0.43	1.4 ± 0.7	7.3 ± 0.6
95118-01-16-01	5.97 ± 0.09	0.69 ± 0.37	1.5 ± 0.6	14.8 ± 0.4
95118-01-17-00	4.78 ± 0.06	0.56 ± 0.18	2.2 ± 0.5	18.9 ± 0.4
95118-01-17-01	3.36 ± 0.05	0.47 ± 0.12	3.2 ± 0.6	23.8 ± 0.4
95118-01-18-00	2.58 ± 0.08	0.28 ± 0.15	1.4 ± 0.5	24.4 ± 1.1
95118-01-19-00	2.19 ± 0.03	0.43 ± 0.08	4.2 ± 0.6	27.0 ± 0.4
95118-01-20-00	2.04 ± 0.04	0.33 ± 0.10	3 ± 1	26.3 ± 0.5
95118-01-21-00	1.63 ± 0.04	0.52 ± 0.16	5 ± 1	27.2 ± 0.5

11 X-ray bursts and burst oscillations from the slowly spinning X-ray pulsar IGR J17480-2446 (Terzan 5)

Sara E. Motta, Antonello D'Aì, Alessandro Papitto, Alessandro Riggio, Tiziana Di Salvo, Luciano Burderi, Tomaso M. Belloni, Luigi Stella, Rosario Iaria

Monthly Notices of the Royal Astronomical Society, 2011, 414, 1508

Abstract

The newly discovered 11 Hz accreting pulsar, IGR J17480-2446, located in the globular cluster Terzan 5, has shown several bursts with a recurrence time as short as few minutes. The source shows the shortest recurrence time ever observed from a neutron star. Here we present a study of the morphological, spectral and temporal properties of 107 of the bursts observed by the Rossi X-ray Timing Explorer. The recurrence time and the fluence of the bursts clearly anticorrelate with the increase of the persistent X-ray flux. The ratio between the energy generated by the accretion of mass and that liberated during bursts indicate that Helium is ignited in a Hydrogen rich layer. Therefore we conclude that all the bursts shown by IGR J17480-2446 are Type-I X-Ray bursts.

Pulsations could be detected in all the brightest bursts and no drifts of the frequency are observed within 0.25 Hz of the spin frequency of the neutron star. These are also phase locked with respect to the pulsations observed during the persistent emission and no rise of the rms associated to the pulse frequency is observed during the burst. This behavior would favor a scenario where the type-I burst, possibly ignited at the polar caps, immediately propagates to the entire neutron star surface.

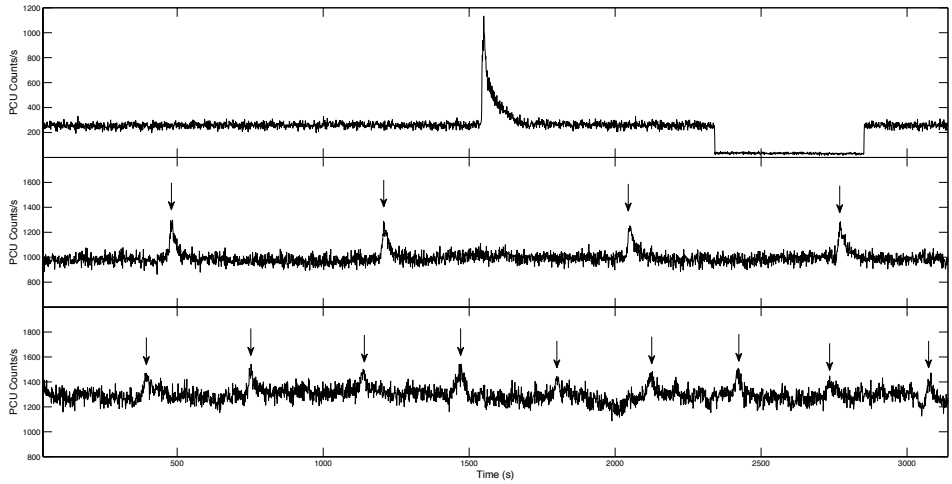

Figure 11.1: Light curves of three RXTE observations of IGR J1748-2446. For each observation we plot the 1s-resolution light curve from the beginning of the RXTE pointing. We show the first 3ks for each observation. From top panel: Obs. 95437-01-01-00, 95437-01-02-01, 95437-01-04-01. Arrows in the second and third panels from top mark the position of the bursts. Note that in Obs. 95437-01-01-00 a clear eclipse due to the moon occultation is visible (see Strohmayer et al. 2010). The recurrence time between bursts is clearly different between the second and third observation (see text).

11.1 Introduction

Type–I X-ray bursts result from unstable thermonuclear ignition of accreted material on the surface of weakly magnetized neutron stars (see Lewin et al. 1976, Strohmayer & Bildsten 2006, Galloway et al. 2008, and references therein for reviews on the subject). This material is accreted through Roche-lobe overflow from a lower-mass companion star (low-mass X-ray binary, LMXB). In systems exhibiting bursts, the temperature and pressure at the base of the accreted layer slowly increase until the nuclear energy generation rate becomes more sensitive to temperature perturbations than to radiative cooling. At this point the resulting thermonuclear instability leads to runaway burning of the matter that has been deposited since the previous burst. During the flash, over 90% of the accreted hydrogen and helium is expected to burn into carbon and heavier elements (Woosley et al. 2004). For the next flash to occur, a fresh layer of hydrogen/helium must first be accreted.

X-ray bursts are observed in about half of the total population of LMXBs in the Galaxy, but only 15 sources from this sample show coherent pulsations (Galloway et al. 2010) at, or within a few Hz from, the spin frequency of the NS during the burst emission. To date, only five LMXBs show coherent pulsations both during the

burst and the persistent X-ray emission (SAX J1808.4-3658, XTE J1814-338, HETE J1900.1-2455 and IGR J17511-3057, and the peculiar case of Aql X-1 that showed coherent pulsations with an extremely low duty cycle, see Altamirano & Watts 2010 and references therein). The spin frequency in these sources is between 245 Hz and 550 Hz.

Notwithstanding the great amount of observational facts collected in the last years, we still lack a clear understanding of the physical mechanism responsible for the onset of the burst oscillations. It would be important to understand why only $\sim$20% of the bursting X-ray sources show pulsations and why a drift of the order of a few Hz of the burst oscillation frequency is often observed during some type-I bursts (Muno et al. 2002), while in accreting millisecond pulsars this drift is less evident (e.g. Altamirano et al. 2010 and references therein).

The recent discovery of an 11 Hz accreting X-ray pulsar in the Globular cluster Terzan 5 showing also burst oscillations at the same frequency can greatly help to shed light on these questions, definitely ruling out the need for high NS spin frequency as a necessary ingredient both for the onset of X-ray burst and the burst oscillations.

Furthermore, since the burst peak flux from IGR J17480-2446 is exceptionally low, compared to the values observed in other bursting sources, this source offers an excellent opportunity to study the effect of a hot NS contribution to the burst emission that arises when the burst luminosity is low compared to the persistent emission and in particular to the blackbody component (see van Paradijs & Lewin 1986).

11.2 Observations and data analysis

INTEGRAL detected a transient source in the Globular Cluster Terzan 5 on 2010 October 10.365 (Bordas et al. 2010), tentatively attributed to the known LMXB transient EXO 1745-248. However, follow-up Swift observations refined the source position, excluding the association with EXO 1745-248; the new source was therefore dubbed as IGR J17480-2446. A *Chandra* observations confirmed the position of the source (see Pooley et al. 2010) and its non-association with EXO 1745-248. The distance to Terzan 5 has been estimated as 5.9$\pm$0.5 kpc (Lanzoni et al. 2010), which is the value we consider in the following.

Subsequent *Rossi X-ray Timing Explorer* (RXTE in the following) observations of IGR J17480-2446 showed coherent pulsations at 11 Hz and the presence of bursts and burst oscillations (Altamirano & Watts 2010, Strohmayer & Markwardt 2010). Timing analysis of the pulse period revealed how the system has an orbital period of 21.327 hr and a companion star mass between 0.4 and 1 $M_{\odot}$ (Papitto et al. 2011, Strohmayer et al. 2010).

In this work, we focus on the X-ray bursts observed in the rising phase of the

outburst of IGR J17480-2446 with RXTE. We consider observations from 13th to 17th October (MJD 55482 to 55486, Obs. ID from 95437–01–01–00 to 95437–01–04–01).

11.2.1 Outburst light curve, persistent emission and burst analysis

IGR J17480-2446 was observed daily by RXTE starting from MJD 55482.01 (Obs.ID from 95437-01-01-00, October 13th 2010), three days after its discovery with INTEGRAL. A sample of the light curves observed with RXTE is shown in Fig. 11.1. The count rate observed by the PCU2 of the Proportional Counter Array (PCA) during the *persistent* emission[1] rises from $\sim$ 250 (October 13.0) to $\sim$ 1300 c s^{-1} PCU^{-1} (October 16.7).

To evaluate the X-ray *persistent* flux just prior each burst onset, we extracted spectra only the PCU2 of the PCA (3.5–25 keV) over a time interval of 32s before T_{peak}. We modelled the spectrum with the sum of a blackbody and a Comptonized component, `compps` (Poutanen & Svensson 1996), and computed unabsorbed fluxes extrapolating in the 0.1-100 keV energy band. The source unabsorbed *persistent* flux rises from $F_{pers} = 0.54(5) \times 10^{-8}$ erg cm^{-2} s^{-1} on October 13.0, up to a peak value of $F_{pers} = 1.7(2) \times 10^{-8}$ erg cm^{-2} s^{-1} during the last observation considered here (October 16.7).

X-ray bursts appearing at regular intervals are detected in all the RXTE observations we consider (October 13th - 16th). The recurrence time between consecutive bursts decreases from $\gtrsim$ 24 min to $\simeq$ 5 min while the *persistent* flux increases (see Fig. 11.2). After October 17th, the bursts disappeared to appear again on October 18th. To analyze the morphological properties of the bursts observed during the rising part of the outburst, we consider background-subtracted light curves extracted from data taken in Event (122μs temporal resolution) and Good Xenon (1μs temporal resolution) packing mode. Binning the light curves in 0.125s intervals, we modelled the burst shape with a five-parameter model: persistent count rate, start time of the burst (T_{rise}), peak time (T_{peak}), amplitude of the burst, exponential decay time of the burst (τ). The model assumes a linear rise between T_{rise} and T_{peak}, and an exponential decay after the peak. The bursts show a typical rise time between few and $\sim$20s and an exponential decay time between $\sim$10 and $\sim$100s. As an example we show in the top panel of Fig. 11.1 the shape of the first and most energetic burst observed by RXTE and in the following panels the typical shapes of the subsequent fainter bursts.

To verify possible photospheric radius expansion episodes during the bursts, we

[1]Even though the source is an X-ray transient, we refer to *persistent* emission as the main body of the outburst emission, and to *burst* emission when the source exhibits thermonuclear flashes

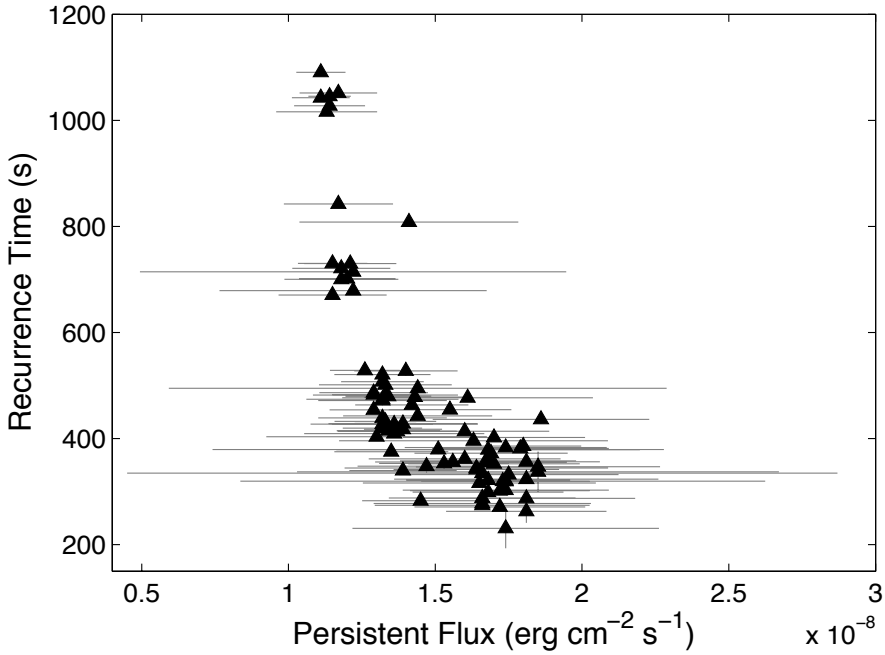

Figure 11.2: Variation of the recurrence time as function of the *persistent* flux.

extracted PCU2 spectra of the brightest burst, over time intervals 2 seconds long and modelled them with an absorbed blackbody. The best-fit values of blackbody temperature and radius are plotted in the middle and lower panel of Fig.11.3, respectively. The apparent radius observed at infinity has a constant value of $R_{app}^{\infty} = (3.3 \pm 0.5)\ d_{5.9}$ km, clearly indicating that no radius expansion takes place. The apparent radius has subsequently been converted into an effective radius taking into account the hardening factor and the effect of the gravitational redshift (see Sec. 11.3 for details). We also measured the mean apparent radii for selected bursts following the first brightest one (see Tab. 11.1). To do this we followed Sztajno et al. (1986). For each selected burst we made a two-component fit to the combined persistent and burst emission, involving a black body component (associated to the NS emission) and a Comptonized component that represents the emission which is promptly radiated upon accretion of matter. We assumed that the latter component is not affected by the occurrence of a thermonuclear flash and we adopted the apparent blackbody radius associated to the other component as the mean radius of the region emitting the blackbody radiation during the Type-I X-Ray bursts. To better constrain the parameters of the persistent emission spectrum, we extracted the persistent emission spectrum immediately before the burst occurrence and we fitted it. Then we used this

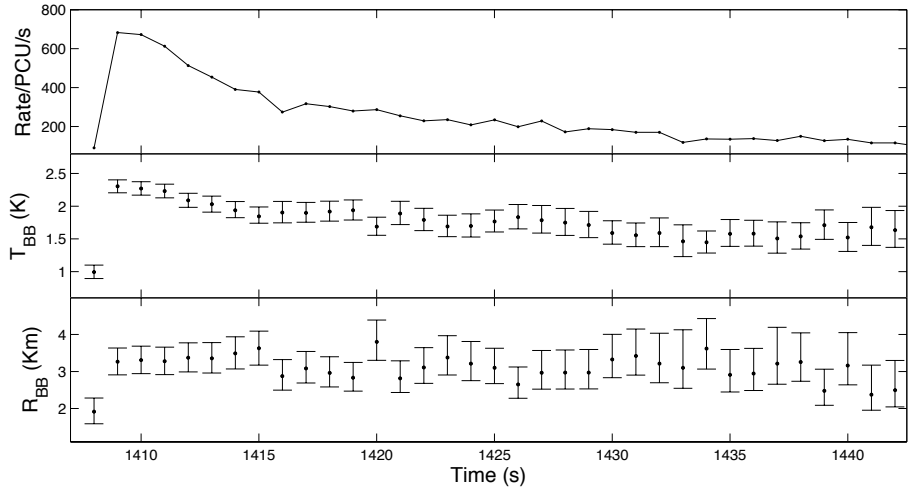

Figure 11.3: Top panel: light curve of the strongest burst, observed on MJD 55482. Middle and bottom panel: evolution of radius and tamperature of the best-fit blackbody component. The integration time of the points is 2s at the peak and 4s during the last part of the decay.

template model to fit the emission during the bursts, keeping the parameters of the comptonisation component and leaving the parameters of the blackbody component free to vary. The resulting measures (where the corrections adopted for the first burst have been applied) are listed in Tab. 11.1.

To verify our results, we attempted to stack data from several faint bursts observed at higher accretion rates (MJD 55485) and applied the same procedure followed for the single bursts. Analyzing the profiles of the fainter bursts, both rise and decay times often resulted different from one burst to another. For this reason, we selected bursts with similar profiles (i.e. similar rise and decay times) and averaged their spectra in order to obtain the measure of the mean radius and temperature of the blackbody emitting region. We obtained values consistent with the ones reported in Tab. 11.1.

The energetics of each burst has been evaluated extracting a PCU2 spectrum taken in a fast timing mode (Generic Event and Good Xenon) over a time range containing the whole burst and of a variable length depending on τ and on the variability of the *persistent* flux. We subtracted as background the spectrum of the persistent emission, extracted over an interval of 32 s before the onset of the burst (T_{rise}). We modelled the resulting spectrum with an absorbed blackbody. The fluence estimates we obtain in the 0.1-100 keV band are listed in Table 11.2. The first burst is the most energetic,

No.	T (keV)	R_{min} (Km)	R_{max} (Km)
2	$1.41^{+0.03}_{-0.08}$	8.36	19.08
6	$1.34^{+0.07}_{-0.08}$	9.26	21.12
10	$1.36^{+0.08}_{-0.10}$	8.31	19.01
28	$1.27^{+0.04}_{-0.06}$	10.60	25.00
31	$1.37^{+0.03}_{-0.06}$	9.42	22.77
32	$1.28^{+0.06}_{-0.06}$	10.19	24.40
80	$1.17^{+0.05}_{-0.01}$	14.56	35.24
93	$1.17^{+0.01}_{-0.03}$	14.86	34.66
106	$1.17^{+0.03}_{-0.03}$	14.82	34.29

Table 11.1: Mean temperature and radius of the blackbody component associated to the thermonuclear burst emission. The upper and lower limit to the radius are corrected for the hardening factor f_c and for gravitational redshift contribution.

showing a bolometric fluence of $\mathcal{F}_{burst} = 3.15(6) \times 10^{-7}$ erg cm^{-2}. As the *persistent* flux of the source increases, bursts become more frequent and less energetic as ~ 3.5d after the first observation they have fluences of the order of $\sim 1 \times 10^{-8}$ erg cm^{-2} (see Fig. 11.1). We have then evaluated the ratio of the integrated persistent flux to the burst fluence, $\alpha = F_{pers} t_{rec} / \mathcal{F}_{burst}$ for each burst for which the recurrence time could be unambiguously defined. Modelling the observed values with a constant α we obtain an average value of $< \alpha >= 96 \pm 3$, with a small variance of 1.32 over 89 points (see Fig. 11.4). As we discuss in the following such values are compatible with a thermonuclear origin of the bursts (see also Chakraborty & Bhattacharyya 2011). To secure such an identification, we searched for evidence of spectral softening during the tails of the bursts, which could be interpreted as cooling of the burst emission. While there is an indication of such a cooling during the first and brightest burst (see middle panel of Fig. 11.3), a similar trend could not be observed for the subsequent, fainter bursts (see Galloway & in't Zand 2010, Chakraborty & Bhattacharyya 2011). We argue that this is not due to the absence of the softening, but to the intrinsic difficulty in disentangling the persistent and the burst emission when the tail of the burst is soon dominated by the persistent emission. Furthermore, as pointed out by Sztajno et al. (1986) and van Paradijs & Lewin (1986), the spectral analysis of X-ray bursts is systematically affected if the persistent emission contains a spectral component which originates from the outer layer of a hot NS, which also transfers an important energetic contribution to the burst emission. In this situation the net burst

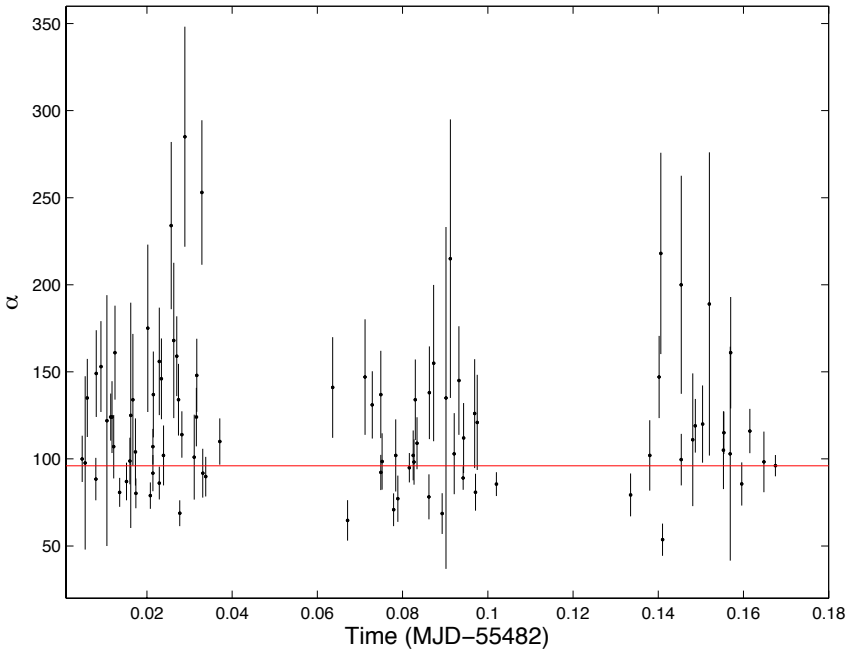

Figure 11.4: Values of α obtained for all the consecutive bursts. The horizontal line marks the mean value $< \alpha >= 96 \pm 3$.

emission (i.e. excess above the persistent emission) is the difference between two blackbody spectra at different temperatures, corresponding to the total emission from the hot NS at different times. As a consequence, the net emission does not have a blackbody spectral distribution, therefore a *standard* blackbody spectral analysis on the net burst emission is not decisive in the identification of the burst nature.

11.2.2 Burst oscillations

Burst-oscillation analysis was conducted using PCA data in Good Xenon mode (for Obs. 95437-01-01-00) and Event Mode (for the following observations), which provide full timing and spectral information. We produced a dynamical power density spectrum (DPDS) computing Fast Fourier Transforms (FFTs) of overlapping windows of data of length 4s, stepped by 0.25s (Fig.11.5, second panel from top). As an example we show the DPDS for the case of the first burst observed on October 13th. In the third panel from top of Fig. 11.5 we show the evolution of the 11 Hz Leahy power (Leahy et al. 1983) as function of time for that burst. Here the rise in the pulsation power during the burst is driven by the increase in count rate. The

increase is consistent with a constant fractional rms, as shown in the bottom panel of Fig. 11.5. We note that no drifting of the pulsation frequency is observed within 0.25 Hz from the best-fitting spin period. Interestingly, while the decay phase of the burst follows the expected exponential profile, the evolution of the power (see Fig. 11.5, third panel from the top) clearly shows a multi-peak structure that does not reflect the decay in the light curve. A similar case in observed in XTE J1814-338 (Strohmayer et al. 2003).

The other bursts also show an increase (although statistically less evident) in the pulsation power. In particular, we observed a stronger power in the 11 Hz pulsations in bursts taking place during MJD 55482 and 55483. Later in the outburst, the increase in power becomes difficult to observe as the bursts become fainter. This effect is likely due to the lack of statistics encountered when the net burst count rate decreases (making detections statistically weaker) as the persistent flux rises.

In order to ascertain the phase relation between the coherent pulsations observed during the *persistent* emission and burst oscillations, we reconstructed pulse profiles over 100 s long intervals before each of the bursts, and over 20s intervals after the bursts' onset. We performed an epoch folding around the best estimate of the spin period (see Papitto et al. 2011) for the two intervals, obtaining two pulse profiles that were fitted according to a standard harmonic decomposition. We then obtained the phase difference between the two profiles and studied the variations of the phase difference for each burst as a function of time. Such difference is in general consistent with zero for all examined bursts (Fig. 11.6). Considering the uncertainties on the phase estimates we thus conclude that the bursts oscillations originate from a region which is very close to the NS polar caps.

11.3 Discussion and conclusions

In this paper we report on the bursting behavior of the newly discovered X-ray pulsar IGR J17480-2446.

The observed spin period and the magnetic field estimated for IGR J17480-2446 (see Papitto et al. 2011) place this source in between the population of classical (B $\gtrsim 10^{11}$G, P $\geq$ 0.1 s) and millisecond accreting X-ray pulsars (B = 10^8- 10^9 G, P = 1.5-10 ms). This source constitutes therefore a *bona fide* candidate as link between these two groups, being a slow, probably mildly recycled, pulsar. IGR J17480-2446 is presently the bursting source with the longest spin period observed.

To convert flux into luminosity and fluence into energy, we assumed geometric isotropy of the emission and a source distance of 5.9 kpc. We further express this quantity in units of Eddington luminosity (=1.8 $\times 10^{38}$ erg s^{-1} for a 1.4 M$_\odot$ NS). From MJD 55482.00872 to MJD 55486.56326 the source *persistent* luminosity rises from $\sim$2.2$\times$ $d_{5.9}^2$ 10^{37} erg s^{-1} to $\sim$7.5$\times 10^{37}$ $d_{5.9}^2$ erg s^{-1}. From these values, we

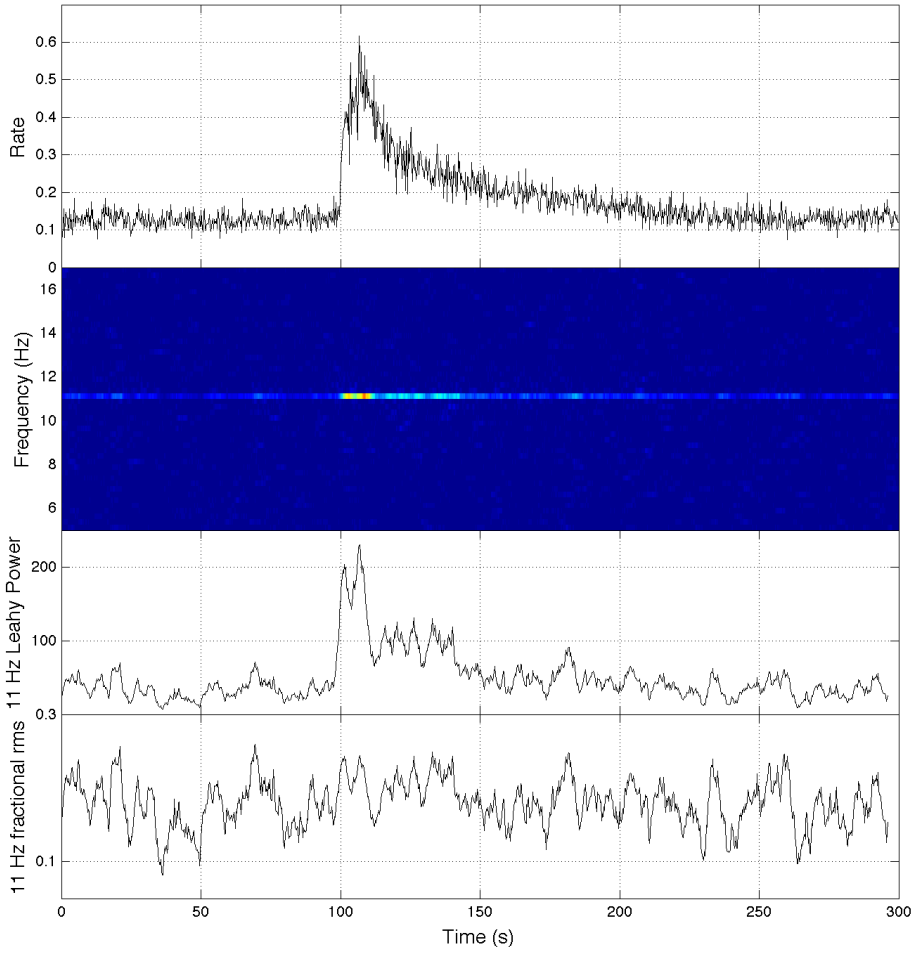

Figure 11.5: Analysis of the burst observed on Oct. 13th. Top panel: light curve. Second panel: Dynamical power density spectrum. Third panel: Evolution of Leahy power at 11.125 Hz. Bottom panel: corresponding fractional rms.

infer an increase of the mass accretion rate[2] from $0.1\dot{M}_{Edd}$ to $0.37\dot{M}_{Edd}$ (see Fig. 11.7). Consistently with this behavior the bursts become more frequent and fainter.

In this paper we report on the analysis of 107 X-ray bursts shown by IGR J17480-2446 during the first four days of the RXTE monitoring. Since the *persistent* bolo-

[2]The expected values of $\dot{M}/\dot{M}_{Edd}$ are calculated as $\frac{\dot{M}}{\dot{M}_{Edd}} = \frac{\dot{L}}{\dot{L}_{Edd}}$

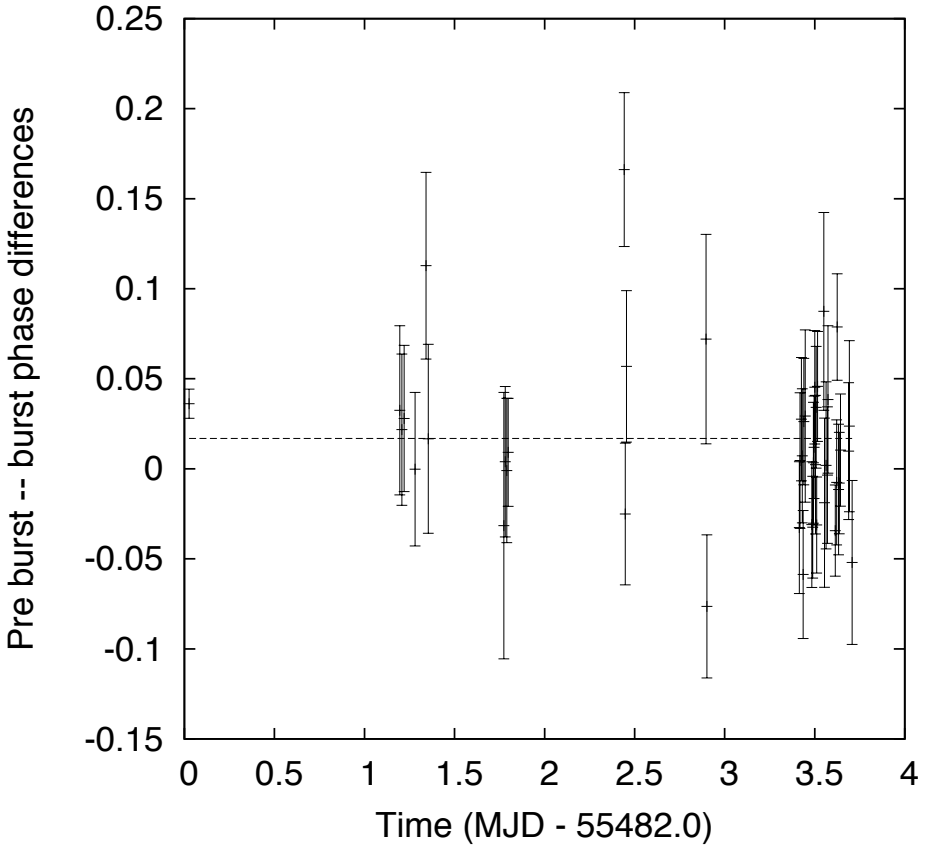

Figure 11.6: Phase difference between the pulse in the persistent emission and during the burst period.

metric X-ray luminosity rises by a factor $\sim$4 during this interval we were able to study the properties of bursts at different mass accretion rates.

The observed bursts have different profiles in the light curve. The rise time varies between few and $\sim$20 seconds, while the decay time (τ) spans the range between $\sim$20 and $\sim$100 seconds. The firsts, more intense bursts (MJD 55483 and 55484), show a typical Type-I X-Ray burst profile, featuring a linear rise and an exponential decay following the burst peak. The subsequent fainter bursts present a less clear profile, with rise times in some cases similar to the decay times. For some of the fainter bursts a clear modeling of the profile was difficult because the excursion in

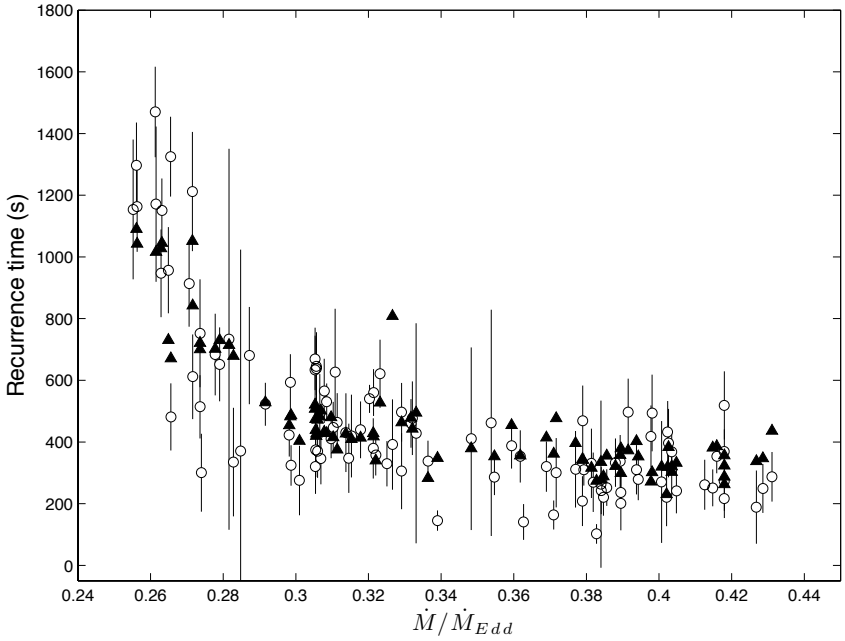

Figure 11.7: Observed (triangles) and predicted (circles) recurrence times plotted in the function of the measured local accretion rate. Error bars related to the accretion rate are not reported for clarity.

intensity above the continuum due to the burst occurrence was comparable with the persistent emission variations.

The pulsation does not show any drifting of the frequency during the decay phase of the bursts. This phenomenon is also observed in bursting millisecond pulsars (XTE J1814–338, Markwardt & Swank 2003; HETE J1900.1–2455, Kaaret et al. 2006; IGR J17511-3057 Altamirano et al. 2010) and can be explained in terms of a non-significant expansion of the NS atmosphere during the thermonuclear combustion. Studying the spectral evolution during the first burst, no photospheric radius expansion is indeed observed (see Fig. 11.3).

Burst oscillations are always phase locked within 0.2 phase units, indicating how the ignition begins in a region not far from the NS polar caps. The radius inferred from spectral fitting for the first and most intense burst is 3.2±0.5 km. Also taking into account the corrective factors to translate this value into a physical size on the NS surface (see below), the obtained radius is compatible, within the uncertainties, with the NS radius.

The recurrence times of X-ray bursts was observed to decrease from $\geq$26 min to $\simeq$5 min in anti-correlation with the persistent X-ray flux. The shortest recurrence time so far observed in IGR J17480-2446 is 3.3 min and it is seen in MJD 55487 (Obs. 95437-01-06-00, not considered in this work). The shortest recurrence time previously reported is 3.8 minutes (see Keek et al. 2010).

The very short recurrence time observed from the bursts shown IGR J17480-2446, together with the unusual spectral and morphological properties, casted doubts on the mechanism powering such bursts. The absence of a significant cooling from all the bursts except than for the first brightest one and the unprecedented observations of long trains of bursts with very short recurrence time led Galloway et al. (2010) to argue that IGR J17480-2446 could be an analogue of GRO J1744-28 in showing Type-II bursts powered by accretion instabilities.

In this paper we have analyzed the bursts shown by IGR J1748-2446 during the first four days of RXTE observations, and we were able to unambiguously measure the recurrence time for a large number of them. We considered the measures of burst fluences and of the *persistent* flux before each burst and we estimated the ratio of the accretion energy liberated into nuclear energy during the bursts, $\alpha = F_{pers}\, t_{rec}/\mathcal{F}_{burst}$. The average value we have obtained (α= 96$\pm$3) strongly favours the hypothesis these bursts are due to unstable thermonuclear burning of the H/He accreted on the NS surface layer. As a matter of fact, under this hypothesis and assuming that all the available H/He nuclear fuel is burnt during bursts such ratio is expected to be $\alpha = Q_{grav}/Q_{nuc}(1+z)$, where $Q_{grav} = GM/R_{NS} = 180$ MeV is the energy liberated per accreted nucleon for a 1.4 $M_\odot$ NS with a radius of 10 km, $1+z = (1-2GM/R_{NS}c^2)^{-1/2}$ measures the gravitational red shift at the NS surface, and $Q_{nuc} = 1.6+4 < X >$ MeV/nucleon is the energy released during thermonuclear burning of a mixture of H and He. Here, $< X >$ is the mass fraction of hydrogen which may not be depleted during the stable burning phase in between bursts and therefore burns with He during the flash (see e.g. Galloway et al. 2008). The average estimate of $\alpha = 96 \pm 3$ we have given for the bursts shown by IGR J17480-2446 is compatible with the burst being of Type-I and indicates $< X >$=0.22(2) for (1 + z) = 1.31. In addition, despite the lower statistic of the bursts observed at higher accretion rates, the values of alpha coming from the fainter bursts are consistent with the ones found for lower accretion rate regimes (see Fig. 11.4), even though the statistics is not enough to clearly identify fluctuations of the values of α driven by the variations of $\dot{m}$. However, the value of α is always close to 96, still indicating the thermonuclear origin as the most probable for all the bursts. It is worth to note that Type-II X-Ray bursters such as MBX 1730-335 and GRO J1744-28 show values of alpha of the order unity ($\leq$1.4, Kunieda et al. 1984, and $\leq$4, Lewin et al. 1976 respectively). Similar reasoning led Chakraborty & Bhattacharyya (2010) and Chakraborty & Bhattacharyya (2011) to question the interpretation of these bursts in

terms of accretion instabilities[3]. We thus conclude that the most probable interpretation for such bursts is in terms of helium ignition in a layer still partly composed by H, as the mass accretion rate is too large to deplete it completely during the phase of *persistent* emission. This conclusion is furthermore supported by the fact that, as stated by Cumming & Bildsten (2000), for accretion rates $\geq 2\times\ 10^{-10}$ M_{sun}/yr (see Bildsten 1998 and references therein), the accumulating hydrogen is thermally stable and burns via the hot CNO cycle of Hoyle & Fowler (1965).

Such a conclusion about the composition of the burst material also fits well into theoretical expectations for local accretion rates $0.1\dot{m}_{Edd} \lesssim \dot{m} \lesssim \dot{m}_{Edd}$ (e.g. Fujimoto et al. 1981). The local accretion rate (defined as the total accretion rate divided by the total surface of the NS) onto the NS in IGR J17480-2446 can be in fact estimated from the persistent X-ray luminosity as $\dot{m} \simeq 0.24(A_{burst}/A_{NS})d_{5.9}^2\dot{m}_{Edd}$, where A_{NS} and A_{burst} are the area of the NS surface and that of the region where the burst is ignited, respectively. Further evaluating the ignition depth from the burst energetics, $y_{ign} = \mathcal{F}_{burst}(1+z)(d/r)^2Q_{nuc}^{-1}$, one obtains that the expected recurrence time, $\Delta t=(y_{ign}/ < \dot{m} >)(1+z)$, fits well the observed values for Q_{nuc}=2.5 Mev/nucl. The values that we found are reported in Tab. 11.2 and plotted together with the observed recurrence times in Fig. 11.7.

Based on the results presented above, combined with the considerations we made according to Sztajno et al. (1986) (see Sec. 11.2.1), we believe that the bursts from IGR J17480-2446, despite their unusual properties, are type-I bursts and that the ambiguity in their classification possibly arises from the presence of a blackbody component in the persistent flux and the relatively low statistics of the spectrum during the bursts following the first one (see. van Paradijs & Lewin 1986).

None of the bursts of IGR J17480-2446 shows photospheric radius expansion. The accurate knowledge of the distance to Terzan 5 makes the estimate of the blackbody radius observed during bursts very appealing (see e.g. Özel et al. 2009). A detailed spectral analysis of the brightest burst indicates a blackbody radius of $R_{app}^{\infty} = (3.3 \pm 0.5)\ d_{5.9}$ km. Such a value can be translated in an effective radius taking into account the spectral hardening induced by Compton scattering in the NS atmosphere and the gravitational redshift, $R = R_{app}^{\infty} f_C^2 (1+z)^{-1}$. For a color temperature of the order of 2 keV like the one observed, the hardening factor f_C was estimated to lie in between 1.33 and 1.84 by Madej et al. (2004), with the larger values appropriate for NS with a smaller gravitational acceleration at the surface. Further taking $1+z = (1-2GM/R_{NS}c^2)^{-1/2} = 1.31$ for 1.4 $M_\odot$ and 10 km radius NS we obtain an estimate of R in between ~ 4.5 and ~ 9 km. The larger value is obtained taking a

[3]Type-II bursts observed from MXB 1730-335 (the Rapid Burster) and the accreting X-ray pulsar GRO J1744-28 (Kouveliotou et al., 1996) are thought to be produced by spasmodic episodes of accretion, probably triggered by thermal instability at the inner edge of the accretion disk.

large hardening correction factor which is predicted to be valid for a relatively large NS. Also an uncertainty on the distance of the source equal to 0.5 kpc was taken into account. The resulting measure indicates a radius compatible with the typical values for a NS. We also measured (see Sec. 11.2.1) the mean apparent radii for selected bursts following the first brightest one (see Tab. 11.2), applying the same corrections that we adopted for the latter. As one can see, also the measures of the radii coming from the fainter bursts confirms that the emitting region during the thermonuclear burst is consistent with the entire NS surface. In addition, this result is in agreement with the fact that the bursts are phase-locked and that there is no variation in the fractional rms associated to the pulse frequency before, during and after the bursts.

Being the NS in IGR J17480-2446 a pulsar, it is worth to ascertain if the magnetic field is able to confine the accreted matter near the magnetic poles. Papitto et al. (2011) estimated an upper limit on the magnetic field of $\sim 2.4 \times 10^{10}$ G considering the lowest flux at which pulsations have been observed. Following the model described in Brown & Bildsten (1998) it results that a similar field can confine the accreted matter near a 5 km magnetic cap up to a column density of $\simeq 3 \times 10^8$ g cm^{-2} (see Cumming & Bildsten 2000). Such a radius is consistent with the vales coming from the spectral analysis (see Sec. 11.2.1). Considering the relation given above, the column depth at which the bursts of IGR J17480-2446 ignite can be estimated to lie within $0.05 \times 10^8 \mathrm{d}_{5.9}^2$ and 0.5×10^8 $\mathrm{d}_{5.9}^2$g cm$^{(-2)}$, where we have used Q_{nuc} = 2.5 Mev /nucleon. It is thus possible that, if the magnetic field is in excess of 10^{10} G, the radius observed during the type I X-ray bursts reflects only a fraction of the NS surface around the polar caps rather than the entire NS radius. Assuming, that the bursts are ignited onto a smaller fraction of the NS surface (A_{burst}) the estimate of the ignition depth grows by a factor $(A_{burst}/A_{NS})^{-2}$, so that values closer to the critical threshold at which helium is thought to start burning unstably on the NS surface, $\geq 6.8 \times 10^8$ (see e.g. Cumming & Bildsten 2000) are obtained as soon as $(A_{burst}/A_{NS}) \leq$0.5. A confinement of the burst ignition region would straightforwardly help in explaining the very short recurrence times observed in between the fainter bursts. However, as noted before, this interpretation would require a magnetic field larger than the one inferred from the observations. For this reason the data coming from IGR J17480-2446 point out the existence of an interpretation problem that cannot be completely solved by the currently accepted model describing accretion and thermonuclear production mechanism.

In a few LMXBs, oscillations with a period of 100-150 seconds (mHz QPO) were discovered and associated to marginally stable nuclear burning on the NS surface (see Heger et al. 2007; Altamirano et al. 2008b). They are observed only in the luminosity range 0.5-1.5 $\times 10^{37}$ erg s^{-1}. The small bursts reported here, with a recurrence time between 300 and 1000 s and associated to a persistent luminosity in the range 2.2–

7.3×10^{37} erg s^{-1} are intermediate between full-fledged type-I X-ray bursts and mHz QPOs, providing an ideal laboratory to study the properties of nuclear burning on the surface of accreting NSs.

The short recurrence time observed in IGR J17480-2446 is particularly interesting not only because it is the shortest observed until now. Type-I X-Ray Bursts with very short recurrence times have been studied before (see eg. Keek et al. 2009, Galloway et al. 2004, Boirin et al. 2007). Even though different ideas have been put forward to explain this rare bursting behavior, the short recurrence time still remains an open issue in the theory of thermonuclear X-Ray bursts. In particular, the extreme behavior of IGR J17480-2446 puts the source in accretion regimes well beyond the ones currently investigated by the theory of thermonuclear X-Ray Bursts (see Narayan & Heyl 2003 for a detailed study on thermonuclear stability of the accreted matter onto NSs). It is worth to notice that before the discovery of IGR J17480-2446, a maximum of 4 consecutive bursts was observed (see Keek et al. 2010). IGR J17480-2446 have shown several tens of Type-I X-Ray bursts with the shortest recurrence time ever observed. It has been argued that short recurrence time could be due to multi-dimensional effects, such as the confinement of accreted material on different parts of the surface, possibly as the result of a magnetic field (e.g., Melatos & Payne 2005; Lamb et al. 2009). However, this scenario seems to be ruled out for the case of IGR J17480-2446 by the radius measures of the emitting region, which suggest that a region comparable with the whole NS surface is burning during the bursts. In addition, the magnetic field of the source appears to be too weak (upper limit $\sim 2.4 \times 10^{10}$) to confine the burning matter in particular regions of the NS surface (see above). Furthermore, magnetic confinement of accreted material would not be a plausible explanation for the short recurrence time of 3.8 min observed for 4U 1705-44 (see Keek et al. 2010), which does not show coherent pulsations, but it may show a very soft spectrum, thus indicating a physically weak interacting magnetic field. Also the idea of a burning layer with an unburned layer on top has been investigated. According to Fujimoto (1988), after the first layer flashes, the second layer could be mixed down to the depth where a thermonuclear runaway occurs thanks to rotational hydrodynamic instabilities (Fujimoto 1988) or by instabilities due to a rotationally induced magnetic field (Piro & Bildsten 2007; Keek et al. 2009). Being a pulsar and showing burst oscillations, IGR J17480-2446 belongs to a small group of sources for which the spin period is known and which show short recurrence time thermonuclear bursts (see Keek et al. 2010, Table 1). All these sources proved to be fast spinning NSs with $\nu_{spin} \geq 500$ Hz. IGR J17480-2446 is the first NS showing short recurrence time bursts *and* a low spin frequency (11 Hz). This fact demonstrates that, contrarily to what has been thought until now, fast rotation is *not* required for the occurrence of multiple-burst events. For this reason, models predicting multiple burst events produced by rotationally induced mixing due to fast spinning frequency should be

revised accordingly (see eg. Fujimoto 1988, Spruit 2002, Keek et al. 2009). Furthermore, the discovery of IGR J17480-2446 and its bursts oscillations demonstrate the fact that a fast spin frequency is also not required for bursts oscillations to be observed. Since the burst characteristics (profile, rise and decay times) and their energetics do not change even in long spin period regimes, we can conclude that the spin frequency of the NS does not affect or only marginally affects the burst production mechanism.

We conclude that thanks to its rare and unique behavior IGR J17480-2446 constitutes an ideal laboratory to investigate in detail the mechanisms that triggers thermonuclear bursts and to test the validity of the theoretical models describing the occurrence of very short recurrence times Type-I X-Ray bursts.

Acknowledgments

This work is supported by the Italian Space Agency, ASI- INAF I/088/06/0 contract for High Energy Astrophysics, as well as by the operating program of Regione Sardegna (European Social Fund 2007-2013), L.R.7/2007, Promotion of scientific research and technological innovation in Sardinia). The research leading to these results has received funding from the European Community's Seventh Framework Programme (FP7/2007-2013) under grant agreement number ITN 215212. "Black Hole Universe".

I'd ike to particularly thank Alessandro and Antonino for their help in drafting this paper.

Table 11.2: Properties of the 107 X-ray bursts from IGR J17480-2446. Columns are: burst number, start time (MJD, referred to the Solar System center of mass), recurrence time (s), rise time (s), decay time τ (s), persistent flux, burst fluence, α, predicted recurrence time (assuming the energy conversion efficiency equal to $\sim$ 2Mev/Nucleon).

No.	Obs.ID	T_{start} (MJD)	T_{rec} (s)	t_{rise} (s)	τ (s)	Persistent flux (10^{-8}erg cm$^{-2}s^{-1}$)	Burst Fluence (10^{-8}erg cm^{-2})	α	T_{rec}^{pred} (s)
1	95437-01-01-00	55482.03	***	5.0 ± 0.1	34 ± 1	0.52 ± 0.01	31.5 ± 0.6	* *	6448 ± 167
2	95437-01-02-00	55483.20	***	7 ± 1	23 ± 3	1.13 ± 0.08	15.7 ± 1.1	* *	1470 ± 147
3	95437-01-02-00	55483.21	1052 ± 1	11 ± 1	17 ± 3	1.17 ± 0.13	13.4 ± 1.5	92 ± 10	1212 ± 193
4	95437-01-02-00	55483.22	1016 ± 2	11 ± 2	20 ± 2	1.13 ± 0.17	12.5 ± 1.9	92 ± 14	1171 ± 252
5	95437-01-02-00	55483.26	***	9 ± 1	21 ± 3	1.10 ± 0.15	12.0 ± 1.7	* *	1154 ± 227
6	95437-01-02-00	55483.27	1043 ± 1	12 ± 1	16 ± 3	1.11 ± 0.10	12.2 ± 1.1	95 ± 8	1163 ± 147
7	95437-01-02-00	55483.28	1090 ± 1	8 ± 1	22 ± 3	1.11 ± 0.08	13.6 ± 1.0	89 ± 7	1297 ± 139
8	95437-01-02-00	55483.33	***	12 ± 1	25 ± 3	1.15 ± 0.08	14.4 ± 1.0	* *	1325 ± 129
9	95437-01-02-00	55483.34	1028 ± 1	10 ± 1	17 ± 2	1.14 ± 0.12	10.2 ± 1.1	115 ± 12	947 ± 142
10	95437-01-02-00	55483.35	1045 ± 2	11 ± 2	17 ± 2	1.14 ± 0.07	12.4 ± 0.8	96 ± 6	1151 ± 103
11	95437-01-02-01	55483.72	***	17 ± 2	16 ± 2	1.17 ± 0.13	10.1 ± 1.1	* *	914 ± 140
12	95437-01-02-01	55483.73	730 ± 3	14 ± 2	21 ± 3	1.15 ± 0.12	10.4 ± 1.1	81 ± 8	957 ± 140
13	95437-01-02-01	55483.74	842 ± 3	13 ± 2	20 ± 2	1.17 ± 0.19	6.8 ± 1.1	146 ± 23	612 ± 137
14	95437-01-02-01	55483.75	721 ± 2	12 ± 2	21 ± 3	1.18 ± 0.17	5.7 ± 0.8	148 ± 21	514 ± 103
15	95437-01-02-01	55483.78	***	14 ± 2	15 ± 3	1.23 ± 1.53	4.3 ± 5.4	* *	371 ± 653
16	95437-01-02-01	55483.79	700 ± 2	14 ± 1	14 ± 2	1.18 ± 0.19	8.4 ± 1.4	99 ± 16	753 ± 175
17	95437-01-02-01	55483.80	702 ± 2	9 ± 1	18 ± 2	1.20 ± 0.16	7.8 ± 1.1	109 ± 15	684 ± 132
18	95437-01-02-01	55483.81	679 ± 2	16 ± 2	13 ± 2	1.22 ± 0.45	3.9 ± 1.4	215 ± 80	335 ± 176
19	95437-01-02-01	55483.85	***	15 ± 2	10 ± 2	1.18 ± 0.35	3.3 ± 1.0	* *	300 ± 126
20	95437-01-02-01	55483.86	671 ± 3	9 ± 2	21 ± 3	1.15 ± 0.18	5.2 ± 0.8	147 ± 24	481 ± 109
21	95437-01-02-01	55483.86	730 ± 3	12 ± 2	19 ± 3	1.21 ± 0.16	7.5 ± 1.0	119 ± 15	652 ± 120
22	95437-01-02-01	55483.87	714 ± 2	15 ± 1	17 ± 2	1.22 ± 0.73	8.4 ± 5.0	103 ± 61	733 ± 618

Continued on next page

Table 11.2 – continued from previous page

No.	Obs.ID	T_{start} (MJD)	T_{rec} (s)	t_{rise} (s)	τ (s)	Persistent flux (10^{-8}erg cm^{-2} s^{-1})	Burst Fluence (10^{-8}erg cm^{-2})	α	T_{rec}^{pred} (s)
23	95437-01-03-00	55484.44	***	4 ± 0	12 ± 2	1.24 ± 0.20	8.0 ± 1.3	* *	680 ± 158
24	95437-01-03-00	55484.44	501 ± 2	12 ± 2	13 ± 3	1.33 ± 0.23	4.4 ± 0.7	153 ± 26	346 ± 83
25	95437-01-03-00	55484.45	521 ± 4	15 ± 3	16 ± 3	1.32 ± 0.16	7.9 ± 1.0	87 ± 11	633 ± 111
26	95437-01-03-00	55484.46	529 ± 5	11 ± 4	17 ± 3	1.26 ± 0.12	6.2 ± 0.6	107 ± 10	522 ± 70
27	95437-01-03-00	55484.46	487 ± 6	17 ± 5	14 ± 4	1.29 ± 0.18	4.0 ± 0.6	159 ± 23	324 ± 66
28	95437-01-03-01	55484.57	***	12 ± 3	19 ± 4	1.36 ± 0.31	4.5 ± 1.0	* *	347 ± 112
29	95437-01-03-01	55484.58	439 ± 4	13 ± 2	20 ± 5	1.32 ± 0.22	4.7 ± 0.8	124 ± 21	374 ± 88
30	95437-01-03-01	55484.59	482 ± 3	9 ± 1	25 ± 4	1.33 ± 0.25	6.2 ± 1.2	104 ± 19	491 ± 129
31	95437-01-03-01	55484.59	483 ± 3	14 ± 2	16 ± 3	1.29 ± 0.14	7.2 ± 0.8	86 ± 9	593 ± 92
32	95437-01-03-01	55484.60	454 ± 3	16 ± 2	13 ± 2	1.29 ± 0.15	5.2 ± 0.6	114 ± 13	423 ± 70
33	95437-01-03-02	55484.63	***	15 ± 3	32 ± 5	1.34 ± 0.31	7.9 ± 1.8	* *	626 ± 206
34	95437-01-03-02	55484.63	472 ± 4	14 ± 2	14 ± 3	1.32 ± 0.22	4.6 ± 0.8	135 ± 22	370 ± 87
35	95437-01-03-02	55484.64	480 ± 3	13 ± 2	11 ± 3	1.34 ± 0.15	5.2 ± 0.6	124 ± 14	411 ± 63
36	95437-01-03-02	55484.65	507 ± 3	8 ± 2	29 ± 20	1.32 ± 0.14	8.3 ± 0.9	80 ± 9	669 ± 101
37	95437-01-03-02	55484.65	474 ± 11	15 ± 11	18 ± 6	1.32 ± 0.26	4.0 ± 0.8	156 ± 31	321 ± 89
38	95437-01-03-02	55484.66	420 ± 14	54 ± 9	113 ± 32	1.32 ± 0.13	8.0 ± 0.8	69 ± 7	645 ± 93
39	95437-01-03-02	55484.66	528 ± 9	19 ± 2	22 ± 4	1.40 ± 0.18	8.2 ± 1.0	90 ± 11	621 ± 110
40	95437-01-03-03	55484.76	***	18 ± 7	10 ± 3	1.53 ± 0.86	6.7 ± 3.7	* *	462 ± 367
41	95437-01-03-03	55484.76	379 ± 8	91 ± 4	92 ± 2	1.51 ± 0.77	5.9 ± 3.0	98 ± 50	411 ± 296
42	95437-01-03-03	55484.77	495 ± 5	13 ± 2	7 ± 2	1.44 ± 0.85	5.8 ± 3.4	122 ± 72	429 ± 357
43	95437-01-03-03	55484.77	463 ± 2	3 ± 1	41 ± 5	1.42 ± 0.19	6.7 ± 0.9	99 ± 13	496 ± 95
44	95437-01-03-03	55484.78	418 ± 5	25 ± 5	74 ± 18	1.39 ± 0.13	7.4 ± 0.7	79 ± 8	560 ± 76
45	95437-01-03-03	55484.78	477 ± 6	10 ± 3	19 ± 5	1.61 ± 0.43	4.6 ± 1.2	168 ± 45	300 ± 113
46	95437-01-03-03	55484.79	454 ± 4	20 ± 3	11 ± 3	1.55 ± 0.21	5.7 ± 0.8	124 ± 17	388 ± 74
47	95437-01-03-03	55484.79	478 ± 4	13 ± 3	19 ± 4	1.43 ± 0.17	6.2 ± 0.8	110 ± 13	460 ± 79
48	95437-01-03-03	55484.82	***	12 ± 4	20 ± 5	1.42 ± 0.41	4.1 ± 1.2	* *	306 ± 123

Continued on next page

Table 11.2 – continued from previous page

No.	Obs.ID	T_{start} (MJD)	T_{rec} (s)	t_{rise} (s)	τ (s)	Persistent flux (10^{-8}erg cm$^{-2}s^{-1}$)	Burst Fluence (10^{-8}erg cm^{-2})	α	T_{rec}^{pred} (s)
49	95437-01-03-03	55484.83	353 ± 11	51 ± 10	12 ± 4	1.53 ± 0.22	4.1 ± 0.6	131 ± 19	286 ± 59
50	95437-01-03-03	55484.83	427 ± 11	39 ± 4	46 ± 9	1.32 ± 0.17	8.0 ± 1.0	71 ± 9	638 ± 118
51	95437-01-03-03	55484.84	415 ± 6	23 ± 3	14 ± 4	1.34 ± 0.18	5.7 ± 0.7	98 ± 13	447 ± 83
52	95437-01-03-03	55484.84	403 ± 4	3 ± 1	82 ± 17	1.30 ± 0.38	3.4 ± 1.0	155 ± 45	275 ± 113
53	95437-01-03-03	55484.85	409 ± 3	19 ± 3	10 ± 2	1.36 ± 0.31	5.4 ± 1.2	103 ± 23	419 ± 134
54	95437-01-03-03	55484.85	432 ± 6	24 ± 5	37 ± 5	1.33 ± 0.17	7.1 ± 0.9	81 ± 11	566 ± 104
55	95437-01-03-03	55484.86	429 ± 6	4 ± 3	48 ± 13	1.33 ± 0.10	6.7 ± 0.5	86 ± 7	531 ± 59
56	95437-01-03-03	55484.89	***	4 ± 4	34 ± 7	1.39 ± 0.08	7.1 ± 0.4	* *	540 ± 46
57	95437-01-03-03	55484.90	808 ± 5	10 ± 3	14 ± 4	1.41 ± 0.37	5.2 ± 1.4	218 ± 58	392 ± 147
58	95437-01-03-03	55484.90	414 ± 4	7 ± 3	45 ± 10	1.37 ± 0.20	5.7 ± 0.8	100 ± 15	440 ± 92
59	95437-01-03-03	55484.91	428 ± 15	54 ± 14	58 ± 15	1.39 ± 0.25	5.0 ± 0.9	120 ± 22	379 ± 98
60	95437-01-03-03	55484.91	427 ± 15	17 ± 4	9 ± 4	1.36 ± 0.28	5.5 ± 1.2	105 ± 22	430 ± 128
61	95437-01-03-03	55484.91	375 ± 5	43 ± 4	18 ± 4	1.35 ± 0.19	5.9 ± 0.9	86 ± 12	464 ± 94
62	95437-01-03-03	55484.92	443 ± 5	10 ± 4	111 ± 18	1.44 ± 0.25	6.5 ± 1.1	98 ± 17	477 ± 119
63	95437-01-04-00	55485.41	***	27 ± 4	9 ± 4	1.41 ± 0.22	4.4 ± 0.7	* *	330 ± 73
64	95437-01-04-00	55485.42	340 ± 4	13 ± 2	14 ± 3	1.39 ± 0.18	4.7 ± 0.6	100 ± 13	358 ± 67
65	95437-01-04-00	55485.42	283 ± 5	32 ± 5	9 ± 3	1.45 ± 0.20	4.6 ± 0.6	88 ± 12	339 ± 66
66	95437-01-04-00	55485.43	356 ± 6	40 ± 3	146 ± 15	1.56 ± 0.26	5.2 ± 0.9	107 ± 18	353 ± 85
67	95437-01-04-00	55485.43	396 ± 4	17 ± 3	10 ± 3	1.63 ± 0.46	4.8 ± 1.3	134 ± 38	312 ± 124
68	95437-01-04-00	55485.44	414 ± 4	12 ± 3	23 ± 5	1.60 ± 0.29	4.8 ± 0.9	137 ± 25	320 ± 82
69	95437-01-04-00	55485.44	362 ± 5	15 ± 4	20 ± 4	1.60 ± 0.33	2.5 ± 0.5	234 ± 48	163 ± 47
70	95437-01-04-00	55485.44	274 ± 7	51 ± 6	17 ± 4	1.66 ± 0.37	1.6 ± 0.4	285 ± 63	102 ± 32
71	95437-01-04-00	55485.45	348 ± 12	50 ± 11	8 ± 3	1.47 ± 0.23	2.0 ± 0.3	253 ± 42	145 ± 33
72	95437-01-04-00	55485.48	***	35 ± 4	516 ± 99	1.57 ± 0.46	2.1 ± 0.6	* *	141 ± 58
73	95437-01-04-00	55485.49	402 ± 5	14 ± 3	18 ± 4	1.70 ± 0.31	5.0 ± 0.9	137 ± 25	310 ± 80
74	95437-01-04-00	55485.49	342 ± 4	18 ± 3	30 ± 7	1.64 ± 0.28	7.3 ± 1.2	77 ± 13	469 ± 114

Continued on next page

Table 11.2 – continued from previous page

No.	Obs.ID	T_{start} (MJD)	T_{rec} (s)	t_{rise} (s)	τ (s)	Persistent flux (10^{-8}erg cm$^{-2}s^{-1}$)	Burst Fluence (10^{-8}erg cm^{-2})	α	T_{rec}^{pred} (s)
75	95437-01-04-00	55485.50	353 ± 4	13 ± 3	19 ± 4	1.70 ± 0.29	4.5 ± 0.8	134 ± 23	279 ± 68
76	95437-01-04-00	55485.50	288 ± 6	20 ± 5	13 ± 3	1.66 ± 0.32	3.5 ± 0.7	138 ± 27	221 ± 60
77	95437-01-04-00	55485.50	335 ± 7	34 ± 5	16 ± 8	1.66 ± 1.21	4.1 ± 3.0	135 ± 98	263 ± 271
78	95437-01-04-00	55485.51	358 ± 6	14 ± 4	27 ± 9	1.68 ± 0.30	5.4 ± 1.0	112 ± 20	338 ± 85
79	95437-01-04-00	55485.51	278 ± 8	32 ± 7	29 ± 9	1.66 ± 0.37	3.8 ± 0.8	121 ± 27	242 ± 76
80	95437-01-04-01	55485.55	***	15 ± 3	43 ± 7	1.65 ± 0.42	4.2 ± 1.1	* *	269 ± 96
81	95437-01-04-01	55485.56	356 ± 3	17 ± 1	111 ± 33	1.67 ± 0.28	4.0 ± 0.7	149 ± 25	252 ± 59
82	95437-01-04-01	55485.56	381 ± 3	27 ± 3	10 ± 5	1.79 ± 0.30	4.3 ± 0.7	161 ± 27	251 ± 60
83	95437-01-04-01	55485.56	320 ± 5	47 ± 4	9 ± 2	1.73 ± 0.89	4.4 ± 2.3	125 ± 65	270 ± 197
84	95437-01-04-01	55485.57	345 ± 8	24 ± 7	42 ± 7	1.64 ± 0.45	3.2 ± 0.9	175 ± 48	208 ± 81
85	95437-01-04-01	55485.57	322 ± 8	20 ± 5	48 ± 17	1.68 ± 0.28	5.3 ± 0.9	102 ± 17	333 ± 78
86	95437-01-04-01	55485.57	299 ± 6	24 ± 5	14 ± 3	1.68 ± 0.26	3.8 ± 0.6	134 ± 21	237 ± 51
87	95437-01-04-01	55485.58	316 ± 5	18 ± 3	33 ± 12	1.65 ± 0.40	5.2 ± 1.2	101 ± 24	331 ± 113
88	95437-01-04-01	55485.61	***	13 ± 3	32 ± 8	1.64 ± 0.27	4.8 ± 0.6	* *	310 ± 52
89	95437-01-04-01	55485.61	287 ± 5	39 ± 4	32 ± 10	1.81 ± 0.37	3.7 ± 0.8	141 ± 29	216 ± 63
90	95437-01-04-01	55485.61	302 ± 7	28 ± 6	92 ± 24	1.72 ± 0.31	8.0 ± 1.4	65 ± 12	494 ± 124
91	95437-01-04-01	55485.62	347 ± 6	17 ± 3	16 ± 4	1.85 ± 0.42	4.4 ± 1.0	147 ± 33	249 ± 79
92	95437-01-04-01	55485.62	321 ± 4	22 ± 2	19 ± 4	1.74 ± 0.19	6.0 ± 0.7	92 ± 10	368 ± 57
93	95437-01-04-01	55485.63	303 ± 5	18 ± 4	48 ± 15	1.74 ± 0.35	5.1 ± 1.0	102 ± 21	313 ± 89
94	95437-01-04-01	55485.63	356 ± 6	17 ± 5	36 ± 7	1.81 ± 0.25	6.3 ± 0.9	102 ± 14	369 ± 72
95	95437-01-04-01	55485.63	319 ± 6	23 ± 3	19 ± 4	1.74 ± 0.29	7.1 ± 1.2	78 ± 13	432 ± 101
96	95437-01-04-01	55485.64	271 ± 6	50 ± 5	20 ± 5	1.72 ± 0.29	6.8 ± 1.1	69 ± 12	418 ± 100
97	95437-01-04-01	55485.64	332 ± 8	24 ± 5	19 ± 5	1.75 ± 0.37	4.0 ± 0.9	145 ± 31	242 ± 73
98	95437-01-04-01	55485.64	323 ± 6	17 ± 3	9 ± 3	1.81 ± 0.45	4.7 ± 1.2	126 ± 31	273 ± 96
99	95437-01-04-01	55485.68	***	40 ± 6	15 ± 3	1.78 ± 0.39	4.4 ± 1.0	* *	262 ± 81
100	95437-01-04-01	55485.68	373 ± 6	5 ± 1	41 ± 9	1.69 ± 0.26	7.9 ± 1.2	79 ± 12	497 ± 108

Continued on next page

Table 11.2 – continued from previous page

No.	Obs.ID	T_{start} (MJD)	T_{rec} (s)	t_{rise} (s)	τ (s)	Persistent flux (10^{-8}erg cm$^{-2}s^{-1}$)	Burst Fluence (10^{-8}erg cm^{-2})	α	T_{rec}^{pred} (s)
101	95437-01-04-01	55485.68	383 ± 3	14 ± 3	42 ± 7	1.74 ± 0.34	6.5 ± 1.3	102 ± 20	397 ± 111
102	95437-01-04-01	55485.69	263 ± 22	110 ± 22	45 ± 20	1.81 ± 0.27	8.9 ± 1.3	54 ± 9	519 ± 111
103	95437-01-04-01	55485.69	379 ± 22	24 ± 5	26 ± 9	1.68 ± 0.52	3.2 ± 1.0	200 ± 63	201 ± 87
104	95437-01-04-01	55485.70	231 ± 38	95 ± 37	32 ± 9	1.74 ± 0.52	3.6 ± 1.1	111 ± 38	221 ± 94
105	95437-01-04-01	55485.70	337 ± 38	81 ± 8	34 ± 8	1.85 ± 0.82	3.3 ± 1.5	189 ± 87	189 ± 119
106	95437-01-04-01	55485.70	436 ± 8	15 ± 3	17 ± 3	1.86 ± 0.37	5.0 ± 1.0	161 ± 32	287 ± 80
107	95437-01-04-01	55485.71	386 ± 4	7 ± 3	37 ± 6	1.80 ± 0.20	6.0 ± 0.7	116 ± 13	353 ± 55

Bibliography

Agrawal P. C., 2006, Advances in Space Research, 38, 2989

Alpar M. A., Cheng A. F., Ruderman M. A., Shaham J., 1982, Nature, 300, 728

Altamirano D., Casella P., Patruno A., Wijnands R., van der Klis M., 2008a, ApJ, 674, L45

Altamirano D., Casella P., Patruno A., Wijnands R., van der Klis M., 2008b, ApJ, 674, L45

Altamirano D., Watts A., 2010, The Astronomer's Telegram, 2932, 1

Altamirano D., Watts A., Linares M., Markwardt C. B., Strohmayer T., Patruno A., 2010, MNRAS, pp 1363–+

Arnaud K. A., 1996, in G. H. Jacoby & J. Barnes ed., Astronomical Data Analysis Software and Systems V Vol. 101 of Astronomical Society of the Pacific Conference Series, XSPEC: The First Ten Years. pp 17–+

Balbus S. A., Hawley J. F., 1991, ApJ, 376, 214

Belloni T., 2005, Interacting Binaries: Accretion, Evolution, and Outcomes, AIP Conference Proceedings, Volume 797, pp. 197-204, 797, 197

Belloni T., Colombo A. P., Homan J., Campana S., van der Klis M., 2002, A&A, 390, 199

Belloni T., Hasinger G., 1990, A&A, 230, 103

Belloni T., Homan J., Casella P., van der Klis M., Nespoli E., Lewin W. H. G., Miller J. M., Méndez M., 2005, A&A, 440, 207

Belloni T., Homan J., Yamaoka K., Swank J., 2008, The Astronomer's Telegram, 1804, 1

Belloni T., Méndez M., Sánchez-Fernández C., 2001, A&A, 372, 551

Belloni T., Motta S., Muñoz-Darias T., 2010, The Astronomer's Telegram, 2927, 1

Belloni T., Muñoz-Darias T., Kuulkers E., 2010, The Astronomer's Telegram, 2926, 1

Belloni T., Parolin I., Del Santo M., Homan J., Casella P., Fender R. P., Lewin W. H. G., Méndez M., Miller J. M., van der Klis M., 2006, MNRAS, 367, 1113

Belloni T., Psaltis D., van der Klis M., 2002, ApJ, 572, 392

Belloni T., van der Klis M., Lewin W. H. G., van Paradijs J., Dotani T., Mitsuda K., Miyamoto S., 1997, A&A, 322, 857

Belloni T. M., 2010, Lecture Notes in Physics, Springer-Verlag Berlin Heidelberg, Volume 794, p. 53. ISBN 978-3-540-76936-1., 794, 53
Belloni T. M., Motta S. E., Muñoz-Darias T., 2011, ArXiv e-prints
Bhattacharya D., van den Heuvel E. P. J., 1991, Phys. Rep., 203, 1
Bildsten L., 1998, ApJ, 501, L89+
Boirin L., Keek L., Méndez M., Cumming A., in't Zand J. J. M., Cottam J., Paerels F., Lewin W. H. G., 2007, A&A, 465, 559
Bradt H. V., Rothschild R. E., Swank J. H., 1993, A&A S.S., 97, 355
Brocksopp C., Bandyopadhyay R. M., Fender R. P., 2004, New Astronomy, 9, 249
Brocksopp C., Corbel S., Fender R. P., Rupen M., Sault R., Tingay S. J., Hannikainen D., O'Brien K., 2005, MNRAS, 356, 125
Brocksopp C., Corbel S., Tzioumis T., Fender R., 2009, The Astronomer's Telegram, 2278, 1
Brocksopp C., Fender R. P., McCollough M., Pooley G. G., Rupen M. P., Hjellming R. M., de la Force C. J., Spencer R. E., Muxlow T. W. B., Garrington S. T., Trushkin S., 2002, MNRAS, 331, 765
Brown E. F., Bildsten L., 1998, ApJ, 496, 915
Caballero-García M. D., Miller J. M., Trigo M. D., Kuulkers E., Fabian A. C., Mas-Hesse J. M., Steeghs D., van der Klis M., 2009, ApJ, 692, 1339
Cabanac C., Fender R. P., Dunn R. J. H., Körding E. G., 2009, MNRAS, 396, 1415
Cadolle Bel M., Ribó M., Rodriguez J., Chaty S., Corbel S., Goldwurm A., Frontera F., Farinelli R., D'Avanzo P., Tarana A., Ubertini P., Laurent P., Goldoni P., Mirabel I. F., 2007, ApJ, 659, 549
Campana S., Stella L., Kennea J. A., 2008, ApJ, 684, L99
Cantrell A. G., Bailyn C. D., Orosz J. A., McClintock J. E., Remillard R. A., Froning C. S., Neilsen J., Gelino D. M., Gou L., 2010, ApJ, 710, 1127
Capitanio F., Belloni T., Del Santo M., Ubertini P., 2009, MNRAS, 398, 1194
Casares J., Bonifacio P., González Hernández J. I., Molaro P., Zoccali M., 2007, A&A, 470, 1033
Casares J., Charles P. A., Naylor T., 1992, Nature, 355, 614
Casella P., Altamirano D., Patruno A., Wijnands R., van der Klis M., 2008, ApJ, 674, L41
Casella P., Belloni T., Homan J., Stella L., 2004, A&A, 426, 587
Casella P., Belloni T., Stella L., 2005, ApJ, 629, 403
Casella P., Maccarone T. J., O'Brien K., Fender R. P., Russell D. M., van der Klis M., Pe'Er A., Maitra D., Altamirano D., Belloni T., Kanbach G., Klein-Wolt M., Mason E., Soleri P., Stefanescu A., Wiersema K., Wijnands R., 2010, MNRAS, 404, L21
Chakrabarty D., Morgan E. H., Muno M. P., Galloway D. K., Wijnands R., van der Klis M., Markwardt C. B., 2003, Nature, 424, 42

Chakraborty M., Bhattacharyya S., 2010, The Astronomer's Telegram, 3044, 1
Chakraborty M., Bhattacharyya S., 2011, ApJ, 730, L23+
Churazov E., Gilfanov M., Revnivtsev M., 2001, MNRAS, 321, 759
Corbel S., Fender R. P., Tzioumis A. K., Tomsick J. A., Orosz J. A., Miller J. M., Wijnands R., Kaaret P., 2002, Science, 298, 196
Corbel S., Kaaret P., Fender R. P., Tzioumis A. K., Tomsick J. A., Orosz J. A., 2005, ApJ, 632, 504
Coriat M., Corbel S., Prat L., Miller-Jones J. C. A., Cseh D., Tzioumis A. K., Brocksopp C., Rodriguez J., Fender R. P., Sivakoff G. R., 2011, MNRAS, 414, 677
Corral-Santana J. M., Casares J., Shahbaz T., Zurita C., Martínez-Pais I. G., Rodríguez-Gil P., 2011, MNRAS, 413, L15
Cumming A., Bildsten L., 2000, ApJ, 544, 453
D'Avanzo P., Goldoni P., Patruno A., Casella P., Campana S., Russell D. M., Belloni T. M., 2010, The Astronomer's Telegram, 2900, 1
de Ugarte Postigo A., Flores H., Wiersema K., Thoene C. C., Fynbo J. P. U., Goldoni P., 2010, GRB Coordinates Network, Circular Service, 11307, 1 (2010), 1307, 1
de Ugarte Postigo A., Lundrgren A., Wyrowski F., Thoene C. C., Castro-Tirado A. J., Gorosabel J., Jelinek M., 2010, GRB Coordinates Network, Circular Service, 11304, 1 (2010), 1304, 1
Debnath D., Chakrabarti S. K., Nandi A., Mandal S., 2009, ArXiv e-prints
Del Santo M., Belloni T. M., Homan J., Bazzano A., Casella P., Fender R. P., Gallo E., Gehrels N., Lewin W. H. G., Méndez M., van der Klis M., 2009, MNRAS, 392, 992
Del Santo M., Malzac J., Jourdain E., Belloni T., Ubertini P., 2008, MNRAS, 390, 227
Dhillon V. S., Marsh T. R., Stevenson M. J., Atkinson D. C., Kerry P., Peacocke P. T., Vick A. J. A., Beard S. M., Ives D. J., Lunney D. W., McLay S. A., Tierney C. J., Kelly J., Littlefair S. P., Nicholson R., Pashley R., Harlaftis E. T., O'Brien K., 2007, MNRAS, 378, 825
Done C., Gierlinski M., Kubota A., 2007, A&A, 15, 1
Done C., Kubota A., 2006, MNRAS, 371, 1216
Dunn R. J. H., Fender R. P., Körding E. G., Belloni T., Cabanac C., 2010, MNRAS, 403, 61
Durant M., Gandhi P., Shahbaz T., Fabian A. P., Miller J., Dhillon V. S., Marsh T. R., 2008, ApJ, 682, L45
Durant M., Gandhi P., Shahbaz T., Peralta H. H., Dhillon V. S., 2009, MNRAS, 392, 309
Elvis M., Page C. G., Pounds K. A., Ricketts M. J., Turner M. J. L., 1975, Nature, 257, 656
Esin A. A., McClintock J. E., Narayan R., 1997, ApJ, 489, 865

Falanga M., Poutanen J., Bonning E. W., Kuiper L., Bonnet-Bidaud J. M., Goldwurm A., Hermsen W., Stella L., 2007, A&A, 464, 1069
Fender R., 2006, Compact stellar X-ray sources, pp 381–419
Fender R. P., Belloni T. M., Gallo E., 2004, MNRAS, 355, 1105
Fender R. P., Gallo E., Jonker P. G., 2003, MNRAS, 343, L99
Fender R. P., Gallo E., Russell D., 2010, MNRAS, 406, 1425
Fender R. P., Homan J., Belloni T. M., 2009, MNRAS, 396, 1370
Feroci M., LOFT Consortium t., 2011, ArXiv e-prints
Fragile P. C., Blaes O. M., Anninos P., Salmonson J. D., 2007, ApJ, 668, 417
Frontera F., Zdziarski A. A., Amati L., Mikołajewska J., Belloni T., Del Sordo S., Haardt F., Kuulkers E., Masetti N., Orlandini M., Palazzi E., Parmar A. N., Remillard R. A., Santangelo A., Stella L., 2001, ApJ, 561, 1006
Fujimoto M. Y., 1988, A&A, 198, 163
Fujimoto M. Y., Hanawa T., Miyaji S., 1981, ApJ, 247, 267
Gallo E., 2010, in T. Belloni ed., Lecture Notes in Physics, Berlin Springer Verlag Vol. 794 of Lecture Notes in Physics, Berlin Springer Verlag, Radio Emission and Jets from Microquasars. pp 85–+
Gallo E., Fender R. P., Miller-Jones J. C. A., Merloni A., Jonker P. G., Heinz S., Maccarone T. J., van der Klis M., 2006, MNRAS, 370, 1351
Gallo E., Fender R. P., Pooley G. G., 2003, MNRAS, 344, 60
Galloway D. K., Cumming A., 2006, ApJ, 652, 559
Galloway D. K., Cumming A., Kuulkers E., Bildsten L., Chakrabarty D., Rothschild R. E., 2004, ApJ, 601, 466
Galloway D. K., in't Zand J. J. M., 2010, The Astronomer's Telegram, 3000, 1
Galloway D. K., Lin J., Chakrabarty D., Hartman J. M., 2010, ApJ, 711, L148
Galloway D. K., Morgan E. H., Krauss M. I., Kaaret P., Chakrabarty D., 2007, ApJ, 654, L73
Galloway D. K., Muno M. P., Hartman J. M., Psaltis D., Chakrabarty D., 2008, ApJS, 179, 360
Garcia M. R., McClintock J. E., Narayan R., Callanan P. J., 1998, ASP Conference Series, 137, 506
George I. M., Fabian A. C., 1991, MNRAS, 249, 352
Giacconi R., Gursky H., Paolini F. R., Rossi B. B., 1962, Physical Review Letters, 9, 439
Gierliński M., Newton J., 2006, MNRAS, 370, 837
Gierliński M., Zdziarski A. A., 2005, MNRAS, 363, 1349
Gilfanov M., 2010, The Jet Paradigm, Lecture Notes in Physics, Springer-Verlag Berlin Heidelberg, Volume 794, p. 17. ISBN 978-3-540-76936-1., 794, 17
Gleissner T., Wilms J., Pottschmidt K., Uttley P., Nowak M. A., Staubert R., 2004, A&A, 414, 1091

Grove J. E., Johnson W. N., Kroeger R. A., McNaron-Brown K., Skibo J. G., Phlips B. F., 1998, ApJ, 500, 899
Gruber D. E., Blanco P. R., Heindl W. A., Pelling M. R., Rothschild R. E., Hink P. L., 1996, A&A S.S., 120, C641+
Hameury J.-M., Barret D., Lasota J.-P., McClintock J. E., Menou K., Motch C., Olive J.-F., Webb N., 2003, A&A, 399, 631
Hannikainen D., Campbell-Wilson D., Hunstead R., McIntyre V., Lovell J., Reynolds J., Tzioumis T., Wu K., 2001, Astrophysics and Space Science Supplement, 276, 45
Hasinger G., van der Klis M., 1989, A&A, 225, 79
Haswell C. A., King A. R., 2001, X-ray Astronomy: Stellar Endpoints, AGN, and the Diffuse X-ray Background, 599, 642
Heger A., Cumming A., Woosley S. E., 2007, ApJ, 665, 1311
Herrero A., Kudritzki R. P., Gabler R., Vilchez J. M., Gabler A., 1995, A&A, 297, 556
Hessels J. W. T., Ransom S. M., Stairs I. H., Freire P. C. C., Kaspi V. M., Camilo F., 2006, Science, 311, 1901
Hiemstra B., Soleri P., Méndez M., Belloni T., Mostafa R., Wijnands R., 2009, MNRAS, 394, 2080
Homan J., Belloni T., 2005, Ap&SS, 300, 107
Homan J., Buxton M., Markoff S., Bailyn C. D., Nespoli E., Belloni T., 2005, ApJ, 624, 295
Homan J., Miller J. M., Wijnands R., van der Klis M., Belloni T., Steeghs D., Lewin W. H. G., 2005, ApJ, 623, 383
Homan J., van der Klis M., Jonker P. G., Wijnands R., Kuulkers E., Méndez M., Lewin W. H. G., 2002, ApJ, 568, 878
Homan J., van der Klis M., Wijnands R., Belloni T., Fender R., Klein-Wolt M., Casella P., Méndez M., Gallo E., Lewin W. H. G., Gehrels N., 2007, ApJ, 656, 420
Homan J., Wijnands R., van der Klis M., Belloni T., van Paradijs J., Klein-Wolt M., Fender R., Méndez M., 2001, ApJS, 132, 377
Houck J. C., Denicola L. A., 2000, in N. Manset, C. Veillet, & D. Crabtree ed., Astronomical Data Analysis Software and Systems IX Vol. 216 of Astronomical Society of the Pacific Conference Series, ISIS: An Interactive Spectral Interpretation System for High Resolution X-Ray Spectroscopy. pp 591–+
Hoyle F., Fowler W. A., 1965, pp 17–+
Hynes R. I., Steeghs D., Casares J., Charles P. A., O'Brien K., 2003, ApJ, 583, L95
Ingram A., Done C., 2010, MNRAS, 405, 2447
Ingram A., Done C., 2011, MNRAS, 415, 2323
Ingram A., Done C., Fragile P. C., 2009, MNRAS, 397, L101

Jahoda K., Markwardt C. B., Radeva Y., Rots A. H., Stark M. J., Swank J. H., Strohmayer T. E., Zhang W., 2006, ApJS, 163, 401
Jelinek M., Zurita C., Visus M., Papics P., Kubanek P., Sabau-Graziati L., de Ugarte Postigo A., Cunniffe R., Gorosabel J., Castro-Tirado A. J., 2010, GRB Coordinates Network, Circular Service, 11301, 1 (2010), 1301, 1
Joinet A., Kalemci E., Senziani F., 2008, ApJ, 679, 655
Kaaret P., Morgan E. H., Vanderspek R., Tomsick J. A., 2006, ApJ, 638, 963
Kalamkar M., Homan J., Altamirano D., van der Klis M., Casella P., Linares M., 2011, ApJ, 731, L2+
Kalemci E., Tomsick J. A., Buxton M. M., Rothschild R. E., Pottschmidt K., Corbel S., Brocksopp C., Kaaret P., 2005, ApJ, 622, 508
Kalemci E., Tomsick J. A., Rothschild R. E., Pottschmidt K., Corbel S., Kaaret P., 2006, ApJ, 639, 340
Kalemci E., Tomsick J. A., Rothschild R. E., Pottschmidt K., Kaaret P., 2004, ApJ, 603, 231
Kaluzienski L. J., Holt S. S., 1977, IAU Circ., 3099, 1
Kanbach G., Straubmeier C., Spruit H. C., Belloni T., 2001, Nature, 414, 180
Kazanas D., Hua X., Titarchuk L., 1997, ApJ, 480, 735
Keek L., Galloway D. K., in't Zand J. J. M., Heger A., 2010, ApJ, 718, 292
Keek L., Langer N., in't Zand J. J. M., 2009, A&A, 502, 871
Kennea J. A., Krimm H., Mangano V., Curran P., Romano P., Evans P., Burrows D. N., 2010, The Astronomer's Telegram, 2877, 1
King A. R., Cannizzo J. K., 1998, ApJ, 499, 348
Kong A. K. H., Kuulkers E., Charles P. A., Homer L., 2000, MNRAS, 312, L49
Körding E., Falcke H., 2004, A&A, 414, 795
Kouveliotou C., van Paradijs J., Fishman G. J., Briggs M. S., Kommers J., Harmon B. A., Meegan C. A., Lewin W. H. G., 1996, Nature, 379, 799
Krimm H. A., Barbier L., Barthelmy S. D., Cummings J., Fenimore E., Gehrels N., Markwardt C., Palmer D., Parsons A., Sakamoto T., Sato G., Stamatikos M., Tueller J., 2006, The Astronomer's Telegram, 968, 1
Krimm H. A., Barthelmy S. D., Baumgartner W., Cummings J., Fenimore E., Gehrels N., Markwardt C. B., Palmer D., Parsons A., Sakamoto T., Skinner G., Tueller J., Ukwatta T., 2009, The Astronomer's Telegram, 2058, 1
Krimm H. A., Soleri P., Barthelmy S. D., Baumgartner W., Cummings J., Fenimore E., Gehrels N., Markwardt C. B., Palmer D., Parsons A., Sakamoto T., Sato G., Skinner G., Stamatikos M., Tueller J., 2008, The Astronomer's Telegram, 1599, 1
Kunieda H., Tawara Y., Hayakawa S., Nagase F., Inoue H., Kawai N., Makino F., Makishima K., Matsuoka M., Murakami T., Oda M., Ogawara Y., Ohashi T., Waki I., 1984, PASJ, 36, 807
Kuulkers E., Ibarra A., Pollock A., 2010, The Astronomer's Telegram, 2912, 1

Kuulkers E., Kouveliotou C., van der Horst A. J., 2010, The Astronomer's Telegram, 2887, 1
Lachowicz P., Done C., 2010, A&A, 515, A65+
Lamb F. K., Boutloukos S., Van Wassenhove S., Chamberlain R. T., Lo K. H., Clare A., Yu W., Miller M. C., 2009, ApJ, 706, 417
Lanzoni B., Ferraro F. R., Dalessandro E., Mucciarelli A., Beccari G., Miocchi P., Bellazzini M., Rich R. M., Origlia L., Valenti E., Rood R. T., Ransom S. M., 2010, ApJ, 717, 653
Laurent P., Titarchuk L., 2001, ApJ, 562, L67
Leahy D. A., Elsner R. F., Weisskopf M. C., 1983, ApJ, 272, 256
Levine A. M., Bradt H., Cui W., Jernigan J. G., Morgan E. H., Remillard R., Shirey R. E., Smith D. A., 1996, ApJ, 469, L33+
Lewin W. H. G., Doty J., Clark G. W., Rappaport S. A., Bradt H. V. D., Doxsey R., Hearn D. R., Hoffman J. A., Jernigan J. G., Li F. K., Mayer W., McClintock J., Primini F., Richardson J., 1976, ApJ, 207, L95
Lin D., Altamirano D., Homan J., Remillard R. A., Wijnands R., Belloni T., 2009, ApJ, 699, 60
Linares M., van der Klis M., Wijnands R., 2007, ApJ, 660, 595
Livio M., Ogilvie G. I., Pringle J. E., 1999, ApJ, 512, 100
Maccarone T. J., 2005, MNRAS, 360, L68
Maccarone T. J., Coppi P. S., 2003, MNRAS, 338, 189
Madej J., Joss P. C., Różańska A., 2004, ApJ, 602, 904
Magdziarz P., Zdziarski A. A., 1995, MNRAS, 273, 837
Malzac J., Merloni A., Fabian A. C., 2004, MNRAS, 351, 253
Mangano V., Hoversten E. A., Markwardt C. B., Sbarufatti B., Starling R. L. C., Ukwatta T. N., 2010, GRB Coordinates Network, Circular Service, 11296, 1 (2010), 1296, 1
Maraschi L., Cavaliere A., 1977, in K. A. van der Hucht ed., X-ray Binaries and Compact Objects X-ray bursts of nuclear origin?. pp 127–128
Markert T. H., Canizares C. R., Clark G. W., Lewin W. H. G., Schnopper H. W., Sprott G. F., 1973, ApJ, 184, L67+
Markoff S., 2010, in T. Belloni ed., Lecture Notes in Physics, Berlin Springer Verlag Vol. 794 of Lecture Notes in Physics, Berlin Springer Verlag, From Multiwavelength to Mass Scaling: Accretion and Ejection in Microquasars and AGN. pp 143–+
Markoff S., Falcke H., Fender R., 2001, A&A, 372, L25
Markoff S., Falcke H., Fender R., 2002, APS Meeting Abstracts, pp 17105–+
Markwardt C. B., Barthelmy S. D., Evans P. A., Swank J. H., 2009, The Astronomer's Telegram, 2261, 1
Markwardt C. B., Swank J. H., 2003, IAU Circ., 8144, 1

Markwardt C. B., Swank J. H., Barthelmy S. D., Baumgartner W. H., Burrows D. N., Evans P. A., Holland S. T., Hoversten E. A., Page K. L., 2009, The Astronomer's Telegram, 2258, 1

Marshall F., 2010, GRB Coordinates Network, Circular Service, 11298, 1 (2010), 1298, 1

McClintock J. E., 1986, in K. O. Mason, M. G. Watson, & N. E. White ed., The Physics of Accretion onto Compact Objects Vol. 266 of Lecture Notes in Physics, Berlin Springer Verlag, Black Holes in X-ray Binaries. pp 211–+

McClintock J. E., Haswell C. A., Garcia M. R., Drake J. J., Hynes R. I., Marshall H. L., Muno M. P., Chaty S., Garnavich P. M., Groot P. J., Lewin W. H. G., Mauche C. W., Miller J. M., Pooley G. G., Shrader C. R., Vrtilek S. D., 2001, ApJ, 555, 477

McClintock J. E., Narayan R., Davis S. W., Gou L., Kulkarni A., Orosz J. A., Penna R. F., Remillard R. A., Steiner J. F., 2011, Classical and Quantum Gravity, 28, 114009

McClintock J. E., Remillard R. A., 2006, pp 157–213

McClintock J. E., Remillard R. A., Rupen M. P., Torres M. A. P., Steeghs D., Levine A. M., Orosz J. A., 2009, ApJ, 698, 1398

Meier D. L., 2001, ApJ, 548, L9

Melatos A., Payne D. J. B., 2005, ApJ, 623, 1044

Mendez M., van der Klis M., 1997, ApJ, 479, 926

Merloni A., Fabian A. C., Ross R. R., 2000, MNRAS, 313, 193

Migliari S., Tomsick J. A., Markoff S., Kalemci E., Bailyn C. D., Buxton M., Corbel S., Fender R. P., Kaaret P., 2007, ApJ, 670, 610

Miller J. M., Fabian A. C., in't Zand J. J. M., Reynolds C. S., Wijnands R., Nowak M. A., Lewin W. H. G., 2002, ApJ, 577, L15

Miller J. M., Fabian A. C., Reynolds C. S., Nowak M. A., Homan J., Freyberg M. J., Ehle M., Belloni T., Wijnands R., van der Klis M., Charles P. A., Lewin W. H. G., 2004, ApJ, 606, L131

Miller J. M., Homan J., Steeghs D., Rupen M., Hunstead R. W., Wijnands R., Charles P. A., Fabian A. C., 2006, ApJ, 653, 525

Miller J. M., Raymond J., Homan J., Fabian A. C., Steeghs D., Wijnands R., Rupen M., Charles P., van der Klis M., Lewin W. H. G., 2006, ApJ, 646, 394

Miller-Jones J. C. A., Sivakoff G. R., Migliari S., Koerding E., Rupen M. P., Remillard R. A., Dhawan V., Russell D. M., Maitra D., Fender R. P., Markoff S., Heinz S., Sarazin C. L., Maccarone T. J., 2009, The Astronomer's Telegram, 2062, 1

Mitsuda K., Inoue H., Koyama K., Makishima K., Matsuoka M., Ogawara Y., Suzuki K., Tanaka Y., Shibazaki N., Hirano T., 1984, PASJ, 36, 741

Miyakawa T., Yamaoka K., Homan J., Saito K., Dotani T., Yoshida A., Inoue H., 2008, PASJ, 60, 637

Miyamoto S., Iga S., Kitamoto S., Kamado Y., 1993, ApJ, 403, L39
Miyamoto S., Kimura K., Kitamoto S., Dotani T., Ebisawa K., 1991, ApJ, 383, 784
Miyamoto S., Kitamoto S., 1991, ApJ, 374, 741
Miyamoto S., Kitamoto S., Iga S., Negoro H., Terada K., 1992, ApJ, 391, L21
Morgan E. H., Remillard R. A., Greiner J., 1997, ApJ, 482, 993
Motta S., Belloni T., Homan J., 2009, MNRAS, 400, 1603
Motta S., Belloni T. M., 2010, 1248, 185
Motta S., Muñoz-Darias T., Casella P., Belloni T., Homan J., 2011, ArXiv e-prints
Muñoz-Darias T., Casares J., Martínez-Pais I. G., 2008, MNRAS, 385, 2205
Muñoz-Darias T., Martínez-Pais I. G., Casares J., Dhillon V. S., Marsh T. R., Cornelisse R., Steeghs D., Charles P. A., 2007, MNRAS, 379, 1637
Muñoz-Darias T., Motta S., Belloni T. M., 2011, MNRAS, 410, 679
Muñoz-Darias T., Motta S., Pawar D., Belloni T. M., Campana S., Bhattacharya D., 2010a, MNRAS, 404, L94
Muñoz-Darias T., Motta S., Pawar D., Belloni T. M., Campana S., Bhattacharya D., 2010b, MNRAS, 404, L94
Muñoz-Darias T., Motta S., Stiele H., Belloni T. M., 2011, MNRAS, 415, 292
Muno M. P., Chakrabarty D., Galloway D. K., Psaltis D., 2002, ApJ, 580, 1048
Narayan R., Heyl J. S., 2003, ApJ, 599, 419
Negoro H., Yamaoka K., Nakahira S., Kawasaki K., Ueno S., Tomida H., Kohama M., Ishikawa M., Mihara T., Nakagawa Y. E., Sugizaki M., Serino M., Yamamoto T., Sootome T., Matsuoka M., Kawai N., Morii M., Sugimori K., Usui R., 2010, The Astronomer's Telegram, 2873, 1
Neilsen J., Lee J. C., 2009, Nature, 458, 481
Nespoli E., Belloni T., Homan J., Miller J. M., Lewin W. H. G., Méndez M., van der Klis M., 2003, A&A, 412, 235
Nowak M. A., Vaughan B. A., 1996, MNRAS, 280, 227
Nowak M. A., Vaughan B. A., Wilms J., Dove J. B., Begelman M. C., 1999, ApJ, 510, 874
Nowak M. A., Wilms J., Dove J. B., 2002, MNRAS, 332, 856
Nowak M. A., Wilms J., Heinz S., Pooley G., Pottschmidt K., Corbel S., 2005, ApJ, 626, 1006
Nowak M. A., Wilms J., Vaughan B. A., Dove J. B., Begelman M. C., 1999, ApJ, 515, 726
Orosz J. A., McClintock J. E., Narayan R., Bailyn C. D., Hartman J. D., Macri L., Liu J., Pietsch W., Remillard R. A., Shporer A., Mazeh T., 2007, Nature, 449, 872
Orosz J. A., Steiner J. F., McClintock J. E., Torres M. A. P., Remillard R. A., Bailyn C. D., Miller J. M., 2011, ApJ, 730, 75
Özel F., Güver T., Psaltis D., 2009, ApJ, 693, 1775
Özel F., Psaltis D., Narayan R., McClintock J. E., 2010, ApJ, 725, 1918

Palmer D. M., Barthelmey S. D., Cummings J. R., Gehrels N., Krimm H. A., Markwardt C. B., Sakamoto T., Tueller J., 2005, The Astronomer's Telegram, 546, 1
Papitto A., D'Aì A., Motta S., Riggio A., Burderi L., di Salvo T., Belloni T., Iaria R., 2011, A&A, 526, L3+
Piro A. L., Bildsten L., 2007, ApJ, 663, 1252
Pooley D., Homan J., Heinke C., 2010, The Astronomer's Telegram, 2974, 1
Pottschmidt K., Wilms J., Nowak M. A., Heindl W. A., Smith D. M., Staubert R., 2000, A&A, 357, L17
Pottschmidt K., Wilms J., Nowak M. A., Pooley G. G., Gleissner T., Heindl W. A., Smith D. M., Remillard R., Staubert R., 2003, A&A, 407, 1039
Poutanen J., Svensson R., 1996, ApJ, 470, 249
Prat L., Rodriguez J., Cadolle Bel M., Kuulkers E., Hanke M., Tomsick J., Corbel S., Coriat M., Wilms J., Goldwurm A., 2009, A&A, 494, L21
Psaltis D., Belloni T., van der Klis M., 1999, ApJ, 520, 262
Ramadevi M. C., Seetha S., 2007, MNRAS, 378, 182
Rao F., Belloni T., Stella L., Zhang S. N., Li T., 2010, ApJ, 714, 1065
Reig P., Belloni T., van der Klis M., 2003, A&A, 412, 229
Reis R. C., Fabian A. C., Miller J. M., 2009, ArXiv e-prints
Remillard R., McClintock J., 2006, Annual Reviews, 44, 49
Remillard R. A., Muno M. P., McClintock J. E., Orosz J. A., 2002, ApJ, 580, 1030
Revnivtsev M., Churazov E., Gilfanov M., Sunyaev R., 2001, A&A, 372, 138
Rodriguez J., Fuchs Y., Hannikainen D., Vilhu O., Shaw S., Belloni T., Corbel S., 2004, 552, 377
Rodriguez J., Shaw S. E., Hannikainen D. C., Belloni T., Corbel S., Cadolle Bel M., Chenevez J., Prat L., Kretschmar P., Lehto H. J., Mirabel I. F., Paizis A., Pooley G., Tagger M., Varnière P., Cabanac C., Vilhu O., 2008, ApJ, 675, 1449
Romani R. W., 1998, in American Astronomical Society Meeting Abstracts Vol. 30 of Bulletin of the American Astronomical Society, Compact and other Faint Object Spectroscopy with the Hobby-Eberly Telescope. pp 1285–+
Rothschild R. E., Heindl W. A., 1998, in American Astronomical Society Meeting Abstracts Vol. 30 of Bulletin of the American Astronomical Society, Hard X-ray Variability of GRO J1655-40 Observed by RXTE. pp 112.01–+
Russell D. M., Fender R. P., Hynes R. I., Brocksopp C., Homan J., Jonker P. G., Buxton M. M., 2006, MNRAS, 371, 1334
Russell D. M., Lewis F., Bersier D., Cano Z., Gandhi P., Patruno A., Kalamkar M., Yang Y. J., Altamirano D., Casella P., Linares M., Padilla M. A., Cavecchi Y., Degenaar N., Kaur R., van der Klis M., Watts 2010, The Astronomer's Telegram, 2884, 1
Russell D. M., Maitra D., Dunn R. J. H., Fender R. P., 2011, ArXiv e-prints
Russell D. M., Maitra D., Dunn R. J. H., Markoff S., 2010, MNRAS, 405, 1759

Shaposhnikov N., Kazutaka Y., 2010, The Astronomer's Telegram, 2951, 1
Shaposhnikov N., Markwardt C., Swank J., Krimm H., 2010, ApJ, 723, 1817
Shaposhnikov N., Markwardt C. B., Swank J. H., 2009, The Astronomer's Telegram, 2269, 1
Shaposhnikov N., Titarchuk L., 2006, ApJ, 643, 1098
Shaposhnikov N., Titarchuk L., 2007, ApJ, 663, 445
Sobczak G. J., McClintock J. E., Remillard R. A., Cui W., Levine A. M., Morgan E. H., Orosz J. A., Bailyn C. D., 2000, ApJ, 531, 537
Sobolewska M. A., Życki P. T., 2006, MNRAS, 370, 405
Soleri P., Belloni T., Casella P., 2008, MNRAS, 383, 1089
Soleri P., Fender R., 2011, MNRAS, 413, 2269
Soleri P., Fender R., Tudose V., Maitra D., Bell M., Linares M., Altamirano D., Wijnands R., Belloni T., Casella P., Miller-Jones J. C. A., Muxlow T., Klein-Wolt M., Garrett M., van der Klis M., 2010, MNRAS, 406, 1471
Spruit H. C., 2002, A&A, 381, 923
Steeghs D., Miller J. M., Kaplan D., Rupen M., 2003, The Astronomer's Telegram, 146, 1
Stella L., Vietri M., 1998, ApJ, 492, L59+
Stiele H., Motta S., Muñoz-Darias T., Belloni T. M., 2011, ArXiv e-prints
Strohmayer T., Bildsten L., 2006, New views of thermonuclear bursts
Strohmayer T. E., Markwardt C. B., 2010, The Astronomer's Telegram, 2929, 1
Strohmayer T. E., Markwardt C. B., Pereira D., 2010, The Astronomer's Telegram, 2946, 1
Strohmayer T. E., Markwardt C. B., Swank J. H., in't Zand J., 2003, ApJ, 596, L67
Sturner S. J., Shrader C. R., 2005, ApJ, 625, 923
Sunyaev R., Revnivtsev M., 2000, A&A, 358, 617
Sunyaev R. A., Titarchuk L. G., 1980, A&A, 86, 121
Swank J. H., 2006, Advances in Space Research, 38, 2959
Sztajno M., van Paradijs J., Lewin W. H. G., Langmeier A., Trumper J., Pietsch W., 1986, MNRAS, 222, 499
Tagger M., Pellat R., 1999, A&A, 349, 1003
Takizawa M., Dotani T., Mitsuda K., Matsuba E., Ogawa M., Aoki T., Asai K., Ebisawa K., Makishima K., Miyamoto S., Iga S., Vaughan B., Rutledge R. E., Lewin W. H. G., 1997, ApJ, 489, 272
Tanaka Y., Lewin W. H. G., 1995, pp 126–174
Tananbaum H., Gursky H., Kellogg E., Giacconi R., Jones C., 1972, ApJ, 177, L5+
Titarchuk L., Hua X.-M., 1995, ApJ, 452, 226
Titarchuk L., Mastichiadis A., Kylafis N. D., 1996, A&A S.S., 120, C171+
Titarchuk L., Osherovich V., 1999, ApJ, 518, L95
Torres M. A. P., Jonker P. G., Steeghs D., Yan H., Huang J., Soderberg A. M., 2009,

The Astronomer's Telegram, 2263, 1
Torres M. A. P., Steeghs D., Jonker P. G., Thompson I., Soderberg A. M., 2009, The Astronomer's Telegram, 2268, 1
Tudose V., Fender R. P., Linares M., Maitra D., van der Klis M., 2009, MNRAS, 400, 2111
Uttley P., McHardy I. M., 2001, MNRAS, 323, L26
Uttley P., Wilkinson T., Cassatella P., Wilms J., Pottschmidt K., Hanke M., Böck M., 2011, MNRAS, 414, L60
van der Horst A. J., Granot J., Paragi Z., Kouveliotou C., Wijers R. A. M. J., Ramirez-Ruiz E., 2010, The Astronomer's Telegram, 2874, 1
van der Horst A. J., limford J. D., Taylor G. B., et al., 2010, The Astronomer's Telegram, 2918, 1
van der Klis M., 1989, Annual Reviews, 27, 517
van der Klis M., 2004, Advances in Space Research, 34, 2646
van der Klis M., 2006, Advances in Space Research, 38, 2675
van Paradijs J., Lewin H. G., 1986, A&A, 157, L10
Vaughan S., Edelson R., Warwick R. S., Uttley P., 2003, MNRAS, 345, 1271
Veledina A., Poutanen J., Vurm I., 2011, ApJ, 737, L17+
Vignarca F., Migliari S., Belloni T., Psaltis D., van der Klis M., 2003, A&A, 397, 729
Vovk I., Kuulkers E., Alfonso-Garzón J., Beckmann V., Bozzo E., Bird T., Chenevez S., Brandt J., Courvoisier T., Del Santo M., Domingo A., Ebisawa K., Jonker P., Kretschmar P., Markwardt C., Oosterbroek T., 2010, The Astronomer's Telegram, 2875, 1
Wagoner R. V., Silbergleit A. S., Ortega-Rodríguez M., 2001, ApJ, 559, L25
Wijnands R., Homan J., van der Klis M., 1999, ApJ, 526, L33
Wijnands R., Miller J. M., 2002, ApJ, 564, 974
Wijnands R., van der Klis M., 1998, Nature, 394, 344
Wilkinson T., Uttley P., 2009, MNRAS, 397, 666
Wilms J., Nowak M. A., Pottschmidt K., Pooley G. G., Fritz S., 2005, VizieR Online Data Catalog, 344, 70245
Wilms J., Nowak M. A., Pottschmidt K., Pooley G. G., Fritz S., 2006, A&A, 447, 245
Woosley S. E., Heger A., Cumming A., Hoffman R. D., Pruet J., Rauscher T., Fisker J. L., Schatz H., Brown B. A., Wiescher M., 2004, ApJS, 151, 75
Wu Y. X., Belloni T. M., Stella L., 2010, MNRAS, 408, 2413
Yu W., Dolence J., 2007, ApJ, 667, 1043
Yu W., van der Klis M., 2002, ApJ, 567, L67
Yu W., Yan Z., 2009, ApJ, 701, 1940
Zdziarski A. A., Gierliński M., Mikołajewska J., Wardziński G., Smith D. M., Harmon B. A., Kitamoto S., 2004, MNRAS, 351, 791

Zdziarski A. A., Grove J. E., Poutanen J., Rao A. R., Vadawale S. V., 2001, ApJ, 554, L45
Zdziarski A. A., Lubiński P., Smith D. A., 1999, MNRAS, 303, L11
Zdziarski A. A., Poutanen J., Mikolajewska J., Gierlinski M., Ebisawa K., Johnson W. N., 1998, MNRAS, 301, 435
Zdziarski A. A., Poutanen J., Paciesas W. S., Wen L., 2002, ApJ, 578, 357
Zhang G.-B., Qu J.-L., Zhang S., Zhang C.-M., Zhang F., Chen W., Song L.-M., Yang S.-P., 2007, ApJ, 659, 1511
Zhang S. N., Fishman G. J., Harmon B. A., Paciesas W. S., 1993, Nature, 366, 245
Zhang W., Jahoda K., Swank J. H., Morgan E. H., Giles A. B., 1995, ApJ, 449, 930
Zurita C., Durant M., Torres M. A. P., Shahbaz T., Casares J., Steeghs D., 2008, ApJ, 681, 1458

List of publications

Refereed journal papers

- Soleri, P., Muñoz-Darias, T., **Motta, S.**, Belloni, T., Casella, P., Mèndez, M., Altamirano, D., Linares, M., Wijnands, R., Fender, R., and van der Klis, M., *A failed spectral transition from the black hole candidate Swift J1753.5-0127*, submitted to MNRAS

- Ratti, E. M., Belloni, T. M., **Motta, S. E.**, *On the harminics of the low-frequency quasi-periodic oscillations in GRS 1915+105*, submitted to MNRAS

- Altamirano, D., Belloni, T., Linares, M., van der Klis, M., Wijnands, R., Curran, P., Kalamkar, M., Stiele, H., **Motta, S.**, Muñoz-Darias, T., Casella, P., Krimm, H., *The faint "heartbeats" of IGR J17091-3624: an exceptional black-hole candidate*, accepted by ApJ

- Russell, D.M., Curran, P.A., Muñoz-Darias, T., Lewis, F., **Motta, S.**, Stiele, H., Belloni, T., Miller-Jones, J.C.A., Jonker, P.G., O'Brien, K., Homan, J., Casella, P., Gandhi, P., Soleri, P., Markoff, S., Maitra, D., Gallo, E., Cadolle Bel, M., *A late jet rebrightening revealed from multi-wavelength monitoring of the black hole candidate XTE J1752-223*, accepted by MNRAS, 2011, arXiv, 1109.3654

- Belloni, T., **Motta, S.**, Muñoz-Darias, T., *Black hole transients*, to appear in 2011 September special issue of the Bulletin of the Astronomical Society of India on transients at different wavelengths, edited by D.J. Saikia and D.A. Green

- Stiele, H., **Motta, S.**, Muñoz-Darias, Belloni, T., *Spectral properties of transitions between soft and hard state in GX 339-4*, arXiv:1108.2198

- **Motta, S.**, Muñoz-Darias, T., Casella, P., Belloni, T., Homan, J., *Low frequency oscillation in black holes: a spectral-timing approach to the case of GX 339-4*, 2011, arXiv1108.0540M

- Muñoz-Darias, T., **Motta, S.**, Stiele, H., Belloni, T., *The black hole candidate MAXI J1659-152: spectral and timing analysis during its 2010 outburst*, 2011, MNRAS, 415, 292

- **Motta, S.**, D'Aì, A., Papitto, A., Riggio, A., Di Salvo, T., Burderi, L., Belloni T., Stella L., Iaria, R., *X-ray bursts and burst oscillations from the slowly spinning X-ray pulsar IGR J17480-2446*, 2011, MNRAS, 414, 1508

- Papitto, A., D'Ai', A., **Motta, S.**, Riggio, A., Burderi, L., Di Salvo, T., Belloni, T., *The spin and orbit of the newly discovered pulsar IGR J17480-2446*, 2011, A&A, 526, L3+

- Muñoz-Darias, T., **Motta, S.**, Belloni, T., *Fast variability as a tracer of accretion regimes in black hole binaries*, 2011, MNRAS, 410, 679-684

- **Motta, S.**, Muñoz-Darias, T. ,Belloni, T., *On the outburst evolution of H1743-322: a 2008/2009 comparison*, 2010, MNRAS, 408, 1796

- Muñoz-Darias, T., **Motta, S.**, Pawar, D., Belloni, T., Campana, S., Bhattacharya, D., *The hard state of black hole candidates: XTE J1752-223*, 2010 MNRAS, 404, L94

- **Motta, S.**, Belloni, T., Homan, J., *The evolution of the high-energy cut-off in the X-ray spectrum of GX 339-4 across a hard-to-soft transition*, 2009, MNRAS, 400, 1603-1612

- Belloni, T., Homan, J., **Motta, S.**, Ratti, E., Mèndez, M., *Rossi XTE monitoring of 4U1636-53 - I. Long-term evolution and kHz quasi-periodic oscillations*, 2007, MNRAS, 379, 247-252

Conference proceedings

- H. Stiele, T. Munoz-Darias, **S. Motta**, T. Belloni, *X-ray spectral and timing investigations of XTE J1752-223*, contribution to the proceedings of the 25th Texas Symposium on Relativistic Astrophysics (December 6-10, 2010, Heidelberg, Germany), accepted by Proceedings of Science (PoS)

- **Motta, S.**, Belloni, T., *Time evolution of the high-energy parameters of GX 339-4*, 2010, American Institute of Physics Conference Series, 1248, 185-186

- Belloni, T. M., **Motta, S.**, *Black-hole Binaries: Life Begins at 40 keV*, 2009, American Institute of Physics Conference Series, 1126, 185-188

Astronomer's Telegrams:

- XTE J1752-223 in transition from a soft to a hard state, ATel #2518; T. Muñoz Darias, S. Motta, T. Belloni (INAF - Brera Observatory), J. Homan (MIT)
- GX 339-4 in transition from the hard state, ATel #2545; S. Motta, T. Belloni, T. Muñoz Darias (INAF - Brera Observatory)
- Transition to the soft state in GX 339-4, ATel #2577; T. Belloni, S. Motta, T. Muñoz Darias (INAF - Brera Observatory)
- Multiple fast state transitions in GX 339-4, ATel #2593; S. Motta, T. Belloni, T. Muñoz-Darias (INAF - Brera Observatory), J. Homan (MIT)
- RXTE pointed observations of H 1743-322, ATel #2788; T.M. Belloni, T. Muñoz-Darias, S. Motta, H. Stiele, D. Carbone (INAF - Osservatorio Astronomico di Brera)
- H 1743-322 approaching state transition, ATel #2792; T.M. Belloni, T. Muñoz-Darias, S. Motta, H. Stiele, D. Carbone (INAF - Osservatorio Astronomico di Brera)
- Transition to the soft-intermediate state of MAXI J1659-152, ATel #2927; T. Belloni, S. Motta, T. Muñoz-Darias (INAF - Brera Observatory, Italy)
- A preliminary orbital solution for the transient eclipsing pulsar in Terzan 5, ATel #2939; A.Papitto, L.Burderi (Univ.Cagliari), A.D'Ai', T.Di Salvo (Univ.Palermo), S.Motta, T.Belloni (INAF-OAB), A.Sanna (Kapteyn Astr.Inst.), A.Riggio (INAF-OAC)
- Changes in the timing properties of MAXI J0556-332, ATel #3112; T. Belloni, S. Motta, T. Muñoz-Darias, H. Stiele (INAF - Brera Observatory, Italy)

  GX 339-4 in transition towards hard states, ATel #3117; T. Muñoz-Darias, S. Motta, T. Belloni, H. Stiele (INAF - Brera Observatory)
- IGR J17091-3624 undergoes 'heartbeat' oscillations similar to those of GRS 1915+105, ATel #3230; D. Altamirano (Univ. Amsterdam), T. Belloni (INAF-OAB), H. Krimm (CRESST/GSFC/USRA), P. Casella (Univ. Southampton), P. Curran (CEA/Saclay), J. Kennea (PSU), M. Kalamkar, M. van der Klis, R. Wijnands (Univ. Amsterdam), M. Linares (MIT), S. Motta, T. Muñoz-Darias, H. Stiele (INAF-OAB)
- A possible IR counterpart to the transient X-ray pulsar IGR J17480-2446 in Terzan 5, ATel #3264; V. Testa (INAF-OAR), T. Di Salvo (Univ. Palermo),

L. Burderi (Univ. Cagliari), M. T. Menna (INAF-OAR), T. M. Belloni (INAF-OAB), A. D'Ai' (Univ. Palermo), R. Iaria (Univ. Palermo), S. Motta (INAF-OAB), A. Papitto (Univ. Cagliari), A. Riggio (INAF-OAC)

- Swift does not detect a source near H 1743-322, ATel #3295; S. Motta, T. Belloni, S. Campana, T. Muñoz-Darias (INAF - Brera Observatory)

- RXTE observations strengthen the similarities between the black hole candidates IGR J17091-3624 and GRS 1915+105, ATel #3299; D. Altamirano (Univ. Amsterdam), T. Belloni (INAF-OAB), H. Krimm (CRESST/GSFC/USRA), P. Casella (Univ. Southampton), P. Curran (CEA/Saclay), J. Kennea (PSU), M. Kalamkar, M. van der Klis, R. Wijnands (Univ. Amsterdam), M. Linares (MIT), S. Motta, T. Muñoz-Darias, H. Stiele (INAF-OAB)

- H 1743-322 moves towards a state transition, ATel #3301; T. Belloni, H. Stiele, S. Motta, T. Muñoz-Darias (INAF - Brera Observatory, Italy)

- MAXI J1543-564 is probably a black hole candidate evolving through the hard intermediate state, ATel #3341; T. Muñoz-Darias, S. Motta, H. Stiele, T. Belloni (INAF - Brera Observatory)

- MAXI J1543-564 is in the soft state, ATel #3355; T. Muñoz-Darias, S. Motta, H. Stiele, T. Belloni (INAF - Brera Observatory)

- Observation of Gamma-Ray Emission from PSR J2022+3842, ATel #3466; M. Pilia, A. Treves (Universita' dell'Insubria), A. Pellizzoni, A. Trois (INAF-OACagliari), S. Motta (Insubria, INAF OABrera)

- Swift detects MAXI J1543-564 transition into hard state, ATel #3662; J. A. Kennea (PSU), S. Motta (INAF/Brera), P. Curran (CEA-Saclay), P. A. Evans (U Leicester). H. A. Krimm (CRESST/GSFC/USRA), P. Romano, V. Mangano (INAF-IASFPA), K. Yamaoka (AGU) and H. Negoro (Nihon U.)

Ringraziamenti

Ed ecco, finalmente, l'unica parte di tesi che (quasi) tutti leggeranno vermente. Evito di blaterare per righe e righe sulle banalitá del caso e parto. Vorrei ringraziare innanzi tutti i miei genitori. Loro mi hanno sempre supportato nelle mie scelte, tutte le scelte, anche quelle che forse non condividevano appieno, consapevoli del fatto che avrei preso la decisione giusta. Grazie papá e mamma per avermi permesso di intraprendere la mia strada e per aver sempre fiducia in me. Grazie anche a mio fratello: Marco, anche se hai un modo veramente bizzarro di mostrarlo, so che sei fiero di me. Grazie infinite a Luca, senza il quale non sarei arrivata fino a qui, tra le tante cose semplicemente perché i miei nervi avrebbero ceduto molto tempo fa. Grazie per avermi supportata e sostenuta sempre, per aver pazientemente assistito (e resistito) alle mie crisi isteriche dei momenti peggiori e per avermi incoraggiata in ogni momento. Grazie per aver gioito con me dei miei successi e per avermi consolata quando non andava troppo bene, ma soprattutto per avermi sempre capita al volo senza bisogno che spiegassi mai niente. Grazie anche al resto della mia famiglia: so che voi non avete idea di come io passi le mie giornate, ma sapere che pensate che quello che faccio è "fico" è sempre una bella cosa! Un enorme grazie a Eva che non ha mai smesso (e non smetterá mai, ne sono sicura) di cercare di convincermi del mio valore. Donna, grazie di aver sempre creduto in me e grazie di essere sempre stata presente. In molti mi hanno supportata in questi anni, ma solo tu potevi veramente capire certe cose e lo hai sempre fatto. Grazie infinite! Grazie anche a Mo, Clau e Paola, che sono sempre state pronte a correre in mio aiuto ogni qual volta l'umore calava e a festeggiare con me quando le cose andavano bene. Grazie anche a tutti i miei amici piu' cari per esserci sempre: grazie Gio, Fede, Ila, Claudio, Mauro, Lele e Davide.

Poi, piccolo salto verso un altro gruppo di esseri umani. Grazie Tomaso per avermi seguita dorante il mio dottorato (e anche prima, ma avevo gia' ringraziato 3 anni fa per quella parte, alla fine di un'altra tesi). Grazie per avermi insegnato molte delle cose che so dandomi gli strumenti per procedere anche da sola, ma soprattutto grazie per avermi sempre lasciata libera di sperimentare e per aver avuto fiducia nelle mie capacitá. Grazie a questo ho veramente imparato tanto ed ho capito come e' che deve funzionare la ricerca. Grazie a Tiziana e Luciano, che mi hanno fatto da supervisori a

distanza. Purtroppo non abbiamo avuto modo di lavorare gomito a gomito spesso, ma da molte delle conversazioni che ho avuto con voi ho imparato molto piu' di quanto potessi imparare leggendo molti molti libri e molti molti articoli. Grazie soprattutto per l'aiuto nel mese post-Creta. Per questo qui ringrazio anche Ale P. e Antonino. Grazie a tutti gli amici dell'Osservatorio, a quelli vecchi e a quelli nuovi. Un grazie particolare a Lorenzo, perché sapere che c'è un'altro Calimero come te è sempre una cosa che fa piacere, e a Teo, per essere un grande collega e un ottimo amico. Grazie a Peppe, che una pacca sulla spalla (la sua) non me l'ha mai negata e grazie a Pablo, che mi ha fatto da analista a distanza da luglio 2009 per curare le mie turbe da dottoranda stressata. Grazie a Betta, Rodolfo, Grazia, Elena, Riky e ... se vi elencassi tutti riempirei una pagina, ma soprattutto conoscendomi potrei dimenticare qualcuno per cui sentitevi inclusi in un bel "tutti gli altri", perdonate la banalitá.

Da ultimo, grazie al mio eterno amico caffè che mi ha sempre fatto compagnia e continuerá farmi compagnia negli anni a venire (anche se a volte nella disgustosa forma di quella cosa che all'estero chiamano caffè) e grazie a Robin Hobb e ai suoi libri, che mi hanno molto spesso permesso di andare a dormire senza pensare alle QPO.

Infine, una pacca sulla spalla a me stessa, che sono arrivata fino a qui e sperabilmente andró pure avanti. Brava!

The Legacy of a Genius
Tribute to Steve Jobs

"I am honored to be with you today at your commencement from one of the finest universities in the world. I never graduated from college. Truth be told, this is the closest I've ever gotten to a college graduation. Today I want to tell you three stories from my life. That's it. No big deal. Just three stories.

The first story is about connecting the dots.

I dropped out of Reed College after the first 6 months, but then stayed around as a drop-in for another 18 months or so before I really quit. So why did I drop out?

It started before I was born. My biological mother was a young, unwed college graduate student, and she decided to put me up for adoption. She felt very strongly that I should be adopted by college graduates, so everything was all set for me to be adopted at birth by a lawyer and his wife. Except that when I popped out they decided at the last minute that they really wanted a girl. So my parents, who were on a waiting list, got a call in the middle of the night asking: "We have an unexpected baby boy; do you want him?" They said: "Of course." My biological mother later found out that my mother had never graduated from college and that my father had never graduated from high school. She refused to sign the final adoption papers. She only relented a few months later when my parents promised that I would someday go to college.

And 17 years later I did go to college. But I naively chose a college that was almost as expensive as Stanford, and all of my working-class parents' savings were being spent on my college tuition. After six months, I couldn't see the value in it. I had no idea what I wanted to do with my life and no idea how college was going to help me figure it out. And here I was spending all of the money my parents had saved their entire life. So I decided to drop out and trust that it would all work out OK. It was pretty scary at the time, but looking back it was one of the best decisions I ever made. The minute I dropped out I could stop taking the required classes that didn't interest me, and begin dropping in on the ones that looked interesting.

It wasn't all romantic. I didn't have a dorm room, so I slept on the floor in friends' rooms, I returned coke bottles for the 5 cents deposits to buy food with, and I would walk the 7 miles across town every Sunday night to get one good meal a week at the Hare Krishna temple. I loved it. And much of what I stumbled into by following my curiosity and intuition turned out to be priceless later on. Let me give you one example:

Reed College at that time offered perhaps the best calligraphy instruction in the country. Throughout the campus every poster, every label on every drawer, was beautifully hand calligraphed. Because I had dropped out and didn't have to take the normal classes, I decided to take a calligraphy class to learn how to do this. I learned about serif and san serif typefaces, about varying the amount of space between different letter combinations, about what makes great typography great. It was beautiful, historical, artistically subtle in a way that science can't capture, and I found it fascinating.

None of this had even a hope of any practical application in my life. But ten years later, when we were designing the first Macintosh computer, it all came back to me. And we designed it all into the Mac. It was the first computer with beautiful typography. If I had never dropped in on that single course in college, the Mac would have never had multiple typefaces or proportionally spaced fonts. And since Windows just copied the Mac, it's likely that no personal computer would have them. If I had never dropped out, I would have never dropped in on this calligraphy class, and personal computers might not have the wonderful typography that they do. Of course it was impossible to connect the dots looking forward when I was in college. But it was very, very clear looking backwards ten years later.

Again, you can't connect the dots looking forward; you can only connect them looking backwards. So you have to trust that the dots will somehow connect in your future. You have to trust in something - your gut, destiny, life, karma, whatever. This approach has never let me down, and it has made all the difference in my life.

My second story is about love and loss.

I was lucky - I found what I loved to do early in life. Woz and I started Apple in my parents garage when I was 20. We worked hard, and in 10 years Apple had

grown from just the two of us in a garage into a 2 billion company with over 4000 employees. We had just released our finest creation - the Macintosh - a year earlier, and I had just turned 30. And then I got fired. How can you get fired from a company you started? Well, as Apple grew we hired someone who I thought was very talented to run the company with me, and for the first year or so things went well. But then our visions of the future began to diverge and eventually we had a falling out. When we did, our Board of Directors sided with him. So at 30 I was out. And very publicly out. What had been the focus of my entire adult life was gone, and it was devastating.

I really didn't know what to do for a few months. I felt that I had let the previous generation of entrepreneurs down - that I had dropped the baton as it was being passed to me. I met with David Packard and Bob Noyce and tried to apologize for screwing up so badly. I was a very public failure, and I even thought about running away from the valley. But something slowly began to dawn on me - I still loved what I did. The turn of events at Apple had not changed that one bit. I had been rejected, but I was still in love. And so I decided to start over.

I didn't see it then, but it turned out that getting fired from Apple was the best thing that could have ever happened to me. The heaviness of being successful was replaced by the lightness of being a beginner again, less sure about everything. It freed me to enter one of the most creative periods of my life.

During the next five years, I started a company named NeXT, another company named Pixar, and fell in love with an amazing woman who would become my wife. Pixar went on to create the worlds first computer animated feature film, Toy Story, and is now the most successful animation studio in the world. In a remarkable turn of events, Apple bought NeXT, I returned to Apple, and the technology we developed at NeXT is at the heart of Apple's current renaissance. And Laurene and I have a wonderful family together.

I'm pretty sure none of this would have happened if I hadn't been fired from Apple. It was awful tasting medicine, but I guess the patient needed it. Sometimes life hits you in the head with a brick. Don't lose faith. I'm convinced that the only thing that kept me going was that I loved what I did. You've got to find what you love. And that is as true for your work as it is for your lovers. Your work is going to fill a large part of your life, and the only way to be truly satisfied is to do what you believe is great work. And the only way to do great work is to love what you do. If you haven't found it yet, keep looking. Don't settle. As with all matters of the heart, you'll know when you find it. And, like any great relationship, it just gets better and better as the years roll on. So keep looking until you find it. Don't settle.

My third story is about death.

When I was 17, I read a quote that went something like: "If you live each day as if it was your last, someday you'll most certainly be right." It made an impression on me, and since then, for the past 33 years, I have looked in the mirror every morning

and asked myself: "If today were the last day of my life, would I want to do what I am about to do today?" And whenever the answer has been "No" for too many days in a row, I know I need to change something.

Remembering that I'll be dead soon is the most important tool I've ever encountered to help me make the big choices in life. Because almost everything - all external expectations, all pride, all fear of embarrassment or failure - these things just fall away in the face of death, leaving only what is truly important. Remembering that you are going to die is the best way I know to avoid the trap of thinking you have something to lose. You are already naked. There is no reason not to follow your heart.

About a year ago I was diagnosed with cancer. I had a scan at 7:30 in the morning, and it clearly showed a tumor on my pancreas. I didn't even know what a pancreas was. The doctors told me this was almost certainly a type of cancer that is incurable, and that I should expect to live no longer than three to six months. My doctor advised me to go home and get my affairs in order, which is doctor's code for prepare to die. It means to try to tell your kids everything you thought you'd have the next 10 years to tell them in just a few months. It means to make sure everything is buttoned up so that it will be as easy as possible for your family. It means to say your goodbyes.

I lived with that diagnosis all day. Later that evening I had a biopsy, where they stuck an endoscope down my throat, through my stomach and into my intestines, put a needle into my pancreas and got a few cells from the tumor. I was sedated, but my wife, who was there, told me that when they viewed the cells under a microscope the doctors started crying because it turned out to be a very rare form of pancreatic cancer that is curable with surgery. I had the surgery and I'm fine now.

This was the closest I've been to facing death, and I hope it's the closest I get for a few more decades. Having lived through it, I can now say this to you with a bit more certainty than when death was a useful but purely intellectual concept:

No one wants to die. Even people who want to go to heaven don't want to die to get there. And yet death is the destination we all share. No one has ever escaped it. And that is as it should be, because Death is very likely the single best invention of Life. It is Life's change agent. It clears out the old to make way for the new. Right now the new is you, but someday not too long from now, you will gradually become the old and be cleared away. Sorry to be so dramatic, but it is quite true.

Your time is limited, so don't waste it living someone else's life. Don't be trapped by dogma - which is living with the results of other people's thinking. Don't let the noise of others' opinions drown out your own inner voice. And most important, have the courage to follow your heart and intuition. They somehow already know what you truly want to become. Everything else is secondary.

When I was young, there was an amazing publication called The Whole Earth Catalog, which was one of the bibles of my generation. It was created by a fellow

named Stewart Brand not far from here in Menlo Park, and he brought it to life with his poetic touch. This was in the late 1960's, before personal computers and desktop publishing, so it was all made with typewriters, scissors, and polaroid cameras. It was sort of like Google in paperback form, 35 years before Google came along: it was idealistic, and overflowing with neat tools and great notions.

Stewart and his team put out several issues of The Whole Earth Catalog, and then when it had run its course, they put out a final issue. It was the mid-1970s, and I was your age. On the back cover of their final issue was a photograph of an early morning country road, the kind you might find yourself hitchhiking on if you were so adventurous. Beneath it were the words: "Stay Hungry. Stay Foolish." It was their farewell message as they signed off. Stay Hungry. Stay Foolish. And I have always wished that for myself. And now, as you graduate to begin anew, I wish that for you.

Stay Hungry. Stay Foolish.

Thank you all very much. "

Steven Paul Jobs,
June 12, 2005, Stanford University